ulm university universität
uulm

Fakultät für
Naturwissenschaften

Understanding Growth and Performance Drawbacks of the Solid-Electrolyte Interphase in Lithium-Ion Batteries

Kumulative Dissertation zur Erlangung des Doktorgrades Dr. rer. nat. der Fakultät für Naturwissenschaften der Universität Ulm

Vorgelegt von:

Lukas Köbbing
aus Bad Neuenahr-Ahrweiler

Ulm, 2025

Dekan:
Prof. Dr. Kay-Eberhard Gottschalk

Erstgutachter:
Prof. Dr. Birger Horstmann

Zweitgutachter:
Prof. Dr. Arnulf Latz

Drittgutachter:
Prof. Dr. Wolfgang Bessler

Viertgutachter:
Prof. Dr.-Ing. Thomas Wetzel

Tag der Promotion:
01. August 2025

Satz: PDF-LaTeX 2$_\varepsilon$

Contents

Preface

The present thesis is based on the results generated during my doctorate in the Department of Computational Electrochemistry at the Institute of Engineering Thermodynamics of the German Aerospace Center (DLR), affiliated with the Helmholtz Institute Ulm (HIU) for Electrochemical Energy Storage. The work was supervised by Prof. Dr. Birger Horstmann and Prof. Dr. Arnulf Latz.

Peer-Reviewed Publications

This thesis recapitulates my thermodynamically consistent theoretical investigations of the solid-electrolyte interphase (SEI). My studies focus on the growth mechanisms of the SEI as well as performance drawbacks due to the chemo-mechanical silicon-SEI interaction causing the silicon voltage hysteresis. Nowadays, lithium-ion batteries enable refined consumer electronics and are increasingly important for the transition towards a sustainable energy system. Thus, an improved theoretical understanding of the main degradation mechanism and the challenges for next-generation anode materials, namely silicon, in terms of efficiency and precise state estimation is of superior relevance. Aiming to contribute to a detailed insight, this cumulative dissertation presents the common theoretical foundation and a summary of the following four scientific papers I published during my doctorate.

I Lukas Köbbing, Arnulf Latz, and Birger Horstmann. Growth of the solid-electrolyte interphase: Electron diffusion versus solvent diffusion. *Journal of Power Sources* **2023**, 561, 232651, doi: 10.1016/j.jpowsour.2023.232651.

II Lukas Köbbing, Arnulf Latz, and Birger Horstmann. Voltage Hysteresis of Silicon Nanoparticles: Chemo-Mechanical Particle-SEI Model. *Advanced Functional Materials* **2024**, 34 (7), 2308818, doi: 10.1002/adfm.202308818.

III Lukas Köbbing, Yannick Kuhn, and Birger Horstmann. Slow Voltage Relaxation of Silicon Nanoparticles with a Chemo-Mechanical Core-Shell Model. *ACS Applied Materials & Interfaces* **2024**, 16 (49), 67609–67619, doi: 10.1021/acsami.4c12976.

IV Raphael Schoof, Lukas Köbbing, Arnulf Latz, Birger Horstmann, and Willy Dörfler. Elliptical Silicon Nanowire Covered by the SEI in a 2D Chemo-

Mechanical Simulation. *Batteries & Supercaps* **2025**, 8 (5), e202400604, doi: 10.1002/batt.202400604.

Journalistic Publication

Furthermore, I had the opportunity to write a journalistic, German-language article about lithium-ion batteries, addressing the members of the German Physical Society (Deutsche Physikalische Gesellschaft, DPG). In addition to the general introduction, the focus was set on the development of next-generation anode materials, presenting their benefits and open challenges for commercialization. This journalistic article is not part of the present cumulative thesis but is stated here for completeness and as a pleasant by-product of my doctorate.

(**V**) Lukas Köbbing, Arnulf Latz, and Birger Horstmann. Batterien wie Sand am Meer. *Physik Journal* **2024**, 23 (5), 28-34, url: https://pro-physik.de/zeitschriften/physik-journal/2024-5/, available preprint: https://elib.dlr.de/204279/.

Contributions to Conferences

Additionally, I got the chance to present preliminary results of my research at several (international) conferences to a broad scientific audience.

1. Lukas Köbbing, Birger Horstmann, and Arnulf Latz. Modeling and Simulation of Transport, Interfaces and Mechanics inside the SEI. *18th Symposium on Modeling and Experimental Validation of Electrochemical Energy Technologies (ModVal2022)*, Hohenkammer, Germany, 14. – 16. March 2022. Poster Presentation

2. Lukas Köbbing, Arnulf Latz, and Birger Horstmann. Theory and Simulation of Transport and Mechanics of a Polycrystalline SEI. *31st Topical Meeting of the International Society of Electrochemistry*, Aachen, Germany, 15. – 19. May 2022. Poster Presentation

3. Lukas Köbbing, Birger Horstmann, and Arnulf Latz. Theory and Modeling of Transport, Interfaces and Mechanics inside the Solid Electrolyte Interphase. *International Meeting on Lithium Batteries (IMLB)*, Sydney, Australia, 26. June – 01. July 2022. Poster Presentation

4. Lukas Köbbing, Lars von Kolzenberg, Arnulf Latz, and Birger Horstmann. How Does the Solid-Electrolyte Interphase Grow? Transport Mechanisms, Mechanics and Interfaces. *Workshop on Computational Modeling of Batteries*, Reisensburg, Germany, 23. – 26. October 2022. Poster Presentation

5. Lukas Köbbing, Arnulf Latz, and Birger Horstmann. Modeling of the Solid-Electrolyte Interphase: Transport Mechanisms and Mechanics. *243rd Meeting of the Electrochemical Society*, Boston, USA, 28. May – 02. June 2023. Oral Presentation

6. Lukas Köbbing, Arnulf Latz, and Birger Horstmann. Description of the Silicon Voltage Hysteresis with a Visco-Elastoplastic SEI Model. *HIU Biennial Meeting*, Ulm, Germany, 11. – 12. July 2023. Oral Presentation

7. Lukas Köbbing, Arnulf Latz, and Birger Horstmann. Continued SEI Growth and its Impact on the Silicon Potential Hysteresis. *74th Annual Meeting of the International Society of Electrochemistry*, Lyon, France, 03. – 08. September 2023. Oral Presentation

8. Lukas Köbbing, Arnulf Latz, and Birger Horstmann. Elucidating the Silicon Voltage Hysteresis by Mechanical Coupling of Anode Particles and the SEI. *Spring Meeting of the Deutsche Physikalische Gesellschaft (DPG)*, Berlin, Germany, 17. – 22. March 2024. Oral Presentation

9. Lukas Köbbing, Arnulf Latz, and Birger Horstmann. Understanding the Silicon Voltage Hysteresis by considering the impact of the Solid-Electrolyte Interphase (SEI). *Advanced Battery Power*, Münster, Germany, 09. – 11. April 2024. Poster Presentation

10. Lukas Köbbing, Arnulf Latz, and Birger Horstmann. Explaining the Voltage Hysteresis and Slow Relaxation of Silicon Nanoparticles with a Chemo-Mechanical Particle-SEI Model. *Pacific Rim Meeting on Electrochemical and Solid State Science (PRiME)*, Honolulu, USA, 06. – 11. October 2024. Poster Presentation

11. Lukas Köbbing, Yannick Kuhn, Arnulf Latz, and Birger Horstmann. Chemo-Mechanical Core-Shell Model Explaining the Silicon Voltage Hysteresis and Long-Term Relaxation. *21st Symposium on Modeling and Experimental Validation of Electrochemical Energy Technologies (ModVal2025)*, Karlsruhe, Germany, 10. – 12. March 2025. Oral Presentation

Acknowledgements

First of all, I would like to thank everyone who has supported and accompanied me on my path to graduation.

Particularly, I want to thank my doctoral adviser, Prof. Dr. Birger Horstmann, and my second supervisor, Prof. Dr. Arnulf Latz. I am grateful to have benefited from your knowledge, experience, and advice throughout my entire doctorate.

I highly appreciate funding from the German Research Foundation (DFG) within the research training group SiMET under project number 281041241/GRK2218. Furthermore, I thank the European Union for funding within Horizon Europe in the project OPINCHARGE under project number 101104032 as part of the Battery2030+ initiative.

In addition to the funding, I thank the people in the two projects who filled the projects with life. I especially want to thank my SiMET supervisor, Prof. Dr. Wolfgang Bessler, for regular discussions at the project meetings and for providing good advice. Moreover, I thank Raphael Schoof for performing the computational work for our joint publication, without whom the two-dimensional aspects of the silicon-SEI interaction would have remained concealed.

On top of these specific connections, I want to thank all my colleagues for greatly supporting my work progress and overall well-being. Particularly, I appreciate fruitful discussions with Lars von Kolzenberg, Martin Werres, Micha Philipp, Felix Schwab, Franziska Kilchert, Linda Bolay, Marvin Gajewski, Yannick Kuhn, and Dominik Wycisk. Moreover, I want to thank all my informal mentors who supported the initiation and progress of my doctorate.

Last but certainly not least, I want to thank my family and friends, who have equipped me with a calibrated compass and have accompanied me on my path or parts of it with tireless commitment. Thank you for offering me all the opportunities to get to this point in my academic education.

Abstract

Modern lithium-ion batteries present an important energy storage technology with a reasonable service life, though still suffering from continued capacity fade. Additionally, pure silicon anodes desired for advanced energy densities face efficiency drawbacks, heat generation, and imprecise state-of-charge (SOC) estimation due to the occurrence of a voltage hysteresis. This thesis elucidates the capacity loss and the silicon voltage hysteresis by considering the solid-electrolyte interphase (SEI), which forms at the anode side owing to electrolyte decomposition. To understand the impact of the SEI and facilitate respective improvements, thermodynamically consistent continuum models are further developed and analyzed.

First, this thesis focuses on the investigation of SEI growth, which is considered the main cause of capacity fade in lithium-ion batteries with standard graphite anodes. Thus, a detailed comprehension of the SEI can support increased battery lifetimes. Generating valuable insights, this study compares the diffusion of electrons and solvent molecules through the SEI as possible drivers of SEI growth during battery storage. The simulation results aim to reproduce experimental findings regarding the time and SOC dependence of capacity loss as well as their interplay. The careful comparison approves the electron diffusion as the decisive mechanism for continued SEI growth on graphite anodes.

For next-generation lithium-ion batteries, silicon is a promising candidate for substituting graphite with a significant capacity increase. However, the enhanced ability of lithiation is accompanied by substantial volume changes during cycling, highlighting mechanical aspects. In particular, the SEI deforms purely mechanically and causes distinct stresses acting on the silicon particle. The arising stresses inside the silicon anode influence the voltage due to chemo-mechanical coupling. Thus, the simulations reveal that the mechanical impact of the SEI causes the observed voltage hysteresis of silicon nanoparticle anodes during cycling and (after) relaxation. Moreover, the chemo-mechanical description fits the observed long-term voltage relaxation. Hence, the model provides a consistent picture of the observed voltage hysteresis phenomena. For ordinary voltage estimations, the study derives a reduced chemo-mechanical hysteresis model, which preserves physical interpretability and covers voltage relaxations contrary to the empirical Plett model. Eventually, the work investigates the effect of the SEI on an elliptical silicon nanowire. The results reveal lithium concentration anomalies due to the anode geometry and the mechanical impact of the SEI.

Overall, this work contributes to an improved understanding of the SEI regarding

growth mechanisms and the mechanical impact on silicon anodes. Particularly, the chemo-mechanical interaction of silicon and SEI is considered the reason for the voltage hysteresis herein for the first time. Consequently, this thesis aims to facilitate enhanced battery lifetime and efficiency by advancing SEI properties.

Kurzfassung

Moderne Lithium-Ionen-Batterien stellen eine wichtige Energiespeichertechnologie mit einer angemessenen Lebensdauer dar, die dennoch unter kontinuierlichem Kapazitätsverlust leidet. Darüber hinaus stehen der Verwendung von reinen Silizium-Anoden für verbesserte Energiedichten Effizienznachteile, Wärmeentwicklung und eine ungenaue Schätzung des Ladezustands (SOC) wegen einer auftretenden Spannungshysterese im Weg. Diese Dissertation beleuchtet den Kapazitätsverlust sowie die Spannungshysterese von Silizium durch Betrachtung der *Solid-Electrolyte Interphase* (SEI), die sich aufgrund von Elektrolytzersetzung an der Anode bildet. Um die Auswirkungen der SEI zu verstehen und entsprechende Verbesserungen zu ermöglichen, werden thermodynamisch konsistente Kontinuums-Modelle weiterentwickelt und analysiert.
Zunächst konzentriert sich diese Arbeit auf die Untersuchung des SEI-Wachstums, das als Hauptursache für den Kapazitätsverlust in Lithium-Ionen-Batterien mit üblichen Graphit-Anoden gilt. Daher kann ein detailliertes Verständnis der SEI zu einer Verlängerung der Batterielebensdauer beitragen. Um wertvolle Erkenntnisse zu gewinnen, vergleicht diese Studie die Diffusion von Elektronen und Lösungsmittelmolekülen durch die SEI als mögliche Verursacher des SEI-Wachstums während der Lagerung der Batterie. Die Simulationsergebnisse zielen darauf ab, die experimentellen Ergebnisse hinsichtlich der Zeit- und SOC-Abhängigkeit des Kapazitätsverlustes sowie deren Zusammenspiel zu reproduzieren. Der sorgfältige Vergleich bestätigt die Elektronendiffusion als den entscheidenden Mechanismus für das kontinuierliche SEI-Wachstum auf Graphit-Anoden.
Für Lithium-Ionen-Batterien der nächsten Generation ist Silizium ein vielversprechender Kandidat für den Ersatz von Graphit mit einer deutlichen Kapazitätssteigerung. Die verbesserte Fähigkeit der Lithiumaufnahme geht jedoch mit erheblichen Volumenänderungen während der Zyklisierung einher, was mechanische Aspekte hervorhebt. Insbesondere die SEI verformt sich rein mechanisch und verursacht deutliche Drücke, die auf die Siliziumpartikel einwirken. Die entstehenden Drücke im Inneren der Siliziumanode beeinflussen die elektrische Spannung aufgrund der chemo-mechanischen Kopplung. Daher zeigen die Simulationen, dass der mechanische Einfluss der SEI die beobachtete Spannungshysterese von Silizium-Nanopartikel-Anoden während der Zyklisierung und (nach) der Relaxation verursacht. Außerdem passt die chemo-mechanische Beschreibung zu der beobachteten langfristigen Spannungsrelaxation. Somit liefert das Modell ein konsistentes Bild der beobachteten Spannungshysterese-

phänomene. Für einfache Spannungsabschätzungen leitet die Studie ein reduziertes chemo-mechanisches Hysteresemodell ab. Das vereinfachte Modell bewahrt physikalische Interpretierbarkeit und umfasst die Beschreibung von Spannungsrelaxation im Gegensatz zum empirischen Plett-Modell. Schließlich untersucht die Arbeit die Auswirkungen der SEI auf einen elliptischen Silizium-Nanodraht. Die Ergebnisse zeigen Anomalien in der Lithiumkonzentration, die sowohl auf die Geometrie der Anode als auch den mechanischen Einfluss der SEI zurückzuführen sind.
Insgesamt trägt diese Arbeit zu einem verbesserten Verständnis der SEI in Bezug auf Wachstumsmechanismen und den mechanischen Einfluss auf Silizium-Anoden bei. Insbesondere wird hierin zum ersten Mal die chemo-mechanische Wechselwirkung von Silizium und SEI als Ursache für die Spannungshysterese betrachtet. Somit beabsichtigt diese Dissertation eine gesteigerte Lebensdauer und Effizienz von Batterien durch die Weiterentwicklung der Eigenschaften der SEI zu ermöglichen.

List of Abbreviations

AIMD	Ab initio molecular dynamics
BEV	Battery electric vehicle
BMS	Battery management system
CE	Center point
cryo-EM	Cryogenic electron microscopy
DEC	Diethyl carbonate
DFT	Density functional theory
DMC	Dimethyl carbonate
EC	Ethylene carbonate
EMC	Ethyl methyl carbonate
FEC	Fluoroethylene carbonate
GITT	Galvanostatic intermittent titration technique
KKT	Karush-Kuhn-Tucker condition
LCO	Lithium cobalt oxide
LFP	Lithium iron phosphate
Li_2EDC	Lithium ethylene dicarbonate
LMFP	Lithium manganese iron phosphate
LR	Lower right point (i.e. end of the major half-axis)
LTO	Lithium titanium oxide
NCA	Lithium nickel cobalt aluminum oxide
NMC	Lithium nickel manganese cobalt oxide
NP	Nanoparticle
OCV	Open-circuit voltage
PC	Propylene carbonate
SEI	Solid-electrolyte interphase
SOC	State-of-charge
SOH	State-of-health
UL	Upper left point (i.e. end of the minor half-axis)
VC	Vinylene carbonate

List of Symbols

Bold letters

$\mathbf{C}$	Cauchy-Green tensor
$\mathbf{E}$	Strain tensor
$\mathbf{F}$	Deformation gradient tensor
$\mathbf{Id}$	Identity matrix
$\mathbf{L}_{\mathrm{pl}}$	Plastic flow
$\mathbf{M}$	Mandel stress
$\mathbf{P}$	First Piola-Kirchhoff stress
$\mathbf{T}_{\mathrm{rev}}$	Reversible second Piola-Kirchhoff stress
σ	Cauchy stress

Capital letters

A	Surface area
$\mathcal{B}$	Continuum material body
C	C-rate
D	Diffusion coefficient
E	Young's modulus
F	Faraday constant
$G_{\mathrm{Si/SEI}}$	Second Lamé constant of silicon/SEI
J	Relative volume change
L	Mobility
L_{SEI}	SEI thickness
$\vec{N}$	Flux
Q	Capacity
$\mathcal{R}$	Entropy production
$R_{(\mathrm{Si})}$	Particle radius
R_{gas}	Universal gas constant
R_{rate}	SEI formation reaction rate
T	Temperature
U	Voltage
U_0	Open-circuit voltage (OCV)
V	Volume

Lowercase letters

$\vec{b}$	Body force
c	Concentration
e	Energy
f	Yield criterion
$\vec{g}$	Momentum
j	Current density
j_0	Exchange current density
k	Rate constant
$\vec{n}$	Normal vector
r	Radial coordinate
s	Entropy
s_{Li}	Mean stoichiometric coefficient of Li in SEI formation
s_ζ	Source of quantity ζ
t	Time
u	Internal energy
v	Partial molar volume of SEI species
v_{Li}	Partial molar volume of lithium inside silicon
$\vec{v}$	Velocity vector
x, $\vec{x}$	Position coordinate, vector
z	Charge number

Greek letters

α	Symmetry factor in Butler-Volmer equation
α_a, α_c	Anodic and cathodic transfer coefficient
α_{red}	Auxiliary parameter for reduced hysteresis model
β	Exponent in power law t^β
ζ	Arbitrary field
η	Viscosity
η_{r}	Overpotential
λ_{ch}	Chemical deformation
$\lambda_{\mathrm{Si/SEI}}$	First Lamé constant of silicon/SEI
μ	Chemical potential
ν	Poisson ratio
ρ	Density
$\boldsymbol{\sigma}$	Cauchy stress
σ_{ref}	Reference stress
σ_{Y}	Yield stress
τ	Time constant
ϕ	Plastic multiplier
φ	Free energy
χ	Mapping of the undeformed to the deformed configuration
Ω	Region of continuum body

Subscripts

a	Adapted quantity
ch	Chemical
core	Silicon core
e^-	Electron
EC	Ethylene carbonate (electrolyte solvent)
educts	Educt species of reaction
ee	Elastic stress in silicon due to elastoplastic stress of SEI
el	Elastic
eq	Equilibrium
ev	Elastic stress in silicon due to viscous stress of SEI
i	Arbitrary species
int	Interface
mag	Magnitudes of entries in tensor
max	Maximum possible value
n	Normal component
O	Oxidized species
pl	Plastic
R	Reduced species
red	Reduced model
ref	Reference value
rev	Reversible
rr	Radial component
shell	SEI shell
t	Tangential component
visc	Viscous
Y	Yield
$\varphi\varphi$	Tangential component
0	Lagrangian frame for chemo-mechanical aspects
0	Reference ($c_{e^-,0}$, j_0) or initial values ($L_{SEI,0}$, t_0) for SEI growth

Superscripts

corr	Corrected
delith	Delithiation
dev	Deviatoric
lith	Lithiation
soft	Soft SEI, i.e. small Young's modulus
stiff	Stiff SEI, i.e. large Young's modulus
T	Transpose

List of Figures

1 Introduction and Motivation

Rechargeable lithium-ion batteries have virtually revolutionized our lives, enabling mobile applications like portable consumer electronics and medical devices. Since their market launch, research and industry are working on advancements to meet the world's demand for better batteries. Improved battery characteristics are desired not only for the sake of additional convenient uses but also for the essential fight against accelerating climate change. Particularly, two of the actual strengths of the lithium-ion technology, a decent lifetime and a superior energy density, have to be further increased for future applications. This thesis deals with the identified bottlenecks, namely the negative electrode degradation and performance, and intends to contribute to their elimination.

The oil crises of the 1970s stimulated the quest for new battery chemistries with advanced energy density to create alternative energy storage technologies [1]. The shared objective was to reduce the dependency on burning fossil fuels delivered from only a few oil states. Additionally, the emergence of portable consumer electronics promoted these efforts [2]. Thus, numerous researchers from industry and academia have been involved in investigating innovative components for novel batteries. Continuing progress eventually led to the commercialization of the first lithium-ion battery by Sony in 1991. Especially the contributions of M. Stanley Whittingham [3–6] and John B. Goodenough [7, 8] for the development of cathode materials as well as Akira Yoshino [2, 9] for the first implementation of carbonaceous anodes have been awarded with the Nobel prize for chemistry in 2019. Since the commercial availability, lithium-ion batteries have significantly influenced our way of living by facilitating various innovations such as smartphones, laptops, smartwatches, e-bikes, or drones [10].

Vehicles with battery-electric drive were invented already at the end of the 19th century but then superseded by the internal combustion engine. Rising oil prices in the 1990s and attempts to reduce air pollution stimulated the automotive industry to engineer and sell battery electric vehicles (BEVs) – though not yet equipped with modern lithium-ion batteries. Only in the last few years has mass production of advanced lithium-ion batteries made BEVs reasonably comfortable and affordable. Policymakers worldwide foster the trend towards electric cars to reduce carbon dioxide emissions and benefit from the superior efficiency of BEVs [11, 12]. The transition to electrified transportation is not limited to cars but also applies to trucks, buses, trains, boats, and efforts for battery electric regional aircraft. However,

transitioning the transportation sector is only one piece of the puzzle towards a carbon-neutral future. To combat climate change, new types of energy storage are urgently required to replace the use of fossil fuels [13]. While several forms of energy storage will be needed in parallel, lithium-ion batteries represent a superior storage system due to the beneficial interplay of lifetime, energy density, costs, efficiency, and simplicity of use. Therefore, lithium-ion batteries are increasingly installed as stationary intermediate energy storage to stabilize the power grid and compensate for fluctuations within the generation of renewable energies like wind and solar power [14–16]. Although an increased lifetime and energy density are two major advancements of lithium-ion batteries compared to previous battery technologies, these factors represent bottlenecks today and have to be further enhanced to facilitate an even wider range of applications.

The lifetime of lithium-ion batteries is in general determined by several degradation mechanisms and their interaction [17–20]. The most important degradation particularly during storage is the continued growth of the solid-electrolyte interphase (SEI). The SEI forms a layer covering the anode due to electrolyte reduction. On the one hand, the SEI formation reaction of lithium ions, electrons, and molecules from the electrolyte consumes cyclable lithium, decreasing the cell capacity. On the other hand, this layer has a passivating effect and limits further growth of the SEI, which decelerates ongoing capacity fade. Thus, the existence of the SEI makes battery operation possible in the first place. As the SEI is decisive for the longevity of the battery, a lot of research effort is put into understanding and improving the interphase characteristics.

The energy density of state-of-the-art lithium-ion batteries is limited by using graphite as ordinary anode material. Silicon anodes promise a superior energy density but come along with substantial volume changes during cycling of up to 300 %. The volume changes cause reduced mechanical stability, which can be enhanced by the application of nano-structured silicon anodes. As silicon anodes are also covered by an SEI layer, it is important to consider the mechanical interaction between the silicon nanoparticles and the SEI during cycling. Besides mechanical stability, performance limitations due to a voltage hysteresis observed for silicon anodes hinder the broad commercial use of batteries with pure silicon anodes.

This thesis aims to contribute to a clearer view of the relevant SEI growth mechanisms as well as the consequences of the mechanical interaction between silicon and SEI. In the introduction, Section 1.1 presents the general functional principle and common anode materials of modern lithium-ion batteries. Subsequently, Section 1.2 introduces the solid-electrolyte interphase (SEI) forming on the anode, causing capacity degradation. Completing the introduction, Section 1.3 outlines the voltage hysteresis phenomenon of silicon anodes, which is a significant performance issue of next-generation batteries. Afterwards, Chapter 2 describes a thermodynamically

consistent continuum theory, and Chapter 3 elaborates on the simulation results with a focus on the growth of the SEI and the chemo-mechanical interaction of silicon and SEI. Finally, this thesis closes with a conclusion in Chapter 4.

1.1 Lithium-Ion Batteries

Since the first commercial lithium-ion batteries in the early 1990s, they are characterized by a higher energy density compared to previous battery chemistries. The basic working principles of these pioneering cells have been used since then, whereas the individual components have been replaced or improved.

1.1.1 Construction Principle

Lithium-ion batteries, as schematically illustrated in Fig. 1.1, consist of two electrodes that are separated by a separator to avoid an electrical short. The negative electrode is called anode, and the positive one cathode. The electrodes as well as the separator are soaked with a typically liquid electrolyte made out of solvent molecules and a lithium salt. The electrolyte supports the transport of lithium ions through the battery but does not allow for electron transport.
The working principle is as follows: Lithium atoms inside the anode possess a high energy corresponding to a low electrical potential. In contrast, lithium atoms inside the cathode possess a low energy corresponding to a high electrical potential. The chemical potential difference between the lithium in the two electrodes corresponds to a voltage, which absorbs energy when lithium moves from the cathode to the anode and releases energy during motion in the opposite direction. To ensure charge neutrality inside the electrodes, lithium ions travel through the battery from one electrode to the other to compensate for the electronic transport through the external circuit. Therefore, neutral lithium is stored inside the anode with high potential energy when the battery is charged and inside the cathode with low potential energy when the battery is discharged [10]. The flow of electrons and lithium ions is permanently controlled by a battery management system (BMS) to stay within the permitted working conditions. The in-operando estimation of the state-of-charge (SOC) and state-of-health (SOH) of the battery is of particular significance and certainly non-trivial [21].
As indicated earlier, the single components used inside modern lithium-ion batteries have changed since the first commercial cells. The electrolyte solvent used in the first commercial cell was propylene carbonate (PC), which tends to cointercalate into graphite and promotes graphite exfoliation [1]. Thus, it was only a few years later replaced by ethylene carbonate (EC) mixed with a linear carbonate like dimethyl carbonate (DMC), ethyl methyl carbonate (EMC), or diethyl carbonate (DEC). Fur-

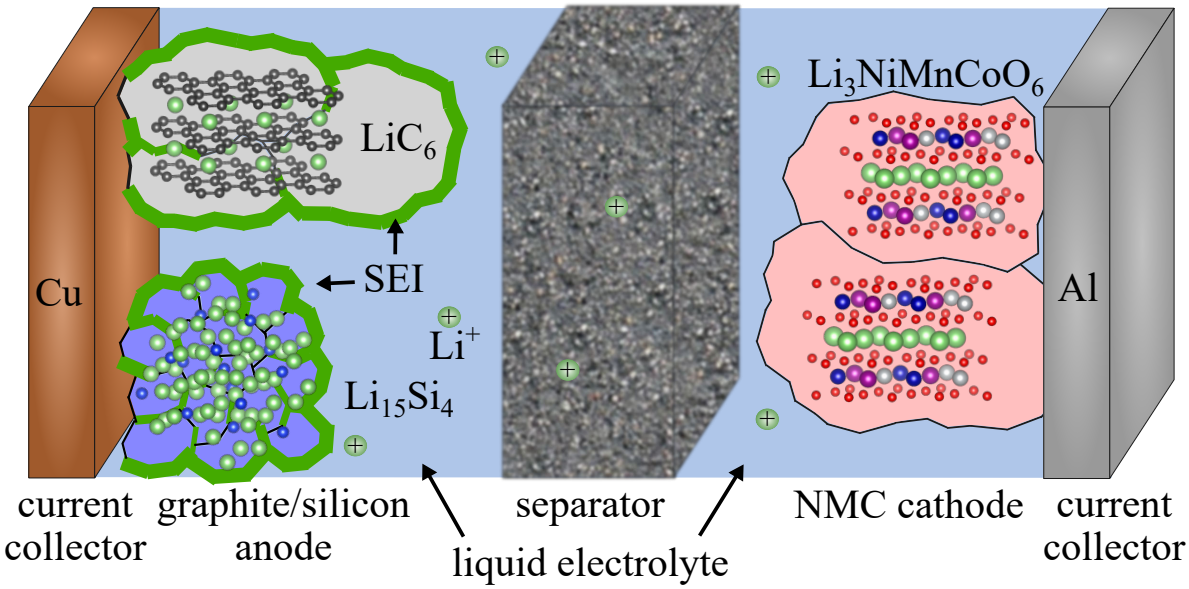

Figure 1.1: Scheme of the construction principle of a lithium-ion battery. Particularly, anodes based on silicon nanoparticles instead of graphite can increase the volumetric and gravimetric energy density. Independent of the material choice, a solid-electrolyte interphase (SEI) covers the anode particles.

thermore, the insertion of additives into the electrolyte ensures the formation of a stable solid-electrolyte interphase layer as introduced in Section 1.2, essential for an extended service life. At the cathode side, the first commercial cell used lithium cobalt oxide (LCO). Nowadays, besides LCO, there is a variety of cathode materials available with reduced cobalt content like lithium nickel manganese cobalt oxide (NMC) and lithium nickel cobalt aluminum oxide (NCA) as well as cobalt-free compounds like lithium iron phosphate (LFP) and more recently lithium manganese iron phosphate (LMFP). To enable fast cycling and thicker electrodes, the cathode and anode active material are mixed with a conductive binder, promoting electronic transport and mechanical stability. In the following, the anode materials and their characteristics are discussed in more detail to reflect their importance for the present work.

1.1.2 Anode Materials and Characteristics

The choice of the anode material crucially impacts the defining properties of the battery, like energy density, specific energy, safety, and lifetime. The first commercial Sony cell deployed soft carbon (carbon that can be converted to graphite at elevated temperatures), while their second generation used hard carbon (carbon that is non-graphitizable) [1]. Afterwards, the transition to PC-free electrolytes enabled the use of graphite, which has been established as the standard anode material for lithium-ion batteries. Nevertheless, the search for improved properties with the focus either on

lifetime or energy density brings other anode materials (back) into play [22–25].

Graphite

Since the mid-1990s, graphite has been the ordinary anode material replacing soft and hard carbons [26, 27]. The carbon atoms inside graphite form layers with a hexagonal lattice structure. The distinct distance between the lattice layers allows the intercalation of lithium into the carbon structure.
Due to the underlying host structure, graphite has a rather restricted ability for lithiation. Only up to one lithium atom can be stored by six carbon atoms, creating the fully lithiated graphite compound LiC_6. Therefore, the theoretical specific capacity is limited to 372 mAh/g referred to the unlithiated state (340 mAh/g referred to the lithiated state).
Nevertheless, the host structure confines the volume expansion during lithiation to only about 10 %, minimizing mechanical degradation issues such as particle cracking. The only minor deformations allow the growth of a well-passivating and resilient solid-electrolyte interphase (SEI), which will be discussed in detail in Section 1.2. The superior mechanical stability of the graphite particles and the SEI facilitates a suitable battery lifetime of more than 1000 cycles and 20 years [28–30].

Lithium Titanium Oxide (LTO)

A commercially available alternative to graphite is lithium titanium oxide (LTO), also called lithium titanate spinel, with the chemical composition $Li_4Ti_5O_{12}$ [31–33]. It is significantly less common than graphite due to a minor theoretical specific capacity of 175 mAh/g (167 mAh/g referred to the lithiated state $Li_7Ti_5O_{12}$) and a higher anode potential of about 1.5 V versus lithium compared to about 0.1 V for graphite. Both properties lead to a decreased energy density of full cells using LTO anodes. Nevertheless, the negligible volume change of less than 0.3 % [32, 34] and the high anode potential suppressing SEI growth (cf. Section 1.2) results in an impressive lifetime of more than 10 000 cycles [33]. Additionally, LTO anodes allow for an increased full-cell power density compared to graphite cells [33]. Thus, LTO anodes can be beneficial for applications requiring very high power and multiple cycles per day, like battery electric trains.

Lithium Metal

In terms of increasing energy density, lithium metal anodes are commonly considered the "holy grail" in battery research. Lithium metal shows the maximum possible theoretical capacity of 3860 mAh/g naturally referred to the lithiated state [35–40].
However, lithium does not plate as a homogeneous, compact layer during charging but forms inhomogeneous structures called mossy lithium and lithium whiskers.

These structures transition to form dendrites depending on the applied current and cycled capacity, which can penetrate the separator and cause an electrical short in the worst case [41]. Moreover, the passivating SEI layer (see Section 1.2) has to regrow in every cycle consuming cyclable lithium. During discharge, inhomogeneous stripping of lithium can cause contact loss of lithium structures with the current collector creating non-cyclable, dead lithium.
The described safety issues caused the failure of the early commercialization of lithium-metal anodes in the 1980s, several years before the commercialization of graphite anode cells [1]. Therefore, research efforts focus on enabling homogeneous lithium plating by improving liquid electrolytes with different additives, proceeding to solid electrolytes, and building artificial interphase layers [42]. Although increased cycle performances have been reported, the commercial application of rechargeable lithium-metal batteries still requires several improvements [39].

Silicon

Due to the challenges of lithium-metal anodes, silicon is regarded as a promising candidate for next-generation lithium-ion batteries [43–48]. Silicon alloys with lithium up to $Li_{15}Si_4$, revealing a high theoretical capacity of 3579 mAh/g referred to the unlithiated state (2100 mAh/g referred to the lithiated state) [22]. The high ability for lithiation facilitates thinner and lighter anodes as indicated in Fig. 1.1, increasing the battery's gravimetric and volumetric energy density. Furthermore, silicon is an abundant and widely spread resource. It can be deployed in principle as pure silicon anodes or as blended electrodes together with graphite, although this complicates the state estimation due to inhomogeneous lithiation behavior and progressive lithium redistribution [49, 50].
The superior lithiability, however, is accompanied by a substantial volume expansion during lithiation of 300 % and respective shrinkage during delithiation [51]. These volume changes are partially reversible and irreversible, generating a volume hysteresis [52–55]. Due to possibly inhomogeneous lithiation of silicon anodes, the expansion causes mechanical instabilities. Particle fracture can be avoided using nanoparticles with a maximum size of 150 nm [56], while large particles pulverize into clusters of smaller ones [57]. Thus, the focus of research is developing nano-structured silicon anodes [58–60]. Nevertheless, significant stresses can also arise inside non-symmetrical silicon nano-structures due to inhomogeneous lithiation [61, 62]. Additionally, severe stresses appear inside the covering SEI layer (discussed in Section 1.2) due to the expansion of the underlying silicon active material. Repeated cracking and healing of this layer is assumed to contribute to a restricted cycle life of silicon [63], while silicon anodes also show a deficient calendar life [64]. A further challenge on the way towards pure silicon anodes is facing performance restrictions due to the occurrence of a voltage hysteresis, which is discussed in detail in Section 1.3.

Nevertheless, silicon anodes are considered promising next-generation anodes because of their improved stability and safety compared to lithium-metal anodes. Moreover, the application of silicon admixed to graphite in blended electrodes allows cell manufacturers already today to take advantage of both the superior lifetime of graphite and the enhanced energy density of silicon. A continuing increase of the silicon content in blended electrodes eventually facilitates a smooth transition to pure silicon anodes.

1.2 Solid-Electrolyte Interphase (SEI)

Interfacial and interphasial processes play an essential role in lithium-ion batteries. The most important interphase is the solid-electrolyte interphase (SEI) [65–69], covering the anode particles as depicted in Fig. 1.1. Emanuel Peled was the first to describe the SEI [70–72] and contributed crucially together with Doron Aurbach [73–75] to a basic understanding of this layer. Many works have investigated the SEI on the various anode materials condensed in the following reviews: SEI on graphite [76, 77], LTO [33, 78], lithium metal [40, 79–82], and silicon [83–85]. Nonetheless, the fundamentals of the SEI layer are mostly independent of the underlying anode material and will be discussed in the following.

1.2.1 Formation

The SEI forms on anode particles due to the electrochemical instability of the electrolyte. For achieving a superior energy density, it is beneficial to make use of low anode potentials close to 0 V versus lithium metal. However, this voltage is significantly below the reduction potential of the electrolyte [86, 87]. Therefore, components of the electrolyte react together with lithium ions and electrons to create reduced compounds adhering to the anode. The resulting interphase is called SEI.
Various reduction reactions contribute to the formation of the SEI [88–93]. The reactants can be either solvent molecules like ethylene carbonate (EC), anions from the dissolved lithium salts like hexafluorophosphate PF_6, additives like fluoroethylene carbonate (FEC) or vinylene carbonate (VC), or their derivatives. Each can react with lithium ions and electrons to form components that precipitate as SEI. An exemplary SEI formation reaction is

$$2\,\mathrm{Li^+} + 2\,\mathrm{e^-} + 2\,\mathrm{EC} \rightarrow \mathrm{Li_2EDC} + \mathrm{R_g}, \tag{1.1}$$

where Li_2EDC is lithium ethylene dicarbonate and R_g is a gaseous byproduct. This reaction is assumed to be one of the dominant SEI formation reactions as cyclic carbonates are more important for interphase formation than linear ones [94, 95].

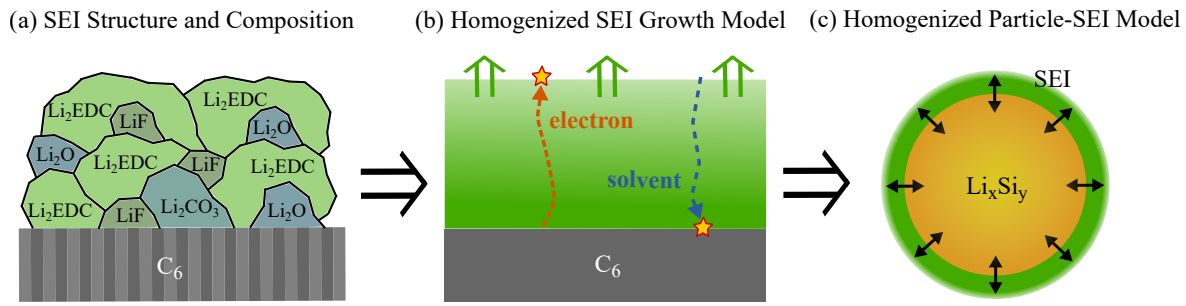

Figure 1.2: Scheme of the solid-electrolyte interphase (SEI). (a) The complex structure and composition observed in experiments is (b) homogenized to a one-dimensional SEI growth and (c) particle-SEI model.

A fundamental SEI layer necessary for the operation of the battery is formed within the very first cycle. This initial cycling is decisive for the performance and lifetime of the battery. In terms of expenses, the respective procedure called formation contributes significantly to the total manufacturing costs [96]. Therefore, an improved understanding can lead to optimized formation cycling, either reducing battery cell production costs, increasing battery longevity, or both [97–99].

1.2.2 Essential Properties

The interphase formed on anode particles due to electrolyte decomposition possesses properties of a solid electrolyte – hence the name solid-electrolyte interphase. The SEI is conductive for lithium ions but passivates the low anode potential from the electrolyte by blocking electrons. Thereby, it retards further growth of the SEI and facilitates the proper operation of the battery.
Nevertheless, the SEI formation reactions consume cyclable lithium ions. Indeed, the continued growth of the SEI discussed in Section 1.2.4 is the main degradation mechanism of state-of-the-art lithium-ion batteries [100]. Therefore, an optimized SEI is necessary to enable battery operation on the one hand but reduce ongoing capacity fade on the other hand.

1.2.3 Structure

The thickness of the SEI ranges from only a few nanometers after initial cycling up to several hundred nanometers after extended storage and cycling. The interphase film consists of several organic and inorganic components [73, 76, 101]. The most common organic component is lithium ethylene dicarbonate Li_2EDC. The inorganic parts reveal a mixture of components like lithium fluoride LiF, lithium oxide Li_2O,

and lithium carbonate Li_2CO_3. The typical appearance illustrated in Fig. 1.2(a) is a mixed layered and mosaic structure [74, 75, 102–104]. The dense inner layer consists of nanometer-sized domains of crystalline, inorganic components either attached to each other or embedded in an amorphous, organic matrix. Although the inorganic components LiF and Li_2CO_3 are insulating for lithium ions, grain boundary effects allow lithium ion transport and support electronic blocking [105, 106]. The porous outer layer consists of predominantly organic compounds and allows the penetration of the liquid electrolyte. Thus, the inner SEI layer is assumed to be responsible for the passivating effect of the SEI.
In recent years, cryogenic electron microscopy (cryo-EM) was used to shed light on the detailed nano-structure of the SEI. Most of these investigations were performed for lithium metal anodes. The observed SEI structures vary from mosaic [103, 107–109], layered [109, 110], inversely layered with inorganic components dominant in the outer layer [103, 107], to the importance of large LiF particles as "indirect SEI" [111]. On a silicon anode, a mixed layered and mosaic structure is observed [112]. On a carbonaceous anode, an either compact or extended SEI is reported to appear on different carbon particles [113]. The reported structures highlight the complexity of the SEI and the importance of a well-passivating, thin inner SEI to hinder uncontrolled SEI growth and limit capacity loss of the cell.
The diverging observations from cryo-EM together with the reported heterogeneity of the SEI thickness [114–116] underline the complex interplay of SEI growth with the components deployed in the cell and the operating conditions. The SEI compounds and structure depend on the underlying anode material, the used electrolyte (solvent, salts, additives), as well as the formation and cycling protocol. Common additives applied in lithium-ion batteries are fluoroethylene carbonate (FEC) [117–120] or vinylene carbonate (VC) [117, 120]. Their specific effect on the SEI structure and composition is still not well understood. Moreover, the question of which components are beneficial inside the SEI, e.g., Li_2O or LiF, is still under debate [121, 122]. Thus, continuum models use a homogenized description of the SEI averaging over the inhomogeneous composition.

1.2.4 Continued Growth

As stated above, the fundamental SEI is formed during the very first cycle. Nonetheless, the SEI continues to grow over time for the whole battery lifespan and is considered the main degradation mechanism [100]. During open-circuit storage of lithium-ion batteries, SEI growth manifesting as capacity fade of the battery is reported to have a square-root dependence in time [28, 100, 123–129]. This $\sqrt{t}$-dependence indicates a transport-limited, self-passivating process. Furthermore, the capacity fade depends on the state-of-charge (SOC), causing pronounced capacity fade at high SOC levels and low anode potentials respectively [28, 100, 126, 128, 130].

Additionally, capacity fade increases significantly at elevated temperatures [28, 100, 126–130].
Different transport mechanisms are considered in literature to determine SEI growth. During the initial cycling, electron tunneling is widely assumed to cause the electron transport necessary for SEI growth [131–133]. For ongoing long-term growth of the SEI, either electron diffusion [63, 87–89, 133–138], electron conduction [102, 139], or solvent diffusion [88, 102, 140–151] are discussed.
Using continuum modeling of the listed mechanisms portrayed in Fig. 1.2(b), Single et al. found that electron diffusion fits best to the experimentally observed SOC dependence [89]. The notion of the electron diffusion mechanism is supported by results from density functional theory (DFT) and ab initio molecular dynamics (AIMD) simulations, reporting hopping of neutral lithium interstitials/radicals, which is a variant of electron diffusion [134–136]. Nevertheless, some experimental results indicate a porous SEI allowing for solvent diffusion. One indication is given by observed swelling of the SEI inside liquid electrolyte interpreted as soaking of the SEI with electrolyte [152]. This suggests the presence of pores inside the SEI, which can, however, be restricted to merely the outer SEI. Another indication is given by redox-shuttle experiments using ferrocene and ferrocenium. The shuttle mechanism is still observed after forming an SEI layer, suggesting diffusion of large ferrocene and ferrocenium molecules through the SEI, which indicates the possibility of solvent diffusion through the SEI [143, 144, 147–149]. However, recent ferrocene shuttle measurements at realistic battery operation potentials support the theory of SEI growth mediated by electron diffusion [138]. Due to the ongoing debate, a comparison of the behavior of SEI growth due to electron diffusion and solvent diffusion was published in Paper I [153] and will be discussed and related to experimental results in Section 2.3 and Section 3.1.
Although calendar aging, i.e., SEI growth during battery storage, is already complex, also cycle aging, i.e., SEI growth during battery operation, is investigated in the literature [29, 154–157]. The theoretical description for the observed capacity fade transitioning from a square-root to a linear time dependence is supposed to be the combination of electron diffusion and electron migration [116, 137, 158]. Despite these efforts, calendar aging can still dominate the total capacity degradation during battery operation depending on the cycling conditions [159, 160]. Effectively, even self-discharge due to SEI growth is a slow form of cycling, which complicates the analysis of SEI growth during battery storage and can cause deviations from the typical square-root growth in time.

1.2.5 Mechanics

The SEI covers the single particles of the electrode as schematically illustrated as a core-shell model in Fig. 1.2(c). Thus, volume changes of the anode material

due to lithiation and delithiation, especially for silicon anodes, impose mechanical deformations of the SEI. These distortions can appear as elastic deformation, plastic flow, and possibly SEI fracture [63, 161, 162].
Due to the mechanical interplay, the SEI on silicon deserves special interest [83–85]. A superior mechanical stability of the SEI is required to achieve sufficient durability of silicon-anode lithium-ion batteries [63]. Indeed, the innermost SEI layer on silicon is reported to stay intact during cycling in experiments and simulations [63, 163–165]. The notion of a stable inner SEI is additionally supported by the observed beneficial influence of the SEI on the mechanical stability of silicon anodes [46, 166, 167]. Presumably, the native silicon oxide layer occurring on silicon particles partially lithiates and contributes to the stiff, inorganic SEI layer [168, 169]. Furthermore, the SEI grows into the interior of the silicon anode, covering and possibly stabilizing silicon nano-domains [170]. The importance of SEI mechanics even applies to solid electrolytes, which also form a certain SEI layer in contact with the anode particles [171, 172]. Therefore, the mechanical interaction of the SEI with silicon nanoparticles investigated in Paper II [173] and Paper III [174], as well as nanowires examined in Paper IV [62], is of major interest.
For the mechanical interaction, the stiffness of the SEI is a critical factor, which is controversially discussed in literature. According to the classification presented in Paper II [173], the SEI is reported to be either

- soft with Young's modulus $E_{\mathrm{SEI}} < 1\,\mathrm{GPa}$ [115, 175–178],
- medium stiff with $1\,\mathrm{GPa} \leq E_{\mathrm{SEI}} < 10\,\mathrm{GPa}$ [115, 177, 179–183],
- stiff with $10\,\mathrm{GPa} \leq E_{\mathrm{SEI}} < 100\,\mathrm{GPa}$ [161, 179–181, 184–186],
- or very stiff SEI with $E_{\mathrm{SEI}} \geq 100\,\mathrm{GPa}$ [179, 186].

Tendentially, the inner SEI containing inorganic compounds is rather stiff, while the porous outer SEI containing organic components soaked with liquid electrolyte is rather soft. Due to the thin SEI layer thickness, it is difficult to experimentally distinguish between the inner and the outer SEI layer. Therefore, experiments reporting lower values of Young's modulus might measure the low stiffness of the outer SEI, whereas the inner SEI layer possesses a higher Young's modulus. Underestimation of the stiffness of the inner SEI is additionally supported by the reported increase of Young's modulus at the nanoscale for different materials [187–191]. Therefore, Young's modulus of the SEI is assumed to be $E_{\mathrm{SEI}} = 100\,\mathrm{GPa}$ within this work. Moreover, the increased stiffness at the nanoscale also affects Young's modulus of nanoscale silicon.
Furthermore, experiments aim to measure the viscosity parameter of the outer, porous SEI layer [117, 178, 186, 192, 193]. Nevertheless, the inner, inorganic layer is assumed to be much stiffer accompanied by a significantly higher viscosity value. However,

due to the thickness of only a few nanometers, neither the viscosity value nor the viscosity model of the inner SEI layer are experimentally accessible. As discussed in Paper II [173], viscosity values between $\eta = 10^7\,\mathrm{Pa\,s}$ measured for the highly viscous polymer pitch [194] and $\eta = 10^{15}\,\mathrm{Pa\,s}$ measured for silicon oxide [195–197] are plausible.

1.3 Voltage Hysteresis of Silicon Anodes

Silicon anodes show a different voltage during lithiation and delithiation, even at low currents and after relaxation periods. This path-dependency of the voltage schematically illustrated in Fig. 1.3 is called hysteresis. The gap between the lithiation and delithiation voltage curves causes a reduced efficiency [198] and leads to detrimental heat generation [199]. Excessive heat hinders fast charging of batteries using silicon anodes, which is desired for applications like battery electric vehicles. Moreover, the ambiguous relation between voltage and SOC impedes precise SOC estimation [198]. As accurate state estimation is required to use the full capacity of the battery, a detailed understanding of the hysteresis behavior is indispensable.

1.3.1 Lithiation and Delithiation Behavior

In general, anodes exhibit lower potentials during lithiation than during delithiation due to overpotentials, like diffusion or reaction overpotentials. These overpotentials become negligible during slow cycling, as observed for common graphite anodes being only in the order of 10 mV. Silicon anodes, however, expose a larger distance between the lithiation and delithiation voltage compared to graphite anodes. The voltage discrepancy of silicon anodes portrayed in Fig. 1.3 also appears during very slow cycling with C/10 or even C/50, remaining in the order of 200 mV. Voltage differences of the same size are observed experimentally in thin-film silicon anodes [53, 54, 200–206], silicon nanowire anodes [207, 208], micrometer-sized silicon particle anodes [209, 210], and silicon nanoparticle anodes [209, 211–216]. Extrapolating the measured voltages to a pseudo-OCV indicates that even the OCV depends on the previous current direction [199, 216]. The direction dependence of the voltage, even at very low C-rates and quasi open-circuit conditions, is termed voltage hysteresis.

1.3.2 GITT Measurements

To determine the OCV more precisely, the voltage can be measured after a relaxation period. Estimation of the OCV curve is commonly performed with the galvanostatic intermittent titration technique (GITT). This procedure consists of alternate (de)lithiation pulses and relaxation periods. For the (de)lithiation steps, the cell is

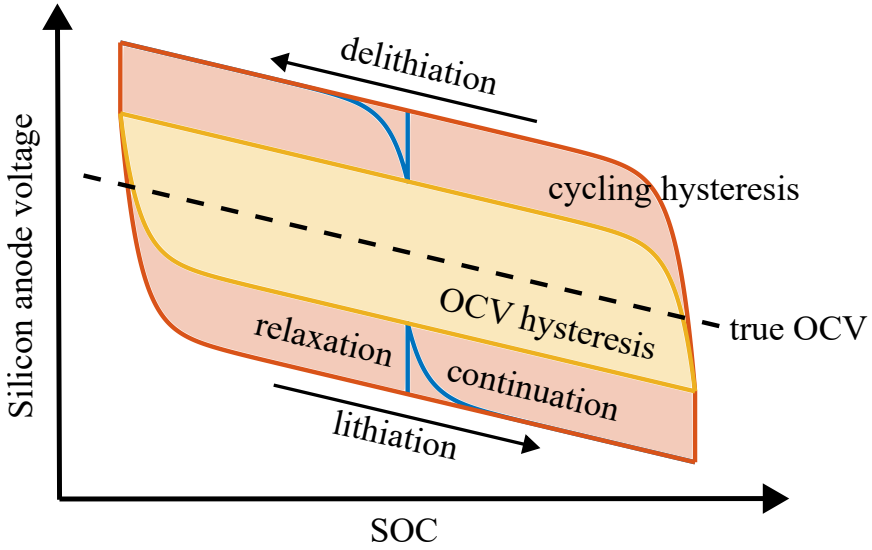

Figure 1.3: Scheme of the silicon voltage hysteresis. Silicon anodes reveal a voltage hysteresis during cycling (red) and a reduced but still significant OCV hysteresis (yellow). The process of relaxation and continued cycling as part of galvanostatic intermittent titration technique (GITT) measurements is depicted in blue.

(dis)charged with a constant current for a certain time, causing a defined SOC change. For the relaxations, the cell is held at open-circuit conditions for a fixed period of time or until the rate of voltage change falls below a specific threshold.
For graphite anodes, basically no voltage hysteresis is left after the relaxation periods in GITT measurements [217]. However, for silicon nanoparticle anodes, a significant voltage hysteresis in the order of 100 mV remains even after several hours of relaxation time [211–216], visualized in Fig. 1.3. Recent experimental results exhibit a slow, non-exponential voltage relaxation of full cells equipped with silicon nanoparticle anodes for over 300 h [216]. This thesis aims to describe the reason for the voltage hysteresis and the slow long-term relaxation process.

1.3.3 Empirical Plett Model

An empirical description of the voltage hysteresis of silicon anodes is provided by the established Plett model [218–220]. The phenomenological Plett model not only considers full lithiation and delithiation cycles but can also depict partial cycles and transitions between lithiation and delithiation with a simple differential equation depending on the SOC.
The Plett model treats the voltage during lithiation and delithiation belonging to different hysteresis states $-1 \leq h(\mathrm{SOC}) \leq 1$, scaled by half of the measured size of the voltage hysteresis $H(\mathrm{SOC})$. Therefore, the voltage $U(\mathrm{SOC})$ predicted by the

Plett model comprises the mean open-circuit voltage $U_0(\mathrm{SOC})$ and the hysteresis contribution according to

$$U(\mathrm{SOC}) = U_0(\mathrm{SOC}) + H(\mathrm{SOC}) \cdot h(\mathrm{SOC}). \tag{1.2}$$

For transitions between the lithiation and the delithiation branch of the anode voltage hysteresis, the Plett model applies the empirically derived differential equation in terms of changes in the SOC

$$\frac{dh(\mathrm{SOC})}{d\mathrm{SOC}} = -k(\mathrm{SOC}) \left(1 + \mathrm{sgn}\left(\frac{d\mathrm{SOC}}{dt}\right) h(\mathrm{SOC})\right). \tag{1.3}$$

The parameter $k > 0$, which can in general depend on the SOC, defines the slope of the transition between the hysteresis branches.
The empirical Plett model can reproduce the voltage during lithiation, delithiation, and respective voltage transitions. Nevertheless, the Plett model cannot describe relaxation processes in time as observed during GITT measurements discussed in Section 1.3.2.

1.3.4 Physical Hypotheses in Literature

Literature presents several explanatory approaches regarding the voltage hysteresis of silicon anodes. In the following, these hypotheses are briefly summarized. Particularly, it is pointed out that these approaches cannot explain the OCV hysteresis observed for amorphous silicon nanoparticle anodes.

Thin-Film Silicon Mechanics

Numerous studies have investigated the voltage hysteresis of silicon thin-film anodes, assigning it to the elasto-plasticity of silicon [53, 200–203, 205, 206, 221, 222]. In this geometry, silicon is deposited as a thin film on a current collector. The current collector constrains the expansion of the silicon anode to the normal direction of the plane, while in-plane expansion is inhibited. This restriction induces significant stresses during lithiation already at low SOC values. Initially, the silicon film deforms elastically generating compressive stress, but as lithiation proceeds, it deforms plastically showing a constant Piola-Kirchhoff stress. During delithiation, the silicon film initially contracts elastically generating tensile stress, followed by plastic deformation. For slow lithiation, these stresses are nearly independent of the applied current. The plastic flow of the silicon anode causes energy dissipation, resulting in an observable voltage hysteresis of thin-film silicon electrodes. This hysteresis explanation, however, only applies to the specific thin-film geometry.

Lithium Diffusion

During lithiation of micrometer-sized silicon particles or during fast lithiation, slow diffusion inside the silicon particle can cause inhomogeneous lithiation [211, 223]. This leads to different SOC values at the outer boundary of the silicon particles compared to the interior. The voltage of the anode is determined by the SOC level of the outer boundary of the silicon particles. Therefore, the higher lithium concentration at the outer boundary causes lower anode voltages during lithiation. During delithiation, the lower lithium concentration at the outer boundary induces higher voltages. Thus, the inhomogeneous lithium distribution can cause a voltage difference between lithiation and delithiation for large silicon particles or during fast cycling.
In addition to the SOC effect on the OCV, the inhomogeneous lithium distribution generates stresses inside the particle. These stresses at the outer boundary are compressive during lithiation and tensile during delithiation, contributing to the voltage gap between lithiation and delithiation during fast cycling. After several hours or even 300 h of relaxation, however, concentration gradients and the corresponding stresses cannot contribute to the remaining hysteresis due to their exponential relaxation profile. Moreover, diffusion overpotentials would reveal a linear C-rate dependence without offset at vanishing currents, contradicting experiments [216].

Phase Transformations

Phase transformations during lithiation and delithiation of silicon are considered to evoke a voltage hysteresis [224, 225]. For crystalline silicon, a phase transformation occurs during the lithiation to an amorphous lithium silicon alloy. Furthermore, at the end of a full lithiation, the amorphous alloy transforms into the crystalline phase $Li_{15}Si_4$. This state can be avoided when restricting the maximum lithiation of the system. For amorphous silicon, phase transformations are observed only during the very first lithiation [226] or at extremely high C-rates of 30 C [227]. Hence, phase transformations cannot explain the voltage hysteresis of amorphous silicon anodes during subsequent (partial) cycling, preventing crystalline phases.

Reaction Kinetics

Furthermore, slow reaction kinetics are discussed in literature to cause significant overpotentials during cycling [203, 211]. This hypothesis, however, requires unreasonable parameters for the anodic and cathodic transfer coefficients $\alpha_a, \alpha_c \gg 1$, tuning the Butler-Volmer equation to describe the slow voltage relaxation [203]. Therefore, slow reaction kinetics cannot explain the voltage hysteresis during very slow cycling and after extended relaxation periods.

1.3.5 Approach in this Thesis: Silicon-SEI Mechanics

Herein, the voltage hysteresis is explained with the chemo-mechanical interaction of silicon nanoparticles with the SEI depicted in Fig. 1.2(c) and presented in detail in Paper II [173] and Paper III [174]. The silicon particle deforms during cycling mainly due to chemical expansion and shrinkage, depending on the lithium concentration. The SEI has to accommodate the particle volume changes with mechanical deformations, causing significant stresses.

During lithiation, the silicon particle expands, and the SEI has to stretch first elastically and then plastically when reaching the yield criterion. The mechanical deformation of the SEI generates compressive stress in the radial direction, acting on the silicon particles. During subsequent delithiation, the silicon particle shrinks as lithium concentration decreases. The SEI has to adjust to the silicon surface and contracts mechanically, again first elastically and then plastically. This releases the compressive stress and generates tensile stress in the radial direction during delithiation. The interplay of elastic and plastic deformation induces a hysteresis of the radial stress component, imposing a stress hysteresis inside the underlying silicon nanoparticle. The stress influences the chemo-mechanical potential of lithium and, therefore, generates the silicon OCV hysteresis.

In addition to the elastoplastic stress, the viscous behavior of the SEI is responsible for an extra stress contribution during cycling. During lithiation, when the silicon particle expands and the SEI stretches in the tangential direction, the SEI gets thinner. The radial contraction rate of the SEI produces a compressive viscous stress. During delithiation, when the silicon particle shrinks and the SEI contracts in the tangential direction, the SEI gets thicker. The radial expansion rate of the SEI produces a tensile viscous stress. Therefore, the viscous stress enlarges the elastoplastic stress hysteresis during cycling. The viscous stress is already significant at low currents and stays considerable during long-term relaxation, as demonstrated in Paper III [174].

The impact of the SEI on the silicon voltage hysteresis is supported in literature by an observed reduced voltage hysteresis for carbon-coated silicon particles [213]. The carbon-coating can potentially affect the SEI composition and the mechanical parameters, influencing the generated stress and voltage hysteresis. Furthermore, the SEI is reported to mechanically stabilize silicon electrodes [46, 166, 167]. The inner SEI is theoretically and experimentally shown to withstand the large particle volume changes during cycling [63, 163–165]. These observations substantiate the mechanical impact of the SEI on the silicon lithiation behavior.

The mechanical notion of the voltage hysteresis is elaborated for silicon nanoparticles covered by the SEI layer. Nevertheless, the explanation can also reason the voltage hysteresis of micron-sized silicon particles due to large particle fracture and pulverization, generating a network of silicon nanoparticles [56, 57]. Moreover, the SEI grows into the interior of the silicon electrode, possibly encapsulating nano-sized silicon

domains [170]. A similar mechanical effect can be evoked in silicon micro-electrodes by active silicon nanodomains surrounded by inactive domains. The existence of silicon nanodomains is reported in literature for amorphous silicon under pressure [228], for crystalline silicon [209], and for silicon oxide [229, 230].
The mechanical explanation of the voltage hysteresis was first presented in Paper II [173]. The model was extended by the description of the long-term relaxation behavior in Paper III [174]. Moreover, Paper IV [62] generalizes the chemo-mechanical simulation to an asymmetric geometry. Herein, the theory and model equations are stated in Section 2.4 and the results are presented in Section 3.2, 3.3, and 3.4.

2 Theory

This chapter presents the continuum theory and modeling approaches, on which the investigations for this thesis are based. It discusses the basics of continuum mechanics in Section 2.1 and of non-equilibrium thermodynamics in Section 2.2. Afterwards, going into more detail, the theory of growth mechanisms of the SEI is elaborated in Section 2.3. Finally, the mechanics of the silicon-SEI system is formulated in Section 2.4. While Sections 2.1 and 2.2 recapitulate the foundations of thermodynamically consistent chemo-mechanical modeling, Sections 2.3 and 2.4 describe the advanced models used for the performed simulations.

2.1 Continuum Mechanics

Herein, continuum mechanics is used to describe the deformations and mechanical interactions of macroscopic systems. Continuum mechanics averages over the mechanical contributions of single atoms or molecules, describing a system as a continuous body with homogenized mechanical properties. A profound introduction to continuum mechanics can be found in Ref. [231], which is condensed in this section to the main principles applied within this thesis.

2.1.1 Frames of Reference

Two perspectives can be taken when treating continuum mechanics: one considering the evolution related to the deformed state and one related to the undeformed state. The following paragraphs introduce these two concepts.

Configurations

In continuum mechanics, a material body $\mathcal{B}$ is modeled to be continuously distributed within a region Ω. The body $\mathcal{B}$ moves with time in space due to initial motion as well as internal or external forces. The state of the material body with the coordinates of the (continuous) material points $\vec{x} \in \Omega$ is called configuration.
The initial state of the continuum body is considered as reference or undeformed configuration Ω_0 depicted on the left-hand side in Fig. 2.1. The position vectors $\vec{X}_0 \in \Omega_0$ describe the coordinates of the body in the undeformed configuration. Therefore, the coordinates $\vec{X}_0$ represent the initial material positions and stay constant in time.

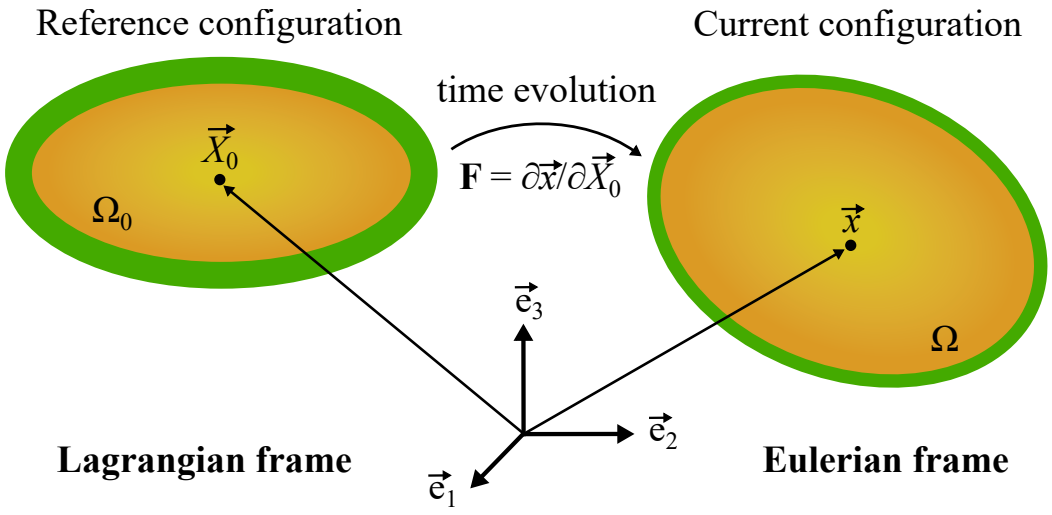

Figure 2.1: Scheme of the reference (initial, undeformed) and current (deformed) configuration of a core-shell body. The Lagrangian frame considers the behavior of the body related to the reference configuration, while the Eulerian frame relates to the current configuration. The deformation gradient tensor **F** relates both configurations. Figure inspired by Ref. [231].

The state of the continuum body at time t is viewed as the current or deformed configuration Ω shown on the right-hand side in Fig. 2.1. The position vectors $\vec{x} \in \Omega$ describe the coordinates of the body after the performed deformations. Hence, the coordinates $\vec{x}$ represent the current material positions after deformation and change in time.

Lagrangian Frame

In the Lagrangian frame, motion and deformation of the material body $\mathcal{B}$ is referenced to the undeformed configuration Ω_0 illustrated on the left-hand side in Fig. 2.1. The current material points $\vec{x}$ are mapped to the initial points $\vec{X}_0$ by the mapping function $\vec{x} = \chi(\vec{X}_0, t)$. After mapping the deformed to the undeformed positions, all equations describing the system can be evaluated respective to the undeformed, initial configuration in the Lagrangian frame. For evaluating the results, the positions are transformed back to the current configuration after performing the calculations of interest.
The Lagrangian perspective is called material description as it describes the behavior and changes of individual (continuum) particles. The material description in the Lagrangian frame is particularly convenient for investigating the mechanical behavior of solid continuum bodies, which are allowed to deform but always keep a basic internal structure.

The equations of the mechanical system investigated within this thesis are expressed in the Lagrangian frame. More details about the mechanical model will be discussed in Section 2.4.

Eulerian Frame

In the Eulerian frame, the behavior of the material body $\mathcal{B}$ is described relative to the current configuration Ω displayed on the right-hand side in Fig. 2.1, which changes in time. In this approach, no transformation of coordinates is necessary as all equations describing the system are evaluated in the deformed configuration in the Eulerian frame. However, the change of coordinates in time for the moving and deforming body affects and potentially complicates the set of equations.
The Eulerian perspective is useful to analyze the mechanical behavior evolving in time at a fixed spatial point. Hence, it is called spatial description. The spatial description in the Eulerian frame is particularly convenient for investigating fluid mechanics, where the evolution of, e.g., velocity or pressure is evaluated in time at a specific point in space.

2.1.2 Spatial and Material Derivatives

Spatial derivatives describe changes with respect to the deformed current configuration with material positions $\vec{x} \in \Omega$. Material derivatives refer to the undeformed reference configuration with coordinates $\vec{X}_0 \in \Omega_0$. For a better understanding, a spatial field $\zeta(\vec{x}, t)$ and a material field $\zeta_0(\vec{X}_0, t)$ of some physical quantity are introduced, which are considered to be scalar for simplicity but can be extended in general to vector and tensor fields.
Spatial derivatives can be simply applied to spatial fields and material derivatives to material fields. Nevertheless, intermixing of the material time derivative and spatial fields is necessary for calculations in the Eulerian frame when the time evolution of a certain material point is under investigation.

Nabla Operator

The spatial derivative with respect to position is defined as $\nabla = \partial/\partial\vec{x}$ considering changes referencing to the spatial coordinates $\vec{x} \in \Omega$. The material derivative is defined as $\nabla_0 = \partial/\partial\vec{X}_0$ considering changes referencing to the material coordinates $\vec{X}_0 \in \Omega_0$.
Spatial and material derivatives with respect to position are typically used referring to a corresponding spatial or material field. Therefore, no mixing of spatial and material coordinates is discussed.

Spatial Time Derivative

The spatial time derivative of the spatial field $\zeta(\vec{x}, t)$ is the time derivative at a fixed current position $\vec{x}$. It expresses the time evolution of the field at a certain point in space in the (deformed) Eulerian frame. The spatial time derivative or local time derivative is denoted as the partial time derivative $\partial\zeta(\vec{x}, t)/\partial t$.

Material Time Derivative

The material time derivative is the time derivative at a fixed material point $\vec{X}_0$. It expresses the time evolution of the field at a certain point in space in the (undeformed) Lagrangian frame. The material time derivative of the spatial field $\zeta(\vec{x}, t)$ is denoted as the total time derivative according to

$$\dot{\zeta}(\vec{x}, t) = \frac{\mathrm{D}\zeta(\vec{x}, t)}{\mathrm{D}t} = \frac{\partial\zeta(\vec{x}, t)}{\partial t} + \frac{\partial\vec{x}}{\partial t} \cdot \frac{\partial\zeta(\vec{x}, t)}{\partial\vec{x}} = \frac{\partial\zeta(\vec{x}, t)}{\partial t} + \vec{v} \cdot \nabla\zeta(\vec{x}, t) \tag{2.1}$$

with the velocity field of the material body $\vec{v} = \partial\vec{x}/\partial t$. Thus, the material time derivative of a spatial field comprises a spatial time derivative and a convective contribution due to the motion of the material body.
Considering a material field $\zeta_0(\vec{X}_0, t)$, the convective term vanishes as the material points $\vec{X}_0$ stay constant in time $\vec{v}_0 = \partial\vec{X}_0/\partial t = 0$. Hence, the material time derivative coincides with the partial time derivative in the Lagrangian frame

$$\dot{\zeta}_0(\vec{X}_0, t) = \frac{\partial\zeta_0(\vec{X}_0, t)}{\partial t}, \tag{2.2}$$

describing the time evolution at a fixed material point $\vec{X}_0$. The simplicity of this equation is appealing for investigations in solid continuum mechanics using the Lagrangian frame.

2.1.3 Deformations

The deformation of a continuum body characterizes the transformation between different configurations. Deformations describe lattice distortions, rigid body rotations, and rigid body translational motion of the material due to internal or external forces.

Deformation Gradient Tensor

The deformation gradient tensor $\mathbf{F} = \partial\vec{x}/\partial\vec{X}_0$ relates the current configuration Ω to the reference configuration Ω_0 as illustrated in Fig. 2.1. The deformation gradient describes distortions of the lattice and rigid body rotations. It does not account for rigid body translation by definition.

The deformation gradient qualifies the transformation of line elements $\mathrm{d}\vec{x} = \mathbf{F}\mathrm{d}\vec{X}_0$, directed surfaces according to Nanson's formula $\mathrm{d}\vec{A} = J\mathbf{F}^{-\mathrm{T}}\mathrm{d}\vec{A}_0$, and volume changes $\mathrm{d}V = J\mathrm{d}V_0$. The volume ratio J is defined by the determinant of the deformation gradient $J = \det \mathbf{F}$.

Strain Tensor

Neither rigid body rotations nor rigid body translation contributes to the potential energy of the system. Therefore, the strain tensor is defined as a measure for merely the lattice distortions

$$\mathbf{E} = \frac{1}{2}\left(\mathbf{F}^{\mathrm{T}}\mathbf{F} - \mathbf{Id}\right). \tag{2.3}$$

The strain quantifies the extent of distortion of a continuum element relative to its original state. The specific strain tensor defined in Eq. (2.3) is called the Green-Lagrange strain tensor. In contrast to measurable deformations, the notion of strains is founded on concepts to facilitate the mechanical investigation [231]. Although literature presents a multitude of alternative definitions of the strain tensor, the Green-Lagrange tensor is applied in this thesis, characterizing the material strain in the Lagrangian frame.

2.1.4 Stress Measures

Deformations of the material caused by externally applied forces and deformations lead to interactions of neighboring material points inside the continuum body. In continuum mechanics, these interactions are characterized by stress tensors expressing internal or external force per unit area. The stress contains the information on how the material responds to external forces and deformations and is responsible for deformations of the material itself.
The concept of stress depends on the reference frame, either the deformed Eulerian frame or the undeformed Lagrangian frame. The different stress tensors applied in this thesis are introduced in the following.

Cauchy Stress

The Cauchy stress tensor $\boldsymbol{\sigma}$ quantifies the local stress state at a material point in the continuum body referenced to the deformed current configuration Ω. The Cauchy stress $\boldsymbol{\sigma}$ relates the force $\mathrm{d}\vec{F}$ acting on a surface area in the current configuration $\mathrm{d}A$ and the surface area itself as

$$\mathrm{d}\vec{F} = \boldsymbol{\sigma} \cdot \vec{n}\,\mathrm{d}A \tag{2.4}$$

with the normal vector $\vec{n}$ of the surface element $\mathrm{d}A$ [231].

As the Cauchy stress represents the stress state in the current configuration, it is also called true stress. The Cauchy stress is particularly useful when performing calculations in the Eulerian frame or relating to experimental results. The Cauchy stress tensor σ is always symmetric.

First Piola-Kirchhoff Stress

The first Piola-Kirchhoff stress tensor $\mathbf{P}$ represents the local stress state at a material point related to the undeformed reference configuration Ω_0. The first Piola-Kirchhoff stress $\mathbf{P}$ relates the force $\mathrm{d}\vec{F}$ acting on a surface area in the current configuration $\mathrm{d}A$ and the surface area in the reference configuration $\mathrm{d}A_0$ as

$$\mathrm{d}\vec{F} = \mathbf{P} \cdot \vec{n}_0 \, \mathrm{d}A_0 \tag{2.5}$$

with the normal vector $\vec{n}_0$ of the surface element $\mathrm{d}A_0$ [231].
The first Piola-Kirchhoff stress is especially convenient for investigations in continuum mechanics of solids, where the Lagrangian frame is preferred for calculations. For example, the convenience of the first Piola-Kirchhoff stress is evidenced in the momentum balance stated in Eq. (2.11).
The first Piola-Kirchhoff stress $\mathbf{P}$ relates to the Cauchy stress σ by the Piola transformation

$$\mathbf{P} = J\sigma\mathbf{F}^{-\mathrm{T}}. \tag{2.6}$$

Contrary to the Cauchy stress, the first Piola-Kirchhoff stress is not symmetric in general. However, when the deformation tensor is symmetric it also imposes symmetry for the first Piola-Kirchhoff stress tensor.

2.2 Non-Equilibrium Thermodynamics

Non-equilibrium thermodynamics is the branch of thermodynamics that describes systems out of the thermodynamic equilibrium [232, 233]. Analog to equilibrium thermodynamics, macroscopic properties like temperature and entropy characterize the state of the system. These measures are, in general, not constant but evolving in time in non-equilibrium thermodynamics. The concept of thermodynamics is governed by fundamental conservation laws of mass, momentum, and total energy. Furthermore, a non-negative entropy production has to be ensured.
This work continues the thermodynamic consistent modeling efforts presented in Refs. [63, 234–237]. The principles of non-equilibrium thermodynamics stated in this section are predominantly based on the thermodynamically-consistent continuum modeling works [63, 173, 236, 237].

2.2.1 Continuity Equation

The laws of conservation discussed in the following can be stated universally by continuity equations. The continuity equation of a physical quantity $\zeta(\vec{x}, t)$ relates its evolution in time to the flux $\vec{N}_\zeta$ and a source s_ζ of this quantity. The differential form of the continuity equation reads

$$\frac{\partial \zeta}{\partial t} = -\nabla \cdot \vec{N}_\zeta + s_\zeta. \tag{2.7}$$

In descriptive words, the quantity ζ in a certain volume element changes in time according to the flux $\vec{N}_\zeta$ into or out of this volume element and a source s_ζ that generates the quantity inside this volume element.
Considering a physical quantity $\zeta_0(\vec{X}_0, t)$ defined with respect to the initial configuration, i.e., in the Lagrangian frame, the partial time derivative coincides with the total time derivative as discussed in Section 2.1.2. Hence, the continuity equation states

$$\dot{\zeta}_0 = -\nabla_0 \cdot \vec{N}_{\zeta,0} + s_{\zeta,0} \tag{2.8}$$

with all quantities expressed in the undeformed Lagrangian domain indicated by the subscript "0". In the following, all equations are stated in the Lagrangian frame.

2.2.2 Species Conservation

A fundamental law of conservation neglecting relativistic effects is the conservation of mass. Without explicit consideration of reactions, i.e., not accounting for the production and consumption of a species i, mass conservation can be portrayed as overall species conservation.
Therefore the concentration $c_{i,0}$ of species i changes in time by the respective species flux $\vec{N}_{i,0}$ according to

$$\dot{c}_{i,0} = -\nabla_0 \cdot \vec{N}_{i,0} \tag{2.9}$$

stated for vanishing source term.
The species i can be any physical or chemical species in general. In this thesis, Eq. (2.9) governs the transport of lithium atoms, lithium ions, electrons, and solvent molecules considered mobile species.

2.2.3 Momentum Conservation

The momentum balance based on Newton's second law of motion states that the momentum of a body changes due to external forces. In continuum mechanics, the temporal evolution of momentum $\vec{g}$ is determined by internal forces due to the divergence of stress and external body forces $\vec{b}$. The momentum balance is stated in

Cauchy's first equation of motion [231], which reads

$$\rho_0 \dot{\vec{g}} = \nabla_0 \cdot \mathbf{P} + \rho_0 \vec{b} \tag{2.10}$$

in the local formulation transformed to the Lagrangian frame.
Assuming mechanical equilibrium, $\dot{\vec{g}} = 0$, and vanishing external body forces, $\vec{b} = 0$, Eq. (2.10) simplifies to

$$0 = \nabla_0 \cdot \mathbf{P}. \tag{2.11}$$

The momentum conservation stated in Eq. (2.11) determines the mechanical contribution to the chemo-mechanical silicon-SEI model presented later in Section 2.4.

2.2.4 Energy Conservation

The first law of thermodynamics states that the energy of a system changes due to heating or mechanical work in interaction with the system's surroundings. In the following, heat contributions are neglected due to an isothermal perspective.
Mechanical power is determined by forces $\vec{F}$ acting on the material body times the velocity field $\vec{v}$. With the forces defined according to Newton's second law of motion stated in Eq. (2.10), the mechanical power in integral form stated in Ref. [237] reads

$$P_{\text{mech}} = \int_{\Omega_0} \rho_0 \vec{v}\vec{b} \mathrm{d}\Omega_0 + \oint_{\partial\Omega_0} \vec{v}\mathbf{P}\mathrm{d}\vec{A}_0 = \int_{\Omega_0} \left[\rho_0 \vec{v}\vec{b} + \nabla_0 \cdot \left(\mathbf{P}^{\mathrm{T}}\vec{v}\right)\right] \mathrm{d}\Omega_0 \tag{2.12}$$

using the divergence theorem. Returning to the local formulation, the total energy of the system changes according to

$$\rho_0 \dot{e} = \rho_0 \vec{v}\vec{b} + \nabla_0 \cdot \left(\mathbf{P}^{\mathrm{T}}\vec{v}\right). \tag{2.13}$$

The internal energy u defined by the difference of the total energy e and the kinetic energy $\frac{1}{2}\vec{v}\vec{g}$ changes as $\dot{u} = \dot{e} - \vec{v}\dot{\vec{g}}$. Applying the product rule

$$\nabla_0 \cdot \left(\mathbf{P}^{\mathrm{T}}\vec{v}\right) = \vec{v}\nabla_0 \cdot \mathbf{P} + \mathbf{P} : \nabla_0 \vec{v} \tag{2.14}$$

with the double contraction of two tensors defined as $\mathbf{A} : \mathbf{B} = \sum_{ij} A_{ij}B_{ij}$. Identifying $\dot{\mathbf{F}} = \nabla_0 \vec{v}$, the internal energy changes according to

$$\rho_0 \dot{u} = \mathbf{P} : \dot{\mathbf{F}}. \tag{2.15}$$

Therefore, the internal energy change is balanced by the mechanical influence determined by the rate of the deformation tensor $\dot{\mathbf{F}}$.
The internal energy u, the entropy of the system s, and the temperature T determine the free energy φ according to the Legendre transformation as $\dot{\varphi} = \dot{u} - T\dot{s}$. Hence,

the time evolution of the free energy by inserting Eq. (2.15) states

$$\rho_0 \dot{\varphi} = \mathbf{P} : \dot{\mathbf{F}} - \rho_0 T \dot{s}. \tag{2.16}$$

In the chemo-mechanical silicon-SEI model under investigation, the change of the free energy depends on the lithium concentration $c_{\mathrm{Li},0}$ and the reversible deformation $\mathbf{F}_{\mathrm{rev}}$. Expressing the deformation in the form of the reversible right Cauchy-Green tensor $\mathbf{C}_{\mathrm{rev}} = \mathbf{F}_{\mathrm{rev}}^{\mathrm{T}} \mathbf{F}_{\mathrm{rev}}$, the change of the free energy density reads

$$\rho_0 \dot{\varphi} = \mu_{\mathrm{Li}} \dot{c}_{\mathrm{Li},0} + \frac{1}{2} \mathbf{T}_{\mathrm{rev}} : \dot{\mathbf{C}}_{\mathrm{rev}}. \tag{2.17}$$

Here, μ_{Li} is the chemical potential of lithium and $\mathbf{T}_{\mathrm{rev}} = J \mathbf{F}_{\mathrm{rev}}^{-1} \boldsymbol{\sigma} \mathbf{F}_{\mathrm{rev}}^{-\mathrm{T}}$ is the reversible second Piola-Kirchhoff stress tensor. From Eq. (2.17) result the constitutive equations for the chemical potential μ_{Li} and the reversible second Piola-Kirchhoff stress tensor as

$$\mu_{\mathrm{Li}} = \frac{\partial(\rho_0 \varphi)}{\partial c_{\mathrm{Li},0}} \tag{2.18}$$

$$\mathbf{T}_{\mathrm{rev}} = 2 \frac{\partial(\rho_0 \varphi)}{\partial \mathbf{C}_{\mathrm{rev}}}. \tag{2.19}$$

The constitutive equations (2.18) and (2.19) determine the chemo-mechanical coupling via the free energy for the silicon-SEI model discussed in Section 2.4.

2.2.5 Entropy Production

The second law of thermodynamics states that heat does not flow spontaneously from a colder body to a hotter body. This law can be reformulated in terms of entropy, namely that the entropy cannot decrease in a closed system.
Accounting for the second law with non-negativity of the entropy production $\mathcal{R} \geq 0$, the entropy balance states

$$\rho_0 T \dot{s} = -\nabla T \vec{N}_{\mathrm{S},0} + \mathcal{R} \tag{2.20}$$

with the entropy flux $\vec{N}_{\mathrm{S},0}$.
Rewriting Eq. (2.20) with the free energy φ expressed in Eq. (2.17), the entropy production reads

$$\mathcal{R} = -\mu_{\mathrm{Li}} \dot{c}_{\mathrm{Li},0} - \frac{1}{2} \mathbf{T}_{\mathrm{rev}} : \dot{\mathbf{C}}_{\mathrm{rev}} + \mathbf{P} : \dot{\mathbf{F}} + \nabla_0 T \vec{N}_{\mathrm{S},0} \geq 0. \tag{2.21}$$

Comparison of the chemical and the entropic term in Eq. (2.21) relates the entropy flux to the lithium flux as $\vec{N}_{\mathrm{S},0} = (\mu_{\mathrm{Li}} \vec{N}_{\mathrm{Li},0})/T$, when accounting for the species balance stated in Eq. (2.9).

The Piola-Kirchhoff stress $\mathbf{P}$ of the silicon-SEI model discussed in Section 2.4 consists of an elastoplastic $\mathbf{P}_{\mathrm{el}}$ and a viscous share $\mathbf{P}_{\mathrm{visc}}$ as $\mathbf{P} = \mathbf{P}_{\mathrm{el}} + \mathbf{P}_{\mathrm{visc}}$. The mechanical power density divides into a reversible contribution due to elastic deformation, an irreversible contribution due to plastic flow, and a dissipation contribution due to viscous behavior

$$\mathbf{P} : \dot{\mathbf{F}} = \frac{1}{2}\mathbf{T}_{\mathrm{rev}} : \dot{\mathbf{C}}_{\mathrm{rev}} + \mathbf{M} : \mathbf{L}_{\mathrm{pl}} + \mathbf{P}_{\mathrm{visc}} : \dot{\mathbf{F}}, \tag{2.22}$$

where $\mathbf{M} = \mathbf{C}_{\mathrm{rev}}\mathbf{T}_{\mathrm{rev}}$ is the Mandel stress and $\mathbf{L}_{\mathrm{pl}} = \dot{\mathbf{F}}_{\mathrm{pl}}\mathbf{F}_{\mathrm{pl}}^{-1}$ is the plastic flow.
Inserting the mechanical power density Eq. (2.22) into the entropy production condition Eq. (2.21) yields

$$\mathcal{R} = -\vec{N}_{\mathrm{Li},0}\nabla_0\mu_{\mathrm{Li}} + \mathbf{M} : \mathbf{L}_{\mathrm{pl}} + \mathbf{P}_{\mathrm{visc}} : \dot{\mathbf{F}} \geq 0. \tag{2.23}$$

Each of the three terms has to fulfill the non-negativity condition, restricting the selection and development of chemo-mechanical models to a thermodynamically consistent framework.

2.3 Growth Mechanisms of the SEI

Understanding the continuing SEI growth is of prevailing importance due to its direct relation to the capacity fade of lithium-ion batteries. The rate of SEI growth is generally determined by the interplay of reaction kinetics and diffusion of educt species. This section presents the theory of SEI growth mediated by two transport mechanisms, namely electron diffusion and solvent diffusion.

2.3.1 Fundamentals of SEI Growth

Before discussing the transport mechanisms of interest, the following paragraphs outline the foundations of SEI growth. In particular, the basics cover the interrelation of SEI thickness and capacity loss as well as the influence of reaction kinetics and species diffusion.

Correlation of SEI Growth and Capacity Fade

Several degradation mechanisms can cause capacity fade of lithium-ion batteries Q_{loss}. Nevertheless, the growth of the SEI layer is considered to be the dominant reason for the capacity loss, particularly during battery storage $Q_{\mathrm{loss}} \simeq Q_{\mathrm{SEI}}$.
The creation of newly formed SEI, extending the SEI thickness from initially $L_{\mathrm{SEI},0}$ to L_{SEI} during battery storage, consumes cyclable lithium ions according to the formation reaction stated in Eq. (1.1). The loss of active lithium ions immediately

causes a capacity loss Q_{SEI}. The SEI thickness L_{SEI} and capacity loss due to SEI growth Q_{SEI} are linearly related by

$$L_{\mathrm{SEI}} = \frac{v}{s_{\mathrm{Li}}} \frac{Q_{\mathrm{SEI}}}{AF} + L_{\mathrm{SEI},0}, \tag{2.24}$$

where v is the mean molar volume of the generated SEI species, s_{Li} is the mean stoichiometric coefficient of lithium ions in the SEI formation reactions, A is the anode surface area, and F is the Faraday constant. Due to the preferential reduction of cyclic carbonates, the characteristic SEI formation reaction in Eq. (1.1) is assumed to determine the mean molar volume v and the stoichiometric coefficient s_{Li}.
The SEI formation current density j^{SEI} determines the evolution of SEI-related capacity fade in time as

$$\partial_t Q_{\mathrm{SEI}} = A j^{\mathrm{SEI}}. \tag{2.25}$$

The interplay of reaction kinetics and charge transport affects the SEI formation current density j^{SEI} as discussed in the following.

Reaction Kinetics

In electrochemical systems, the Butler-Volmer equation is typically considered to characterize the reaction kinetics [238], also in the context of thermodynamic-consistent modeling [234, 235, 239]. The Butler-Volmer equation describes the dynamics of a one-step charge-transfer reaction at reasonable reaction overpotentials. For particularly large overpotentials, more sophisticated theories, e.g., Marcus-Hush-Chidsey theory, have to be considered.
The Butler-Volmer equation relating the reaction current j to the overpotential of the reaction η_{r} states

$$j = j_0 \cdot \left[\exp\left(\frac{\alpha_a z F}{R_{\mathrm{gas}} T} \eta_{\mathrm{r}} \right) - \exp\left(-\frac{\alpha_c z F}{R_{\mathrm{gas}} T} \eta_{\mathrm{r}} \right) \right]. \tag{2.26}$$

The first term describes the anodic contribution (oxidation reaction), and the second term describes the cathodic part (reduction reaction). The parameters α_a and α_c are the anodic and cathodic charge transfer coefficients, weighting the contributions of the anodic and cathodic direction. Usually, for single-electron processes, the charge transfer coefficients are related by $\alpha_c = 1 - \alpha_a$. Thus, the parameter $\alpha = \alpha_a$ is often called symmetry factor and is typically assumed to be $\alpha = 0.5$. The residual parameters in Eq. (2.26) are the number of transferred charges z, the universal gas constant R_{gas}, and the ambient temperature T. The overpotential of the reaction is defined as

$$\eta_{\mathrm{r}} = U - \left(U_{\mathrm{ref}} + \frac{R_{\mathrm{gas}} T}{zF} \ln \frac{\tilde{c}_{\mathrm{O}}}{\tilde{c}_{\mathrm{R}}} \right). \tag{2.27}$$

with the potential difference at the electrochemical interface U, the equilibrium potential difference at reference conditions U_{ref}, and the concentration of the oxidized species $\tilde{c}_{\text{O}} = c_{\text{O}}/c_{\text{O,ref}}$ and the reduced species $\tilde{c}_{\text{R}} = c_{\text{R}}/c_{\text{R,ref}}$, respectively, normalized by their reference concentrations. The exchange current density j_0 is estimated as

$$j_0 = k c_{\text{O}}^{\alpha_a} c_{\text{R}}^{\alpha_c} (c_{\text{R,max}} - c_{\text{R}})^{\alpha_a} \tag{2.28}$$

with the reaction rate constant k and the maximum concentration of the reduced species $c_{\text{R,max}}$.
Combining Eqs. (2.26), (2.27), and (2.28), the Butler-Volmer equation can be reformulated as

$$j = j_0' \cdot \left[\tilde{c}_{\text{R}} \exp\left(\frac{\alpha_a z F}{R_{\text{gas}} T} (U - U_{\text{ref}}) \right) - \tilde{c}_{\text{O}} \exp\left(-\frac{\alpha_c z F}{R_{\text{gas}} T} (U - U_{\text{ref}}) \right) \right] \tag{2.29}$$

with the exchange current density j_0' defined as

$$j_0' = k' (c_{\text{R,max}} - c_{\text{R}})^{\alpha_a} \tag{2.30}$$

and the reaction rate constant k'.
The Butler-Volmer equation can be applied in general to describe various charge-transfer reactions, e.g., lithium intercalation into graphite or lithium insertion into silicon with the equilibrium voltage at reference conditions given by the anode open-circuit voltage $U_{\text{ref}} = U_0$. In this case, negative current densities correspond to lithiation of the anode, while positive ones correspond to delithiation. In the context of SEI growth, the Butler-Volmer equation describes the rate of the SEI formation reaction stated in Eq. (1.1) with the equilibrium voltage at reference conditions given by the SEI formation potential $U_{\text{ref}} = U_{\text{SEI,ref}}$. In this case, negative current densities express growth of the SEI.

Fickian Diffusion

A precondition for the SEI formation reaction to take place is that all reaction compounds have to be in the same place. In literature, the convening of the reactants is commonly assumed to be facilitated by diffusion of either electrons or solvent molecules as introduced in Section 1.2.4.
The diffusion process described by Fick's law quantifies mass transport driven by concentration gradients. The diffusive flux density $\vec{N}_i$ of species i states

$$\vec{N}_i = -D_i \nabla c_i \tag{2.31}$$

with c_i the concentration of a species i and D_i the respective diffusion coefficient.
In the most general form, the equation of Fickian diffusion quantifying concentration

changes in time reads

$$\frac{\partial c_i}{\partial t} = \nabla \cdot (D_i \nabla c_i) \tag{2.32}$$

For a constant diffusion coefficient and restriction to one-dimensional motion in x-direction, the diffusion equation simplifies to

$$\frac{\partial c_i}{\partial t} = D_i \cdot \frac{\partial^2 c_i}{\partial x^2}. \tag{2.33}$$

In the following, the simplified diffusion formulation in Eq. (2.33) is applied to determine the diffusion process of electrons and solvent molecules and its implications for the growth behavior of the SEI.

2.3.2 Electron Diffusion Mechanism

As discussed in Section 1.2.4, electron diffusion is a widely assumed mechanism to cause long-term SEI growth during battery storage [63, 87–89, 133–138]. The electron diffusion mechanism explains the transport of electrons from the anode-SEI interface towards the SEI-electrolyte interface by diffusion of localized electrons, schematically illustrated in Fig. 2.2. The electrons can be accompanied by lithium ions perceived together as neutral lithium interstitials supported by density functional theory (DFT) calculations [134, 135]. Nevertheless, localized electrons can also occur in localized states generated by crystal inhomogeneities [240], grain boundaries of distinct SEI compounds [105], or radicals inside the SEI [136].

The detailed derivation of the electron diffusion mechanism was presented by Single et al. in Ref. [89]. In the following, the basic concepts of this deduction are reflected.

The first assumption is the chemical equilibrium of electrons at the anode-SEI interface, expressed as chemical potentials $\mu_{e^-}^{anode} = \mu_{e^-}^{SEI}$. On the one hand, the anode open-circuit voltage U_0 determines the chemical potential of electrons inside the anode as $\mu_{e^-}^{anode} = -FU_0$. On the other hand, ideal solution theory describes the chemical potential of electrons inside the SEI as

$$\mu_{e^-}^{SEI} = \mu_{e^-,ref}^{SEI} + R_{gas} T \ln \frac{c_{e^-}|_{x=0}}{c_{e^-,max}} \tag{2.34}$$

with $\mu_{e^-,ref}^{SEI}$ a reference chemical potential, $c_{e^-}|_{x=0}$ the concentration of electrons inside the SEI at the anode-SEI interface, and $c_{e^-,max}$ the maximum concentration of localized electrons inside the SEI.

The concentration of localized electrons inside the SEI at the anode-SEI interface is

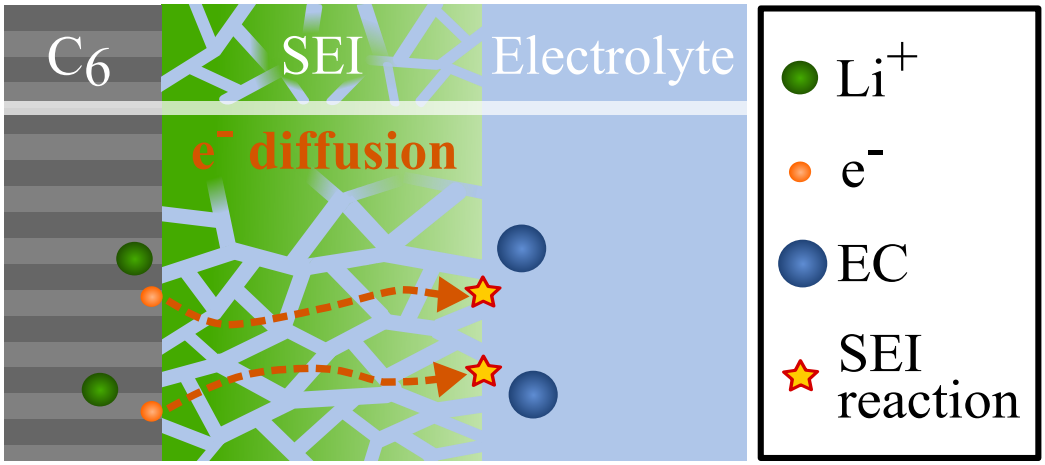

Figure 2.2: Scheme of the electron diffusion mechanism mediating SEI growth. Reprinted and modified from Ref. [153] with permission from Elsevier.

determined by the equilibrium condition of the chemical potential to

$$c_{e^-}|_{x=0} = c_{e^-,0} \cdot \exp\left(-\frac{FU_0}{R_{gas}T}\right), \tag{2.35}$$

where $c_{e^-,0}$ is the concentration of localized electrons at $U_0 = 0\,\mathrm{V}$.

The second assumption is that diffusion governs the transport of electrons from the anode-SEI interface towards the SEI-electrolyte interface. This diffusive charge transport is recognized as SEI formation current density $j_{e^-}^{SEI}$ as

$$j_{e^-}^{SEI} = z_{e^-} F \vec{N}_{e^-} = z_{e^-} F D_{e^-} \frac{\partial c_{e^-}}{\partial x} \tag{2.36}$$

with z_{e^-} the electron charge number, $\vec{N}_{e^-}$ the species flux density of electrons, and D_{e^-} the diffusion coefficient of electrons inside the SEI.

The capacity fade due to SEI growth mediated by electron diffusion is determined by solving Eq. (2.36). The boundary condition for the electron concentration at the anode-SEI interface is given by Eq. (2.35). At the SEI-electrolyte interface, a vanishing concentration of electrons is assumed due to fast SEI formation reaction kinetics, $c_{e^-}|_{x=L_{SEI}} = 0$. The resulting equation quantifying SEI growth combining Eq. (2.25) and Eq. (2.36) with the specified boundary conditions states

$$\partial_t Q_{SEI} = \frac{A^2 s_{Li} F^2 D_{e^-}}{v} \cdot \frac{c_{e^-,0} \cdot e^{-\tilde{U}_0}}{Q_{SEI} + Q_{SEI,0}} \tag{2.37}$$

with the normalized anode voltage $\tilde{U}_0 = FU_0/(R_{gas}T)$ and initial capacity loss $Q_{SEI,0}$. Assuming a constant voltage, Eq. (2.37) can be solved analytically, revealing the

renowned square-root time dependence of SEI growth

$$Q_{\mathrm{SEI}} = AF\sqrt{\frac{2s_{\mathrm{Li}}}{v}D_{\mathrm{e}^-}c_{\mathrm{e}^-,0}}e^{-\tilde{U}_0/2}\sqrt{t+t_0} - Q_{\mathrm{SEI},0}, \tag{2.38}$$

where the time constant t_0 accounts for passivation by the initial SEI thickness.
Examining Eq. (2.37) and Eq. (2.38), capacity fade due to the electron diffusion mechanism of SEI growth contains a parabolic time dependence as well as an intrinsic dependence on the anode OCV. Nonetheless, changing anode voltages over time can cause deviations from the typical square-root time behavior as discussed later in Section 3.1.3.

2.3.3 Solvent Diffusion Mechanism

As an alternative transport mechanism, literature considers the diffusion of solvent molecules through the SEI towards the anode-SEI interface to cause continued SEI growth [88, 102, 140–151]. The schematic in Fig. 2.3 visualizes the SEI growth mediated by solvent diffusion. Reasons for the notion of solvent diffusion are possible porosity of the SEI [152] and deduced motion of large (solvent and redox) molecules through the SEI in redox shuttle experiments [143, 144, 147–149] as outlined in Section 1.2.4. However, in opposition to the electron diffusion mechanism, Single et al. demonstrated that solvent diffusion cannot explain the experimentally observed SOC dependence of capacity fade, at least in the transport limited regime [89].
To investigate the solvent diffusion mechanism more thoroughly, the restriction to the transport limited regime was lifted in Paper I [153]. The generalized approach accounts for the interplay of reaction kinetics and diffusion, allowing both steps to limit the overall SEI growth behavior. In the following, a detailed derivation of the solvent diffusion mechanism is provided, which was published in a condensed form in Paper I [153].
In order to estimate the rate of the SEI formation reaction stated in Eq. (1.1), the chemical potentials for the reaction educts μ_{educts} and the reaction product identified as SEI μ_{SEI} state

$$\begin{aligned} \mu_{\mathrm{educts}} &= \mu_{\mathrm{Li}^+} + \mu_{\mathrm{e}^-} + \mu_{\mathrm{EC}} = -FU_0 + \mu_{\mathrm{EC,ref}} + R_{\mathrm{gas}}T\ln\left(\tilde{c}_{\mathrm{EC}}\right) \\ \mu_{\mathrm{SEI}} &= \mu_{\mathrm{SEI,ref}} \end{aligned} \tag{2.39}$$

with the normalized concentration of ethylene carbonate (EC) solvent molecules $\tilde{c}_{\mathrm{EC}} = c_{\mathrm{EC}}/c_{\mathrm{EC,bulk}}$ specified by the ratio of the actual concentration c_{EC} and the bulk concentration $c_{\mathrm{EC,bulk}}$. The parameter $\mu_{\mathrm{EC,ref}}$ represents the reference chemical potential of the bulk electrolyte and $\mu_{\mathrm{SEI,ref}}$ the constant chemical potential of the SEI. Due to chemical equilibrium, the anode open-circuit voltage U_0 determines the chemical potential of the electrons. Furthermore, the number of transferred charges

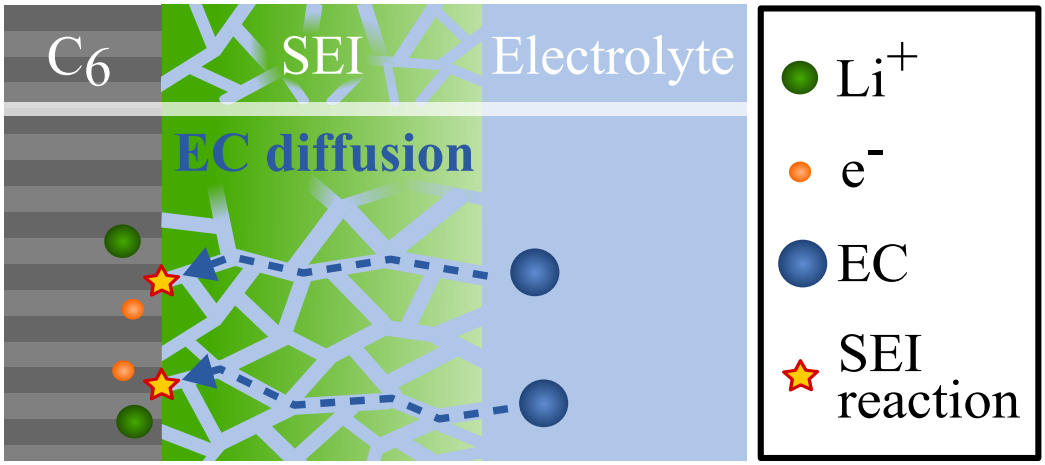

Figure 2.3: Scheme of the solvent diffusion mechanism mediating SEI growth. Reprinted and modified from Ref. [153] with permission from Elsevier.

of the rate-limiting step is assumed as $z = 1$.

The normalized overpotential $\tilde{\eta}_\mathrm{r} = F\eta_\mathrm{r}/(R_\mathrm{gas}T)$ driving the SEI formation reaction is defined as the Gibbs free energy change ΔG due to the reaction, which is the difference of the chemical potentials $\tilde{\eta}_\mathrm{r} = \Delta G/(R_\mathrm{gas}T) = (\mu_\mathrm{SEI} - \mu_\mathrm{educts})/(R_\mathrm{gas}T)$. Therefore, the normalized overpotential of the SEI formation reaction during open-circuit storage conditions reads

$$\tilde{\eta}_\mathrm{r} = \frac{FU_0}{R_\mathrm{gas}T} - \ln\left(\tilde{c}_\mathrm{EC}\right) - \frac{\mu_\mathrm{EC,ref} - \mu_\mathrm{SEI}}{R_\mathrm{gas}T}. \tag{2.40}$$

For initialization of the Butler-Volmer equation analog to Eq. (2.26) describing SEI formation, the normalized concentration of SEI species inside the SEI is set to $\tilde{c}_\mathrm{SEI} = 1$. The concentration of educt species impacting the reaction rate is the solvent concentration at the anode-SEI interface $\tilde{c}_\mathrm{EC}(x = 0)$. The charge transfer coefficients are assumed to be $\alpha_a = \alpha$ and $\alpha_c = 1 - \alpha$ as commonly supposed due to simple charge transfer kinetics. Therefore, the initialized Butler-Volmer equation quantifying the reaction rate of SEI growth reads

$$R_\mathrm{rate} = r_0 \tilde{c}_\mathrm{EC}^{\alpha}(x = 0)\left[e^{-(1-\alpha)\tilde{\eta}_\mathrm{r}} - e^{\alpha\tilde{\eta}_\mathrm{r}}\right] \tag{2.41}$$

with the reaction rate constant r_0.

As boundary condition, the Butler-Volmer equation (2.41) is constrained to yield vanishing rates at the SEI formation voltage $U = U_\mathrm{SEI,ref} = 0.8\,\mathrm{V}$, when the solvent concentration at the anode-SEI interface equals the bulk concentration $\tilde{c}_\mathrm{EC}(x = 0) = 1$. The specified condition identifies the reference term in Eq. (2.40) to be equivalent to $(\mu_\mathrm{EC,ref} - \mu_\mathrm{SEI,ref})/(R_\mathrm{gas}T) = \tilde{U}_\mathrm{SEI,ref}$ with the normalized SEI formation voltage calculated as $\tilde{U}_\mathrm{SEI,ref} = FU_\mathrm{SEI,ref}/(R_\mathrm{gas}T)$. Inserting the normalized overpotential expressed in Eq. (2.40) and applying the reference condition into the Butler-Volmer

equation (2.41) yields the derived Butler-Volmer equation defining the SEI formation reaction rate due to solvent diffusion as

$$R_{\text{rate}} = \frac{j_0}{F}\left[\tilde{c}_{\text{EC}}(x=0)e^{-(1-\alpha)\left(\tilde{U}_0-\tilde{U}_{\text{SEI,ref}}\right)} - e^{\alpha\left(\tilde{U}_0-\tilde{U}_{\text{SEI,ref}}\right)}\right] \tag{2.42}$$

with the exchange current density defined as $j_0 = Fr_0$ and the normalized anode open-circuit voltage $\tilde{U}_0 = FU_0/(R_{\text{gas}}T)$.

The so far non-quantified value of the solvent concentration at the anode-SEI interface occurring in the derived Butler-Volmer equation is determined by the residual concentration of diffusing solvent molecules towards this interface and solvent species lost due to the SEI formation reaction. The diffusion equation analog to Eq. (2.33) for EC molecules diffusing through the SEI from the SEI-electrolyte interface to the anode-SEI interface states

$$\frac{\partial \tilde{c}_{\text{EC}}}{\partial t} = \frac{D_{\text{EC}}}{L_{\text{SEI}}^2}\cdot\frac{\partial^2 \tilde{c}_{\text{EC}}}{\partial \tilde{x}^2} \tag{2.43}$$

with D_{EC} the diffusion coefficient of EC molecules and $\tilde{x} = x/L_{\text{SEI}}$ the non-dimensional distance from the anode-SEI interface.

The boundary conditions for the diffusion equation relate the solvent concentration to the respective bulk value at the SEI-electrolyte interface and to the Butler-Volmer reaction rate at the anode-SEI interface according to

$$\tilde{c}_{\text{EC}}\big|_{\tilde{x}=1} = 1 \tag{2.44}$$

$$\frac{Dc_{\text{EC,bulk}}}{L_{\text{SEI}}}\cdot\left.\frac{\partial \tilde{c}_{\text{EC}}}{\partial \tilde{x}}\right|_{x=0} = R_{\text{rate}}. \tag{2.45}$$

The solution of the coupled equations for the reaction rate in Eq. (2.42) and the diffusion equation in Eq. (2.43) is combined with the relation to capacity loss due to SEI growth stated in Eq. (2.25). The resulting equation defining SEI growth mediated by solvent diffusion reads

$$\partial_t Q_{\text{SEI}} = Aj_0\frac{e^{-(1-\alpha)\left(\tilde{U}_0-\tilde{U}_{\text{SEI,ref}}\right)} - e^{\alpha\left(\tilde{U}_0-\tilde{U}_{\text{SEI,ref}}\right)}}{1+\frac{vj_0}{s_{\text{Li}}AF^2D_{\text{EC}}c_{\text{EC,bulk}}}e^{-(1-\alpha)\left(\tilde{U}_0-\tilde{U}_{\text{SEI,ref}}\right)}\left(Q_{\text{SEI}}+Q_{\text{SEI,0}}\right)}. \tag{2.46}$$

The capacity loss according to Eq. (2.46) states the SEI-related capacity fade mediated by solvent diffusion limited in general by the interplay of reaction kinetics and solvent species transport. Analyzing the SEI growth in the regimes of transport limitation and reaction limitation, respectively, simplifies the intertwined functional behavior and facilitates analytic expressions for the capacity fade.

As a first case, transport can limit the overall SEI growth if $FD_{\text{EC}}c_{\text{EC,bulk}}/L_{\text{SEI}} \ll j_0$. In the transport-limited regime, Eq. (2.46) reduces for a constant voltage to the analytical

expression for SEI-related capacity fade

$$Q_{\mathrm{SEI}} = AF\sqrt{\frac{2s_{\mathrm{Li}}}{v}D_{\mathrm{EC}}c_{\mathrm{EC,bulk}}\left(t+t_0\right)} - Q_{\mathrm{SEI},0} \tag{2.47}$$

when the term of the backward reaction, i.e., SEI dissolution, is neglected. Assuming transport limitation, Eq. (2.47) demonstrates that the solvent diffusion mechanism reveals the typical square-root behavior of capacity fade in time. However, no dependence on the OCV remains in this case.
As a second case, the reaction step can dominate the SEI growth behavior for low exchange current densities $j_0 \ll FD_{\mathrm{EC}}c_{\mathrm{EC,bulk}}/L_{\mathrm{SEI}}$. In the reaction-limited regime, Eq. (2.46) simplifies to

$$Q_{\mathrm{SEI}} = Aj_0\left(e^{-(1-\alpha)\left(\tilde{U}_0-\tilde{U}_{\mathrm{SEI,ref}}\right)} - e^{\alpha\left(\tilde{U}_0-\tilde{U}_{\mathrm{SEI,ref}}\right)}\right)t. \tag{2.48}$$

Thus, the solvent diffusion mechanism reveals a non-trivial SOC dependence for SEI growth with reaction limitation stated in Eq. (2.48). However, in this case, a linear time dependence results, opposing capacity fade experiments.

2.4 Silicon-SEI Mechanics

Silicon is a promising next-generation anode material, as it shows a significantly raised theoretical capacity. Nevertheless, the high ability for lithiation involves substantial volume expansion during lithiation and respective shrinkage during delithiation. Therefore, changes in lithium concentration inside silicon, as well as mechanical responses of silicon and SEI, cause deformations of the silicon-SEI system. The mechanical deformations and the deformation rates of the SEI generate stresses, impacting the lithiation behavior of silicon anodes. The following chemo-mechanical model illustrates the interplay of silicon and SEI in the Lagrangian frame, investigated thoroughly in Paper II [173], Paper III [174], and Paper IV [62].

2.4.1 Model Free Energy Density

The investigated silicon-SEI model is founded on a free energy density to obey the restrictions of thermodynamic consistent modeling discussed in Section 2.2. The free energy density $\rho_0\varphi$ in the Lagrangian frame, constituting of a chemical contribution $\rho_0\varphi_{\mathrm{ch}}$ and a mechanical contribution $\rho_0\varphi_{\mathrm{el}}$, states

$$\rho_0\varphi = \rho_0\varphi_{\mathrm{ch}} + \rho_0\varphi_{\mathrm{el}} \tag{2.49}$$

$$= -\int_0^{c_{\mathrm{Li},0}} FU_0\left(c'_{\mathrm{Li},0}\right)\mathrm{d}c'_{\mathrm{Li},0} + \frac{1}{2}\left(\lambda\left(\mathrm{tr}\left(\mathbf{E}_{\mathrm{el}}\right)\right)^2 + 2G\,\mathrm{tr}\left(\mathbf{E}_{\mathrm{el}}^2\right)\right). \tag{2.50}$$

The chemical share is determined by the lithium concentration $c_{\mathrm{Li},0}$ and the observed open-circuit voltage $U_0\left(c_{\mathrm{Li},0}\right)$. It is empirically motivated, such that the chemical potential of lithium matches the observed true OCV [234–236]

$$\mu_{\mathrm{Li,ch}} = \frac{\partial \rho_0 \varphi_{\mathrm{ch}}}{\partial c_{\mathrm{Li},0}} = -FU_0. \tag{2.51}$$

In the case of silicon anodes, the observed voltage hysteresis impedes precise measurements of the true OCV value. Thus, the SOC-dependent mean value of the open-circuit voltages in the lithiation and delithiation branch, $U_0^{\mathrm{lith}}(c_{\mathrm{Li},0})$ and $U_0^{\mathrm{delith}}(c_{\mathrm{Li},0})$, is considered as true OCV

$$U_0(c_{\mathrm{Li},0}) = \frac{1}{2}\left(U_0^{\mathrm{lith}}(c_{\mathrm{Li},0}) + U_0^{\mathrm{delith}}(c_{\mathrm{Li},0})\right). \tag{2.52}$$

For the mechanical share, the Saint Venant–Kirchhoff model, a compressible hyperelastic material model, describes the mechanical free energy [231]. The elastic strain $\mathbf{E}_{\mathrm{el}}$ stated later in Eq. (2.55) determines the amount of strain energy. The mechanical parameters are the first Lamé constant $\lambda = 2G\nu/\left(1-2\nu\right)$ and the second Lamé constant $G = E/(2(1+\nu))$. They include Young's modulus E and the Poisson ratio ν of the underlying material, either silicon or SEI.

2.4.2 Chemo-Mechanical Deformation Contributions

The deformation gradient tensor $\mathbf{F}$ introduced in Section 2.1.3 is described multiplicatively for the silicon-SEI system in large deformation or finite strain theory

$$\mathbf{F} = \mathbf{F}_{\mathrm{pl}}\mathbf{F}_{\mathrm{el}}\mathbf{F}_{\mathrm{ch}}. \tag{2.53}$$

The total deformation consists of the chemical contribution $\mathbf{F}_{\mathrm{ch}}$ due to lithium concentration changes, the elastic part $\mathbf{F}_{\mathrm{el}}$ accounting for reversible mechanical deformations, and the plastic share $\mathbf{F}_{\mathrm{pl}}$ describing irreversible mechanical deformations. The deformation contributions are defined in detail in the following.
The multiplicative approach chosen for the silicon-SEI model is in contrast to small deformation or infinitesimal strain theory, where the total strain is the sum of the single strain contributions. Finite strain theory is necessary to describe the investigated system due to substantial deformations during cycling.

Chemical Expansion

The chemical deformation $\mathbf{F}_{\mathrm{ch}}$ describes reversible expansion due to an increase in lithium concentration $c_{\mathrm{Li},0}$ and respective shrinkage during delithiation. Lithium atoms alloying with silicon occupy a certain amount of space, expressed as the partial

molar volume $v_{\mathrm{Li}} = 9 \cdot 10^{-6}\ \frac{\mathrm{m}^3}{\mathrm{mol}}$ [241, 242]. The chemical deformation is considered to be isotropic, i.e., uniform in all directions of space,

$$\mathbf{F}_{\mathrm{ch}} = \lambda_{\mathrm{ch}}\mathbf{Id} = (1 + v_{\mathrm{Li}} c_{\mathrm{Li},0})^{1/3}\mathbf{Id}. \tag{2.54}$$

The size of the deformation components λ_{ch} is derived from the volume expansion of the lithium-silicon alloy during lithiation $J_{\mathrm{ch}} = \lambda_{\mathrm{ch}}^3$. The lithium concentration is expressed in the undeformed Lagrangian frame and can take any positive value up to $c_{\mathrm{Li},0,\mathrm{max}} = 311 \cdot 10^3\ \frac{\mathrm{mol}}{\mathrm{m}^3}$ [212, 243]. Therefore, the chemical deformation contribution ranges between the values $1 \leq \lambda_{\mathrm{ch}} \lesssim 1.56$.

Elasticity

Elastic deformation generates stress, which has to obey the momentum balance stated in Eq. (2.11). The elastic strain tensor is defined analog to the general strain equation in Eq. (2.3) as

$$\mathbf{E}_{\mathrm{el}} = \frac{1}{2}\left(\mathbf{F}_{\mathrm{el}}^{\mathrm{T}}\mathbf{F}_{\mathrm{el}} - \mathbf{Id}\right). \tag{2.55}$$

The first Piola-Kirchhoff stress $\mathbf{P}_{\mathrm{el}}$ generated due to the elastic deformation is defined by the constitutive equation (2.19) and the relation to the reversible second Piola-Kirchhoff stress via $\mathbf{P}_{\mathrm{el}} = \mathbf{F}_{\mathrm{rev}}\mathbf{T}_{\mathrm{rev}}\mathbf{F}_{\mathrm{pl}}^{-\mathrm{T}}$. The reversible deformation combines the chemical and elastic contributions, $\mathbf{F}_{\mathrm{rev}} = \mathbf{F}_{\mathrm{el}}\mathbf{F}_{\mathrm{ch}}$. Resulting from the Saint Venant-Kirchhoff model defining the mechanical contribution to the free energy density in Eq. (2.50), the stress reads

$$\mathbf{P}_{\mathrm{el}} = 2\mathbf{F}\frac{\partial \rho_0 \varphi}{\partial \mathbf{C}} = \lambda_{\mathrm{ch}}^{-2}\mathbf{F}\mathbf{F}_{\mathrm{pl}}^{-\mathrm{T}}\mathbf{F}_{\mathrm{pl}}^{-1}\left(\lambda\,\mathrm{tr}(\mathbf{E}_{\mathrm{el}})\mathbf{Id} + 2G\mathbf{E}_{\mathrm{el}}\right). \tag{2.56}$$

The stress determined by Eq. (2.56) is generated purely by elastic strains. However, as plastic deformation influences the stress value, it is termed elastoplastic stress in the following.

Plasticity

Plastic flow of silicon arises when reaching pronounced distortional stress levels. As an irreversible effect, plastic flow causes deformations that do not generate an additional stress contribution but influence the elastic stress stated in Eq. (2.56). The von Mises yield criterion for plastic flow states

$$f = \frac{\frac{3}{2}|\mathbf{M}_{\mathrm{a}}^{\mathrm{dev}}|^2}{\sigma_{\mathrm{Y}}^2} - 1 \leq 0 \tag{2.57}$$

with the deviatoric contribution $\mathbf{M}_\mathrm{a}^\mathrm{dev} = \mathbf{M}_\mathrm{a} - 1/3\,\mathrm{tr}\,\mathbf{M}_\mathrm{a}$ of the adapted Mandel stress $\mathbf{M}_\mathrm{a} = \frac{1}{J}\mathbf{M} = \mathbf{F}_\mathrm{rev}^\mathrm{T}\sigma\mathbf{F}_\mathrm{rev}^{-\mathrm{T}}$ and the yield stress σ_Y. No plastic flow occurs when $f < 0$, while plastic flow sets in when the yield criterion is reached $f = 0$.
The plastic flow expressed as $\mathbf{L}_\mathrm{pl} = \dot{\mathbf{F}}_\mathrm{pl}\mathbf{F}_\mathrm{pl}^{-1}$ is determined by

$$\mathbf{L}_\mathrm{pl} = \phi\frac{\partial f}{\partial \mathbf{M}_\mathrm{a}}, \tag{2.58}$$

where the plastic multiplier ϕ results from the Karush–Kuhn–Tucker (KKT) condition for ideal plastic flow $\phi f = 0$. The KKT condition ensures that the plastic multiplier vanishes $\phi = 0$ for $f < 0$, i.e., no plastic flow occurs when the norm of the deviatoric stress is below the yield stress. When reaching the yield criterion $f = 0$, the plastic flow has to ensure that the yield criterion is not exceeded to obey the KKT condition. Thus, the plastic multiplier results from the consistency condition $\dot{f} = 0$ during plastic flow. The requirement of non-negative entropy production $\mathbf{M} : \mathbf{L}_\mathrm{pl} \geq 0$ from Eq. (2.23) restricts the plastic multiplier to non-negative values $\phi \geq 0$.

2.4.3 Viscosity Models

The literature discusses several approaches to describe viscous material behavior. As these models are based on positive correlations between viscous stress and the deformation or strain rate, the condition of non-negative entropy production $\mathbf{P}_\mathrm{visc} : \dot{\mathbf{F}} \geq 0$ from Eq. (2.23) is immediately fulfilled. In the following, the viscosity models relevant to this thesis are presented.

Newtonian Viscosity

The simplest approach to describe the viscous behavior of a material is the Newtonian viscosity model. It relates the viscous stress σ_visc proportionally to the strain rate $\dot{\mathbf{E}}$ according to

$$\sigma_\mathrm{visc} = \eta\dot{\mathbf{E}}. \tag{2.59}$$

The proportionality constant in Eq. (2.59) is the viscosity η, determining the size of viscous stress for a certain strain rate. In the description of the Lagrangian frame, the first Piola-Kirchhoff stress tensor reads

$$\mathbf{P}_\mathrm{visc} = J\eta\dot{\mathbf{F}}. \tag{2.60}$$

The Newtonian viscosity model is characterized by its simplicity but typically applies only to low strain rates. For higher strain rates, the Newtonian model is prone to overestimate the generated viscous stress, as the viscosity of many materials decreases for increasing strain rates.

Shear-Thinning Viscosity

An advancement of the linear Newtonian viscosity is the shear-thinning viscosity model. It assumes that the viscosity is not constant but scales as a power law depending on the strain rate

$$\eta\left(\dot{\mathbf{E}}\right) = \eta_0 \dot{\mathbf{E}}_{\mathrm{mag}}^{n-1}, \tag{2.61}$$

where η_0 is the shear-thinning viscosity, n is the shear-thinning exponent, and the tensor $\dot{\mathbf{E}}_{\mathrm{mag}}$ composes of component-wise magnitudes of the strain rate tensor. The viscosity values η in Eq. (2.61) and the viscous stress values σ_{visc} in Eq. (2.59) are calculated component-wise. The shear-thinning model is empirically motivated and oftentimes fits better to experimental results, revealing a decreasing slope of the viscous stress for higher strain rates.

Garofalo Viscosity

Another viscosity model accounting for the decreasing slope of the viscous stress for higher strain rates is the Garofalo viscosity model or inverse hyperbolic sine model first presented in Ref. [244]. The Garofalo law utilizes the flattening profile of the inverse hyperbolic sine to describe the viscous Cauchy stress

$$\sigma_{\mathrm{visc}} = \sigma_{\mathrm{ref}} \cdot \operatorname{asinh}\left(\tau \dot{\mathbf{E}}\right) \tag{2.62}$$

with a reference stress measure σ_{ref} and the time constant τ. The first Piola-Kirchhoff stress in the Lagrangian frame states

$$\mathbf{P}_{\mathrm{visc}} = J\sigma_{\mathrm{ref}} \cdot \operatorname{asinh}\left(\tau \dot{\mathbf{E}}\right) \mathbf{F}^{-\mathrm{T}}. \tag{2.63}$$

The Garofalo viscosity model is theoretically motivated in Ref. [245] by lattice distortions, influencing hopping energy barriers between neighboring lattice positions. The strain rate results from the difference between forward and backward hopping, indicated by the hyperbolic sine of the stress, which is responsible for the energy barriers. Inverse formulation of the relation between strain rate and viscous stress reasons the Garofalo law in Eq. (2.63).
In the limit of small stresses, the Garofalo model coincides with the Newtonian viscosity model, revealing linear behavior. For extensive stresses, however, the Garofalo low predicts a logarithmic dependence of the viscous stress on the strain rate, flattening faster for higher strain rates than the shear-thinning approach.

2.4.4 Chemo-Mechanical Coupling

The free energy density of the silicon-SEI model stated in Eq. (2.50) consists of a chemical and a mechanical contribution. The chemical potential is defined by the

constitutive equation (2.18), accounting for the whole free energy density. Consequently, the chemical potential couples chemistry with mechanics and will be called chemo-mechanical potential in the following.
The chemo-mechanical potential derived from the constitutive equation (2.18) and the free energy density in Eq. (2.50) reads

$$\mu_{\mathrm{Li}} = \frac{\partial \rho_0 \varphi}{\partial c_{\mathrm{Li},0}} = -FU_0 - \frac{v_{\mathrm{Li}}}{3\lambda_{\mathrm{ch}}^3}\mathbf{P} : \mathbf{F}. \tag{2.64}$$

The first term describes the purely chemical contribution, depending on the lithium concentration via $U_0(c_{\mathrm{Li},0})$. The second term represents the chemo-mechanical coupling, depending on stress and the chemical expansion.
The chemo-mechanical potential of lithium relates to the anode voltage U according to $\mu_{\mathrm{Li}} = -FU$. Hence, the anode voltage affected by chemistry and mechanics states

$$U = U_0 + \frac{v_{\mathrm{Li}}}{3F\lambda_{\mathrm{ch}}^3}\mathbf{P} : \mathbf{F}. \tag{2.65}$$

The chemo-mechanical expression of the anode voltage demonstrates that it is crucial to consider not only chemical but also mechanical effects for the voltage estimation of silicon anodes.

2.4.5 Chemo-Mechanical Silicon-SEI Model

So far, the chemo-mechanical model considering chemical expansion, elasticity, plasticity, and viscosity is derived and stated in a general form. The following paragraphs present the specific model equations solved for the silicon nanoparticle core, the SEI shell, and their interface.

Chemo-Elastoplastic Silicon Core

Inside the silicon particle, the state is defined by the lithium concentration $c_{\mathrm{Li},0}$ and the respective deformation $\mathbf{F}_{\mathrm{Si,ch}}$, elastic deformation $\mathbf{F}_{\mathrm{Si,el}}$, and plastic deformation $\mathbf{F}_{\mathrm{Si,pl}}$. The lithium concentration change during lithiation and delithiation of a silicon particle reads

$$\dot{c}_{\mathrm{Li},0} = -\nabla_0 \cdot \vec{N}_{\mathrm{Li},0} = \nabla_0 \cdot L \nabla_0 \mu_{\mathrm{Li}} \tag{2.66}$$

driven by the chemo-mechanical potential μ_{Li} to account for non-negative entropy production in Eq. (2.23). The mobility of lithium is defined as $L = D_{\mathrm{Li}} \left(\partial \mu_{\mathrm{Li}} / \partial c_{\mathrm{Li},0}\right)^{-1}$ with D_{Li} the diffusion coefficient of lithium inside silicon. The definition of the mobility L ensures compatibility with the Fickian diffusion equation (2.33). At the particle boundary $r = R$, the lithium flux $\vec{N}_{\mathrm{Li},0}(R)$ is specified by the applied (de)lithiation rate.

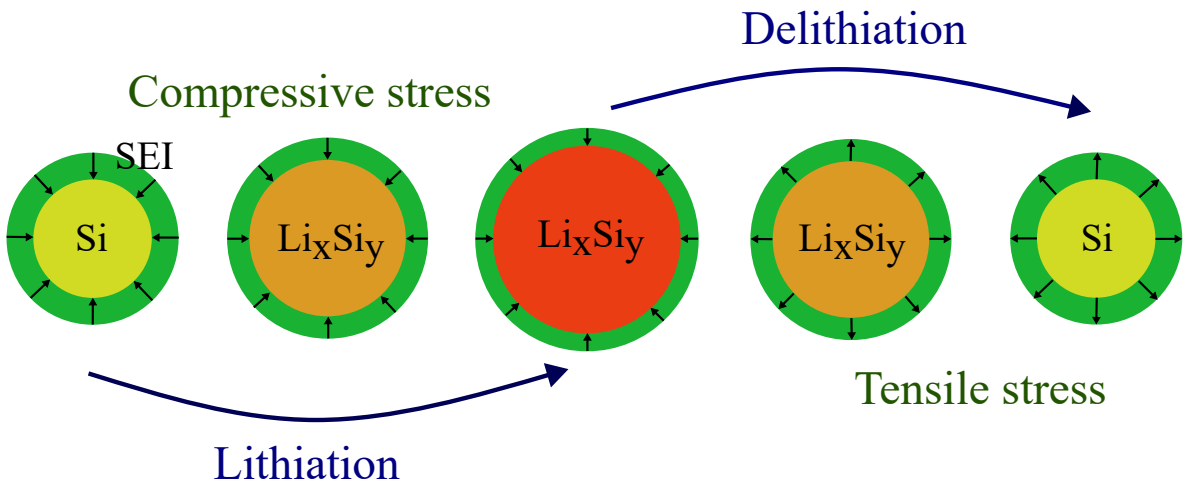

Figure 2.4: Scheme of the volume changes of silicon nanoparticles and the radial stress at the particle-SEI interface during cycling. Reprinted from Ref. [173], licensed under CC BY 4.0, https://creativecommons.org/licenses/by/4.0/.

Regarding the elastic deformation, the momentum balance

$$0 = \nabla_0 \cdot \mathbf{P}_{\mathrm{Si}} \tag{2.67}$$

determines the time evolution of the stress inside silicon. Viscous effects are neglected for the silicon particle model. Thus, the momentum balance specifies the elastic stress $\mathbf{P}_{\mathrm{Si}} = \mathbf{P}_{\mathrm{Si,el}}$ and elastic strain $\mathbf{E}_{\mathrm{Si,el}}$ via Eq. (2.56).
The plastic deformation results from plastic flow $\mathbf{L}_{\mathrm{Si,pl}}$ analog to Eq. (2.58) when reaching the von Mises yield criterion $f_{\mathrm{Si}} \leq 0$ in Eq. (2.57). For the silicon particle, plastic flow obeys

$$\mathbf{L}_{\mathrm{Si,pl}} = \phi_{\mathrm{Si}} \frac{\partial f_{\mathrm{Si}}}{\partial \mathbf{M}_{\mathrm{a,Si}}} \qquad \text{with} \qquad f_{\mathrm{Si}} = \frac{\frac{3}{2} |\mathbf{M}_{\mathrm{a,Si}}^{\mathrm{dev}}|^2}{\sigma_{\mathrm{Y,Si}}^2} - 1 \leq 0 \tag{2.68}$$

with the deviatoric part $\mathbf{M}_{\mathrm{a,Si}}^{\mathrm{dev}}$ of the adapted Mandel stress $\mathbf{M}_{\mathrm{a,Si}} = \mathbf{F}_{\mathrm{Si,rev}}^{\mathrm{T}} \sigma_{\mathrm{Si}} \mathbf{F}_{\mathrm{Si,rev}}^{-\mathrm{T}}$ and the yield stress $\sigma_{\mathrm{Y,Si}}$ of the silicon particle. The plastic multiplier ϕ_{Si} results from the consistency condition $\dot{f}_{\mathrm{Si}} = 0$.

Visco-Elastoplastic SEI Shell

The SEI model considers no chemical deformation but elastic deformation $\mathbf{F}_{\mathrm{SEI,el}}$ and plastic deformation $\mathbf{F}_{\mathrm{SEI,pl}}$. Furthermore, the elastic stress is complemented by a viscous stress contribution.

The stress inside the SEI $\mathbf{P}_{\mathrm{SEI}}$ is composed of an elastic stress share $\mathbf{P}_{\mathrm{SEI,el}}$ and a viscous stress share $\mathbf{P}_{\mathrm{SEI,visc}}$ according to

$$\mathbf{P}_{\mathrm{SEI}} = \mathbf{P}_{\mathrm{SEI,el}} + \mathbf{P}_{\mathrm{SEI,visc}}. \tag{2.69}$$

The viscous stress relates to the strain rate of the SEI $\dot{\mathbf{E}}_{\mathrm{SEI}}$, depending on the choice of the viscosity model presented in Section 2.4.3.
The momentum balance

$$0 = \nabla_0 \cdot \mathbf{P}_{\mathrm{SEI}} = \nabla_0 \cdot (\mathbf{P}_{\mathrm{SEI,el}} + \mathbf{P}_{\mathrm{SEI,visc}}) \tag{2.70}$$

yields the temporal evolution of the stress inside the SEI. Together with the viscous stress, Eq. (2.70) determines the evolution of the elastic strain $\mathbf{E}_{\mathrm{SEI,el}}$.
Plastic flow $\mathbf{L}_{\mathrm{SEI,pl}}$ occurs when reaching the yield condition $f_{\mathrm{SEI}} \leq 0$ stated generally in Eq. (2.57). The plastic flow inside the SEI follows

$$\mathbf{L}_{\mathrm{SEI,pl}} = \phi_{\mathrm{SEI}} \frac{\partial f_{\mathrm{SEI}}}{\partial \mathbf{M}_{\mathrm{a,SEI,el}}} \qquad \text{with} \qquad f_{\mathrm{SEI}} = \frac{\frac{3}{2}|\mathbf{M}^{\mathrm{dev}}_{\mathrm{a,SEI,el}}|^2}{\sigma^2_{\mathrm{Y,SEI}}} - 1 \leq 0 \tag{2.71}$$

with the deviatoric part $\mathbf{M}^{\mathrm{dev}}_{\mathrm{a,SEI,el}}$ of the elastic contribution to the adapted Mandel stress $\mathbf{M}_{\mathrm{a,SEI,el}} = \mathbf{F}^{\mathrm{T}}_{\mathrm{SEI,el}} \boldsymbol{\sigma}_{\mathrm{SEI,el}} \mathbf{F}^{-\mathrm{T}}_{\mathrm{SEI,el}}$ and the yield stress $\sigma_{\mathrm{Y,SEI}}$ of the SEI shell. Plastic flow inside the SEI is assumed to be caused by elastic stress and not by viscous stress. The consistency condition $\dot{f}_{\mathrm{SEI}} = 0$ determines the plastic multiplier ϕ_{SEI}.

Particle-SEI Interface Coupling

At the interface between the silicon particle and the SEI, both domains are coupled geometrically and mechanically. The underlying assumption is perfect sticking between the silicon and the SEI domain.
The geometric connection effects equal radial coordinates at the interface of the silicon particle and the SEI shell, $r_{\mathrm{Si,int}} = r_{\mathrm{SEI,int}} = R$. Furthermore, the spherical geometry causes equal deformations of silicon and SEI in the tangential direction at the interface, $\mathbf{F}_{\mathrm{Si},\varphi\varphi}\big|_{r=R} = \mathbf{F}_{\mathrm{SEI},\varphi\varphi}\big|_{r=R}$.
The mechanical coupling imposes equal stress components in the radial direction at the silicon-SEI interface

$$\mathbf{P}_{\mathrm{Si,rr}}\big|_{r=R} = \mathbf{P}_{\mathrm{SEI,rr}}\big|_{r=R}. \tag{2.72}$$

While the chemical expansion dominates the deformation inside the silicon particle, the SEI deforms solely mechanically. Therefore, large mechanical strains and stresses arise inside the SEI to accommodate the volume changes during cycling. In terms of the chemo-mechanical silicon-SEI model, it is essential to account for the mechanical influence of the SEI on the lithiation behavior of the silicon particle.

2.4.6 Reduced Chemo-Mechanical Model

In addition to the spatially-resolved chemo-mechanical continuum model for the silicon-SEI system, a reduced model is derived in Paper III [174]. This model considers the chemo-mechanical interaction of silicon and SEI based on the current state at the interface. It accounts for voltage changes due to elastic stress inside the silicon particle generated by elastoplastic stress of the SEI ΔU_{ee} and viscous stress of the SEI ΔU_{ev} applying the Garofalo viscosity model. Due to the detailed derivation in Paper III [174] and the corresponding supporting information, only the model equations are stated in the following.
The system of differential equations defining the reduced chemo-mechanical hysteresis model reads

$$\frac{\mathrm{d}\,\mathrm{SOC}}{\mathrm{d}t} = \frac{\dot{c}_{\mathrm{Li},0}}{c_{\mathrm{Li},0,\mathrm{max}}} = \pm\frac{C_{\mathrm{rate}}}{3600}\,\frac{1}{\mathrm{s}} \tag{2.73}$$

$$\frac{\mathrm{d}\,\Delta U_{\mathrm{ee}}}{\mathrm{d}t} = \begin{cases} -E_{\mathrm{SEI}}\dfrac{2v_{\mathrm{Li}}^2}{3F\lambda_{\mathrm{ch}}^7}\dot{c}_{\mathrm{Li},0}, & \text{if } f_{\mathrm{red}} < 0 \\ \dfrac{\alpha_{\mathrm{red}}\sigma_{\mathrm{Y,SEI}}v_{\mathrm{Li}}^2}{F\left(1+\alpha_{\mathrm{red}}\lambda_{\mathrm{ch}}^3\right)^2}\left|\dot{c}_{\mathrm{Li},0}\right|, & \text{otherwise} \end{cases} \tag{2.74}$$

$$\frac{\mathrm{d}\,\Delta U_{\mathrm{ev}}}{\mathrm{d}t} = -\frac{E_{\mathrm{Si}}v_{\mathrm{Li}}}{\tau F\lambda_{\mathrm{ch}}^2}\sinh\left(\frac{\alpha_{\mathrm{red}}\lambda_{\mathrm{ch}}^3 F\Delta U_{\mathrm{ev}}}{\sigma_{\mathrm{ref}}v_{\mathrm{Li}}}\right) - \frac{E_{\mathrm{Si}}v_{\mathrm{Li}}^2}{3F\lambda_{\mathrm{ch}}^3}\dot{c}_{\mathrm{Li},0} \tag{2.75}$$

with the auxiliary parameter $\alpha_{\mathrm{red}} = \frac{1}{2}\left(\frac{R_{\mathrm{Si},0}}{L_{\mathrm{SEI},0}} - 1\right)$ and the yield criterion for plastic flow for the reduced model

$$f_{\mathrm{red}} = -\operatorname{sgn}\left(\dot{c}_{\mathrm{Li},0}\right)\left(1+\alpha_{\mathrm{red}}\lambda_{\mathrm{ch}}^3\right)\frac{F\Delta U_{\mathrm{ee}}}{v_{\mathrm{Li}}\sigma_{\mathrm{Y,SEI}}} - 1 \leq 0. \tag{2.76}$$

The reduced model describes the silicon anode voltage as the sum of the mean open-circuit voltage U_0, the elasto-elastoplastic contribution ΔU_{ee}, and the elasto-viscous contribution ΔU_{ev} stating

$$U = U_0 + \Delta U_{\mathrm{ee}} + \Delta U_{\mathrm{ev}}. \tag{2.77}$$

In descriptive terms, Eq. (2.73) describes the change of SOC for lithiation ($+$) and delithiation ($-$). The upper case in Eq. (2.74) represents the elasto-elastic voltage evolution resulting from the elastic stress of the silicon core imposed by the elastic behavior of the SEI. The lower case in Eq. (2.74) states the elasto-plastic voltage contribution due to elastic silicon stress arising from the plastic behavior of the SEI. For the elasto-viscous voltage contribution in Eq. (2.75), elastic stress inside the silicon particle is imposed by the viscous stress of the SEI. The first term in Eq. (2.75) accounts for the relaxation of the viscous SEI stress, while the second term states the increase in viscous SEI stress due to silicon volume changes.

Considering the voltage relaxation, the analytical solution of the viscous contribution stated in Eq. (2.75) states

$$\Delta U_{\mathrm{ev}} = \frac{2 v_{\mathrm{Li}} \sigma_{\mathrm{ref}}}{\alpha_{\mathrm{red}} F \lambda_{\mathrm{ch}}^3} \operatorname{atanh}\left(C \cdot \exp\left(-\frac{E_{\mathrm{core}} \alpha_{\mathrm{red}} \lambda_{\mathrm{ch}}}{\tau \sigma_{\mathrm{ref}}} t \right) \right) \tag{2.78}$$

with the integration constant C specified by the boundary condition of the initial voltage before the relaxation process.
Appealing in its simplicity, the reduced chemo-mechanical hysteresis model rationally complements the spatially resolved silicon-SEI model. Based on differential equations with respect to time, the reduced model preserves the physical context of the voltage hysteresis explanation. Moreover, the reduced model covers voltage relaxation processes in time. Both physical interpretation and relaxation predictions distinguish the presented reduced chemo-mechanical hysteresis model from the empirical Plett model outlined in Section 1.3.3.

3 Results and Discussion

Based on the thermodynamically consistent theory addressed in Chapter 2, this chapter investigates the characteristics of SEI growth mechanisms discussed in Paper I. Moreover, it presents the chemo-mechanical silicon-SEI model relating to the silicon voltage hysteresis published in Paper II, Paper III, and Paper IV. The corresponding publications, including the manuscript and supporting information, are placed at the end of this thesis.

First of all, Section 3.1 refers to the simulation results of SEI growth mechanisms during open-circuit storage as published in Paper I [153]. Particularly, the work compares the characteristics of the electron diffusion and solvent diffusion mechanisms. The focus of the investigation is on relating the simulation results to experimental data, considering the observed SOC and time dependence to reassess the relevant growth mechanism.

The as-grown SEI constitutes the precondition for the chemo-mechanical interaction of silicon and SEI treated afterwards in this chapter. As introduced in Section 1.3, silicon anodes show a voltage hysteresis behavior, lacking a consistent physical explanation. Considering the substantial volume changes of silicon upon cycling, Section 3.2 deals with the chemo-mechanical interplay of silicon and SEI presented as the reason for the voltage hysteresis in Paper II [173]. The model describes the hysteresis behavior during cycling and after short relaxation periods for spherically symmetric silicon nanoparticles.

Nevertheless, recent experimental results report a slow long-term voltage relaxation process of silicon anodes [216]. Extending the hysteresis description, Section 3.3 discusses an advancement of the chemo-mechanical model, which reproduces the long-term relaxation behavior as presented in Paper III [174]. The improved model incorporates the Garofalo viscosity model for the SEI, portraying a more realistic material behavior and providing a consistent description of the observed voltage hysteresis phenomena.

So far, the chemo-mechanical model is restricted to a spherically symmetric geometry. Generalizing to a two-dimensional geometry, Section 3.4 directs the main emphasis to the chemo-mechanical interaction of silicon and SEI for an elliptical nanowire discussed in Paper IV [62]. The investigation considers mechanical and lithiation inhomogeneities in the asymmetric geometry featured by either a soft or a stiff SEI, closing the circle towards the voltage hysteresis.

3.1 SEI Growth During Battery Storage

This section summarizes the results of Paper I [153], not claiming completeness but referring to the corresponding publication for further details. The original publication and information about the author's contribution are provided on Pages 103 to 117.

As discussed in Section 1.2.4, the capacity fade of lithium-ion batteries is predominantly attributed to the long-term growth of the SEI. Despite extensive research efforts, the exact growth mechanism is still debated within the scientific community. The theory of the two prevailing notions, namely electron diffusion and solvent diffusion, is presented in Section 2.3, condensing the results of Paper I [153].
The capacity fade due to SEI growth mediated by electron diffusion obeys Eq. (2.37) and the one mediated by solvent diffusion complies with Eq. (2.46). All parameter values are stated in Paper I [153]. For the investigation, the capacity loss Q_{loss} is subdivided into an SOC-dependent capacity loss due to electron or solvent diffusion Q_{SEI} and an additional SOC-independent contribution Q_{add} [89]. The additional capacity loss determined from capacity fade at SOC $= 0$ might account for SEI growth during check-up cycles or other degradation effects like particle fracture.
To establish the relevant mechanism, electron diffusion and solvent diffusion are contrasted in Sections 3.1.1 and 3.1.2. The properties of these SEI growth mechanisms are compared to the experimentally observed SOC and time dependence of capacity fade measured by Keil et al. [126]. Furthermore, the effect of self-discharge during SEI growth is presented in Section 3.1.3 as a reason for deviations of the typical square-root time dependence during storage in comparison to experimental data by Attia et al. [246].

3.1.1 Electron Diffusion

The electron diffusion mechanism considers the diffusion of electrons from the anode through the SEI towards the SEI-electrolyte interface. Formation of new SEI happens at the SEI-electrolyte interface, where the diffused electrons react with the present lithium ions and solvent molecules. The time evolution of capacity fade produced by the electron diffusion mechanism is stated in Eq. (2.37). In the following, the features of capacity loss due to electron diffusion are compared to the experimental SOC and time dependence observed by Keil et al. [126].
First, Fig. 3.1(a) depicts the simulated capacity fade depending on the SOC according to the electron diffusion model in comparison to the experimental data [126]. Simulation and experiment describe the capacity fade at different SOC values after a fixed period of 9.5 months of open-circuit storage. The single parameter of the electron diffusion model, the prefactor in Eq. (2.37), is fitted to meet the experimentally observed SOC dependence. Indeed, Fig. 3.1(a) reveals a fairly precise agreement between the

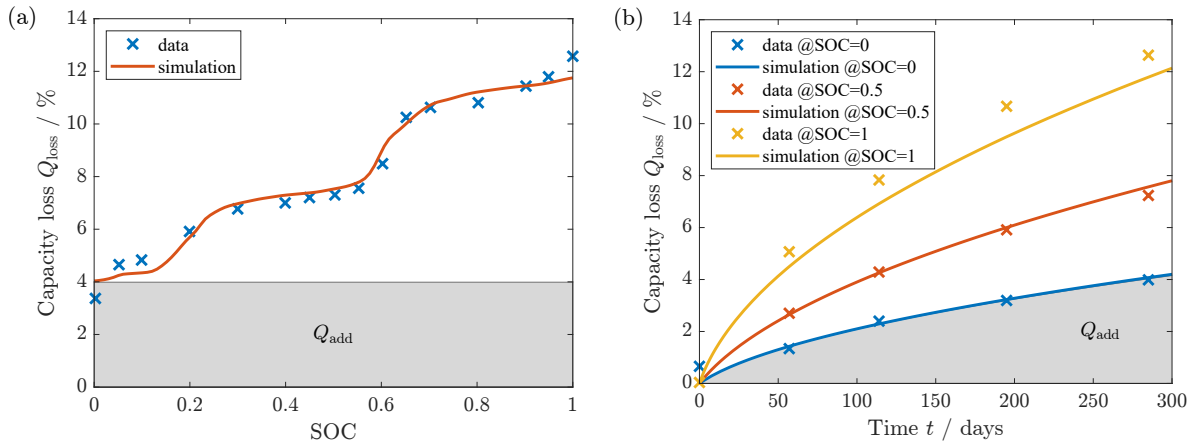

Figure 3.1: Simulated capacity loss due to the electron diffusion mechanism fitted to the SOC dependence in comparison to experimental data [126]. (a) SOC dependence of capacity loss. (b) Time dependence of capacity loss at different SOC levels. Reprinted from Ref. [153] with permission from Elsevier.

simulated and measured capacity loss depending on SOC.
Second, the simulated and experimental time evolution of capacity loss is depicted in Fig. 3.1(b) for different SOC values. The parameters of the electron diffusion model are unmodified compared to the simulation of the SOC dependence in Fig. 3.1(a). As expected for battery storage, simulation and experiment exhibit a square-root profile in time. Moreover, Fig. 3.1(b) shows that the simulated capacity fade reasonably matches the observed time dependence.
Combining the results of Fig. 3.1, the electron diffusion mechanism explains the observed SOC and time dependence. In particular, electron diffusion achieves both agreements with the same model parameters.

3.1.2 Solvent Diffusion

The solvent diffusion mechanism describes SEI growth mediated by the diffusion of solvent molecules from the electrolyte through the SEI towards the anode. The SEI formation reaction takes place at the anode-SEI interface, where the diffused solvent molecules meet the available lithium ions and electrons. The SEI-related capacity loss generated by the solvent diffusion mechanism is represented by the universal form in Eq. (2.46). SEI growth mediated by solvent diffusion in this description is generally limited by the interplay of reaction kinetics and solvent transport.
Figure 3.2 depicts the capacity fade profile depending on SOC and time for the solvent diffusion mechanism compared to the experiment [126], analog to the electron diffusion mechanism illustrated in Fig. 3.1. In Fig. 3.2(a) and (b), the curves reveal the solvent diffusion model fitted to the experimental SOC dependence, while Fig. 3.2(c) and (d) show the model fitted to the experimental time dependence. The fitted

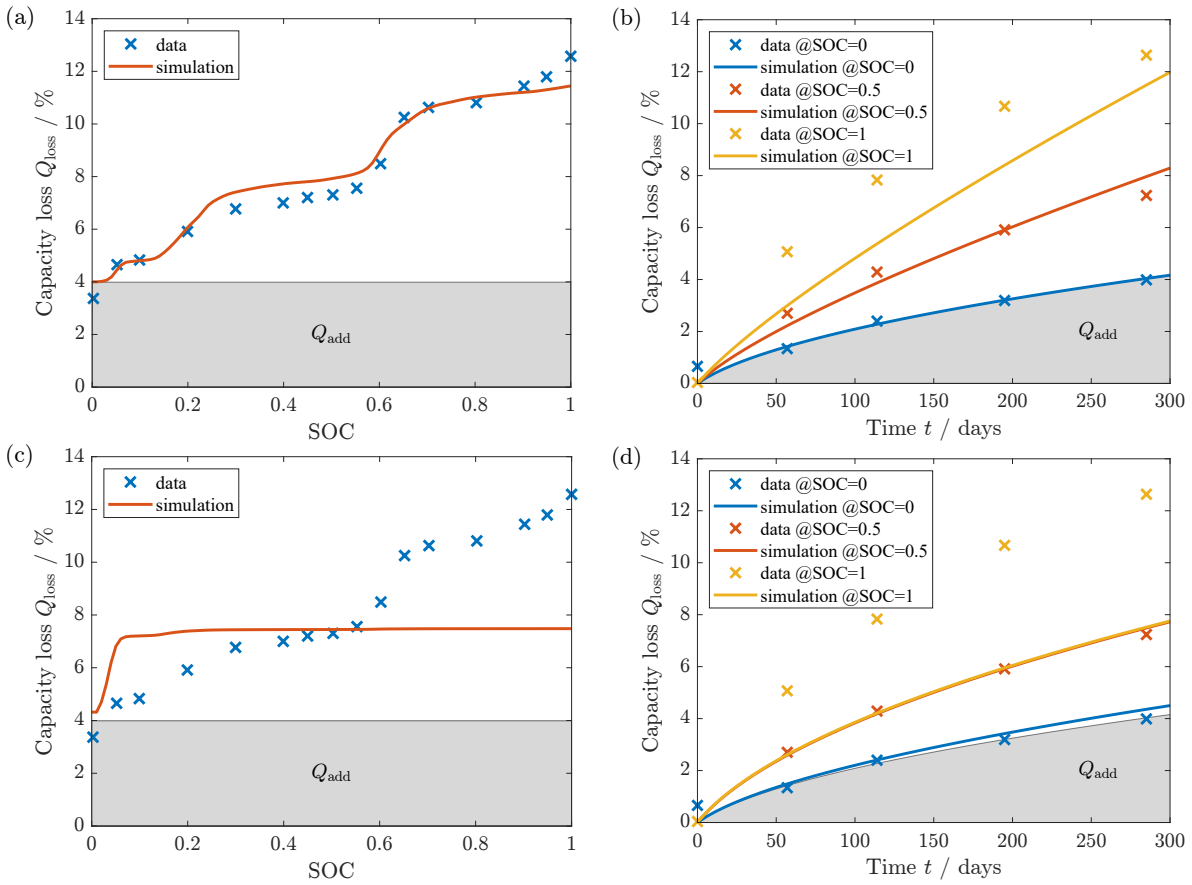

Figure 3.2: Simulated capacity loss due to the solvent diffusion mechanism in comparison to experimental data [126]. (a) and (b) Solvent diffusion mechanism fitted to the observed SOC dependence. (a) SOC dependence of capacity loss for SOC-fit. (b) Time dependence of capacity loss at different SOC levels for SOC-fit. (c) and (d) Solvent diffusion mechanism fitted to the observed time dependence at SOC = 50%. (c) SOC dependence of capacity loss for time-fit. (d) Time dependence of capacity loss at different SOC levels for time-fit. Reprinted from Ref. [153] with permission from Elsevier.

parameters are the exchange current density j_0 and the diffusion coefficient D_{EC}. The symmetry factor is set to $\alpha = 0.5$, not influencing the main outcomes as substantiated in Paper I [153].

The fit of capacity loss generated by the solvent diffusion mechanism to the SOC dependence is depicted in Fig. 3.2(a). The plot reveals a proper agreement between simulation and experiment, demonstrating that the solvent diffusion mechanism can, in principle, reproduce the experimental SOC dependence. Nevertheless, the electron diffusion model achieves a slightly more precise match to the experiment depending on the SOC. Applying the parameters adjusted to meet the SOC dependence, Fig. 3.2(b) illustrates the time dependence of solvent diffusion compared to the experiment. The simulated profiles for SOC = 50% and SOC = 100% disagree with

the experiment by predicting a minor curvature. Hence, the solvent diffusion model fitted to the SOC dependence does not reproduce the observed time dependence.
In contrast, Fig. 3.2(d) depicts the fit of capacity fade due to the solvent diffusion model to the experimental time dependence at SOC = 50%. The simulated capacity loss reveals precise accordance with the experiment at SOC = 0% and SOC = 50%. However, the simulation does not match the observed capacity fade at SOC = 100%. Figure 3.2(c) elucidates the disagreement at high SOC levels. It depicts the SOC dependence of the solvent diffusion model with the parameters obtained from the fit to the time dependence. The capacity loss predicted by the solvent diffusion model exhibits a plateau between SOC = 10% and SOC = 100%, contradicting the experimental profile. Thus, the solvent diffusion model fitted to the time dependence cannot coincide with the experimental SOC dependence.
In order to find an intermediate regime, a parameter study for the exchange current density j_0 and the diffusion coefficient D_{EC} is performed in Paper I [153]. The variation of the reaction and diffusion rate unveils two distinct regimes. On the one hand, the reaction limited regime, i.e., a small exchange current density and a high diffusion coefficient, fits the SOC dependence. On the other hand, the transport limited regime, i.e., a large exchange current density and a small diffusion coefficient, matches the observed time dependence. Nevertheless, the parameter variation excludes an intermediate regime, where the solvent diffusion mechanism explains the experimental capacity loss depending on SOC as well as depending on time.
Evaluating the results from Fig. 3.2 and the parameter variation, the solvent diffusion mechanism reproduces either the SOC dependence or the time dependence. There is no regime where the solvent diffusion model reasonably accounts for both dependencies with the same parameters.

3.1.3 Deviation from $\sqrt{t}$ Behavior

The comparison of the SEI growth mechanisms in the previous Sections 3.1.1 and 3.1.2 assigns the electron diffusion mechanism to be responsible for SEI growth. Capacity fade generated by electron diffusion shows the observed SOC dependence and the observed, square-root shaped time dependence for constant SOC. Nevertheless, SEI growth during battery storage consumes lithium ions and electrons from the anode, causing self-discharge of the cell. The corresponding change in SOC effects a change of the anode OCV, which crucially impacts SEI growth. The change in the OCV can, in principle, cause deviations from the typical square-root time dependence.
In Fig. 3.3, the experimental data by Attia et al. [246] illustrate the capacity fade of a half-cell with carbon black anode. The data reveal a substantial capacity loss of about 60% after 130 days of open-circuit storage. The curve exhibits a particularly steep increase in the beginning, flattening over storage time. The description of the capacity loss profile with the typical square-root dependence $t^{0.5}$ does not agree with

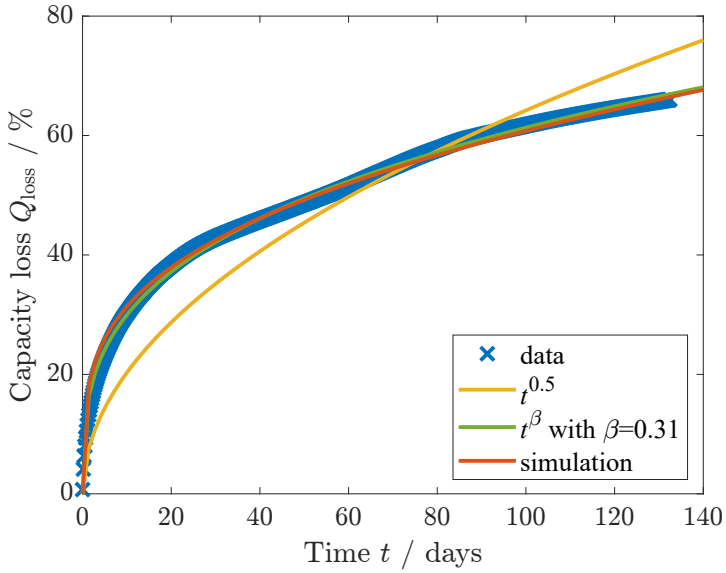

Figure 3.3: Deviation from the typical $t^{0.5}$ behavior simulated with the electron diffusion mechanism in comparison to experimental data [246]. Reprinted from Ref. [153] with permission from Elsevier.

the experiment. Instead, a power law t^{β} describes the experimental curve with the empirically determined exponent $\beta = 0.31$ [246].
In addition to the experiment, Fig. 3.3 depicts the simulated SEI-related capacity loss due to electron diffusion obeying Eq. (2.37). Thus, the electron diffusion mechanism depends on the anode OCV, accounting for SOC changes and self-discharge effects. As evident in Fig. 3.3, self-discharge crucially impacts the simulated capacity loss, resulting in a deviation from the typical square-root time dependence predicted for constant SOC. The simulated capacity fade mediated by the electron diffusion mechanism matches the experimentally observed profile. In particular, the influence of self-discharge decreases the effective time exponent $\beta < 0.5$, while the impact of reaction limitation or electron migration effects on SEI growth would increase the effective time exponent $\beta > 0.5$.
Hence, the electron diffusion mechanism provides a physical description of deviations from the square-root dependence in time due to self-discharge. It considers the transport-limited regime but accounts for changes in SOC during storage due to SEI growth.

3.2 Voltage Hysteresis of Silicon Anodes

This section summarizes the results of Paper II [173], not claiming completeness but referring to the corresponding publication for further details. The original publication and information about the author's contribution are provided on Pages 119 to 141.

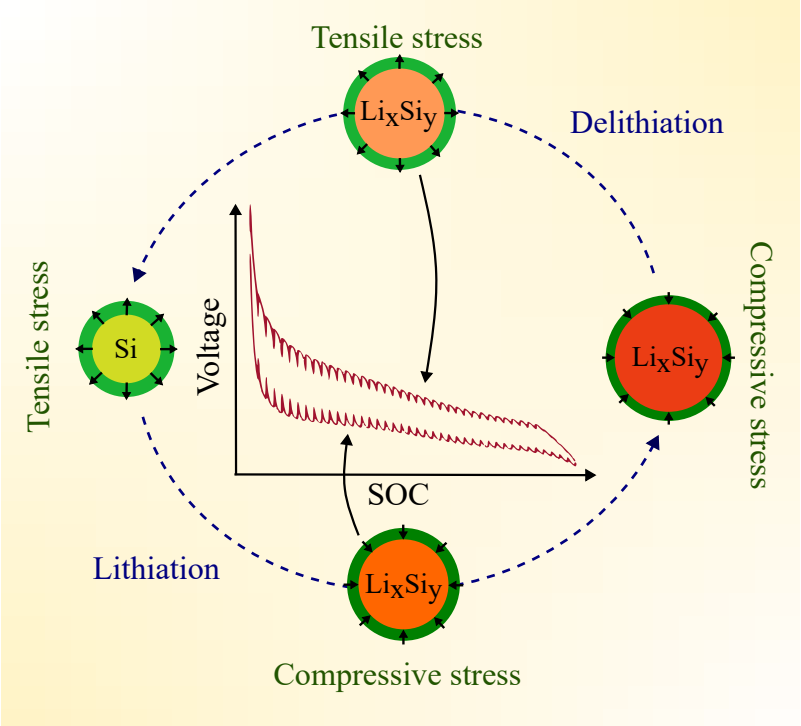

Figure 3.4: Graphical abstract from Paper II [173]. Illustration of the radial stress generated inside the SEI during cycling and the impact on the voltage of the silicon anode. Reprinted from Ref. [173], licensed under CC BY 4.0, https://creativecommons.org/licenses/by/4.0/.

Nano-structured silicon anodes are desired for next-generation lithium-ion batteries, concerning silicon's high theoretical capacity but mechanical instability of large particles introduced in Section 1.1.2. However, silicon anodes suffer from a voltage hysteresis during slow cycling and after relaxation, as discussed in Section 1.3. The several hypotheses in literature, reasoning a hysteresis behavior, do not apply to amorphous silicon nanoparticles.
Therefore, Paper II [173] considers the chemo-mechanical interplay of silicon and SEI presented in Section 2.4 as the cause of the voltage hysteresis illustrated in Fig. 3.4. Within this model, the SEI generates stress due to visco-elastoplastic behavior depending on the deformation and the deformation rate. Accordingly, the SEI stress acting on the silicon particle differs during cycling and after (short) relaxation periods. The induced stress inside the silicon particle influences the anode voltage owing to

the chemo-mechanical coupling in Eq. (2.65).
In the following, Section 3.2.1 explains the OCV hysteresis after relaxation through elastoplastic stress generated inside the SEI. In Section 3.2.2, viscous behavior of the SEI originates an additional stress contribution, which reproduces GITT measurements. To gain a better understanding of the chemo-mechanical interaction, Section 3.2.3 provides a variation of the mechanical parameters and the system's size ratio, influencing the voltage hysteresis.

3.2.1 Open-Circuit Voltage (OCV) Hysteresis

The voltage hysteresis of silicon anodes exists even after relaxation periods under open-circuit storage conditions, where no overpotentials occurring during cycling remain. This work explains the OCV hysteresis with elastoplastic stress generated inside the SEI acting on the silicon particle. Significant stresses inside the SEI arise due to primarily chemical volume changes of the silicon particle during (de)lithiation, which the SEI has to comply with exclusively mechanical deformations. The elastoplastic stress depends only on deformations and explicitly not on deformation rates. The presented results consider the visco-elastoplastic model consistent with Section 3.2.2 after relaxation, where the viscous contribution can be neglected.
Regarding the simulation results, Paper II [173] states the complete list of parameter values. The essential parameters are the initial particle radius $R_{\mathrm{Si},0} = 50\,\mathrm{nm}$, the SEI thickness $L_{\mathrm{SEI},0} = 20\,\mathrm{nm}$, as well as Young's modulus of the nanoscale silicon particle $E_{\mathrm{Si}} = 200\,\mathrm{GPa}$ and the SEI $E_{\mathrm{SEI}} = 100\,\mathrm{GPa}$.
The schemes in Fig. 2.4 and Fig. 3.4 illustrate the chemo-mechanical model in the lithiation and delithiation branches. In the lithiation branch, the silicon particle expands chemically. The SEI has to deform mechanically to accommodate the increase in the surface area of the silicon particle. Hence, the SEI stretches in the tangential direction, causing tensile tangential stress inside the SEI. Simultaneously, the SEI becomes thinner and generates compressive radial stress. The SEI adapts to the geometric changes initially by elastic and subsequently by plastic deformations. During delithiation, the silicon particle shrinks continuously, decreasing its surface area. The SEI contracts in the tangential direction, which results in compressive tangential stress. This is accompanied by thickening of the SEI and tensile radial stress. In total, the interplay of elastic and plastic deformations produces a stress hysteresis inside the SEI in tangential and radial direction.
For a clear visualization, Fig. 3.5(a) depicts the elastoplastic SEI stress at the silicon-SEI interface in radial and tangential direction during cycling. Investigating the radial component $\mathbf{P}_{\mathrm{SEI,rr}}$, the SEI contracts and reveals compressive stress during lithiation. The SEI deforms first elastically with a steep stress profile and then plastically with rather constant stress values. Plastic flow leads to irreversible SEI deformations without generating additional stress. During delithiation, the SEI extends, and tensile

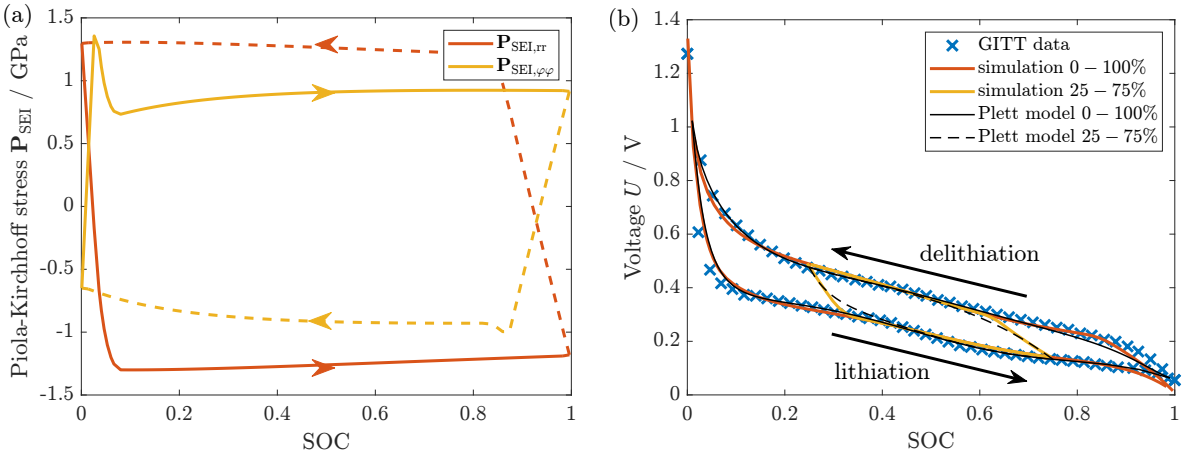

Figure 3.5: Elastoplastic SEI stress and the respective OCV hysteresis in comparison to GITT data [214]. (a) Hysteresis of the radial and tangential elastoplastic SEI stress at the silicon-SEI interface. Solid lines indicate lithiation, while dashed lines indicate delithiation. (b) OCV hysteresis generated by a visco-elastoplastic SEI after relaxation together with GITT data [214]. Simulation of a full cycle and a partial cycle compared to the empirical Plett model. Reprinted and modified from Ref. [173], licensed under CC BY 4.0, https://creativecommons.org/licenses/by/4.0/.

stress occurs in the radial direction. The deformation is again elastically followed by plastic flow. Regarding the full cycle, the plasticity of the SEI causes the discrepancy between lithiation and delithiation stress, identified as stress hysteresis.
Additionally, Fig. 3.5(a) illustrates the tangential stress component $\mathbf{P}_{\mathrm{SEI},\varphi\varphi}$. The tangential stress behaves inversely to the radial stress. The SEI stretches during lithiation, resulting in tensile tangential stress, while contraction during delithiation causes compressive tangential stress. For both half-cycles, the kind of deformation is again first elastic and then plastic, producing the displayed hysteresis behavior.
Regarding the silicon OCV hysteresis, the radial SEI stress component imposes the stress inside the silicon particle. The silicon stress affects the voltage according to the chemo-mechanical coupling stated in Eq. (2.65). The compressive stress during lithiation reduces the anode voltage, whereas the tensile stress during delithiation increases the voltage. Consequently, the stress hysteresis yields the voltage hysteresis depicted in Fig. 3.5(b). The chemo-mechanical simulation of the full cycle considering elastoplastic SEI behavior agrees with the experimental OCV hysteresis measured by Pan et al. [214]. The yield stress of the SEI, $\sigma_{\mathrm{Y,SEI}} = 2.5\,\mathrm{GPa}$, is chosen to meet the size of the experimental voltage hysteresis. In addition to the complete cycle, Fig. 3.5(b) shows the simulation of a partial cycle and the hysteresis prediction by the empirical Plett model, oftentimes used for hysteresis descriptions. The chemo-mechanical OCV hysteresis curves reveal a good coincidence not only with the experiment but also with the phenomenological Plett model introduced in Section 1.3.3.
Hence, the chemo-mechanical silicon-SEI model featuring an elastoplastic SEI explains

the observed silicon OCV hysteresis. The stress generated by the SEI acting on the silicon particle is responsible for the voltage hysteresis behavior.

3.2.2 Voltage Hysteresis During Slow Cycling

In addition to the OCV hysteresis, silicon anodes exhibit an enlarged voltage hysteresis during slow cycling. The difference between cycling and open-circuit voltage is clearly observable with the galvanostatic intermittent titration technique (GITT) introduced in Section 1.3.2, consisting of alternate constant current and relaxation periods. As diffusion or reaction overpotentials are negligible during slow cycling of silicon nano-anodes, this work assigns the extra voltage hysteresis contribution to the viscous behavior of the SEI.

In contrast to the elastoplastic contribution discussed in Section 3.2.1, viscous stress depends on the deformation rate instead of the actual deformation. Thus, viscous SEI characteristics create additional stress and a respective voltage contribution during cycling. This section applies the empirically motivated shear-thinning viscosity model to account for more realistic material behavior than the linear Newtonian model. Paper II [173] provides a comparison of the results from both models.

Concerning visco-elastoplastic SEI behavior, Fig. 3.6(a) shows the simulated GITT profile in comparison to experimental data [214]. The GITT procedure involves alternate constant current steps with C/20 and relaxation periods of 3 h. The shear-thinning viscosity $\eta_{\mathrm{SEI},0} = 15\,\mathrm{GPa\,s}^n$ with the shear-thinning exponent $n = 0.15$ is adjusted to

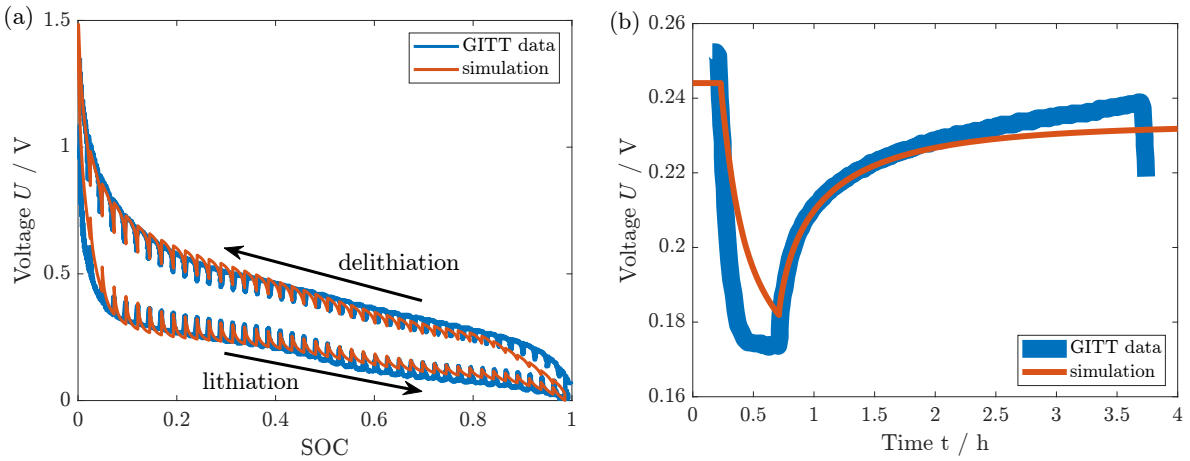

Figure 3.6: Simulation of the full GITT procedure and a single pulse with visco-elastoplastic SEI behavior. (a) Simulated voltage hysteresis during GITT procedure due to visco-elastoplastic SEI behavior compared to experimental data [214]. (b) Simulated voltage profile of lithiation pulse and rest period compared to an experimental GITT pulse [215]. Reprinted and modified from Ref. [173], licensed under CC BY 4.0, https://creativecommons.org/licenses/by/4.0/.

meet the experimental data and justified in Paper II [173]. The simulation of the GITT measurement incorporating the visco-elastoplastic SEI reveals a good accordance with the experiment. Only for large SOC values does the chemo-mechanical model underestimate the size of the additional hysteresis contribution during cycling. The deviation could be reduced with a more distinct shear-thinning property.
To investigate the voltage transition between cycling and rest, Fig. 3.6(b) depicts the voltage profile for a single GITT pulse in the simulation and the experiment [215]. During the lithiation step, the simulation shows a slightly too slow voltage decrease compared to the experiment. In the subsequent short-term relaxation phase, the simulation reveals a good agreement with the measurement. Nevertheless, the shear-thinning model predicts an almost completed relaxation after 3 h, while the voltage trend in the data indicates a continuing relaxation process. Regarding the long-term relaxation, Section 3.3 will discuss the slow relaxation behavior of silicon anodes over 300 h using the Garofalo viscosity model.
In summary, the results displayed in Fig. 3.6 demonstrate that the viscosity of the SEI explains the enlarged hysteresis observed during slow cycling. Particularly, the chemo-mechanical silicon-SEI model involving visco-elastoplastic SEI characteristics reproduces the GITT measurement.

3.2.3 Impact of Mechanical Parameters and Size Ratio

The previous Sections 3.2.1 and 3.2.2 addressed the chemo-mechanical particle-SEI model as the reason for the OCV and cycling voltage hysteresis of silicon nanoparticles. The following paragraphs evaluate the influence of mechanical parameters, viz Young's modulus of the SEI and the silicon nanoparticle, as well as the impact of the SEI-to-silicon size ratio.

Influence of Young's Modulus of the SEI

Young's modulus is a measure of the stiffness of a material, relating elastic stress to elastic strain. Owing to the importance of the mechanical impact of the SEI elaborated in Sections 3.2.1 and 3.2.2, the variation of Young's modulus of the SEI is of particular interest.
Elucidating the influence of the SEI stiffness on the hysteresis shape, Fig. 3.7(a) depicts the OCV hysteresis of the chemo-mechanical simulation with varying Young's modulus of the SEI compared to the experimental data [214]. Young's modulus of silicon is fixed to $E_{\mathrm{Si}} = 200\,\mathrm{GPa}$. The shape of the simulated OCV hysteresis reveals that a small Young's modulus $E_{\mathrm{SEI}} = 10\,\mathrm{GPa}$ does not reproduce the OCV data. Applying this parameter, the simulated voltage crossover between the lithiation and the delithiation OCV branch proceeds too slowly. Merely the simulations with higher values of Young's modulus, $E_{\mathrm{SEI}} = 100\,\mathrm{GPa}$ and $E_{\mathrm{SEI}} = 200\,\mathrm{GPa}$, properly

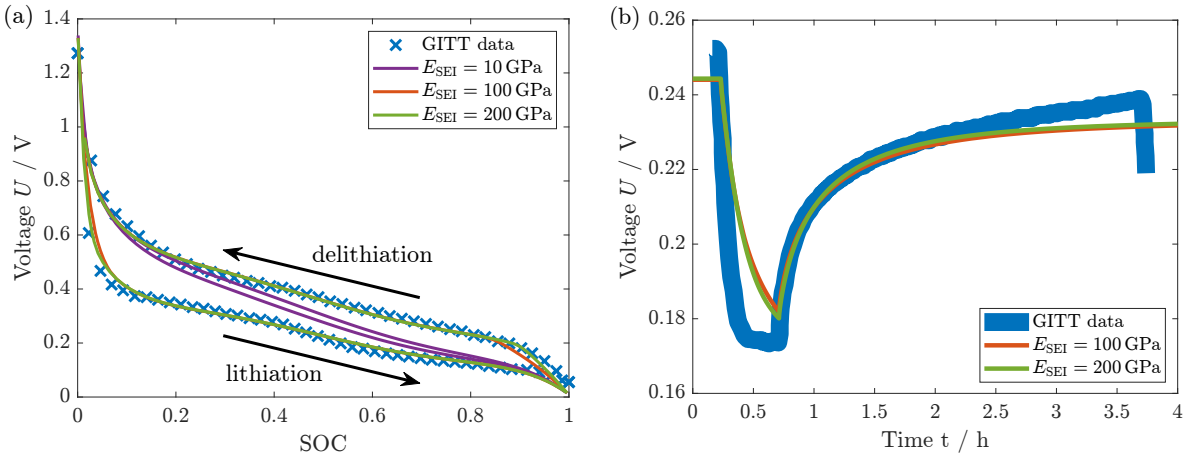

Figure 3.7: Influence of Young's modulus of the SEI on the voltage hysteresis and transition. (a) Simulated OCV hysteresis for different values of Young's modulus of the SEI compared to GITT data [214]. (b) Simulated voltage transition profile for different values of Young's modulus of the SEI compared to a GITT pulse [215]. Reprinted and modified from Ref. [173], licensed under CC BY 4.0, https://creativecommons.org/licenses/by/4.0/.

match the measured values. Hence, a high Young's modulus of the SEI is necessary to reproduce the shape of the observed OCV hysteresis.
Regarding a single GITT pulse, Fig. 3.7(b) illustrates the voltage transition during a lithiation pulse and a subsequent relaxation period for different Young's moduli of the SEI together with the experimental voltage profile [215]. The smallest value of Young's modulus is not displayed, as the simulation does not reproduce the lithiation and rest voltage to any extent. Comparing $E_{SEI} = 100\,GPa$ and $E_{SEI} = 200\,GPa$, the voltage transition is insignificantly faster for the higher value of Young's modulus, but the influence is essentially negligible.
In total, Fig. 3.7 exhibits the necessity of a high Young's modulus of the SEI to reproduce the hysteresis behavior. As a reasonable choice concerning the experimental values discussed in Section 1.2.5, the value of Young's modulus $E_{SEI} = 100\,GPa$ is assumed in this work. According to the chemo-mechanical model, a softer SEI would facilitate a reduced hysteresis, advantageous for the application of silicon anodes.

Influence of Young's Modulus of Nanoscale Silicon

Analog to the stiffness of the SEI, a parameter study of Young's modulus of the silicon nanoparticle is insightful due to the reported ambiguity of silicon stiffness and nanoscale effects. The variation of Young's modulus orientates on the reported values for amorphous silicon of $90\,GPa \leq E_{Si} \leq 125\,GPa$ [247–250] and silicon at the nanoscale with $E_{Si} = 200\,GPa$ [251, 252]. Young's modulus of the SEI is fixed to $E_{SEI} = 100\,GPa$ to estimate the influence of solely the silicon stiffness.

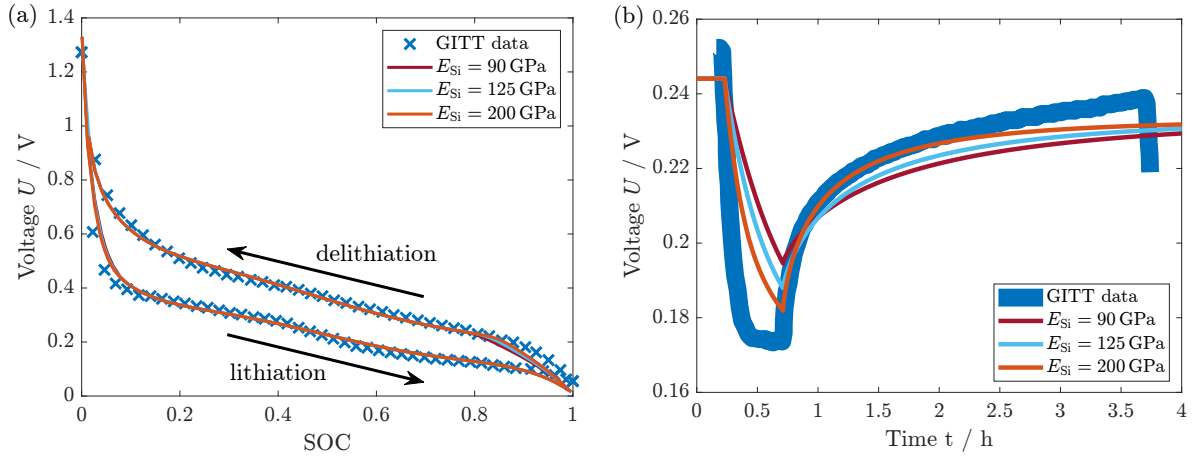

Figure 3.8: Influence of Young's modulus of the silicon nanoparticle on the voltage hysteresis and transition. (a) Simulated OCV hysteresis for different values of Young's modulus of the silicon nanoparticle compared to GITT data [214]. (b) Simulated voltage transition profile for different values of Young's modulus of the silicon nanoparticle compared to a GITT pulse [215]. Reprinted and modified from Ref. [173], licensed under CC BY 4.0, https://creativecommons.org/licenses/by/4.0/.

Figure 3.8(a) depicts the simulated OCV hysteresis for the different values of Young's modulus of silicon and the experimental data [214]. The simulated shape of the OCV hysteresis matches the experiment independent of the silicon stiffness. Merely, the simulated curves exhibit a marginally faster crossover from the lithiation to the delithiation branch for higher values of silicon Young's modulus.
In Fig. 3.8(b), the voltage profiles display the transitions during a GITT pulse for the varied nanoscale silicon stiffness in comparison to the experiment [215]. The simulated voltage profiles unveil that larger values of Young's modulus of silicon promote a faster voltage transition in the lithiation as well as the relaxation phase. The accelerated transition for the higher silicon stiffness fits considerably better with the experimental data.
Therefore, a large value of Young's modulus of the silicon nanoparticle is necessary to describe the voltage hysteresis phenomenon consistently. According to the justified parameter range, Young's modulus of the silicon nanoparticle is assumed as $E_{Si} = 200\,\text{GPa}$ in this work.

Influence of SEI Thickness and Particle Radius

The stress created by the chemo-mechanical silicon-SEI interaction depends on the system's size, namely the SEI thickness $L_{SEI,0}$ and the particle radius $R_{Si,0}$. Physical intuition suggests that a relatively thinner SEI layer has less influence than a thicker one. To estimate this dependence, the voltage hysteresis is investigated for a varying size ratio $L_{SEI,0}/R_{Si,0}$.

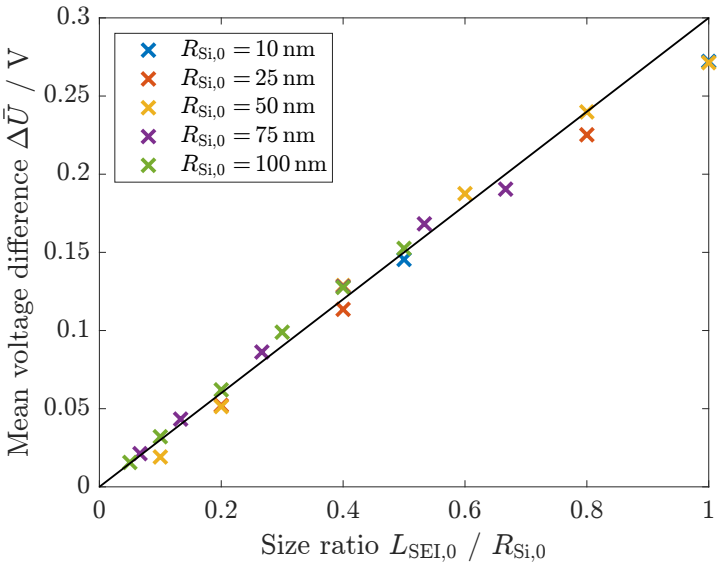

Figure 3.9: Influence of SEI thickness $L_{SEI,0}$ and particle radius $R_{Si,0}$ on the size of the mean voltage hysteresis $\Delta\bar{U}$. Reprinted and modified from Ref. [173], licensed under CC BY 4.0, https://creativecommons.org/licenses/by/4.0/.

For that purpose, Fig. 3.9 depicts the mean voltage difference between the OCV in the delithiation and the lithiation branch $\Delta\bar{U} = \bar{U}_0^{delith} - \bar{U}_0^{lith}$ versus the size ratio $L_{SEI,0}/R_{Si,0}$. The colors indicate separate variations of the SEI thickness $L_{SEI,0}$ and the particle radius $R_{Si,0}$. Independent of the absolute values, the mean size of the voltage hysteresis exhibits a linear dependence on the size ratio $L_{SEI,0}/R_{Si,0}$. The linear dependence can be theoretically reasoned by the momentum balance expressed in radial coordinates.
As different experiments reveal very similar hysteresis sizes, the impact of the size ratio might not be relevant for typical experiments. This assumption is justified by the reported pulverization of large silicon particles [56, 57] and the notion of an optimum particle size of $R = 50\,nm$ [162]. Therefore, the size ratio of the SEI and the underlying silicon particle is comparable in conventional experiments.
To conclude the size variation, a thicker SEI relative to the silicon nanoparticle size predicts a large voltage hysteresis. Thus, creating a thinner SEI on silicon nanoparticles could be beneficial in reducing the voltage hysteresis effect. Overall, the results presented in this section unveil that a mechanically improved SEI can diminish the hysteresis size, facing the challenges of low efficiency, heat generation, and imprecise SOC estimation.

3.3 Voltage Relaxation of Silicon Anodes

This section summarizes the results of Paper III [174], not claiming completeness but referring to the corresponding publication for further details. The original publication and information about the author's contribution are provided on Pages 143 to 166.

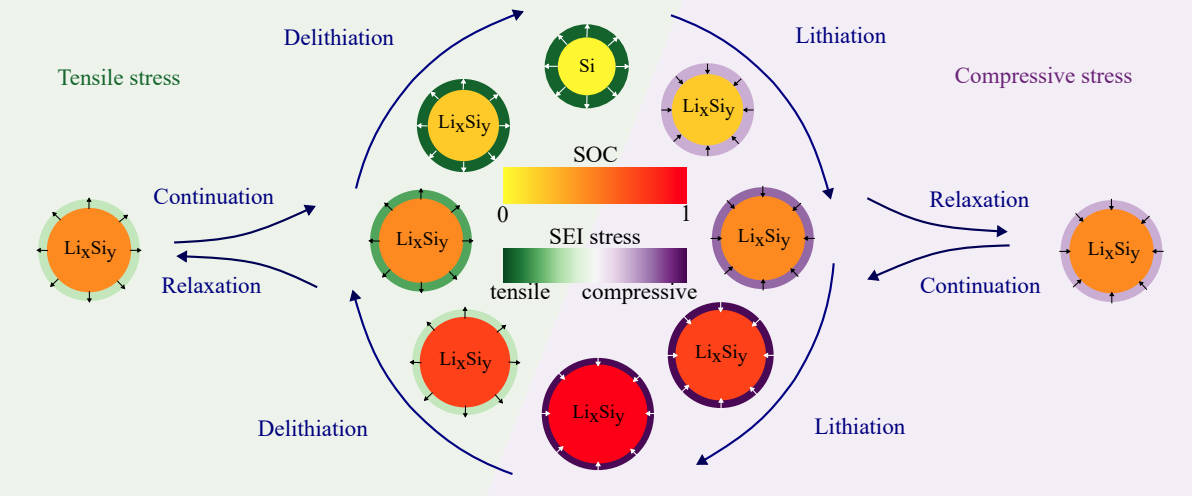

Figure 3.10: Illustration of the radial stress generated inside the SEI during cycling and relieved during relaxation. Reprinted and modified from Ref. [174], licensed under CC BY 4.0, https://creativecommons.org/licenses/by/4.0/.

The preceding Section 3.2 analyzed the chemo-mechanical silicon-SEI model regarding the voltage hysteresis and short-term relaxation within the GITT procedure. However, the experimental data from Ref. [215] depicted in Fig. 3.6(b) indicate a continuing relaxation process even after 3 h. Hence, this section focuses on the long-term voltage relaxation characteristics after lithiation and delithiation phases as schematically illustrated in Fig. 3.10.
Recent experimental data by Wycisk et al. [216] report a long-term voltage relaxation of nanoparticle silicon anodes for at least 300 h. The novel data reveal a non-exponential but logarithmic voltage relaxation behavior over a wide range of time. Paper III [174] addresses the long-term relaxation by incorporating the established Garofalo law for the description of viscous SEI stress. Furthermore, the work examines consistency with the voltage hysteresis phenomenon and deduces a reduced chemo-mechanical hysteresis model stated in Section 2.4.6.
Hereinafter, Section 3.3.1 investigates the slow long-term voltage relaxation of the chemo-mechanical model featuring Garofalo viscosity. In Section 3.3.2, the analysis describes consistency with the measured OCV and cycling voltage hysteresis as well as observed voltage transition profiles. To achieve superior agreement with the experimental hysteresis, Section 3.3.3 presents an approach to improve the notion of the true OCV curve in the extreme SOC limits. Eventually, Section 3.3.4 illustrates the

reduced chemo-mechanical model in terms of the voltage hysteresis and relaxation.

3.3.1 Logarithmic Voltage Relaxation

The open-circuit voltage of silicon anodes differs from the voltage during cycling as examined in Section 3.2. Indicated by the experimental data from Ref. [215], the voltage relaxation depicted in Fig. 3.6(b) continues even after several hours of open-circuit storage. A recent experimental publication reports slow voltage relaxation over at least 300 h [216].
The new data from Ref. [216] displayed in Fig. 3.11(a) describe the voltage relaxation at SOC = 0.3 over 300 h after preceding lithiation and delithiation with C/10. The experimental curves disclose a non-exponential relaxation behavior. In particular, the relaxation follows a logarithmic trend over a wide time span, as evident from the semi-logarithmic plot in Fig. 3.11(b). Only for pronounced relaxation times $t > 20$ h, the relaxation profile leaves the logarithmic regime and enters exponential behavior to terminate the relaxation process. The similarity of the voltage relaxation profiles after lithiation and delithiation excludes the influence of side reactions on the voltage relaxation curves.
To account for the logarithmic trend, the theoretically motivated Garofalo model presented in Section 2.4.3 substitutes the purely empirical shear-thinning viscosity model applied in Section 3.2 for the SEI behavior. The Garofalo viscosity possesses a dependence of the viscous stress on the inverse hyperbolic sine of the strain rate. In the limit of large strain rates and stresses, this relation leads to a logarithmic behavior. In the limit of small strain rates and stresses, the relation simplifies to a linear trend.

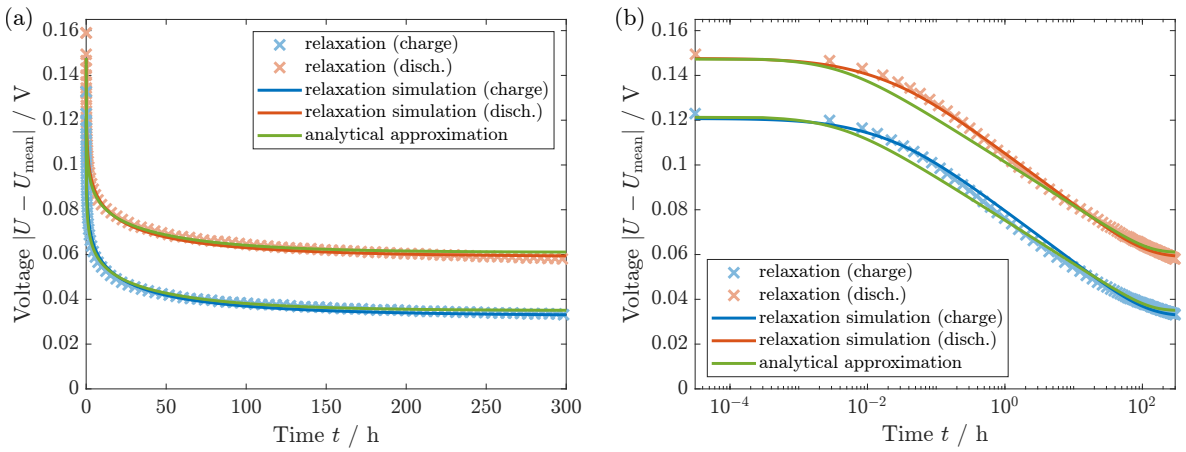

Figure 3.11: Simulated voltage relaxation at SOC = 0.3 for 300 h after a C/10 (de)lithiation in comparison to experimental data [216] and the analytic approximation based on the Garofalo viscosity. Plots with (a) linear and (b) logarithmic time axis. Reprinted and modified from Ref. [174], licensed under CC BY 4.0, https://creativecommons.org/licenses/by/4.0/.

Therefore, the Garofalo law provides a better description of typical material behavior concerning both strain rate and stress limits.
Incorporating the Garofalo viscosity, Fig. 3.11 depicts the simulated voltage relaxation of the chemo-mechanical silicon-SEI model in addition to the experimental data [216]. The reference stress $\sigma_{\mathrm{ref}} = 133\,\mathrm{MPa}$ and the time constant $\tau = 3 \cdot 10^8\,\mathrm{s}$ are fitted to the experimental data. The remaining simulation parameters are stated in Paper III [174]. Regarding Fig. 3.11(b), the simulation reveals a logarithmic relaxation behavior over a wide range of times, leaving the logarithmic regime at times $t > 20\,\mathrm{h}$. Hence, the simulation agrees well with the experimental relaxation profile in both the linear and the semi-logarithmic graphs. Furthermore, Fig. 3.11 illustrates the analytical approximation of the voltage relaxation stated in Eq. (2.78) considering the Garofalo viscosity model without spatial resolution discussed in Section 2.4.6. Despite a slight deviation of the absolute values, the approximation reveals logarithmic behavior similar to the simulated and experimental profile, supporting the results of the chemo-mechanical simulation. Moreover, the logarithmic voltage relaxation contradicts alternative origins of the hysteresis, as diffusion overpotentials inhere an exponential relaxation behavior and reaction overpotentials require unreasonable parameter values [203], thereby strongly supporting the chemo-mechanical hysteresis explanation.
Hence, the chemo-mechanical model involving Garofalo viscosity for the SEI reproduces the logarithmic voltage relaxation of silicon nanoparticle anodes. More generally, mechanics is responsible for the long-term relaxation process.

3.3.2 Consistent Description of the Voltage Hysteresis

As demonstrated in Section 3.3.1, the chemo-mechanical simulation considering Garofalo viscosity fits the experimentally observed logarithmic voltage relaxation behavior from Ref. [216]. Based on this agreement, this section examines the consistency of the chemo-mechanical model featuring the Garofalo viscosity for the SEI with the observed voltage hysteresis phenomena. Particularly, the agreement of the model with the OCV and cycling voltage hysteresis as well as voltage transitions reported in Ref. [216] is analyzed.
For that purpose, Fig. 3.12(a) displays the experimental voltage hysteresis during slow cycling with C/20 and after 12 h relaxation from Ref. [216]. Note that the size of the OCV and cycling voltage hysteresis is similar compared to the envelopes of the GITT measurement from Ref. [214] depicted in Fig. 3.6(a). The accordance suggests consistency of the experimental results from Ref. [216] and Ref. [214], although the investigated cells differ from each other. Nevertheless, both experimental cells have an anode based on silicon nanoparticles in common.
In addition to the data, Fig. 3.12(a) depicts the voltage hysteresis described by the chemo-mechanical model during cycling and after relaxation with Garofalo viscosity. The simulation shows an enlarged hysteresis during cycling than after relaxation,

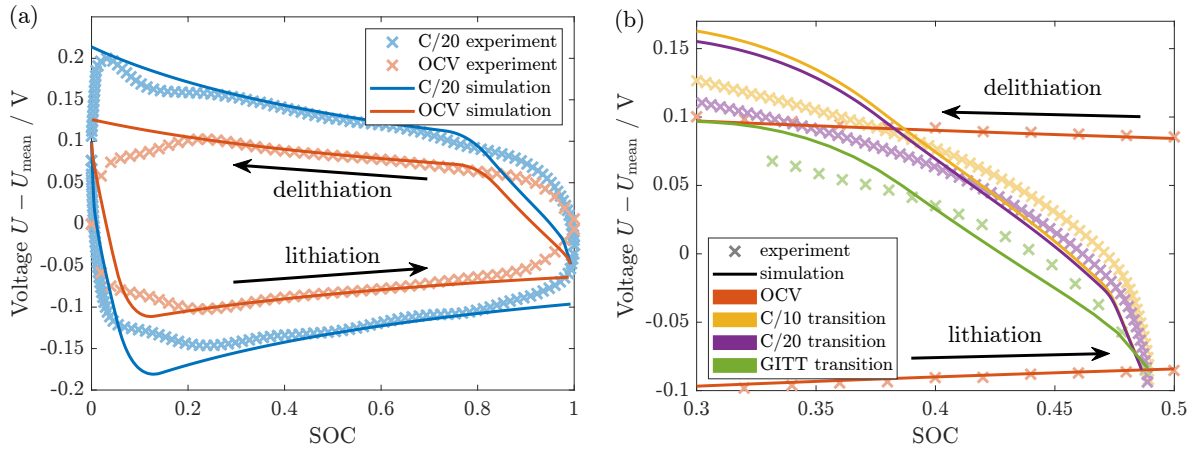

Figure 3.12: Consistency check of chemo-mechanical simulation applying Garofalo viscosity with experimental voltage hysteresis and transition [216]. (a) Simulated and experimental OCV hysteresis after 12 h and cycling voltage hysteresis. (b) Simulated and experimental voltage transition from lithiation to delithiation branch. Reprinted from Ref. [174], licensed under CC BY 4.0, https://creativecommons.org/licenses/by/4.0/.

agreeing well with the experimental data from [216]. A deviation between simulation and measurement occurs only in the extreme SOC regimes, SOC < 0.2 and SOC > 0.8, which will be treated in Section 3.3.3.

Furthermore, Fig. 3.12(b) illustrates the experimental voltage transition from the lithiation to the delithiation branch [216]. The plot shows the experimental transition curves with small continuous currents and GITT data after 12 h relaxation. All experimental voltage profiles reveal a fast transition directly after applying the delithiation current, which slows down smoothly with the passed SOC range.

For the consistency check, Fig. 3.12(b) also shows the simulation of the voltage transition profile for slow cycling and after relaxation. The simulated voltage profiles exhibit an initial steep transition followed by slower behavior over a wide SOC regime and a final slow convergence to the delithiation branch. The three phases arise from the influence of the viscous, elastic, and plastic contribution to the transition profile. Hence, the steep voltage increase in the beginning is largely suppressed for the GITT simulation, reducing viscous stress. The general trend of a mitigating voltage transition in the simulation suits the experimental data, although the exact shape is smoother in the experiment, where the distinct phases merge.

Moreover, Paper III [174] compares the C-rate dependence of the size of the voltage hysteresis and demonstrates that the inverse hyperbolic sine reveals a flattened behavior for larger C-rates approaching the linear experimental results from Ref. [216]. The chemo-mechanical simulation can, in addition, omit the offset at vanishing currents, which is inevitable for the linear interpretation. As demonstrated in Paper III [174], the experimental C-rate dependence excludes diffusion or reaction overpotentials as

a source of the voltage hysteresis, clearly promoting the chemo-mechanical origin. Further, Paper III [174] validates the Garofalo characteristics of the SEI by comparison of the simulation with the experimental GITT data from Refs. [214, 215] treated in Section 3.2.2. Although the experimental cells differ, the simulation shows reasonable agreement with the GITT measurement from Ref. [214, 215] with the parameters obtained from the long-term relaxation of Ref. [216].
Summarizing the comparisons of simulation and experiment, the chemo-mechanical model equipped with Garofalo viscosity presents a consistent description of the silicon voltage hysteresis phenomena. The simulation does not only reproduce the logarithmic voltage relaxation behavior but also describes the voltage hysteresis, transition profiles, and the C-rate dependence. Finally, the Garofalo model appropriately characterizes the GITT measurement from a different publication using differing cells, verifying consensus with the model results presented in Section 3.2.

3.3.3 Corrected Open-Circuit Voltage (OCV) Curve

The simulated and experimental voltage hysteresis reveal a deviation in the SOC limits, SOC < 0.2 and SOC > 0.8, visible in Fig. 3.12(a). The true OCV, on which the chemo-mechanical model is based, is determined by the mean experimental OCV curve U_0 according to Eq. (2.52). However, this approach is inaccurate in the extreme SOC ranges because of asymmetric stress levels and can be improved by a corrected OCV in the following.
The asymmetry of stress levels in the limits arises owing to the elastoplastic behavior of the SEI as depicted previously in Fig. 3.5(a). Concerning the large SOC regime, elastically generated compressive stress is fully built up in the lithiation branch, being in the realm of plastic flow. In contrast, the compressive stress only gradually decreases, and tensile stress increases upon delithiation. For the low SOC limit, tensile stress is fully established in the delithiation direction. In opposition to this, tensile stress continuously reduces, and compressive stress develops in the lithiation direction. As the stresses generate the voltage hysteresis, a precise description has to account for the asymmetry in the SOC limits for the determination of the true OCV. Therefore, Paper III [174] presents an approach defining a corrected OCV curve considering this effect. Instead of calculating the mean voltage U_0, the corrected OCV approximates the size of the hysteresis to be constant in the extreme SOC regimes

$$U_0^{\mathrm{corr}}(\mathrm{SOC}) = \begin{cases} U_0^{\mathrm{delith}}(\mathrm{SOC}) - \left(U_0^{\mathrm{delith}}(0.2) - U_0(0.2)\right), & \text{if SOC} < 0.2 \\ U_0(\mathrm{SOC}), & \text{if } 0.2 \leq \mathrm{SOC} \leq 0.8 \\ U_0^{\mathrm{lith}}(\mathrm{SOC}) - \left(U_0^{\mathrm{lith}}(0.8) - U_0(0.8)\right), & \text{if SOC} > 0.8. \end{cases} \tag{3.1}$$

The corrected OCV stated in Eq. (3.1) orientates on the lithiation voltage in the

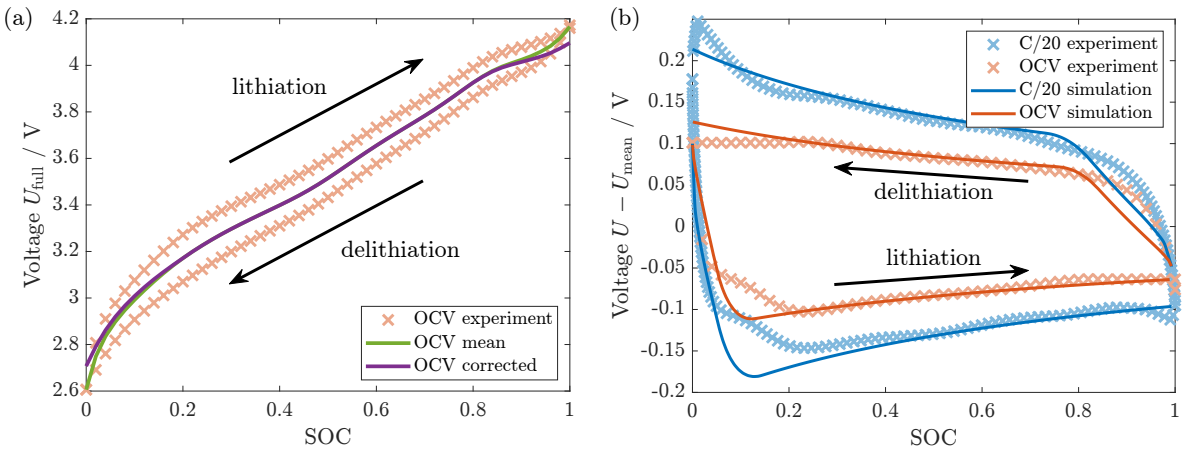

Figure 3.13: Corrected OCV curve and effect on simulated voltage hysteresis compared to experimental data [216]. (a) Corrected OCV compared to mean OCV and measured (de)lithiation OCV. (b) Simulated and experimental voltage hysteresis considering the corrected OCV. Reprinted and modified from Ref. [174], licensed under CC BY 4.0, https://creativecommons.org/licenses/by/4.0/.

large SOC regime and on the delithiation voltage in the small SOC regime, where the elastoplastic stress is fully generated and constant in the respective branch. Figure 3.13(a) depicts the corrected OCV in comparison to the measured direction-dependent OCV and the mean OCV curve. While the corrected OCV coincides with the mean OCV in the medium SOC range, the plot illustrates the adjustment of the corrected OCV curve in the SOC limits.
Applying the corrected OCV, Fig. 3.13(b) displays the simulated voltage hysteresis during cycling and after relaxation. The simulated voltage hysteresis based on the corrected OCV reveals less deviation from the experiment compared to the simulated hysteresis based on the mean OCV as depicted in Fig. 3.12(a). Although a slight deviation remains, the difference is significantly reduced, especially at high SOC in the lithiation direction and at low SOC in the delithiation direction.
As presented, the corrected OCV curve accounts for the asymmetry of the elastoplastic stress levels in the extreme SOC regimes. Consequently, applying the corrected OCV minimizes deviations between the simulated and the experimental voltage hysteresis. Nevertheless, the mean OCV is considered as true OCV within this work for clarity.

3.3.4 Results of the Reduced Chemo-Mechanical Hysteresis Model

To reduce computational efforts, the spatially resolved chemo-mechanical model is approximated and simplified to a system of differential equations evaluated at the particle-SEI interface. While Section 2.4.6 provides the defining differential equations and declarations of the individual terms, Paper III [174] presents the detailed derivation of the reduced chemo-mechanical hysteresis model. Here, the

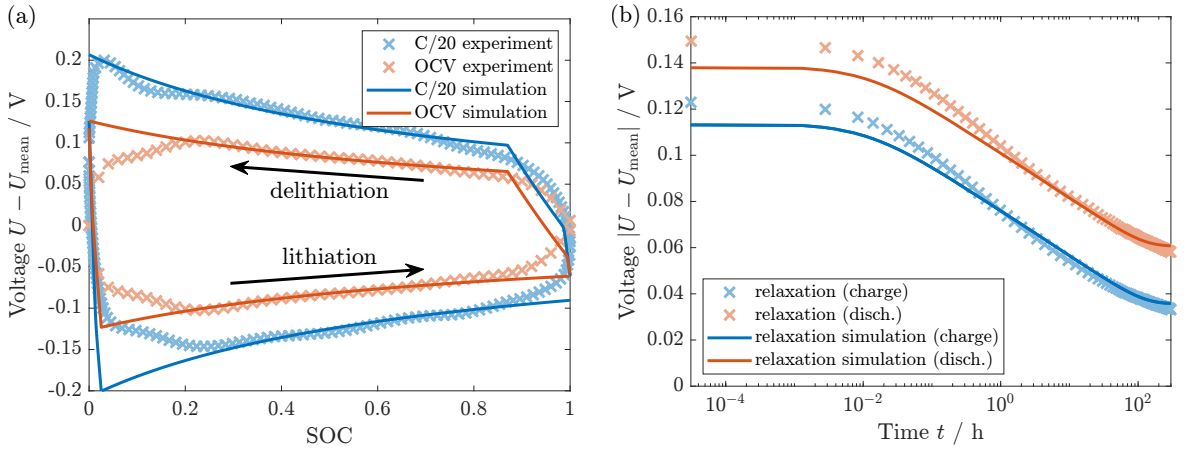

Figure 3.14: Voltage hysteresis and relaxation estimated by the reduced chemo-mechanical hysteresis model compared to experimental data [216]. (a) Reduced model and experimental OCV hysteresis after 12 h and cycling voltage hysteresis. (b) Reduced model and experimental voltage relaxation for 300 h after C/10 (de)lithiation at SOC = 0.3. Reprinted from Ref. [174], licensed under CC BY 4.0, https://creativecommons.org/licenses/by/4.0/.

results of the reduced model are compared to the experimental data in terms of the voltage hysteresis and the relaxation profile.

First, Fig. 3.14(a) shows the voltage hysteresis predicted by the reduced chemo-mechanical model in comparison to experimental data [216]. The reduced model reveals both an OCV hysteresis and an enlarged voltage hysteresis during cycling, exhibiting good accordance with the experiment. Similar to the full simulation, the results of the simplified model deviate slightly in the SOC limits, which could be partially resolved by applying the corrected OCV curve discussed in Section 3.3.3. Due to the omitted spatial resolution, the reduced model possesses more pronounced kinks at the transition between elastic and plastic behavior than the spatially resolved simulation.

Second, Fig. 3.14(b) depicts the voltage relaxation profile of the reduced model. The results exhibit a logarithmic relaxation behavior terminated by an attenuated process, reasonably matching the experimental curve. Merely the slope of the voltage relaxation predicted by the reduced model is slightly smaller compared to the experiment. Thus, the reduced model also shows a minor deviation from the full simulation results, matching the experiment quite accurately.

Contrary to the empirical Plett model outlined in Section 1.3.3, the reduced chemo-mechanical hysteresis model is based on physical processes and facilitates substantiated interpretation. Moreover, the reduced model can describe voltage relaxation processes in time, while the Plett model relies on changes in SOC. As the reduced model is expressed as differential equations in time disregarding spatial resolution, both advantages come at comparable costs compared to the Plett model, which is

based on differential equations in SOC.
In total, the reduced chemo-mechanical hysteresis model approximately reproduces the results of the spatially resolved simulation and fits reasonably to the experimental data concerning voltage hysteresis and relaxation. Outperforming the empirical Plett model, the reduced model is appealing for basic estimations of the voltage hysteresis phenomena of silicon anodes predicted by the chemo-mechanical model.

3.4 Elliptical Silicon Nanowire with SEI

This section summarizes the results of Paper IV [62], not claiming completeness but referring to the corresponding publication for further details. The original publication and information about the author's contribution are provided on Pages 167 to 185.

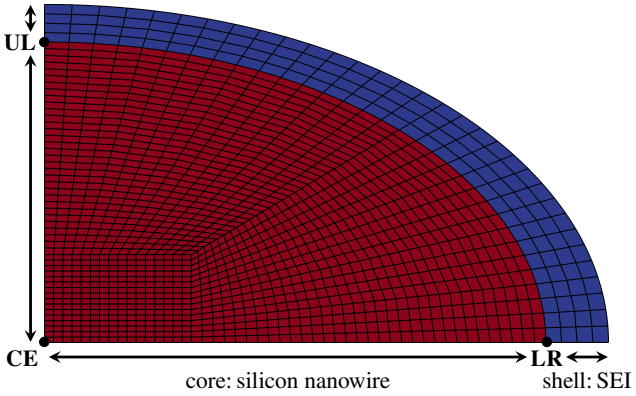

Figure 3.15: Cross-section of the elliptical silicon nanowire (red) with the covering SEI layer (blue). The scheme depicts the computational grid and defines the points of investigation **LR** (lower right), **UL** (upper left), and **CE** (center). The ratio of the half-axes is 0.6:1, and the SEI-to-silicon ratio is 1:8. Reprinted from Ref. [62], licensed under CC BY 4.0, https://creativecommons.org/licenses/by/4.0/.

So far, Sections 3.2 and 3.3 addressed the chemo-mechanical interaction of silicon and SEI in a spherically symmetric geometry. The spherical symmetry restricts inhomogeneities to the radial direction. Investigating the chemo-mechanical interaction of silicon and SEI in an asymmetric geometry promises to be insightful. Therefore, Paper IV [62] extends the nanoparticle-SEI approach to an elliptical silicon nanowire covered by SEI with the profile illustrated in Fig. 3.15.

The two-dimensional silicon-SEI simulation relies on the works and numerical implementation of Schoof et al., which describe the spherically symmetric silicon-SEI system [253] and an elliptical silicon nanowire without SEI [61] focusing on computational efficiency. Inspired by the mechanical impact of the SEI demonstrated in Paper II [173], the elliptical nanowire is extended by an SEI layer with once soft and once stiff mechanical properties. Thus, Paper IV [62] evaluates the characteristics of an elliptical silicon nanowire with SEI concerning mechanics and lithiation.

In the following, Section 3.4.1 discusses the mechanical behavior of the elliptical silicon nanowire covered by a soft and stiff SEI layer. This part focuses on the normal and the tangential Cauchy stress distribution occurring during cycling in the two-dimensional geometry. Afterwards, Section 3.4.2 examines inhomogeneities in the lithiation characteristics during cycling, comparing the impact of a soft and a stiff SEI. Finally, the investigation targets towards the examination of the voltage hysteresis in

the two-dimensional setup in Section 3.4.3 imposed by the SEI-dependent mechanics and lithiation characteristics.

3.4.1 Mechanical Behavior

The elliptical silicon nanowire covered by SEI allows for spatial inhomogeneities in the mechanical response. The study focuses on the stress distribution of the normal and tangential components affected by the asymmetric geometry. Thereby, the analysis aims to unveil the impact of the SEI with different mechanical properties.
The mechanical parameters and models used up to this section are adjusted to meet the mechanical description from Refs. [61, 222, 253]. Particularly, the visco-elastoplastic approach based on explicit viscosity and ideal plastic SEI behavior is replaced by an elasto-viscoplastic approach based on rate-dependent viscoplastic behavior with implicit viscosity. The viscoplastic model allows treating the plastic deformation as an internal variable different from Paper II [173] and Paper III [174]. That reduces the set of coupled differential equations, which is crucial for managing the computational costs for two-dimensional simulations. Both approaches reveal a similar chemo-mechanical behavior [253]. Furthermore, the two-dimensional model disregards the plasticity of the silicon nanowire to minimize the numerical effort.
The subsequent lines compare the mechanical impact of a soft SEI with Young's modulus $E_{\mathrm{SEI}}^{\mathrm{soft}} = 900\,\mathrm{MPa}$ and yield stress $\sigma_{\mathrm{Y,SEI}}^{\mathrm{soft}} = 49.5\,\mathrm{MPa}$ to the impact of a stiff SEI with $E_{\mathrm{SEI}}^{\mathrm{stiff}} = 90\,\mathrm{GPa}$ and $\sigma_{\mathrm{Y,SEI}}^{\mathrm{stiff}} = 4.95\,\mathrm{GPa}$ on the silicon-SEI mechanics. Regarding the geometry illustrated in Fig. 3.15, the ratio of the half-axes is 0.6:1, and the ratio of the SEI shell to the silicon core is 1:8. Paper IV [62] provides a complete list of simulation parameters.

Mechanics of Silicon Nanowire with Soft SEI

To investigate the mechanical behavior of the two-dimensional system, first, the soft SEI layer covers the elliptical silicon nanowire. Therefore, Fig. 3.16 allows evaluating the distribution of the normal and tangential Cauchy stress during the second lithiation with 1 C at SOC = 0.3. During lithiation, the expected concentration gradients generate compressive stress at the outer boundary and tensile stress at the center of the silicon nanowire.
For a detailed analysis, Fig. 3.16(a) depicts the normal Cauchy stress inside silicon and SEI for the soft SEI case. The SEI shows small compressive stress in the normal direction, with the largest magnitude occurring at the silicon-SEI interface. The stress magnitude is especially pronounced at the end of the major half-axis at point **LR** and vanishes at the outer boundary of the SEI. Inside the silicon nanowire, small compressive stress emerges at the boundary towards the SEI as imposed by the SEI. Concurrently, significant tensile stress arises in the interior of the silicon nanowire,

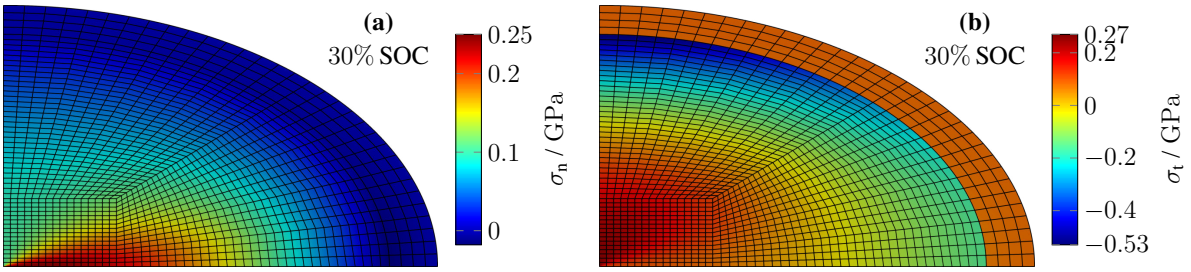

Figure 3.16: Cauchy stress of the elliptical silicon nanowire and soft SEI layer during the second lithiation at SOC = 0.3. Distribution of the (a) normal and (b) tangential component of the Cauchy stress. Reprinted from Ref. [62], licensed under CC BY 4.0, https://creativecommons.org/licenses/by/4.0/.

with its maximum close to the center along the major half-axis. The general trend of compressive stress in the outer region and tensile stress in the inner region fits the expectation during lithiation.

Concerning the tangential component, Fig. 3.16(b) illustrates the tangential Cauchy stress for the silicon nanowire and the soft SEI shell. The SEI region shows approximately constant tensile tangential stress with a minor absolute value. The silicon nanowire exhibits compressive stress at the outer boundary, with the largest magnitude occurring at the end of the minor half-axis at point **UL**. The compressive tangential stress in Fig. 3.16(b) reaches substantially larger magnitudes than the compressive radial stress in Fig. 3.16(a). In the interior of the silicon nanowire, Fig. 3.16(b) exhibits tensile stress with the maximum around the center region along the minor half-axis. Consequently, the nanowire is prone to plastic flow or particle fracture in this region. Analog to the normal component, the tangential stress inside silicon reveals the general trend of compressive stress close to the outer boundary and tensile stress close to the center, as expected.

Regarding the full cycle, Paper IV [62] demonstrates the dominance of the tangential stress magnitude inside the silicon nanowire, particularly at the end of the minor half-axis at point **UL** during the entire simulation. Naturally, the signs of the stress components change during delithiation. Concerning SEI mechanics, the compressive normal and tensile tangential stress in SEI during lithiation and opposite during delithiation agrees with the results of Paper II [173] and Paper III [174].

Concluding the mechanical behavior of the elliptical silicon nanowire with soft SEI, the SEI shows compressive normal stress and tensile tangential stress during lithiation analog to the spherical geometry. The silicon nanowire exhibits compressive stress in the outer region and tensile stress close to the center, meeting the expectations. During delithiation, compressive stress changes to tensile stress and vice versa. Overall, the largest stress magnitude inside silicon appears at the end of the minor half-axis at point **UL** in the tangential direction.

Mechanical Impact of Stiff SEI

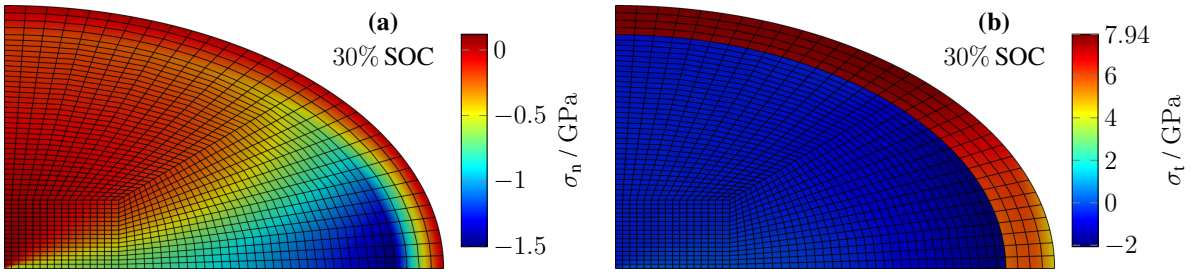

Figure 3.17: Cauchy stress of the elliptical silicon nanowire and stiff SEI layer during the second lithiation at SOC = 0.3. Distribution of the (a) normal and (b) tangential component of the Cauchy stress. Reprinted from Ref. [62], licensed under CC BY 4.0, https://creativecommons.org/licenses/by/4.0/.

After the soft SEI scenario, a stiff SEI covers the elliptical silicon nanowire to elucidate the mechanical impact of the SEI. The increased stiffness of the SEI has the capability to significantly influence the stress distribution inside the silicon nanowire.
To evaluate the mechanical effect of the stiff SEI, Fig. 3.17(a) depicts the normal stress distribution of the silicon nanowire and the stiff SEI layer during the second lithiation. Inside the SEI, compressive stress occurs again but with significantly larger magnitudes compared to the soft SEI shown in Fig. 3.16(a). As before, the normal stress reveals the largest magnitude at the end of the major half-axis at point **LR**. Inside the silicon nanowire, compressive stress emerges everywhere due to the mechanical impact of the stiff SEI except a small region along the minor half-axis close to the center. The most significant compressive stress exists at the end of the major half-axis at point **LR**, owing to the largest curvature of the interface in this region, which magnifies the mechanical impact of the SEI. This agrees with the position of largest compressive stress for the soft SEI case depicted in Fig. 3.16(a).
In contrast to the normal component, the tangential component depicted in Fig. 3.17(b) reveals substantial tensile stresses inside the stiff SEI in comparison to slight tensile stresses in the soft SEI in Fig. 3.16(a). Pronounced tensile stress appears at the minor half-axis, where the SEI possesses the lowest curvature. The tangential stress inside silicon nanowire is compressive everywhere, with the largest values reached at the end of the major half-axis at point **LR**. This is in contrast to the tangential stress of the silicon nanowire with soft SEI, where the largest compressive stress occurs at the end of the minor half-axis at point **UL**, as illustrated in Fig. 3.16(b).
Paper IV [62] reveals that the largest stress magnitudes within the entire cycle are reached inside silicon at the end of the major half-axis at point **LR** also during delithiation. Compressive stresses evolve into tensile stresses and vice versa during delithiation, although not instantaneously. Regarding the mechanical impact of the stiff SEI, compressive normal and tensile tangential stress inside the SEI during

lithiation and vice versa during delithiation agrees again with Paper II [173] and Paper III [174], discussing the OCV hysteresis.
Summarizing the mechanical impact of the SEI, the larger stresses inside the stiff SEI generate considerably enlarged stresses within the silicon nanowire. Overall, the largest stress magnitude inside the elliptical silicon nanowire occurs at the end of the major half-axis at point **LR** for the stiff SEI scenario, while it appears at the end of the minor half-axis at point **UL** for the soft SEI case. This disparity emphasizes the mechanical impact of the SEI on the silicon nanowire.

3.4.2 Lithiation Characteristics

Based on the chemo-mechanical interaction, the asymmetric stress distribution implies an inhomogeneous lithium concentration distribution. The following results discuss the lithiation characteristics in terms of the lithium concentration of the elliptical silicon nanowire, comparing the influence of the soft and the stiff SEI layers.

Lithiation of Silicon Nanowire with Soft SEI

First, the soft SEI covers the elliptical silicon nanowire. Figure 3.18 illustrates the lithium concentration distribution within the silicon nanowire during the second lithiation at three different SOC values, SOC $\in \{0.05, 0.3, 0.9\}$. The color bar is adjusted for each subplot to visualize the concentration gradients at each SOC.
At the beginning of the lithiation process, Fig. 3.18(a) reveals the general trend of increased concentrations at the outer region of the silicon nanowire, as expected. A particularly accelerated concentration increase occurs at the end of the major half-axis at point **LR**. The geometry has the most extensive curvature at this point, coinciding with the largest surface-to-volume ratio, which causes faster lithiation. These general trends are also observable for the continued lithiation in Fig. 3.18(b) and (c).
However, Fig. 3.18(b) discloses a lithium concentration depletion at the end of the minor half-axis at point **UL** at SOC $= 0.3$. The significant compressive stress in this

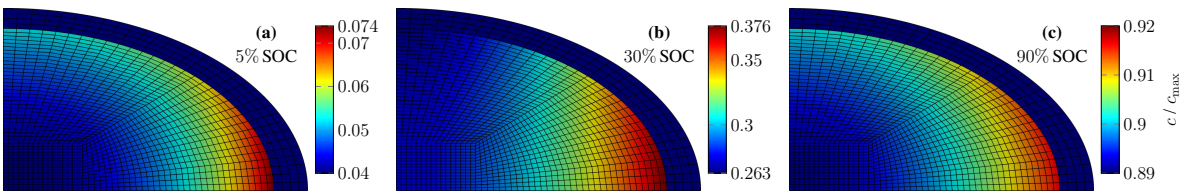

Figure 3.18: Lithium concentration of the elliptical silicon nanowire covered by a soft SEI layer during the second lithiation. Distribution of the lithium concentration at (a) SOC $= 0.05$, (b) SOC $= 0.3$, and (c) SOC $= 0.9$. Reprinted from Ref. [62], licensed under CC BY 4.0, https://creativecommons.org/licenses/by/4.0/.

region displayed in Fig. 3.16(b) represents a penalty for the accumulation of lithium, leading to a decreased concentration compared to the interior of the silicon nanowire. The concentration depletion arises due to the mechanics and asymmetry of the silicon nanowire itself. Paper IV [62] demonstrates that this effect also occurs for an elliptical nanowire without any SEI and during slow cycling.
Regarding the complete cycle, Paper IV [62] validates the general trend of increased concentration at the end of the major half-axis at point **LR** during lithiation and decreased concentration during delithiation. The concentration anomaly at the end of the minor half-axis at point **UL** is a temporary effect, occurring during lithiation in the span $0.2 < \mathrm{SOC} < 0.45$ and during delithiation around $0.05 < \mathrm{SOC} < 0.3$. In the anomalous region, stress-driven convective flux dominates the concentration-driven diffusive flux.
In total, the elliptical silicon nanowire covered by the soft SEI shows an accelerated concentration increase at the end of the major half-axis during lithiation and a respective decrease during delithiation. Simultaneously, a concentration anomaly appears at the end of the minor half-axis in a small to medium SOC regime. The specific lithiation characteristics of the elliptical silicon nanowire are determined by the silicon mechanics and geometry instead of the impact of the soft SEI.

Impact of Stiff SEI on the Lithiation Characteristics

Second, the stiff SEI covers the silicon nanowire to increase the mechanical impact of the SEI layer. The discussion of the mechanical behavior in Section 3.4.1 unveiled a pronounced influence of the stiff SEI at the end of the major half-axis. Therefore, Fig. 3.19 illustrates inhomogeneities of the lithium concentration during the second lithiation at $\mathrm{SOC} \in \{0.05, 0.3, 0.9\}$, evaluating the concentration asymmetry.
Initially, Fig. 3.19(a) reveals lithiation from the outside towards the interior of the silicon nanowire as expected. The region of the largest lithium concentration shifts away from the end of the major half-axis, where the maximum occurs for the soft SEI

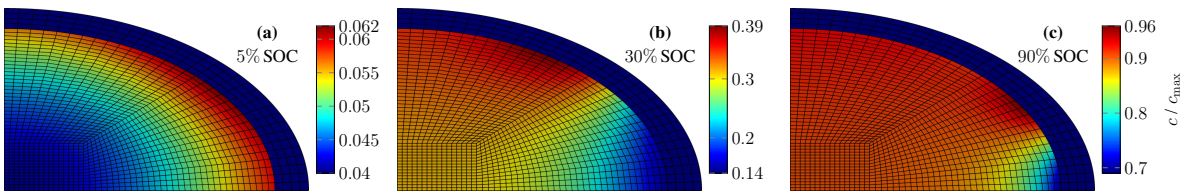

Figure 3.19: Lithium concentration of the elliptical silicon nanowire covered by a stiff SEI layer during the second lithiation. Distribution of the lithium concentration at (a) $\mathrm{SOC} = 0.05$, (b) $\mathrm{SOC} = 0.3$, and (c) $\mathrm{SOC} = 0.9$. Reprinted from Ref. [62], licensed under CC BY 4.0, https://creativecommons.org/licenses/by/4.0/.

scenario in Fig. 3.18. The largest concentration is reached neither at the end of the major half-axis nor the end of the minor half-axis, owing to the interplay of lithiation and mechanical effects, which are both dependent on the surface-to-volume ratio. For continued lithiation in Fig. 3.19(b) and (c), a substantial concentration depletion develops at the end of the major half-axis at point **LR** due to the pronounced mechanical impact of the stiff SEI in this region visible in Fig. 3.17(a).
The investigation of the full cycle in Paper IV [62] shows that the concentration depletion at the end of the major half-axis at point **LR** reduces during delithiation, and a concentration excess appears towards the end of the delithiation process. This profile corresponds to the gradual evolution of the Cauchy stress inside the silicon for the stiff SEI scenario from compressive to tensile stress. Compared to the soft SEI, no concentration anomaly appears at the end of the minor half-axis at point **UL**. However, for the stiff SEI, a considerably larger concentration anomaly appears at the end of the major half-axis at point **LR**, where the soft SEI shows no anomaly.
In summary, the impact of the stiff SEI causes a significant concentration anomaly at the end of the major half-axis, where the highest surface-to-volume ratio of the interface leads to an enhanced mechanical influence of the SEI. In contrast, the slight concentration anomaly observed for the soft SEI case at the end of the minor half-axis disappears for the stiff SEI case. This emphasizes once again the importance of considering the SEI in chemo-mechanical simulations of silicon-based anodes. Moreover, an experimental examination of the lithium concentration distribution can allow to draw conclusions about Young's modulus of the SEI.

3.4.3 Voltage Hysteresis of Elliptical Silicon Nanowire

According to the findings in Sections 3.2 and 3.3, the stiff SEI is responsible for the voltage hysteresis of spherically symmetric silicon nanoparticle anodes. The impact of the SEI is potentially affected by the inhomogeneous mechanical influence on the lithiation characteristics in asymmetric geometries. Thus, the purpose of this section is to investigate the voltage hysteresis predicted in the elliptical simulation, accounting for the soft and the stiff SEI shell.
Focusing on the influence of the asymmetric geometry, Fig. 3.20 depicts the voltage of the elliptical silicon nanowire covered by the soft SEI layer during the second lithiation and the first delithiation with C/20 (blue line). Investigating the second lithiation excludes effects occurring during the initial lithiation. The simulated voltage reveals negligible hysteresis behavior in agreement with the trend of the parameter variation of Young's modulus of the SEI depicted in Fig. 3.7. Hence, the elliptical geometry featured with the soft SEI and the respective concentration anomaly generates no voltage hysteresis.
Focusing on the mechanical impact of the SEI, Fig. 3.20 furthermore illustrates the voltage of the elliptical silicon nanowire during cycling for the stiff SEI case (red

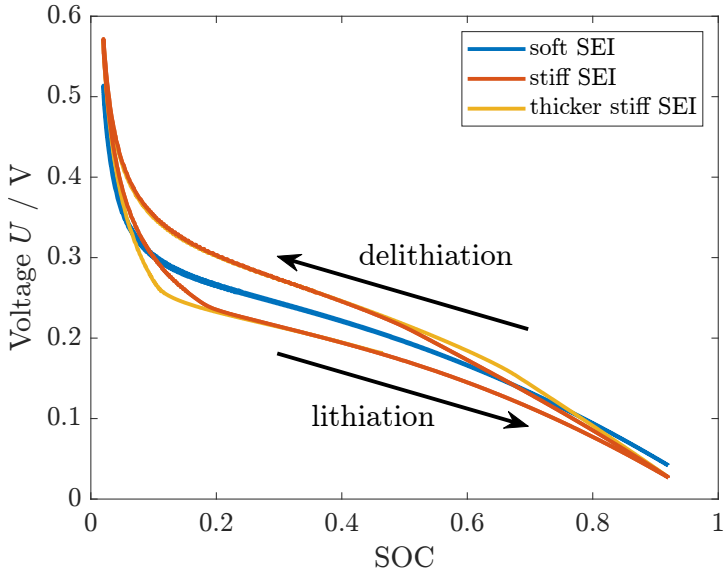

Figure 3.20: Voltage hysteresis of the elliptical silicon nanowire covered by SEI. Voltage during slow cycling with C/20 for the soft and stiff SEI scenario. Additionally, the figure includes the voltage hysteresis with a thicker stiff SEI with an SEI-to-silicon ratio of 1:4. Figure based on Ref. [62].

line). The stiff SEI scenario exhibits a voltage hysteresis similar to the one obtained for the spherically symmetric simulations in Sections 3.2 and 3.3. Thus, the stiff SEI causes not only a substantial lithium concentration anomaly inside the elliptical silicon nanowire but also a significant hysteresis behavior. The elliptical simulation reveals a smaller size of the voltage hysteresis for large SOC values compared to the spherically symmetric results depicted in Fig. 3.6. The diminished hysteresis is attributed to the reduced thickness of the considered SEI layer.
Therefore, Fig. 3.20 also depicts the voltage hysteresis generated by an enlarged stiff SEI (yellow line) to assess the influence of the SEI thickness on the voltage hysteresis in the elliptical geometry. The size ratio of the thicker SEI to the silicon core is 1:4 instead of 1:8. The yield stress for the enlarged SEI is reduced to $\sigma_{\mathrm{SEI,Y}} = 2.5\,\mathrm{GPa}$ to keep the size of the predicted hysteresis constant for comparison. As expected, the thicker SEI reveals an accelerated transition from the lithiation to the delithiation branch, causing an enlarged voltage hysteresis size at high SOC values.
To conclude, a soft SEI does not generate a voltage hysteresis for elliptical silicon nanowires. Contrarily, a stiff SEI causes a voltage hysteresis in accordance with the discussions from Sections 3.2 and 3.3. Overall, the analysis in this thesis demonstrates that a stiff SEI is necessary to explain the voltage hysteresis for the elliptical silicon nanowire as well as for the spherically symmetric silicon nanoparticle.

4 Conclusion and Outlook

4.1 Conclusion

The presented thesis addresses the origin of capacity fade in lithium-ion batteries and the silicon voltage hysteresis with thermodynamically consistent continuum modeling. Regarding capacity fade, comparing the electron and solvent diffusion model confirms electron diffusion as the relevant transport mechanism for SEI growth. Moreover, this thesis demonstrates that the mechanical impact of the SEI generates the silicon voltage hysteresis, owing to the chemo-mechanical coupling.

In Paper I [153], the investigation of the relevant SEI growth mechanism considering electron diffusion versus solvent diffusion is based on the work of Single et al. [89], which is further developed. In particular, the advanced solvent diffusion model accounts for the interplay of reaction and transport limitation. The predictions of both models are correlated to experimental data obtained by Keil et al. [126] concerning the state-of-charge (SOC) and time dependence of capacity fade. The examination demonstrates that the electron diffusion mechanism can explain the experimental SOC and time dependence with the same parameter values. In contrast, the solvent diffusion mechanism can reproduce either the SOC or the time dependence of capacity fade, especially not both with the same parameters. Furthermore, electron diffusion can explain deviations of the typical square-root in time behavior observed by Attia et al. [246] due to the interaction of the SOC and the time dependence in experiments with significant capacity loss. Therefore, the study confirms electron diffusion as the relevant transport mechanism mediating SEI growth.

Accounting for a grown SEI layer, Paper II [173] analyzes the chemo-mechanical interaction of a silicon nanoparticle and the covering SEI based on the work of Kolzenberg et al. [63], focusing herein on the silicon voltage hysteresis. Silicon anodes show a voltage hysteresis during slow cycling and a reduced but still significant hysteresis after several hours of relaxation, observed even for silicon nanoparticle anodes by Pan et al. [214, 215]. This work explains the voltage hysteresis after relaxation by the elastoplastic impact of the SEI on the silicon nanoparticle, generating compressive stress during lithiation and tensile stress during delithiation. Considering a high Young's modulus of the SEI, the layer creates a substantial mechanical impact, affecting the anode voltage. The enlarged hysteresis during cycling arises due to viscous behavior of the SEI. In total, the chemo-mechanical silicon-SEI simulation featuring

a visco-elastoplastic SEI explains the hysteresis during cycling, after relaxation, and voltage transitions observed during the galvanostatic intermittent titration technique (GITT) procedure. Concluding the simulation results, a softer SEI might reduce the voltage hysteresis of silicon nanoparticle anodes.
After focusing on the voltage hysteresis and short-term relaxation within GITT measurements, Paper III [174] examines the long-term relaxation process of silicon anodes. A recent publication by Wycisk et al. [216] reports slow, non-exponential voltage relaxation over 300 h. To account for the long-term relaxation, the description of the SEI viscosity is enhanced by the incorporation of the Garofalo viscosity model, representing more realistic material behavior. The logarithmic voltage relaxation of the advanced chemo-mechanical model agrees well with the experimentally reported relaxation profiles. Furthermore, the model with Garofalo viscosity provides a consistent description of the observed voltage hysteresis phenomena, i.e., the full hysteresis during cycling and after relaxation, voltage transitions, and the C-rate dependence of the hysteresis size. In addition to the full simulation, the study derives a reduced chemo-mechanical hysteresis model disregarding spatial resolution based on differential equations with respect to time, providing physical interpretability and covering open-circuit relaxation in contrast to the empirical Plett model.
Generalizing the simulation to two-dimensional geometries, Paper IV [62] investigates the chemo-mechanical interaction of an elliptical silicon nanowire with the covering SEI layer. The work compares the impact of a soft and a stiff SEI on the mechanics inside silicon and SEI, as well as the effects on the lithiation of the elliptical silicon nanowire. The results demonstrate that in the case of the soft SEI, the largest stress magnitude inside silicon occurs at the end of the minor half-axis, caused by the elliptical geometry rather than the influence of the SEI. For the stiff SEI scenario, the largest stress magnitude appears at the end of the major half-axis due to the mechanical impact of the stiff SEI layer, pronounced in this region due to the largest surface-to-volume ratio. Regarding the lithiation characteristics, the domains of the most extensive stress magnitudes exhibit lithium concentration anomalies, i.e., concentration depletion during lithiation and concentration excess during delithiation. The stress and respective concentration anomaly generated by the stiff SEI is significantly larger than in the soft SEI case, highlighting the importance of the chemo-mechanical interplay of silicon and SEI. To complete the circle back to the voltage hysteresis, the elliptical silicon nanowire reveals a similar hysteresis behavior compared to the spherically symmetric silicon nanoparticle when covered by a stiff SEI shell.
In conclusion, this thesis provides an improved understanding of the growth of the SEI as well as its mechanical impact on the cycling behavior of silicon, causing the voltage hysteresis. Finally, the deeper insights into the SEI can help to mitigate capacity fade and performance drawbacks due to the voltage hysteresis by the ambitious task of creating a softer but electronically superior passivating SEI layer.

4.2 Outlook

For the future, combined efforts of continuum modeling, density functional theory, and quantum chemistry investigating interfaces inside the SEI are necessary to identify improved SEI compositions and structures. The common objective has to be to reduce electronic leakage by decreasing the overall diffusion coefficient of electrons inside the SEI. At the same time, experiments on all scales, starting with cryogenic electron microscopy to enlighten the SEI up to cell-scale capacity fade measurements under varying storage or cycling conditions, are essential to confirm the theoretical results. Gaining a more detailed understanding of the growth and characteristics of the SEI promises enhanced battery lifetimes highly demanded for mobile and stationary storage solutions.
Concerning the silicon voltage hysteresis, experiments are required to check the mechanical impact of the SEI on the voltage hysteresis by applying different electrolytes or artificial SEI layers with different mechanical properties. Furthermore, it would be insightful to evaluate the influence of silicon nanodomains for the lithiation of larger silicon particles with high-resolution imaging techniques like the focused ion beam. From a simulation perspective, the incorporation of particle and SEI fracture, as well as SEI healing, present attractive and fruitful model advancements. Reducing the voltage hysteresis with a designed SEI promises to reach higher efficiencies and faster charging capabilities, strongly desired for improved energy storage systems, especially for the transportation sector.
For future developments, the influence of aging and mechanical aspects will gain increasing importance. The desired application of lithium metal anodes providing ultimate capacity coincides with accelerated SEI growth and enormous volume changes, even compared to silicon anodes. Moreover, the use of solid-state electrolytes promising higher energy densities and improved safety further pronounces the impact of mechanics. Therefore, research efforts from academia and industry are needed to ever improve the characteristics of modern lithium-ion and post-lithium-ion batteries. Enhanced batteries are essential for the continuing challenge of transitioning from fossil to sustainable energy. As battery research is currently making great strides, it remains intriguing to see what innovations the future has in store for us.

Bibliography

[1] M. Winter, B. Barnett, K. Xu, "Before Li Ion Batteries", *Chemical Reviews* **2018**, *118*, 11433–11456, DOI 10.1021/acs.chemrev.8b00422.

[2] A. Yoshino, "The Birth of the Lithium-Ion Battery", *Angewandte Chemie International Edition* **2012**, *51*, 5798–5800, DOI 10.1002/anie.201105006.

[3] M. Whittingham, F. R. Gamble, "The lithium intercalates of the transition metal dichalcogenides", *Materials Research Bulletin* **1975**, *10*, 363–371, DOI 10.1016/0025-5408(75)90006-9.

[4] M. S. Whittingham, "The Role of Ternary Phases in Cathode Reactions", *Journal of The Electrochemical Society* **1976**, *123*, 315, DOI 10.1149/1.2132817.

[5] M. S. Whittingham, "Electrical Energy Storage and Intercalation Chemistry", *Science* **1976**, *192*, 1126–1127, DOI 10.1126/science.192.4244.1126.

[6] M. Whittingham, "Chemistry of intercalation compounds: Metal guests in chalcogenide hosts", *Progress in Solid State Chemistry* **1978**, *12*, 41–99, DOI 10.1016/0079-6786(78)90003-1.

[7] K. Mizushima, P. Jones, P. Wiseman, J. Goodenough, "LixCoO2 (0<x<-1): A new cathode material for batteries of high energy density", *Materials Research Bulletin* **1980**, *15*, 783–789, DOI 10.1016/0025-5408(80)90012-4.

[8] A. K. Padhi, K. S. Nanjundaswamy, J. B. Goodenough, "Phospho-olivines as Positive-Electrode Materials for Rechargeable Lithium Batteries", *Journal of The Electrochemical Society* **1997**, *144*, 1188–1194, DOI 10.1149/1.1837571.

[9] A. Yoshino, "From polyacetylene to carbonaceous anodes", *Nature Energy* **2021**, *6*, 449–449, DOI 10.1038/s41560-021-00801-0.

[10] L. Köbbing, A. Latz, B. Horstmann, "Batterien wie Sand am Meer", *Physik Journal* **2024**, *5*, 28–34, URL https://pro-physik.de/zeitschriften/physik-journal/2024-5/, Preprint https://elib.dlr.de/204279/.

[11] F. Ueckerdt, C. Bauer, A. Dirnaichner, J. Everall, R. Sacchi, G. Luderer, "Potential and risks of hydrogen-based e-fuels in climate change mitigation", *Nature Climate Change* **2021**, *11*, 384–393, DOI 10.1038/s41558-021-01032-7.

[12] G. Pasini, G. Lutzemberger, L. Ferrari, "Renewable Electricity for Decarbonisation of Road Transport: Batteries or E-Fuels?", *Batteries* **2023**, *9*, 135, DOI 10.3390/batteries9020135.

[13] J. Mitali, S. Dhinakaran, A. Mohamad, "Energy storage systems: a review", *Energy Storage and Saving* **2022**, *1*, 166–216, DOI 10.1016/j.enss.2022.07.002.

[14] H. Hesse, M. Schimpe, D. Kucevic, A. Jossen, "Lithium-Ion Battery Storage for the Grid—A Review of Stationary Battery Storage System Design Tailored for Applications in Modern Power Grids", *Energies* **2017**, *10*, 2107, DOI 10.3390/en10122107.

[15] L. M. S. de Siqueira, W. Peng, "Control strategy to smooth wind power output using battery energy storage system: A review", *Journal of Energy Storage* **2021**, *35*, 102252, DOI 10.1016/j.est.2021.102252.

[16] M. Hannan, S. Wali, P. Ker, M. A. Rahman, M. Mansor, V. Ramachandaramurthy, K. Muttaqi, T. Mahlia, Z. Dong, "Battery energy-storage system: A review of technologies, optimization objectives, constraints, approaches, and outstanding issues", *Journal of Energy Storage* **2021**, *42*, 103023, DOI 10.1016/j.est.2021.103023.

[17] J. S. Edge, S. O'Kane, R. Prosser, N. D. Kirkaldy, A. N. Patel, A. Hales, A. Ghosh, W. Ai, J. Chen, J. Yang, S. Li, M.-C. Pang, L. Bravo Diaz, A. Tomaszewska, M. W. Marzook, K. N. Radhakrishnan, H. Wang, Y. Patel, B. Wu, G. J. Offer, "Lithium ion battery degradation: what you need to know", *Physical Chemistry Chemical Physics* **2021**, *23*, 8200–8221, DOI 10.1039/D1CP00359C.

[18] S. E. J. O'Kane, W. Ai, G. Madabattula, D. Alonso-Alvarez, R. Timms, V. Sulzer, J. S. Edge, B. Wu, G. J. Offer, M. Marinescu, "Lithium-ion battery degradation: how to model it", *Physical Chemistry Chemical Physics* **2022**, *24*, 7909–7922, DOI 10.1039/D2CP00417H.

[19] P. M. Attia, A. Bills, F. Brosa Planella, P. Dechent, G. dos Reis, M. Dubarry, P. Gasper, R. Gilchrist, S. Greenbank, D. Howey, O. Liu, E. Khoo, Y. Preger, A. Soni, S. Sripad, A. G. Stefanopoulou, V. Sulzer, "Review—"Knees" in Lithium-Ion Battery Aging Trajectories", *Journal of The Electrochemical Society* **2022**, *169*, 060517, DOI 10.1149/1945-7111/ac6d13.

[20] S. Carelli, W. G. Bessler, "Coupling Lithium Plating with SEI Formation in a Pseudo-3D Model: A Comprehensive Approach to Describe Aging in Lithium-Ion Cells", *Journal of The Electrochemical Society* **2022**, *169*, 050539, DOI 10.1149/1945-7111/ac716a.

[21] J. A. Braun, R. Behmann, D. Schmider, W. G. Bessler, "State of charge and state of health diagnosis of batteries with voltage-controlled models", *Journal of Power Sources* **2022**, *544*, 231828, DOI 10.1016/j.jpowsour.2022.231828.

[22] M. N. Obrovac, V. L. Chevrier, "Alloy Negative Electrodes for Li-Ion Batteries", *Chemical Reviews* **2014**, *114*, 11444–11502, DOI 10.1021/cr500207g.

[23] H. Cheng, J. G. Shapter, Y. Li, G. Gao, "Recent progress of advanced anode materials of lithium-ion batteries", *Journal of Energy Chemistry* **2021**, *57*, 451–468, DOI 10.1016/j.jechem.2020.08.056.

[24] P. Nzereogu, A. Omah, F. Ezema, E. Iwuoha, A. Nwanya, "Anode materials for lithium-ion batteries: A review", *Applied Surface Science Advances* **2022**, *9*, 100233, DOI 10.1016/j.apsadv.2022.100233.

[25] M. H. Hossain, M. A. Chowdhury, N. Hossain, M. A. Islam, M. H. Mobarak, "Advances of lithium-ion batteries anode materials—A review", *Chemical Engineering Journal Advances* **2023**, *16*, 100569, DOI 10.1016/j.ceja.2023.100569.

[26] J. Asenbauer, T. Eisenmann, M. Kuenzel, A. Kazzazi, Z. Chen, D. Bresser, "The success story of graphite as a lithium-ion anode material – fundamentals, remaining challenges, and recent developments including silicon (oxide) composites", *Sustainable Energy & Fuels* **2020**, *4*, 5387–5416, DOI 10.1039/D0SE00175A.

[27] W. Zhao, C. Zhao, H. Wu, L. Li, C. Zhang, "Progress, challenge and perspective of graphite-based anode materials for lithium batteries: A review", *Journal of Energy Storage* **2024**, *81*, 110409, DOI 10.1016/j.est.2023.110409.

[28] M. Naumann, M. Schimpe, P. Keil, H. C. Hesse, A. Jossen, "Analysis and modeling of calendar aging of a commercial LiFePO4/graphite cell", *Journal of Energy Storage* **2018**, *17*, 153–169, DOI 10.1016/j.est.2018.01.019.

[29] M. Naumann, F. Spingler, A. Jossen, "Analysis and modeling of cycle aging of a commercial LiFePO4/graphite cell", *Journal of Power Sources* **2020**, *451*, 227666, DOI 10.1016/j.jpowsour.2019.227666.

[30] W. Vermeer, G. R. Chandra Mouli, P. Bauer, "A Comprehensive Review on the Characteristics and Modeling of Lithium-Ion Battery Aging", *IEEE Transactions on Transportation Electrification* **2022**, *8*, 2205–2232, DOI 10.1109/TTE.2021.3138357.

[31] C. P. Sandhya, B. John, C. Gouri, "Lithium titanate as anode material for lithium-ion cells: a review", *Ionics* **2014**, *20*, 601–620, DOI 10.1007/s11581-014-1113-4.

[32] G. Xu, P. Han, S. Dong, H. Liu, G. Cui, L. Chen, "Li4Ti5O12-based energy conversion and storage systems: Status and prospects", *Coordination Chemistry Reviews* **2017**, *343*, 139–184, DOI 10.1016/j.ccr.2017.05.006.

[33] H. Zhang, Y. Yang, H. Xu, L. Wang, X. Lu, X. He, "Li4Ti5O12 spinel anode: Fundamentals and advances in rechargeable batteries", *InfoMat* **2022**, *4*, 1–29, DOI 10.1002/inf2.12228.

[34] K. Kanamura, T. Umegaki, H. Naito, Z. Takehara, T. Yao, "Structural and electrochemical characteristics of Li4/3Ti5/3O4 as an anode material for rechargeable lithium batteries", *Journal of Applied Electrochemistry* **2001**, *31*, 73–78, DOI 10.1023/A:1004170009354.

[35] X.-B. Cheng, R. Zhang, C.-Z. Zhao, Q. Zhang, "Toward Safe Lithium Metal Anode in Rechargeable Batteries: A Review", *Chemical Reviews* **2017**, *117*, 10403–10473, DOI 10.1021/acs.chemrev.7b00115.

[36] D. Lin, Y. Liu, Y. Cui, "Reviving the lithium metal anode for high-energy batteries", *Nature Nanotechnology* **2017**, *12*, 194–206, DOI 10.1038/nnano.2017.16.

[37] J. Liu, Z. Bao, Y. Cui, E. J. Dufek, J. B. Goodenough, P. Khalifah, Q. Li, B. Y. Liaw, P. Liu, A. Manthiram, Y. S. Meng, V. R. Subramanian, M. F. Toney, V. V. Viswanathan, M. S. Whittingham, J. Xiao, W. Xu, J. Yang, X.-Q. Yang, J.-G. Zhang, "Pathways for practical high-energy long-cycling lithium metal batteries", *Nature Energy* **2019**, *4*, 180–186, DOI 10.1038/s41560-019-0338-x.

[38] R. Wang, W. Cui, F. Chu, F. Wu, "Lithium metal anodes: Present and future", *Journal of Energy Chemistry* **2020**, *48*, 145–159, DOI 10.1016/j.jechem.2019.12.024.

[39] G. M. Hobold, J. Lopez, R. Guo, N. Minafra, A. Banerjee, Y. Shirley Meng, Y. Shao-Horn, B. M. Gallant, "Moving beyond 99.9% Coulombic efficiency for lithium anodes in liquid electrolytes", *Nature Energy* **2021**, *6*, 951–960, DOI 10.1038/s41560-021-00910-w.

[40] B. Horstmann, J. Shi, R. Amine, M. Werres, X. He, H. Jia, F. Hausen, I. Cekic-Laskovic, S. Wiemers-Meyer, J. Lopez, D. Galvez-Aranda, F. Baakes, D. Bresser, C. Su, Y. Xu, W. Xu, P. Jakes, R.-A. Eichel, E. Figgemeier, U. Krewer, J. M. Seminario, P. B. Balbuena, C. Wang, S. Passerini, Y. Shao-Horn, M. Winter, K. Amine, R. Kostecki, A. Latz, "Strategies towards enabling lithium metal in batteries: interphases and electrodes", *Energy & Environmental Science* **2021**, *14*, 5289–5314, DOI 10.1039/D1EE00767J.

[41] P. Bai, J. Li, F. R. Brushett, M. Z. Bazant, "Transition of lithium growth mechanisms in liquid electrolytes", *Energy & Environmental Science* **2016**, *9*, 3221–3229, DOI 10.1039/C6EE01674J.

[42] G. Lu, J. Nai, D. Luan, X. Tao, X. W. D. Lou, "Surface engineering toward stable lithium metal anodes", *Science Advances* **2023**, *9*, 21–26, DOI 10.1126/sciadv.adf1550.

[43] X. Zuo, J. Zhu, P. Müller-Buschbaum, Y.-J. Cheng, "Silicon based lithium-ion battery anodes: A chronicle perspective review", *Nano Energy* **2017**, *31*, 113–143, DOI 10.1016/j.nanoen.2016.11.013.

[44] M. Kim, Z. Yang, I. Bloom, "Review—The Lithiation/Delithiation Behavior of Si-Based Electrodes: A Connection between Electrochemistry and Mechanics", *Journal of The Electrochemical Society* **2021**, *168*, 010523, DOI 10.1149/1945-7111/abd56f.

[45] C. Zhang, F. Wang, J. Han, S. Bai, J. Tan, J. Liu, F. Li, "Challenges and Recent Progress on Silicon-Based Anode Materials for Next-Generation Lithium-Ion Batteries", *Small Structures* **2021**, *2*, 2100009, DOI 10.1002/sstr.202100009.

[46] L. Sun, Y. Liu, R. Shao, J. Wu, R. Jiang, Z. Jin, "Recent progress and future perspective on practical silicon anode-based lithium ion batteries", *Energy Storage Materials* **2022**, *46*, 482–502, DOI 10.1016/j.ensm.2022.01.042.

[47] Y. Li, Q. Li, J. Chai, Y. Wang, J. Du, Z. Chen, Y. Rui, L. Jiang, B. Tang, "Si-based Anode Lithium-Ion Batteries: A Comprehensive Review of Recent Progress", *ACS Materials Letters* **2023**, *5*, 2948–2970, DOI 10.1021/acsmaterialslett.3c00253.

[48] J. Lin, X. Zhang, E. Fan, R. Chen, F. Wu, L. Li, "Carbon neutrality strategies for sustainable batteries: from structure, recycling, and properties to applications", *Energy & Environmental Science* **2023**, *16*, 745–791, DOI 10.1039/D2EE03257K.

[49] L. Boveleth, A. Lindner, W. Menesklou, T. Danner, A. Latz, "Material parameters affecting Li plating in Si/graphite composite electrodes", *Electrochimica Acta* **2024**, *506*, 145010, DOI 10.1016/j.electacta.2024.145010.

[50] C. Hogrefe, N. Paul, L. Boveleth, M. Bolsinger, M. Flügel, T. Danner, A. Latz, R. Gilles, V. Knoblauch, M. Wohlfahrt-Mehrens, M. Hölzle, T. Waldmann, "Lithium Redistribution Mechanism within Silicon-Graphite Electrodes: Multi-Method Approach and Method Validation", *Journal of The Electrochemical Society* **2024**, *171*, 070503, DOI 10.1149/1945-7111/ad59c7.

[51] L. Y. Beaulieu, K. W. Eberman, R. L. Turner, L. J. Krause, J. R. Dahn, "Colossal Reversible Volume Changes in Lithium Alloys", *Electrochemical and Solid-State Letters* **2001**, *4*, A137, DOI 10.1149/1.1388178.

[52] J. Duay, K. W. Schroder, S. Murugesan, K. J. Stevenson, "Monitoring Volumetric Changes in Silicon Thin-Film Anodes through In Situ Optical Diffraction Microscopy", *ACS Applied Materials & Interfaces* **2016**, *8*, 17642–17650, DOI 10.1021/acsami.6b03822.

[53] I. Yoon, D. P. Abraham, B. L. Lucht, A. F. Bower, P. R. Guduru, "In Situ Measurement of Solid Electrolyte Interphase Evolution on Silicon Anodes Using Atomic Force Microscopy", *Advanced Energy Materials* **2016**, *6*, 1600099, DOI 10.1002/aenm.201600099.

[54] B. Jerliu, E. Hüger, L. Dörrer, B. K. Seidlhofer, R. Steitz, M. Horisberger, H. Schmidt, "Lithium insertion into silicon electrodes studied by cyclic voltammetry and operando neutron reflectometry", *Physical Chemistry Chemical Physics* **2018**, *20*, 23480–23491, DOI 10.1039/C8CP03540G.

[55] K. Dong, H. Markötter, F. Sun, A. Hilger, N. Kardjilov, J. Banhart, I. Manke, "In situ and Operando Tracking of Microstructure and Volume Evolution of Silicon Electrodes by using Synchrotron X-ray Imaging", *ChemSusChem* **2019**, *12*, 261–269, DOI 10.1002/cssc.201801969.

[56] X. H. Liu, L. Zhong, S. Huang, S. X. Mao, T. Zhu, J. Y. Huang, "Size-Dependent Fracture of Silicon Nanoparticles During Lithiation", *ACS Nano* **2012**, *6*, 1522–1531, DOI 10.1021/nn204476h.

[57] M. Wetjen, S. Solchenbach, D. Pritzl, J. Hou, V. Tileli, H. A. Gasteiger, "Morphological Changes of Silicon Nanoparticles and the Influence of Cutoff Potentials in Silicon-Graphite Electrodes", *Journal of The Electrochemical Society* **2018**, *165*, A1503–A1514, DOI 10.1149/2.1261807jes.

[58] X. Su, Q. Wu, J. Li, X. Xiao, A. Lott, W. Lu, B. W. Sheldon, J. Wu, "Silicon-Based Nanomaterials for Lithium-Ion Batteries: A Review", *Advanced Energy Materials* **2014**, *4*, 1–23, DOI 10.1002/aenm.201300882.

[59] Z. Xiao, C. Wang, L. Song, Y. Zheng, T. Long, "Research progress of nano-silicon-based materials and silicon-carbon composite anode materials for lithium-ion batteries", *Journal of Solid State Electrochemistry* **2022**, *26*, 1125–1136, DOI 10.1007/s10008-022-05141-x.

[60] M. M. Hossain, M. Hannan, P. J. Ker, S. K. Tiong, M. Salam, M Abdillah, T. I. Mahlia, "Silicon-based nanosphere anodes for lithium-ion batteries: Features, progress, effectiveness, challenges, and prospects", *Journal of Energy Storage* **2024**, *99*, 113371, DOI 10.1016/j.est.2024.113371.

[61] R. Schoof, J. Niermann, A. Dyck, T. Böhlke, W. Dörfler, "Modeling and simulation of chemo-elasto-plastically coupled battery active particles", *Computational Mechanics* **2024**, DOI 10.1007/s00466-024-02499-9.

[62] R. Schoof, L. Köbbing, A. Latz, B. Horstmann, W. Dörfler, "Elliptical Silicon Nanowire Covered by the SEI in a 2D Chemo-Mechanical Simulation", *Batteries & Supercaps* **2025**, *8*, DOI 10.1002/batt.202400604.

[63] L. von Kolzenberg, A. Latz, B. Horstmann, "Chemo-Mechanical Model of SEI Growth on Silicon Electrode Particles", *Batteries & Supercaps* **2022**, *5*, e202100216, DOI 10.1002/batt.202100216.

[64] J. D. McBrayer, M.-t. F. Rodrigues, M. C. Schulze, D. P. Abraham, C. A. Apblett, I. Bloom, G. M. Carroll, A. M. Colclasure, C. Fang, K. L. Harrison, G. Liu, S. D. Minteer, N. R. Neale, G. M. Veith, C. S. Johnson, J. T. Vaughey, A. K. Burrell, B. Cunningham, "Calendar aging of silicon-containing batteries", *Nature Energy* **2021**, *6*, 866–872, DOI 10.1038/s41560-021-00883-w.

[65] M. Winter, "The Solid Electrolyte Interphase – The Most Important and the Least Understood Solid Electrolyte in Rechargeable Li Batteries", *Zeitschrift für Physikalische Chemie* **2009**, *223*, 1395–1406, DOI 10.1524/zpch.2009.6086.

[66] P. Verma, P. Maire, P. Novák, "A review of the features and analyses of the solid electrolyte interphase in Li-ion batteries", *Electrochimica Acta* **2010**, *55*, 6332–6341, DOI 10.1016/j.electacta.2010.05.072.

[67] E. Peled, S. Menkin, "Review—SEI: Past, Present and Future", *Journal of The Electrochemical Society* **2017**, *164*, A1703–A1719, DOI 10.1149/2.1441707jes.

[68] A. Wang, S. Kadam, H. Li, S. Shi, Y. Qi, "Review on modeling of the anode solid electrolyte interphase (SEI) for lithium-ion batteries", *npj Computational Materials* **2018**, *4*, 15, DOI 10.1038/s41524-018-0064-0.

[69] U. S. Meda, L. Lal, S. M, P. Garg, "Solid Electrolyte Interphase (SEI), a boon or a bane for lithium batteries: A review on the recent advances", *Journal of Energy Storage* **2022**, *47*, 103564, DOI 10.1016/j.est.2021.103564.

[70] E. Peled, "The Electrochemical Behavior of Alkali and Alkaline Earth Metals in Nonaqueous Battery Systems—The Solid Electrolyte Interphase Model", *Journal of The Electrochemical Society* **1979**, *126*, 2047–2051, DOI 10.1149/1.2128859.

[71] E. Peled, D. Golodnitsky, G. Ardel, V. Eshkenazy, "The SEI model—application to lithium-polymer electrolyte batteries", *Electrochimica Acta* **1995**, *40*, 2197–2204, DOI 10.1016/0013-4686(95)00163-9.

[72] E. Peled, D. Golodnitsky, G. Ardel, "Advanced Model for Solid Electrolyte Interphase Electrodes in Liquid and Polymer Electrolytes", *Journal of The Electrochemical Society* **1997**, *144*, L208–L210, DOI 10.1149/1.1837858.

[73] D. Aurbach, Y. Ein-Ely, A. Zaban, "The Surface Chemistry of Lithium Electrodes in Alkyl Carbonate Solutions", *Journal of The Electrochemical Society* **1994**, *141*, L1–L3, DOI 10.1149/1.2054718.

[74] D. Aurbach, B. Markovsky, M. Levi, E. Levi, A. Schechter, M. Moshkovich, Y. Cohen, "New insights into the interactions between electrode materials and electrolyte solutions for advanced nonaqueous batteries", *Journal of Power Sources* **1999**, *81-82*, 95–111, DOI 10.1016/S0378-7753(99)00187-1.

[75] D. Aurbach, "Review of selected electrode–solution interactions which determine the performance of Li and Li ion batteries", *Journal of Power Sources* **2000**, *89*, 206–218, DOI 10.1016/S0378-7753(00)00431-6.

[76] S. J. An, J. Li, C. Daniel, D. Mohanty, S. Nagpure, D. L. Wood, "The state of understanding of the lithium-ion-battery graphite solid electrolyte interphase (SEI) and its relationship to formation cycling", *Carbon* **2016**, *105*, 52–76, DOI 10.1016/j.carbon.2016.04.008.

[77] S. H. Beheshti, M. Javanbakht, H. Omidvar, M. S. Hosen, A. Hubin, J. Van Mierlo, M. Berecibar, "Development, retainment, and assessment of the graphite-electrolyte interphase in Li-ion batteries regarding the functionality of SEI-forming additives", *iScience* **2022**, *25*, 103862, DOI 10.1016/j.isci.2022.103862.

[78] C. Han, Y.-B. He, M. Liu, B. Li, Q.-H. Yang, C.-P. Wong, F. Kang, "A review of gassing behavior in Li 4 Ti 5 O 12 -based lithium ion batteries", *Journal of Materials Chemistry A* **2017**, *5*, 6368–6381, DOI 10.1039/C7TA00303J.

[79] X. Cheng, R. Zhang, C. Zhao, F. Wei, J. Zhang, Q. Zhang, "A Review of Solid Electrolyte Interphases on Lithium Metal Anode", *Advanced Science* **2016**, *3*, 1–20, DOI 10.1002/advs.201500213.

[80] H. Wu, H. Jia, C. Wang, J. Zhang, W. Xu, "Recent Progress in Understanding Solid Electrolyte Interphase on Lithium Metal Anodes", *Advanced Energy Materials* **2021**, *11*, 1–35, DOI 10.1002/aenm.202003092.

[81] B. Wu, C. Chen, L. H. Raijmakers, J. Liu, D. L. Danilov, R.-A. Eichel, P. H. Notten, "Li-growth and SEI engineering for anode-free Li-metal rechargeable batteries: A review of current advances", *Energy Storage Materials* **2023**, *57*, 508–539, DOI 10.1016/j.ensm.2023.02.036.

[82] Z. Shen, J. Huang, Y. Xie, D. Wei, J. Chen, Z. Shi, "Solid Electrolyte Interphase on Lithium Metal Anodes", *ChemSusChem* **2024**, *17*, DOI 10.1002/cssc.202301777.

[83] Y. Zhang, N. Du, D. Yang, "Designing superior solid electrolyte interfaces on silicon anodes for high-performance lithium-ion batteries", *Nanoscale* **2019**, *11*, 19086–19104, DOI 10.1039/C9NR05748J.

[84] J. Kim, O. B. Chae, B. L. Lucht, "Perspective—Structure and Stability of the Solid Electrolyte Interphase on Silicon Anodes of Lithium-ion Batteries", *Journal of The Electrochemical Society* **2021**, *168*, 030521, DOI 10.1149/1945-7111/abe984.

[85] Q. Man, Y. An, C. Liu, H. Shen, S. Xiong, J. Feng, "Interfacial design of silicon/carbon anodes for rechargeable batteries: A review", *Journal of Energy Chemistry* **2023**, *76*, 576–600, DOI 10.1016/j.jechem.2022.09.020.

[86] J. B. Goodenough, Y. Kim, "Challenges for Rechargeable Li Batteries", *Chemistry of Materials* **2010**, *22*, 587–603, DOI 10.1021/cm901452z.

[87] B. Horstmann, F. Single, A. Latz, "Review on multi-scale models of solid-electrolyte interphase formation", *Current Opinion in Electrochemistry* **2019**, *13*, 61–69, DOI 10.1016/j.coelec.2018.10.013.

[88] F. Single, B. Horstmann, A. Latz, "Revealing SEI Morphology: In-Depth Analysis of a Modeling Approach", *Journal of The Electrochemical Society* **2017**, *164*, E3132–E3145, DOI 10.1149/2.0121711jes.

[89] F. Single, A. Latz, B. Horstmann, "Identifying the Mechanism of Continued Growth of the Solid–Electrolyte Interphase", *ChemSusChem* **2018**, *11*, 1950–1955, DOI 10.1002/cssc.201800077.

[90] S. K. Heiskanen, J. Kim, B. L. Lucht, "Generation and Evolution of the Solid Electrolyte Interphase of Lithium-Ion Batteries", *Joule* **2019**, *3*, 2322–2333, DOI 10.1016/j.joule.2019.08.018.

[91] L. Alzate-Vargas, S. M. Blau, E. W. C. Spotte-Smith, S. Allu, K. A. Persson, J.-L. Fattebert, "Insight into SEI Growth in Li-Ion Batteries using Molecular Dynamics and Accelerated Chemical Reactions", *The Journal of Physical Chemistry C* **2021**, *125*, 18588–18596, DOI 10.1021/acs.jpcc.1c04149.

[92] E. W. C. Spotte-Smith, R. L. Kam, D. Barter, X. Xie, T. Hou, S. Dwaraknath, S. M. Blau, K. A. Persson, "Toward a Mechanistic Model of Solid–Electrolyte Interphase Formation and Evolution in Lithium-Ion Batteries", *ACS Energy Letters* **2022**, *7*, 1446–1453, DOI 10.1021/acsenergylett.2c00517.

[93] J. Wagner-Henke, D. Kuai, M. Gerasimov, F. Röder, P. B. Balbuena, U. Krewer, "Knowledge-driven design of solid-electrolyte interphases on lithium metal via multi-scale modelling", *Nature Communications* **2023**, *14*, 6823, DOI 10.1038/s41467-023-42212-7.

[94] K. Xu, A. von Cresce, "Interfacing electrolytes with electrodes in Li ion batteries", *Journal of Materials Chemistry* **2011**, *21*, 9849, DOI 10.1039/c0jm04309e.

[95] A. von Wald Cresce, O. Borodin, K. Xu, "Correlating Li + Solvation Sheath Structure with Interphasial Chemistry on Graphite", *The Journal of Physical Chemistry C* **2012**, *116*, 26111–26117, DOI 10.1021/jp303610t.

[96] A. Weng, P. Mohtat, P. M. Attia, V. Sulzer, S. Lee, G. Less, A. Stefanopoulou, "Predicting the impact of formation protocols on battery lifetime immediately after manufacturing", *Joule* **2021**, *5*, 2971–2992, DOI 10.1016/j.joule.2021.09.015.

[97] B. K. Antonopoulos, C. Stock, F. Maglia, H. E. Hoster, "Solid electrolyte interphase: Can faster formation at lower potentials yield better performance?", *Electrochimica Acta* **2018**, *269*, 331–339, DOI 10.1016/j.electacta.2018.03.007.

[98] F. Schomburg, B. Heidrich, S. Wennemar, R. Drees, T. Roth, M. Kurrat, H. Heimes, A. Jossen, M. Winter, J. Y. Cheong, F. Röder, "Lithium-ion battery cell formation: status and future directions towards a knowledge-based process design", *Energy & Environmental Science* **2024**, *17*, 2686–2733, DOI 10.1039/D3EE03559J.

[99] D. Witt, L. Bläubaum, F. Baakes, U. Krewer, "Origin of Performance Improvements in Lithium-Ion Cells after Fast Formation", *Batteries & Supercaps* **2024**, *7*, e202400023, DOI 10.1002/batt.202400023.

[100] P. Keil, A. Jossen, "Calendar Aging of NCA Lithium-Ion Batteries Investigated by Differential Voltage Analysis and Coulomb Tracking", *Journal of The Electrochemical Society* **2017**, *164*, A6066–A6074, DOI 10.1149/2.0091701jes.

[101] H.-L. Zhang, F. Li, C. Liu, J. Tan, H.-M. Cheng, "New Insight into the Solid Electrolyte Interphase with Use of a Focused Ion Beam", *The Journal of Physical Chemistry B* **2005**, *109*, 22205–22211, DOI 10.1021/jp053311a.

[102] F. Single, B. Horstmann, A. Latz, "Dynamics and morphology of solid electrolyte interphase (SEI)", *Physical Chemistry Chemical Physics* **2016**, *18*, 17810–17814, DOI 10.1039/C6CP02816K.

[103] Y. Li, Y. Li, A. Pei, K. Yan, Y. Sun, C.-L. Wu, L.-M. Joubert, R. Chin, A. L. Koh, Y. Yu, J. Perrino, B. Butz, S. Chu, Y. Cui, "Atomic structure of sensitive battery materials and interfaces revealed by cryo–electron microscopy", *Science* **2017**, *358*, 506–510, DOI 10.1126/science.aam6014.

[104] M. Gerasimov, F. A. Soto, J. Wagner, F. Baakes, N. Guo, F. Ospina-Acevedo, F. Röder, P. B. Balbuena, U. Krewer, "Species Distribution During Solid Electrolyte Interphase Formation on Lithium Using MD/DFT-Parameterized Kinetic Monte Carlo Simulations", *The Journal of Physical Chemistry C* **2023**, *127*, 4872–4886, DOI 10.1021/acs.jpcc.2c05898.

[105] J. Pan, Q. Zhang, X. Xiao, Y.-T. Cheng, Y. Qi, "Design of Nanostructured Heterogeneous Solid Ionic Coatings through a Multiscale Defect Model", *ACS Applied Materials & Interfaces* **2016**, *8*, 5687–5693, DOI 10.1021/acsami.5b12030.

[106] Q. Zhang, J. Pan, P. Lu, Z. Liu, M. W. Verbrugge, B. W. Sheldon, Y.-T. Cheng, Y. Qi, X. Xiao, "Synergetic Effects of Inorganic Components in Solid Electrolyte Interphase on High Cycle Efficiency of Lithium Ion Batteries", *Nano Letters* **2016**, *16*, 2011–2016, DOI 10.1021/acs.nanolett.5b05283.

[107] Y. Li, W. Huang, Y. Li, A. Pei, D. T. Boyle, Y. Cui, "Correlating Structure and Function of Battery Interphases at Atomic Resolution Using Cryoelectron Microscopy", *Joule* **2018**, *2*, 2167–2177, DOI 10.1016/j.joule.2018.08.004.

[108] Y. Xu, H. Wu, H. Jia, J.-G. Zhang, W. Xu, C. Wang, "Current Density Regulated Atomic to Nanoscale Process on Li Deposition and Solid Electrolyte Interphase Revealed by Cryogenic Transmission Electron Microscopy", *ACS Nano* **2020**, *14*, 8766–8775, DOI 10.1021/acsnano.0c03344.

[109] Y. Xu, H. Wu, Y. He, Q. Chen, J.-G. Zhang, W. Xu, C. Wang, "Atomic to Nanoscale Origin of Vinylene Carbonate Enhanced Cycling Stability of Lithium Metal Anode Revealed by Cryo-Transmission Electron Microscopy", *Nano Letters* **2020**, *20*, 418–425, DOI 10.1021/acs.nanolett.9b04111.

[110] J. Wang, W. Huang, A. Pei, Y. Li, F. Shi, X. Yu, Y. Cui, "Improving cyclability of Li metal batteries at elevated temperatures and its origin revealed by cryo-electron microscopy", *Nature Energy* **2019**, *4*, 664–670, DOI 10.1038/s41560-019-0413-3.

[111] W. Huang, H. Wang, D. T. Boyle, Y. Li, Y. Cui, "Resolving Nanoscopic and Mesoscopic Heterogeneity of Fluorinated Species in Battery Solid-Electrolyte Interphases by Cryogenic Electron Microscopy", *ACS Energy Letters* **2020**, *5*, 1128–1135, DOI 10.1021/acsenergylett.0c00194.

[112] W. Huang, J. Wang, M. R. Braun, Z. Zhang, Y. Li, D. T. Boyle, P. C. McIntyre, Y. Cui, "Dynamic Structure and Chemistry of the Silicon Solid-Electrolyte Interphase Visualized by Cryogenic Electron Microscopy", *Matter* **2019**, *1*, 1232–1245, DOI 10.1016/j.matt.2019.09.020.

[113] W. Huang, P. M. Attia, H. Wang, S. E. Renfrew, N. Jin, S. Das, Z. Zhang, D. T. Boyle, Y. Li, M. Z. Bazant, B. D. McCloskey, W. C. Chueh, Y. Cui, "Evolution of the Solid–Electrolyte Interphase on Carbonaceous Anodes Visualized by Atomic-Resolution Cryogenic Electron Microscopy", *Nano Letters* **2019**, *19*, 5140–5148, DOI 10.1021/acs.nanolett.9b01515.

[114] A. V. Cresce, S. M. Russell, D. R. Baker, K. J. Gaskell, K. Xu, "In Situ and Quantitative Characterization of Solid Electrolyte Interphases", *Nano Letters* **2014**, *14*, 1405–1412, DOI 10.1021/nl404471v.

[115] J. Zheng, H. Zheng, R. Wang, L. Ben, W. Lu, L. Chen, L. Chen, H. Li, "3D visualization of inhomogeneous multi-layered structure and Young's modulus of the solid electrolyte interphase (SEI) on silicon anodes for lithium ion batteries", *Phys. Chem. Chem. Phys.* **2014**, *16*, 13229–13238, DOI 10.1039/C4CP01968G.

[116] L. J. Bolay, T. Schmitt, S. Hein, O. S. Mendoza-Hernandez, E. Hosono, D. Asakura, K. Kinoshita, H. Matsuda, M. Umeda, Y. Sone, A. Latz, B. Horstmann, "Microstructure-resolved degradation simulation of lithium-ion batteries in space applications", *Journal of Power Sources Advances* **2022**, *14*, 100083, DOI 10.1016/j.powera.2022.100083.

[117] P. G. Kitz, M. J. Lacey, P. Novák, E. J. Berg, "Operando investigation of the solid electrolyte interphase mechanical and transport properties formed from vinylene carbonate and fluoroethylene carbonate", *Journal of Power Sources* **2020**, *477*, 228567, DOI 10.1016/j.jpowsour.2020.228567.

[118] Y. Surace, D. Leanza, M. Mirolo, Ł. Kondracki, C. Vaz, M. El Kazzi, P. Novák, S. Trabesinger, "Evidence for stepwise formation of solid electrolyte interphase in a Li-ion battery", *Energy Storage Materials* **2022**, *44*, 156–167, DOI 10.1016/j.ensm.2021.10.013.

[119] J. E. N. Swallow, M. W. Fraser, N.-j. H. Kneusels, J. F. Charlton, C. G. Sole, C. M. E. Phelan, E. Björklund, P. Bencok, C. Escudero, V. Pérez-Dieste, C. P. Grey, R. J. Nicholls, R. S. Weatherup, "Revealing solid electrolyte interphase formation through interface-sensitive Operando X-ray absorption spectroscopy", *Nature Communications* **2022**, *13*, 6070, DOI 10.1038/s41467-022-33691-1.

[120] K. Geuder, S. Klick, P. Finster, K. M. Graff, M. Winter, S. Nowak, H. J. Seifert, C. Ziebert, "Influence of Vinylene Carbonate and Fluoroethylene Carbonate on Open Circuit and Floating SoC Calendar Aging of Lithium-Ion Batteries", *Batteries* **2024**, *10*, 275, DOI 10.3390/batteries10080275.

[121] M. He, R. Guo, G. M. Hobold, H. Gao, B. M. Gallant, "The intrinsic behavior of lithium fluoride in solid electrolyte interphases on lithium", *Proceedings of the National Academy of Sciences* **2020**, *117*, 73–79, DOI 10.1073/pnas.1911017116.

[122] G. M. Hobold, C. Wang, K. Steinberg, Y. Li, B. M. Gallant, "High lithium oxide prevalence in the lithium solid–electrolyte interphase for high Coulombic efficiency", *Nature Energy* **2024**, *9*, 580–591, DOI 10.1038/s41560-024-01494-x.

[123] M. Broussely, S. Herreyre, P. Biensan, P. Kasztejna, K. Nechev, R. Staniewicz, "Aging mechanism in Li ion cells and calendar life predictions", *Journal of Power Sources* **2001**, *97-98*, 13–21, DOI 10.1016/S0378-7753(01)00722-4.

[124] A. J. Smith, J. C. Burns, X. Zhao, D. Xiong, J. R. Dahn, "A High Precision Coulometry Study of the SEI Growth in Li/Graphite Cells", *Journal of The Electrochemical Society* **2011**, *158*, A447, DOI 10.1149/1.3557892.

[125] J. Wang, J. Purewal, P. Liu, J. Hicks-Garner, S. Soukazian, E. Sherman, A. Sorenson, L. Vu, H. Tataria, M. W. Verbrugge, "Degradation of lithium ion batteries employing graphite negatives and nickel–cobalt–manganese oxide + spinel manganese oxide positives: Part 1, aging mechanisms and life estimation", *Journal of Power Sources* **2014**, *269*, 937–948, DOI 10.1016/j.jpowsour.2014.07.030.

[126] P. Keil, S. F. Schuster, J. Wilhelm, J. Travi, A. Hauser, R. C. Karl, A. Jossen, "Calendar Aging of Lithium-Ion Batteries", *Journal of The Electrochemical Society* **2016**, *163*, A1872–A1880, DOI 10.1149/2.0411609jes.

[127] A. Karger, J. Schmitt, C. Kirst, J. P. Singer, L. Wildfeuer, A. Jossen, "Mechanistic calendar aging model for lithium-ion batteries", *Journal of Power Sources* **2023**, *578*, 233208, DOI 10.1016/j.jpowsour.2023.233208.

[128] L. Wildfeuer, A. Karger, D. Aygül, N. Wassiliadis, A. Jossen, M. Lienkamp, "Experimental degradation study of a commercial lithium-ion battery", *Journal of Power Sources* **2023**, *560*, 232498, DOI 10.1016/j.jpowsour.2022.232498.

[129] K. Bischof, M. Flügel, M. Hölzle, M. Wohlfahrt-Mehrens, T. Waldmann, "Aging Mechanism For Calendar Aging of Li-Ion Cells With Si/Graphite Anodes", *Journal of The Electrochemical Society* **2024**, *171*, 010510, DOI 10.1149/1945-7111/ad1b7c.

[130] D. Werner, S. Paarmann, T. Wetzel, "Calendar Aging of Li-Ion Cells – Experimental Investigation and Empirical Correlation", *Batteries* **2021**, *7*, 28, DOI 10.3390/batteries7020028.

[131] D. Li, D. Danilov, Z. Zhang, H. Chen, Y. Yang, P. H. L. Notten, "Modeling the SEI-Formation on Graphite Electrodes in LiFePO 4 Batteries", *Journal of The Electrochemical Society* **2015**, *162*, A858–A869, DOI 10.1149/2.0161506jes.

[132] D. Li, D. L. Danilov, J. Xie, L. Raijmakers, L. Gao, Y. Yang, P. H. Notten, "Degradation Mechanisms of C6/LiFePO4 Batteries: Experimental Analyses of Calendar Aging", *Electrochimica Acta* **2016**, *190*, 1124–1133, DOI 10.1016/j.electacta.2015.12.161.

[133] S Ramasubramanian, F Schomburg, F Röder, "Modelling of solid electrolyte interphase growth using neural ordinary differential equations", *Electrochimica Acta* **2024**, *473*, 143479, DOI 10.1016/j.electacta.2023.143479.

[134] S. Shi, P. Lu, Z. Liu, Y. Qi, L. G. Hector, H. Li, S. J. Harris, "Direct Calculation of Li-Ion Transport in the Solid Electrolyte Interphase", *Journal of the American Chemical Society* **2012**, *134*, 15476–15487, DOI 10.1021/ja305366r.

[135] S. Shi, Y. Qi, H. Li, L. G. Hector, "Defect Thermodynamics and Diffusion Mechanisms in Li 2 CO 3 and Implications for the Solid Electrolyte Interphase in Li-Ion Batteries", *The Journal of Physical Chemistry C* **2013**, *117*, 8579–8593, DOI 10.1021/jp310591u.

[136] F. A. Soto, Y. Ma, J. M. Martinez de la Hoz, J. M. Seminario, P. B. Balbuena, "Formation and Growth Mechanisms of Solid-Electrolyte Interphase Layers in Rechargeable Batteries", *Chemistry of Materials* **2015**, *27*, 7990–8000, DOI 10.1021/acs.chemmater.5b03358.

[137] L. von Kolzenberg, J. Stadler, J. Fath, M. Ecker, B. Horstmann, A. Latz, "A four parameter model for the solid-electrolyte interphase to predict battery aging during operation", *Journal of Power Sources* **2022**, *539*, 231560, DOI 10.1016/j.jpowsour.2022.231560.

[138] F. T. Krauss, I. Pantenburg, V. Lehmann, M. Stich, J. O. Weiershäuser, A. Bund, B. Roling, "Elucidating the Transport of Electrons and Molecules in a Solid Electrolyte Interphase Close to Battery Operation Potentials Using a Four-Electrode-Based Generator–Collector Setup", *Journal of the American Chemical Society* **2024**, *146*, 19009–19018, DOI 10.1021/jacs.4c03029.

[139] Y. Xu, H. Jia, P. Gao, D. E. Galvez-Aranda, S. P. Beltran, X. Cao, P. M. L. Le, J. Liu, M. H. Engelhard, S. Li, G. Ren, J. M. Seminario, P. B. Balbuena, J.-g. Zhang, W. Xu, C. Wang, "Direct in situ measurements of electrical properties of solid–electrolyte interphase on lithium metal anodes", *Nature Energy* **2023**, *8*, 1345–1354, DOI 10.1038/s41560-023-01361-1.

[140] H. J. Ploehn, P. Ramadass, R. E. White, "Solvent Diffusion Model for Aging of Lithium-Ion Battery Cells", *Journal of The Electrochemical Society* **2004**, *151*, A456, DOI 10.1149/1.1644601.

[141] R. P. Ramasamy, J.-W. Lee, B. N. Popov, "Simulation of capacity loss in carbon electrode for lithium-ion cells during storage", *Journal of Power Sources* **2007**, *166*, 266–272, DOI 10.1016/j.jpowsour.2006.12.086.

[142] S. Sankarasubramanian, B. Krishnamurthy, "A capacity fade model for lithium-ion batteries including diffusion and kinetics", *Electrochimica Acta* **2012**, *70*, 248–254, DOI 10.1016/j.electacta.2012.03.063.

[143] M. Tang, S. Lu, J. Newman, "Experimental and Theoretical Investigation of Solid-Electrolyte-Interphase Formation Mechanisms on Glassy Carbon", *Journal of The Electrochemical Society* **2012**, *159*, A1775–A1785, DOI 10.1149/2.025211jes.

[144] M. Tang, J. Newman, "Transient Characterization of Solid-Electrolyte-Interphase Using Ferrocene", *Journal of The Electrochemical Society* **2012**, *159*, A281–A289, DOI 10.1149/2.073203jes.

[145] M. B. Pinson, M. Z. Bazant, "Theory of SEI Formation in Rechargeable Batteries: Capacity Fade, Accelerated Aging and Lifetime Prediction", *Journal of The Electrochemical Society* **2013**, *160*, A243–A250, DOI 10.1149/2.044302jes.

[146] F. Hao, Z. Liu, P. B. Balbuena, P. P. Mukherjee, "Mesoscale Elucidation of Solid Electrolyte Interphase Layer Formation in Li-Ion Battery Anode", *The Journal of Physical Chemistry C* **2017**, *121*, 26233–26240, DOI 10.1021/acs.jpcc.7b09465.

[147] T. Kranz, S. Kranz, V. Miß, J. Schepp, B. Roling, "Interrelation between Redox Molecule Transport and Li + Ion Transport across a Model Solid Electrolyte Interphase Grown on a Glassy Carbon Electrode", *Journal of The Electrochemical Society* **2017**, *164*, A3777–A3784, DOI 10.1149/2.1171714jes.

[148] S. Kranz, T. Kranz, A. G. Jaegermann, B. Roling, "Is the solid electrolyte interphase in lithium-ion batteries really a solid electrolyte? Transport experiments on lithium bis(oxalato)borate-based model interphases", *Journal of Power Sources* **2019**, *418*, 138–146, DOI 10.1016/j.jpowsour.2019.01.060.

[149] F. T. Krauss, I. Pantenburg, B. Roling, "Transport of Ions, Molecules, and Electrons across the Solid Electrolyte Interphase: What Is Our Current Level of Understanding?", *Advanced Materials Interfaces* **2022**, *9*, 2101891, DOI 10.1002/admi.202101891.

[150] F. Brosa Planella, W. D. Widanage, "A Single Particle model with electrolyte and side reactions for degradation of lithium-ion batteries", *Applied Mathematical Modelling* **2023**, *121*, 586–610, DOI 10.1016/j.apm.2022.12.009.

[151] M. Esmaeilpour, S. Jana, H. Li, M. Soleymanibrojeni, W. Wenzel, "A Solution-Mediated Pathway for the Growth of the Solid Electrolyte Interphase in Lithium-Ion Batteries", *Advanced Energy Materials* **2023**, *13*, DOI 10.1002/aenm.202203966.

[152] Z. Zhang, Y. Li, R. Xu, W. Zhou, Y. Li, S. T. Oyakhire, Y. Wu, J. Xu, H. Wang, Z. Yu, D. T. Boyle, W. Huang, Y. Ye, H. Chen, J. Wan, Z. Bao, W. Chiu, Y. Cui, "Capturing the swelling of solid-electrolyte interphase in lithium metal batteries", *Science* **2022**, *375*, 66–70, DOI 10.1126/science.abi8703.

[153] L. Köbbing, A. Latz, B. Horstmann, "Growth of the solid-electrolyte interphase: Electron diffusion versus solvent diffusion", *Journal of Power Sources* **2023**, *561*, 232651, DOI 10.1016/j.jpowsour.2023.232651.

[154] P. M. Attia, S. Das, S. J. Harris, M. Z. Bazant, W. C. Chueh, "Electrochemical Kinetics of SEI Growth on Carbon Black: Part I. Experiments", *Journal of The Electrochemical Society* **2019**, *166*, E97–E106, DOI 10.1149/2.0231904jes.

[155] S. Das, P. M. Attia, W. C. Chueh, M. Z. Bazant, "Electrochemical Kinetics of SEI Growth on Carbon Black: Part II. Modeling", *Journal of The Electrochemical Society* **2019**, *166*, E107–E118, DOI 10.1149/2.0241904jes.

[156] J. M. Reniers, G. Mulder, D. A. Howey, "Review and Performance Comparison of Mechanical-Chemical Degradation Models for Lithium-Ion Batteries", *Journal of The Electrochemical Society* **2019**, *166*, A3189–A3200, DOI 10.1149/2.0281914jes.

[157] A. Karger, J. Schmitt, C. Kirst, J. P. Singer, L. Wildfeuer, A. Jossen, "Mechanistic cycle aging model for the open-circuit voltage curve of lithium-ion batteries", *Journal of Power Sources* **2024**, *593*, 233947, DOI 10.1016/j.jpowsour.2023.233947.

[158] L. von Kolzenberg, A. Latz, B. Horstmann, "Solid–Electrolyte Interphase During Battery Cycling: Theory of Growth Regimes", *ChemSusChem* **2020**, *13*, 3901–3910, DOI 10.1002/cssc.202000867.

[159] A. J. Smith, H. M. Dahn, J. C. Burns, J. R. Dahn, "Long-Term Low-Rate Cycling of LiCoO 2 /Graphite Li-Ion Cells at 55°C", *Journal of The Electrochemical Society* **2012**, *159*, A705–A710, DOI 10.1149/2.056206jes.

[160] J. Stadler, J. P. Fath, M. Ecker, A. Latz, "Combining a Data Driven and Mechanistic Model to Predict Capacity and Potential-Curve Degradation", *Batteries & Supercaps* **2024**, *279*, 4510–4524, DOI 10.1002/batt.202400211.

[161] M. Tanaka, J. B. Hooper, D. Bedrov, "Role of Plasticity in Mechanical Failure of Solid Electrolyte Interphases on Nanostructured Silicon Electrode: Insight from Continuum Level Modeling", *ACS Applied Energy Materials* **2018**, *1*, 1858–1863, DOI 10.1021/acsaem.8b00344.

[162] M. Y. Jin, K. Guo, X. Xiao, M. W. Verbrugge, H. Gao, B. W. Sheldon, "Optimum Particle Size in Silicon Electrodes Dictated by Chemomechanical Deformation of the SEI", *Advanced Functional Materials* **2021**, *31*, 2010640, DOI 10.1002/adfm.202010640.

[163] W. Zhang, T. H. Cai, B. W. Sheldon, "The Impact of Initial SEI Formation Conditions on Strain-Induced Capacity Losses in Silicon Electrodes", *Advanced Energy Materials* **2019**, *9*, 1–15, DOI 10.1002/aenm.201803066.

[164] K. Guo, R. Kumar, X. Xiao, B. W. Sheldon, H. Gao, "Failure progression in the solid electrolyte interphase (SEI) on silicon electrodes", *Nano Energy* **2020**, *68*, 104257, DOI 10.1016/j.nanoen.2019.104257.

[165] J. Lee, J.-y. Jeong, J. Ha, Y.-t. Kim, J. Choi, "Understanding solid electrolyte interface formation on graphite and silicon anodes in lithium-ion batteries: Exploring the role of fluoroethylene carbonate", *Electrochemistry Communications* **2024**, *163*, 107708, DOI 10.1016/j.elecom.2024.107708.

[166] Q. Li, X. Liu, X. Han, Y. Xiang, G. Zhong, J. Wang, B. Zheng, J. Zhou, Y. Yang, "Identification of the Solid Electrolyte Interface on the Si/C Composite Anode with FEC as the Additive", *ACS Applied Materials & Interfaces* **2019**, *11*, 14066–14075, DOI 10.1021/acsami.8b22221.

[167] J. Chen, X. Fan, Q. Li, H. Yang, M. R. Khoshi, Y. Xu, S. Hwang, L. Chen, X. Ji, C. Yang, H. He, C. Wang, E. Garfunkel, D. Su, O. Borodin, C. Wang, "Electrolyte design for LiF-rich solid–electrolyte interfaces to enable high-performance microsized alloy anodes for batteries", *Nature Energy* **2020**, *5*, 386–397, DOI 10.1038/s41560-020-0601-1.

[168] K. W. Schroder, A. G. Dylla, S. J. Harris, L. J. Webb, K. J. Stevenson, "Role of Surface Oxides in the Formation of Solid–Electrolyte Interphases at Silicon Electrodes for Lithium-Ion Batteries", *ACS Applied Materials & Interfaces* **2014**, *6*, 21510–21524, DOI 10.1021/am506517j.

[169] C. Cao, I. I. Abate, E. Sivonxay, B. Shyam, C. Jia, B. Moritz, T. P. Devereaux, K. A. Persson, H.-G. Steinrück, M. F. Toney, "Solid Electrolyte Interphase on Native Oxide-Terminated Silicon Anodes for Li-Ion Batteries", *Joule* **2019**, *3*, 762–781, DOI 10.1016/j.joule.2018.12.013.

[170] Y. He, L. Jiang, T. Chen, Y. Xu, H. Jia, R. Yi, D. Xue, M. Song, A. Genc, C. Bouchet-Marquis, L. Pullan, T. Tessner, J. Yoo, X. Li, J.-G. Zhang, S. Zhang, C. Wang, "Progressive growth of the solid–electrolyte interphase towards the Si anode interior causes capacity fading", *Nature Nanotechnology* **2021**, *16*, 1113–1120, DOI 10.1038/s41565-021-00947-8.

[171] H. Huo, J. Janek, "Silicon as Emerging Anode in Solid-State Batteries", *ACS Energy Letters* **2022**, *7*, 4005–4016, DOI 10.1021/acsenergylett.2c01950.

[172] H. Huo, M. Jiang, Y. Bai, S. Ahmed, K. Volz, H. Hartmann, A. Henss, C. V. Singh, D. Raabe, J. Janek, "Chemo-mechanical failure mechanisms of the silicon anode in solid-state batteries", *Nature Materials* **2024**, *23*, 543–551, DOI 10.1038/s41563-023-01792-x.

[173] L. Köbbing, A. Latz, B. Horstmann, "Voltage Hysteresis of Silicon Nanoparticles: Chemo-Mechanical Particle-SEI Model", *Advanced Functional Materials* **2024**, *34*, 2308818, DOI 10.1002/adfm.202308818.

[174] L. Köbbing, Y. Kuhn, B. Horstmann, "Slow Voltage Relaxation of Silicon Nanoparticles with a Chemo-Mechanical Core–Shell Model", *ACS Applied Materials & Interfaces* **2024**, *16*, 67609–67619, DOI 10.1021/acsami.4c12976.

[175] V. Kuznetsov, A.-H. Zinn, G. Zampardi, S. Borhani-Haghighi, F. La Mantia, A. Ludwig, W. Schuhmann, E. Ventosa, "Wet Nanoindentation of the Solid Electrolyte Interphase on Thin Film Si Electrodes", *ACS Applied Materials & Interfaces* **2015**, *7*, 23554–23563, DOI 10.1021/acsami.5b06700.

[176] I. Yoon, S. Jurng, D. P. Abraham, B. L. Lucht, P. R. Guduru, "Measurement of mechanical and fracture properties of solid electrolyte interphase on lithium metal anodes in lithium ion batteries", *Energy Storage Materials* **2020**, *25*, 296–304, DOI 10.1016/j.ensm.2019.10.009.

[177] M. Gu, A. M. Rao, J. Zhou, B. Lu, "In situ formed uniform and elastic SEI for high-performance batteries", *Energy & Environmental Science* **2023**, *16*, 1166–1175, DOI 10.1039/D2EE04148K.

[178] Y. Chen, W. Wu, S. Gonzalez-Munoz, L. Forcieri, C. Wells, S. P. Jarvis, F. Wu, R. Young, A. Dey, M. Isaacs, M. Nagarathinam, R. G. Palgrave, N. Tapia-Ruiz, O. V. Kolosov, "Nanoarchitecture factors of solid electrolyte interphase formation via 3D nano-rheology microscopy and surface force-distance spectroscopy", *Nature Communications* **2023**, *14*, 1321, DOI 10.1038/s41467-023-37033-7.

[179] H. Shin, J. Park, S. Han, A. M. Sastry, W. Lu, "Component-/structure-dependent elasticity of solid electrolyte interphase layer in Li-ion batteries: Experimental and computational studies", *Journal of Power Sources* **2015**, *277*, 169–179, DOI 10.1016/j.jpowsour.2014.11.120.

[180] I. A. Shkrob, J. F. Wishart, D. P. Abraham, "What Makes Fluoroethylene Carbonate Different?", *The Journal of Physical Chemistry C* **2015**, *119*, 14954–14964, DOI 10.1021/acs.jpcc.5b03591.

[181] Y. He, H. Hu, K. Zhang, S. Li, J. Chen, "Mechanical insights into the stability of heterogeneous solid electrolyte interphase on an electrode particle", *Journal of Materials Science* **2017**, *52*, 2836–2848, DOI 10.1007/s10853-016-0575-3.

[182] Y. Kamikawa, K. Amezawa, K. Terada, "Elastic–Plastic Deformation of a Solid Electrolyte Interface Formed by Reduction of Fluoroethylene Carbonate: A Nanoindentation and Finite Element Analysis Study", *The Journal of Physical Chemistry C* **2020**, *124*, 22488–22495, DOI 10.1021/acs.jpcc.0c06420.

[183] Y. Liu, X. Xu, O. O. Kapitanova, P. V. Evdokimov, Z. Song, A. Matic, S. Xiong, "Electro-Chemo-Mechanical Modeling of Artificial Solid Electrolyte Interphase to Enable Uniform Electrodeposition of Lithium Metal Anodes", *Advanced Energy Materials* **2022**, *12*, 2103589, DOI 10.1002/aenm.202103589.

[184] Q. Zhang, X. Xiao, W. Zhou, Y.-T. Cheng, M. W. Verbrugge, "Toward High Cycle Efficiency of Silicon-Based Negative Electrodes by Designing the Solid Electrolyte Interphase", *Advanced Energy Materials* **2015**, *5*, 1401398, DOI 10.1002/aenm.201401398.

[185] H. Zhang, D. Wang, C. Shen, "In-situ EC-AFM and ex-situ XPS characterization to investigate the mechanism of SEI formation in highly concentrated aqueous electrolyte for Li-ion batteries", *Applied Surface Science* **2020**, *507*, 145059, DOI 10.1016/j.apsusc.2019.145059.

[186] Y. Chai, W. Jia, Z. Hu, S. Jin, H. Jin, H. Ju, X. Yan, H. Ji, L.-J. Wan, "Monitoring the mechanical properties of the solid electrolyte interphase (SEI) using electrochemical quartz crystal microbalance with dissipation", *Chinese Chemical Letters* **2021**, *32*, 1139–1143, DOI 10.1016/j.cclet.2020.09.008.

[187] C. Q. Chen, Y. Shi, Y. S. Zhang, J. Zhu, Y. J. Yan, "Size Dependence of Young's Modulus in ZnO Nanowires", *Physical Review Letters* **2006**, *96*, 075505, DOI 10.1103/PhysRevLett.96.075505.

[188] A. Mathur, J. Erlebacher, "Size dependence of effective Young's modulus of nanoporous gold", *Applied Physics Letters* **2007**, *90*, 061910, DOI 10.1063/1.2436718.

[189] R. Agrawal, B. Peng, E. E. Gdoutos, H. D. Espinosa, "Elasticity Size Effects in ZnO Nanowires - A Combined Experimental-Computational Approach", *Nano Letters* **2008**, *8*, 3668–3674, DOI 10.1021/nl801724b.

[190] J. He, C. M. Lilley, "Surface Effect on the Elastic Behavior of Static Bending Nanowires", *Nano Letters* **2008**, *8*, 1798–1802, DOI 10.1021/nl0733233.

[191] Y. Chen, Q. Gao, Y. Wang, X. An, X. Liao, Y.-W. Mai, H. H. Tan, J. Zou, S. P. Ringer, C. Jagadish, "Determination of Young's Modulus of Ultrathin Nanomaterials", *Nano Letters* **2015**, *15*, 5279–5283, DOI 10.1021/acs.nanolett.5b01603.

[192] P. G. Kitz, M. J. Lacey, P. Novák, E. J. Berg, "Operando EQCM-D with Simultaneous in Situ EIS: New Insights into Interphase Formation in Li Ion Batteries", *Analytical Chemistry* **2019**, *91*, 2296–2303, DOI 10.1021/acs.analchem.8b04924.

[193] P. G. Kitz, P. Novák, E. J. Berg, "Influence of Water Contamination on the SEI Formation in Li-Ion Cells: An Operando EQCM-D Study", *ACS Applied Materials & Interfaces* **2020**, *12*, 15934–15942, DOI 10.1021/acsami.0c01642.

[194] R. Edgeworth, B. J. Dalton, T. Parnell, "The pitch drop experiment", *European Journal of Physics* **1984**, *5*, 198–200, DOI 10.1088/0143-0807/5/4/003.

[195] P. Sutardja, W. Oldham, "Modeling of stress effects in silicon oxidation", *IEEE Transactions on Electron Devices* **1989**, *36*, 2415–2421, DOI 10.1109/16.43661.

[196] V. Senez, D. Collard, B. Baccus, M. Brault, J. Lebailly, "Analysis and application of a viscoelastic model for silicon oxidation", *Journal of Applied Physics* **1994**, *76*, 3285–3296, DOI 10.1063/1.357450.

[197] M. I. Ojovan, "Viscosity and Glass Transition in Amorphous Oxides", *Advances in Condensed Matter Physics* **2008**, *2008*, 1–23, DOI 10.1155/2008/817829.

[198] M. T. McDowell, S. W. Lee, W. D. Nix, Y. Cui, "25th Anniversary Article: Understanding the Lithiation of Silicon and Other Alloying Anodes for Lithium-Ion Batteries", *Advanced Materials* **2013**, *25*, 4966–4985, DOI 10.1002/adma.201301795.

[199] D. Wycisk, G. K. Mertin, M. Oldenburger, A. Latz, "Analysis of heat generation due to open-circuit voltage hysteresis in lithium-ion cells", *Journal of Energy Storage* **2023**, *61*, 106817, DOI 10.1016/j.est.2023.106817.

[200] L. Baggetto, R. A. H. Niessen, F. Roozeboom, P. H. L. Notten, "High Energy Density All-Solid-State Batteries: A Challenging Concept Towards 3D Integration", *Advanced Functional Materials* **2008**, *18*, 1057–1066, DOI 10.1002/adfm.200701245.

[201] V. A. Sethuraman, M. J. Chon, M. Shimshak, V. Srinivasan, P. R. Guduru, "In situ measurements of stress evolution in silicon thin films during electrochemical lithiation and delithiation", *Journal of Power Sources* **2010**, *195*, 5062–5066, DOI 10.1016/j.jpowsour.2010.02.013.

[202] V. A. Sethuraman, V. Srinivasan, A. F. Bower, P. R. Guduru, "In Situ Measurements of Stress-Potential Coupling in Lithiated Silicon", *Journal of The Electrochemical Society* **2010**, *157*, A1253, DOI 10.1149/1.3489378.

[203] V. A. Sethuraman, V. Srinivasan, J. Newman, "Analysis of Electrochemical Lithiation and Delithiation Kinetics in Silicon", *Journal of The Electrochemical Society* **2013**, *160*, A394–A403, DOI 10.1149/2.008303jes.

[204] M. W. Verbrugge, D. R. Baker, X. Xiao, Q. Zhang, Y.-T. Cheng, "Experimental and Theoretical Characterization of Electrode Materials that Undergo Large Volume Changes and Application to the Lithium–Silicon System", *The Journal of Physical Chemistry C* **2015**, *119*, 5341–5349, DOI 10.1021/jp512585z.

[205] B. Lu, Y. Song, Q. Zhang, J. Pan, Y.-T. Cheng, J. Zhang, "Voltage hysteresis of lithium ion batteries caused by mechanical stress", *Physical Chemistry Chemical Physics* **2016**, *18*, 4721–4727, DOI 10.1039/C5CP06179B.

[206] D. R. Baker, M. W. Verbrugge, X. Xiao, "An approach to characterize and clarify hysteresis phenomena of lithium-silicon electrodes", *Journal of Applied Physics* **2017**, *122*, 165102, DOI 10.1063/1.4995277.

[207] C. K. Chan, H. Peng, G. Liu, K. McIlwrath, X. F. Zhang, R. A. Huggins, Y. Cui, "High-performance lithium battery anodes using silicon nanowires", *Nature Nanotechnology* **2008**, *3*, 31–35, DOI 10.1038/nnano.2007.411.

[208] H. Wu, G. Chan, J. W. Choi, I. Ryu, Y. Yao, M. T. McDowell, S. W. Lee, A. Jackson, Y. Yang, L. Hu, Y. Cui, "Stable cycling of double-walled silicon nanotube battery anodes through solid–electrolyte interphase control", *Nature Nanotechnology* **2012**, *7*, 310–315, DOI 10.1038/nnano.2012.35.

[209] V. L. Chevrier, L. Liu, D. B. Le, J. Lund, B. Molla, K. Reimer, L. J. Krause, L. D. Jensen, E. Figgemeier, K. W. Eberman, "Evaluating Si-Based Materials for Li-Ion Batteries in Commercially Relevant Negative Electrodes", *Journal of The Electrochemical Society* **2014**, *161*, A783–A791, DOI 10.1149/2.066405jes.

[210] A. Durdel, S. Friedrich, L. Hüsken, A. Jossen, "Modeling Silicon-Dominant Anodes: Parametrization, Discussion, and Validation of a Newman-Type Model", *Batteries* **2023**, *9*, 558, DOI 10.3390/batteries9110558.

[211] R. Chandrasekaran, A. Magasinski, G. Yushin, T. F. Fuller, "Analysis of Lithium Insertion/Deinsertion in a Silicon Electrode Particle at Room Temperature", *Journal of The Electrochemical Society* **2010**, *157*, A1139, DOI 10.1149/1.3474225.

[212] R. Chandrasekaran, T. F. Fuller, "Analysis of the Lithium-Ion Insertion Silicon Composite Electrode/Separator/Lithium Foil Cell", *Journal of The Electrochemical Society* **2011**, *158*, A859, DOI 10.1149/1.3589301.

[213] P. Bernard, J. P. Alper, C. Haon, N. Herlin-Boime, M. Chandesris, "Electrochemical analysis of silicon nanoparticle lithiation – Effect of crystallinity and carbon coating quantity", *Journal of Power Sources* **2019**, *435*, 226769, DOI 10.1016/j.jpowsour.2019.226769.

[214] K. Pan, F. Zou, M. Canova, Y. Zhu, J.-H. Kim, "Systematic electrochemical characterizations of Si and SiO anodes for high-capacity Li-Ion batteries", *Journal of Power Sources* **2019**, *413*, 20–28, DOI 10.1016/j.jpowsour.2018.12.010.

[215] K. Pan, "A Systematic Methodology for Characterization and Prediction of Performance of Si-based Materials for Li-ion Batteries", PhD thesis, Ohio State University, **2020**.

[216] D. Wycisk, G. K. Mertin, M. Oldenburger, O. von Kessel, A. Latz, "Challenges of open-circuit voltage measurements for silicon-containing Li-Ion cells", *Journal of Energy Storage* **2024**, *89*, 111617, DOI 10.1016/j.est.2024.111617.

[217] J. Schmalstieg, C. Rahe, M. Ecker, D. U. Sauer, "Full Cell Parameterization of a High-Power Lithium-Ion Battery for a Physico-Chemical Model: Part I. Physical and Electrochemical Parameters", *Journal of The Electrochemical Society* **2018**, *165*, A3799–A3810, DOI 10.1149/2.0321816jes.

[218] G. L. Plett, "Extended Kalman filtering for battery management systems of LiPB-based HEV battery packs", *Journal of Power Sources* **2004**, *134*, 262–276, DOI 10.1016/j.jpowsour.2004.02.032.

[219] C. P. Graells, M. S. Trimboli, G. L. Plett in 2020 IEEE Transportation Electrification Conference & Expo (ITEC), *Vol. 1*, IEEE, **2020**, pp. 175–180, DOI 10.1109/ITEC48692.2020.9161591.

[220] D. Wycisk, M. Oldenburger, M. G. Stoye, T. Mrkonjic, A. Latz, "Modified Plett-model for modeling voltage hysteresis in lithium-ion cells", *Journal of Energy Storage* **2022**, *52*, 105016, DOI 10.1016/j.est.2022.105016.

[221] A. Bower, P. Guduru, V. Sethuraman, "A finite strain model of stress, diffusion, plastic flow, and electrochemical reactions in a lithium-ion half-cell", *Journal of the Mechanics and Physics of Solids* **2011**, *59*, 804–828, DOI 10.1016/j.jmps.2011.01.003.

[222] C. V. Di Leo, E. Rejovitzky, L. Anand, "Diffusion–deformation theory for amorphous silicon anodes: The role of plastic deformation on electrochemical performance", *International Journal of Solids and Structures* **2015**, *67-68*, 283–296, DOI 10.1016/j.ijsolstr.2015.04.028.

[223] K. Zhao, M. Pharr, S. Cai, J. J. Vlassak, Z. Suo, "Large Plastic Deformation in High-Capacity Lithium-Ion Batteries Caused by Charge and Discharge", *Journal of the American Ceramic Society* **2011**, *94*, s226–s235, DOI 10.1111/j.1551-2916.2011.04432.x.

[224] Z. Cui, F. Gao, J. Qu, "Interface-reaction controlled diffusion in binary solids with applications to lithiation of silicon in lithium-ion batteries", *Journal of the Mechanics and Physics of Solids* **2013**, *61*, 293–310, DOI 10.1016/j.jmps.2012.11.001.

[225] Y. Jiang, G. Offer, J. Jiang, M. Marinescu, H. Wang, "Voltage Hysteresis Model for Silicon Electrodes for Lithium Ion Batteries, Including Multi-Step Phase Transformations, Crystallization and Amorphization", *Journal of The Electrochemical Society* **2020**, *167*, 130533, DOI 10.1149/1945-7111/abbbba.

[226] M. T. McDowell, S. W. Lee, J. T. Harris, B. A. Korgel, C. Wang, W. D. Nix, Y. Cui, "In Situ TEM of Two-Phase Lithiation of Amorphous Silicon Nanospheres", *Nano Letters* **2013**, *13*, 758–764, DOI 10.1021/nl3044508.

[227] X. Wang, S. S. Singh, T. Ma, C. Lv, N. Chawla, H. Jiang, "Quantifying Electrochemical Reactions and Properties of Amorphous Silicon in a Conventional Lithium-Ion Battery Configuration", *Chemistry of Materials* **2017**, *29*, 5831–5840, DOI 10.1021/acs.chemmater.7b00701.

[228] V. L. Deringer, N. Bernstein, G. Csányi, C. Ben Mahmoud, M. Ceriotti, M. Wilson, D. A. Drabold, S. R. Elliott, "Origins of structural and electronic transitions in disordered silicon", *Nature* **2021**, *589*, 59–64, DOI 10.1038/s41586-020-03072-z.

[229] K. Kitada, O. Pecher, P. C. M. M. Magusin, M. F. Groh, R. S. Weatherup, C. P. Grey, "Unraveling the Reaction Mechanisms of SiO Anodes for Li-Ion Batteries by Combining in Situ 7 Li and ex Situ 7 Li/ 29 Si Solid-State NMR Spectroscopy", *Journal of the American Chemical Society* **2019**, *141*, 7014–7027, DOI 10.1021/jacs.9b01589.

[230] J. Wang, X. Wang, B. Liu, H. Lu, G. Chu, J. Liu, Y.-G. Guo, X. Yu, F. Luo, Y. Ren, L. Chen, H. Li, "Size effect on the growth and pulverization behavior of Si nanodomains in SiO anode", *Nano Energy* **2020**, *78*, 105101, DOI 10.1016/j.nanoen.2020.105101.

[231] G. Holzapfel, *Nonlinear Solid Mechanics: A Continuum Approach for Engineering*, John Wiley & Sons, **2000**.

[232] S. R. de Groot, P. Mazur, *Non-Equilibrium Thermodynamics*, Dover Publications, New York, **1984**.

[233] G. Lebon, D. Jou, J. Casas-Vázquez, *Understanding Non-equilibrium Thermodynamics*, Springer-Verlag Berlin Heidelberg, **2008**.

[234] A. Latz, J. Zausch, "Thermodynamic consistent transport theory of Li-ion batteries", *Journal of Power Sources* **2011**, *196*, 3296–3302, DOI 10.1016/j.jpowsour.2010.11.088.

[235] A. Latz, J. Zausch, "Thermodynamic derivation of a Butler–Volmer model for intercalation in Li-ion batteries", *Electrochimica Acta* **2013**, *110*, 358–362, DOI 10.1016/j.electacta.2013.06.043.

[236] A. Latz, J. Zausch, "Multiscale modeling of lithium ion batteries: thermal aspects", *Beilstein Journal of Nanotechnology* **2015**, *6*, 987–1007, DOI 10.3762/bjnano.6.102.

[237] L. G. V. Kolzenberg, "Prolonging Lithium-Ion Battery Lifetime : How Operating Conditions Affect Solid Electrolyte Interphase Growth", PhD thesis, Ulm University, **2022**.

[238] T. F. Fuller, M. Doyle, J. Newman, "Simulation and Optimization of the Dual Lithium Ion Insertion Cell", *Journal of The Electrochemical Society* **1994**, *141*, 1–10, DOI 10.1149/1.2054684.

[239] M. Z. Bazant, "Theory of Chemical Kinetics and Charge Transfer based on Nonequilibrium Thermodynamics", *Accounts of Chemical Research* **2013**, *46*, 1144–1160, DOI 10.1021/ar300145c.

[240] M. Smeu, K. Leung, "Electron leakage through heterogeneous LiF on lithium-metal battery anodes", *Physical Chemistry Chemical Physics* **2021**, *23*, 3214–3218, DOI 10.1039/D0CP06310J.

[241] M. N. Obrovac, L. Christensen, D. B. Le, J. R. Dahn, "Alloy Design for Lithium-Ion Battery Anodes", *Journal of The Electrochemical Society* **2007**, *154*, A849, DOI 10.1149/1.2752985.

[242] R. Koerver, W. Zhang, L. de Biasi, S. Schweidler, A. O. Kondrakov, S. Kolling, T. Brezesinski, P. Hartmann, W. G. Zeier, J. Janek, "Chemo-mechanical expansion of lithium electrode materials – on the route to mechanically optimized all-solid-state batteries", *Energy & Environmental Science* **2018**, *11*, 2142–2158, DOI 10.1039/C8EE00907D.

[243] A. Verma, A. A. Franco, P. P. Mukherjee, "Mechanistic Elucidation of Si Particle Morphology on Electrode Performance", *Journal of The Electrochemical Society* **2019**, *166*, A3852–A3860, DOI 10.1149/2.0961915jes.

[244] F Garofalo, O Richmond, W. F. Domis, F. von Gemmingen, "Strain-Time, Rate-Stress and Rate-Temperature Relations during Large Deformations in Creep", *Proceedings of the Institution of Mechanical Engineers Conference Proceedings* **1963**, *178*, 31–39, DOI 10.1243/PIME_CONF_1963_178_010_02.

[245] E. T. Stang, "Constitutive Modeling of Creep in Leaded and Lead-Free Solder Alloys Using Constant Strain-Rate Tensile Testing", Master thesis, Wright State University, **2018**.

[246] P. M. Attia, W. C. Chueh, S. J. Harris, "Revisiting the t 0.5 Dependence of SEI Growth", *Journal of The Electrochemical Society* **2020**, *167*, 090535, DOI 10.1149/1945-7111/ab8ce4.

[247] S. I. Tan, B. S. Berry, B. L. Crowder, "Elastic and Anelastic Behavior of Ion-Implanted Silicon", *Applied Physics Letters* **1972**, *20*, 88–90, DOI 10.1063/1.1654060.

[248] M. D. Kluge, J. R. Ray, "Elastic constants and density of states of a molecular-dynamics model of amorphous silicon", *Physical Review B* **1988**, *37*, 4132–4136, DOI 10.1103/PhysRevB.37.4132.

[249] M. Szabadi, P. Hess, A. J. Kellock, H. Coufal, J. E. E. Baglin, "Elastic and mechanical properties of ion-implanted silicon determined by surface-acoustic-wave spectrometry", *Physical Review B* **1998**, *58*, 8941–8948, DOI 10.1103/PhysRevB.58.8941.

[250] V. Shenoy, P. Johari, Y. Qi, "Elastic softening of amorphous and crystalline Li–Si Phases with increasing Li concentration: A first-principles study", *Journal of Power Sources* **2010**, *195*, 6825–6830, DOI 10.1016/j.jpowsour.2010.04.044.

[251] D.-M. Tang, C.-L. Ren, M.-S. Wang, X. Wei, N. Kawamoto, C. Liu, Y. Bando, M. Mitome, N. Fukata, D. Golberg, "Mechanical Properties of Si Nanowires as Revealed by in Situ Transmission Electron Microscopy and Molecular Dynamics Simulations", *Nano Letters* **2012**, *12*, 1898–1904, DOI 10.1021/nl204282y.

[252] M. Nasr Esfahani, B. E. Alaca, "A Review on Size-Dependent Mechanical Properties of Nanowires", *Advanced Engineering Materials* **2019**, *21*, 1900192, DOI 10.1002/adem.201900192.

[253] R. Schoof, G. Castelli, W. Dörfler, "Comparison of different elastic strain definitions for largely deformed SEI of chemo-mechanically coupled silicon battery particles", *Examples and Counterexamples* **2024**, *6*, 100157, DOI 10.1016/j.exco.2024.100157.

Journal Articles

Paper I

Growth of the Solid-Electrolyte Interphase: Electron Diffusion versus Solvent Diffusion

Authors	Lukas Köbbing, Arnulf Latz, Birger Horstmann
Journal	Journal of Power Sources
Year	2023
Volume	561
Pages	232651
DOI	10.1016/j.jpowsour.2023.232651
Copyright	© 2023 Elsevier B.V. All rights reserved.
Copyright link	https://www.elsevier.com/about/policies/copyright
Copyright notice	Reprinted from Ref. [153] with permission from Elsevier.
Preprint DOI	10.48550/arXiv.2209.10854

Author's Contribution

L. Köbbing further developed and implemented the SEI growth models mediated by electron diffusion and solvent diffusion based on the publication by Single et al. [89]. Particularly, L. Köbbing extended the solvent diffusion model by considering the interplay of reaction and transport limitation. Furthermore, L. Köbbing analyzed the results of the SEI growth models, evaluating the performance of the growth mechanisms in comparison to published experimental data. Thereby, L. Köbbing identified the significance of self-discharge for the capacity fade predicted by the electron diffusion model. The model development and analysis was supervised by B. Horstmann. In addition, L. Köbbing created the initial draft of the manuscript and the supporting information including text and figures. The writing was then thoroughly reviewed by B. Horstmann and remarked and approved by A. Latz.

Journal of Power Sources 561 (2023) 232651

Contents lists available at ScienceDirect

Journal of Power Sources

journal homepage: www.elsevier.com/locate/jpowsour

Growth of the solid-electrolyte interphase: Electron diffusion versus solvent diffusion

Lukas Köbbing [a,b], Arnulf Latz [a,b,c], Birger Horstmann [a,b,c,*]

[a] Institute of Engineering Thermodynamics, German Aerospace Center (DLR), Wilhelm-Runge-Straße 10, 89081 Ulm, Germany
[b] Helmholtz Institute Ulm (HIU), Helmholtzstraße 11, 89081 Ulm, Germany
[c] Institute of Electrochemistry, Ulm University, Albert-Einstein-Allee 47, 89081 Ulm, Germany

HIGHLIGHTS

- Discussion of state-of-charge (SOC) dependence and time dependence of SEI growth.
- Electron diffusion describes time and SOC dependence of SEI growth simultaneously.
- Interplay between reaction and diffusion is considered for solvent diffusion.
- Solvent diffusion describes either time or SOC dependence of SEI growth.
- Deviation from square-root behavior in time can be explained with self-discharge.

ARTICLE INFO

Keywords:
Lithium-ion batteries
Solid-electrolyte interphase (SEI)
Battery aging and degradation
SEI growth
Diffusion mechanisms
SOC and time dependence

ABSTRACT

The solid-electrolyte interphase (SEI) substantially influences the lifetime of lithium-ion batteries. Nevertheless, the transport mechanism responsible for the long-term growth of the SEI remains controversial. This study aims at discussing the characteristic time and state-of-charge dependence of SEI growth mediated by electron diffusion versus solvent diffusion. We describe both transport mechanisms with continuum models and compare them to experimental results. We show that electron diffusion can explain both the observed state-of-charge dependence and the time dependence. In contrast, we demonstrate that solvent diffusion can reproduce either the state-of-charge dependence or the time dependence of capacity fade. There is no intermediate regime where solvent diffusion can explain both dependencies simultaneously. Furthermore, we emphasize the crucial role of anode voltage and state-of-charge on SEI growth in general. Due to self-discharge, this dependence can explain deviations from the typical square-root behavior in the time domain. We conclude that electron diffusion is the relevant process leading to the state-of-charge dependent SEI growth. Further experiments are needed to investigate the reason for contributions to the capacity fade that are independent of the state-of-charge.

1. Introduction

The solid-electrolyte interphase (SEI) crucially determines the performance and degradation of lithium-ion batteries. Since its first observation, Peled contributed significantly to the theoretical understanding of the SEI: Peled provided the first theoretical description of the SEI in 1979 [1], considered its complex structure and composition [2], and constructed an equivalent circuit model for a mosaic SEI [3]. His recent review from 2017 highlights the great importance of ongoing SEI research for the improvement of future batteries [4].

Despite a lot of effort that has been going into the theoretical and experimental investigation of the SEI for many years, the SEI is still not fully understood [5–7]. This results from the complexity of the SEI due to the variety of organic and inorganic SEI components [8–10], mixed layered and mosaic SEI structures [11–15], a heterogeneous SEI morphology [16–18], and the contribution of different SEI formation reactions to the evolution of the SEI [19–23].

One major open question is the exact growth mechanism responsible for the long-term SEI growth. In this paper, we focus on the two most widely used mechanisms: electron diffusion through localized states [19,20,24–27] and solvent diffusion [20,28–32]. We illustrate both mechanisms in Fig. 1. The most promising mechanism for describing experimental data for SEI growth is electron diffusion [7], e.g. in form of neutral lithium interstitial diffusion [20,27]. This transport process was proposed by density functional theory calculations that found the two most prominent defects within a dense SEI at low anode voltages to be lithium interstitial ions and neutral lithium

* Corresponding author at: Institute of Engineering Thermodynamics, German Aerospace Center (DLR), Wilhelm-Runge-Straße 10, 89081 Ulm, Germany.
E-mail address: birger.horstmann@dlr.de (B. Horstmann).

https://doi.org/10.1016/j.jpowsour.2023.232651
Received 26 September 2022; Received in revised form 20 December 2022; Accepted 5 January 2023
Available online 25 January 2023

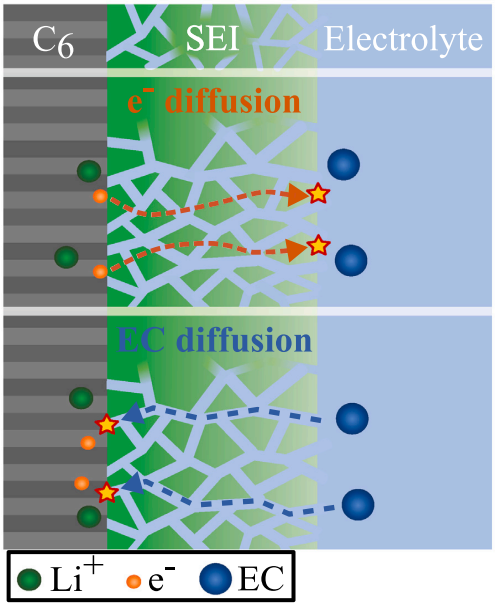

Fig. 1. Schematic of the two transport mechanisms investigated in this study. The upper part depicts the diffusion of electrons from the electrode through the SEI towards the electrolyte. The lower part illustrates the diffusion of solvent molecules from the electrolyte through the SEI towards the electrode.

interstitial atoms [24]. Further calculations of the diffusion of these neutral lithium interstitials concluded that it may be the limiting transport mechanism leading to continued SEI growth [25]. However, the literature also provides arguments supporting a porous SEI allowing for solvent diffusion [33]. Arguments for solvent diffusion reported in the literature are observed currents from redox shuttles through the SEI [34,35] as well as swelling of the SEI inside the electrolyte compared to a dried SEI [36].

To compare these two mechanisms, we investigate the SEI growth during open-circuit battery storage, usually called calendar aging. During calendar aging, the growth of the SEI is the main issue leading to capacity loss of the battery [37,38]. Under storage conditions, the literature reports two important observations. The first one is the dependence of capacity loss on the state-of-charge (SOC) [37–40], and the second one is the square-root behavior in time [41–44].

Although SEI growth under storage conditions still lacks a complete understanding, some efforts were made to evaluate the SEI growth during cycling of batteries [27,45,46]. The experimentally observed heterogeneity of the SEI during cycling was rationalized by electron diffusion [18] in contrast to solvent diffusion [47]. In fact, even self-discharge during battery storage is a sort of battery operation and influences the growth of the SEI [20].

To reexamine the usual square-root behavior, Attia et al. investigated the exact behavior of SEI growth in time during storage and cycling [48]. They provide measurements of capacity loss on carbon black over time during open-circuit storage. The experimental data show a particularly large capacity loss and a clear deviation from the usual square-root behavior in the time domain. This evidences that it is crucial to consider additional effects like self-discharge, at least for large capacity losses.

In this paper, we discuss the theory of SEI growth mediated by electron diffusion and solvent diffusion. We compare the observed dependence of capacity loss on SOC and time to the simulation results. We check first for electron diffusion and second for solvent diffusion whether the two mechanisms can describe both dependencies with the same parameters. For solvent diffusion, we look additionally for an intermediate regime revealing a trade-off between SOC and time dependence. In the last section, we highlight the important role of self-discharge on SEI growth for large capacity losses.

2. Theoretical methods

We use continuum modeling to describe homogeneous long-term growth of the SEI. From this perspective, the SEI formation consists of a diffusion and a reaction step.

As we investigate SEI growth on a long time-scale compared to a single chemical reaction, the capacity fade observed in storage experiments results from a multitude of different reactions happening in parallel. In our reductionist approach, we do not need to account for the plethora of possible reactions and their details, such as nucleation and growth processes. Instead, we try to deduce universal properties from the total observable reaction rate.

In real battery systems, there is a variety of possible SEI formation reactions creating different SEI components. However, the aim of our study is to discuss the overall capacity fade observed in experiments rather than explain the multi-component nature of the SEI. In addition, high-resolution images of the SEI in the literature find different materials and internal structures. The capacity fade experiments we refer to did not investigate the exact composition of the SEI. Thus, we restrict to a single reaction to avoid overfitting,

$$2\mathrm{Li}^+ + 2\mathrm{e}^- + 2\mathrm{EC} \rightarrow \mathrm{Li_2EDC} + \mathrm{R_g}, \tag{1}$$

where lithium ions Li^+, electrons e^-, and solvent molecules ethylene carbonate (EC) react to lithium ethylene dicarbonate ($\mathrm{Li_2EDC}$) which is often considered as the main SEI component. Here, $\mathrm{R_g}$ is a gaseous byproduct.

To enable the reaction (1), all the reagents need to be close together. We consider two possible transport mechanisms to achieve this condition. The first one is the diffusion of electrons through the SEI towards the SEI-electrolyte interface, where the reaction takes place in this case. The second one is the diffusion of solvent molecules through the SEI towards the electrode-SEI interface, where the reaction takes place then. In the following, we derive the SEI growth rate for both diffusion mechanisms.

2.1. Electron diffusion through localized states

For the derivation of the theory of electron diffusion in the transport limited regime, we refer to Ref. [20]. Importantly, electron diffusion is driven by a concentration gradient of localized electrons. This is in contrast to electron conduction, for which conduction band electrons are driven by a potential gradient.

In Ref. [20], the authors illustrate the electron diffusion mechanism with the diffusion of neutral lithium interstitials supported by results from density functional theory [24,25]. In this case, an electron is localized in the vicinity of a lithium interstitial ion to accompany its movement. Density functional theory calculations suggest that these neutral lithium interstitials move via a knock-off mechanism [25]. However, as the SEI is not a homogeneous crystal, electrons can exist as well in different localized states, for example created by inhomogeneities [49], grain boundaries between different SEI components [50], or radicals inside the SEI [26]. These electrons diffuse by transitioning from one localized state to another.

The capacity loss Q_{SEI} observed in experiments is related to the thickness of the SEI L_{SEI} via

$$L_{\mathrm{SEI}} = \frac{\upsilon}{s}\frac{Q_{\mathrm{SEI}}}{AF} + L_{\mathrm{SEI},0}, \tag{2}$$

where υ is the mean molar volume of the SEI, s is the mean stoichiometric coefficient of lithium in the SEI formation reaction, A is

the surface of the anode, and F is the Faraday constant. The initial capacity loss $Q_{\mathrm{SEI},0}$ is related to the initial thickness of the SEI by $L_{\mathrm{SEI},0} = \upsilon Q_{\mathrm{SEI},0}/(sAF)$.

According to Ref. [20], the capacity loss over time due to SEI growth mediated by electron diffusion is given by

$$\partial_t Q_{\mathrm{SEI}} = \frac{A^2 s F^2 D_{\mathrm{e}^-}}{\upsilon} \cdot \frac{c_{\mathrm{e}^-,0} \cdot e^{-\tilde{U}}}{Q_{\mathrm{SEI}} + Q_{\mathrm{SEI},0}} \tag{3}$$

with $\tilde{U} = FU/R_{\mathrm{gas}}T$, where U is the anode open circuit potential, R_{gas} is the universal gas constant, and T is the temperature. D_{e^-} is the diffusion coefficient of electrons through the SEI and $c_{\mathrm{e}^-,0}$ is the electron concentration at $U = 0$ V.

For constant voltage, Eq. (3) leads to the well-known square-root behavior in time,

$$Q_{\mathrm{SEI}} = AF\sqrt{\frac{2s}{\upsilon} D_{\mathrm{e}^-} c_{\mathrm{e}^-,0} e^{-\tilde{U}/2}}\sqrt{t + t_0} - Q_{\mathrm{SEI},0}, \tag{4}$$

where t_0 depends on the initial capacity loss such that Q_{SEI} vanishes at $t = 0$.

2.2. Solvent diffusion

Next, we need to derive the theory of SEI growth generated by solvent diffusion in detail. In the transport limited regime, solvent diffusion shows no SOC dependence contradicting experimental observations [20]. In contrast, in the reaction limited regime, the time behavior is linear, which does not match experiments as well [27]. Therefore, we consider an interplay between the diffusion of solvent molecules and the SEI formation reaction.

The rate of charge consumption due to the SEI formation reaction is described by a Butler-Volmer equation as

$$R = \frac{j_0}{F}\left[\tilde{c}_{\mathrm{EC}}(0) e^{-(1-\alpha)\tilde{U}} - e^{\alpha\tilde{U} - \tilde{U}_{\mathrm{SEI}}}\right]. \tag{5}$$

Here, j_0 is the maximum reaction current, $\tilde{c}_{\mathrm{EC}}(0)$ is the normalized solvent concentration at the electrode-SEI interface, α is the symmetry factor and $\tilde{U}_{\mathrm{SEI}} = FU_{\mathrm{SEI}}/R_{\mathrm{gas}}T$ is the SEI formation potential with $U_{\mathrm{SEI}} = 0.8$ V. Typically, the first exponential term in Eq. (5) describing SEI formation dominates as the SEI product is assumed to be insoluble.

The transport of solvent molecules through the SEI is described by Fickian diffusion,

$$\frac{\partial \tilde{c}_{\mathrm{EC}}}{\partial t} = \frac{D_{\mathrm{EC}}}{L_{\mathrm{SEI}}^2} \cdot \frac{\partial^2 \tilde{c}_{\mathrm{EC}}}{\partial \tilde{x}^2}, \tag{6}$$

where $\tilde{c}_{\mathrm{EC}} = c_{\mathrm{EC}}/c_{\mathrm{EC,bulk}}$ is the normalized concentration, $\tilde{x} = x/L_{\mathrm{SEI}}$ is the distance from the electrode, and D_{EC} is the diffusion coefficient of solvent through the SEI.

At the boundaries, the SEI reaction rate R and the bulk concentration, respectively, determine the concentration,

$$\begin{aligned} \frac{D_{\mathrm{EC}} c_{\mathrm{EC,bulk}}}{L_{\mathrm{SEI}}} \cdot \left.\frac{\partial \tilde{c}_{\mathrm{EC}}}{\partial \tilde{x}}\right|_{x=0} &= R, \\ \tilde{c}_{\mathrm{EC}}(\tilde{x} \to 1) &= 1. \end{aligned} \tag{7}$$

From the Eqs. (5)–(7) we derive the concentration at the electrode-SEI interface as

$$\tilde{c}_{\mathrm{EC}}(0) = \frac{1 + \frac{j_0 L_{\mathrm{SEI}}}{F D_{\mathrm{EC}} c_{\mathrm{EC,bulk}}} e^{\alpha\tilde{U} - \tilde{U}_{\mathrm{SEI}}}}{1 + \frac{j_0 L_{\mathrm{SEI}}}{F D_{\mathrm{EC}} c_{\mathrm{EC,bulk}}} e^{-(1-\alpha)\tilde{U}}}. \tag{8}$$

The resulting equation describing capacity loss due to SEI growth mediated by solvent diffusion derived from Eqs. (5) and (8) then reads

$$\partial_t Q_{\mathrm{SEI}} = A j_0 \frac{e^{-(1-\alpha)\tilde{U}} - e^{\alpha\tilde{U} - \tilde{U}_{\mathrm{SEI}}}}{1 + \frac{\upsilon j_0}{sAF^2 D_{\mathrm{EC}} c_{\mathrm{EC,bulk}}} e^{-(1-\alpha)\tilde{U}} \left(Q_{\mathrm{SEI}} + Q_{\mathrm{SEI},0}\right)}. \tag{9}$$

In the transport limited regime, i.e. $FD_{\mathrm{EC}} c_{\mathrm{EC,bulk}}/L_{\mathrm{SEI}} \ll j_0$, Eq. (9) reveals the square-root behavior in time for constant voltage neglecting the term of the backward reaction,

$$Q_{\mathrm{SEI}} = AF\sqrt{\frac{2s}{\upsilon} D_{\mathrm{EC}} c_{\mathrm{EC,bulk}} \left(t + t_0\right)} - Q_{\mathrm{SEI},0}. \tag{10}$$

In the reaction limited regime, i.e. $j_0 \ll FD_{\mathrm{EC}} c_{\mathrm{EC,bulk}}/L_{\mathrm{SEI}}$, Eq. (9) shows a linear time dependence, but non-trivial SOC dependence,

$$Q_{\mathrm{SEI}} = A j_0 \left(e^{-(1-\alpha)\tilde{U}} - e^{\alpha\tilde{U} - \tilde{U}_{\mathrm{SEI}}}\right) t. \tag{11}$$

3. Results and discussion

Now, we evaluate the dependence of capacity fade on SOC and time for open-circuit storage. We analyze the data by Keil et al. [37], who measured the capacity loss depending on the SOC for lithium-ion batteries with a nickel cobalt aluminum oxide (NCA) cathode. By measuring the SOC dependence at different times up to 9.5 months, they also provide the time dependence of capacity fade at different states-of-charge. Importantly, they also measured the anode open circuit voltage $U(\mathrm{SOC})$ for the same cells.

The authors have already analyzed the SOC dependence in Ref. [20]. Here, we evaluate not only the SOC dependence but also the time dependence. A theory that aims at explaining the observed capacity fade has to describe both dependencies simultaneously.

3.1. Electron diffusion: SOC and time dependence

First of all, we want to review the electron diffusion mechanism. The experimentally observed capacity loss Q_{loss} consists of a contribution due to SEI growth depending on the SOC and an additional contribution that does not depend on the SOC, i.e. $Q_{\mathrm{loss}} = Q_{\mathrm{SEI}} + Q_{\mathrm{add}}$ [20]. At high SOC, both terms contribute significantly to the total capacity loss. At low SOC, the constant contribution, which serves as an offset for the capacity loss, is the dominant part. We can investigate the time dependence of the SOC depending capacity fade by subtracting the capacity fade observed at SOC = 0.

To determine the behavior of capacity loss that is independent of the SOC, we analyze the time dependence of the capacity fade at SOC = 0. Due to the influence of the anode overhang area, we neglect the data point at $t = 0$. The investigated cells were delivered and stored at a higher SOC before the start of the storage experiment. For cells investigated at low SOC, lithium stored inside the overhang area enters the anode and leads to an increase in the measured capacity [20,38,51]. Therefore, we assume the capacity fade at $t = 0$ should not vanish but rather show a capacity gain, i.e. a negative capacity fade. We find that a square-root behavior in time agrees well with the data points (see SI-1). Due to the initial SEI thickness, we observe a time offset in the square root that can be related to the initial capacity loss $Q_{\mathrm{SEI},0}$. For further use, we shift the data such that the curve describing the capacity loss vanishes initially, i.e. it starts at the origin.

The cause of the capacity loss at SOC = 0 is not known. Possible reasons are SEI growth during the check-up cycles or mediated by a different transport mechanism independent of the SOC. In addition, other degradation than SEI growth, like particle fracture and contact loss, can cause the observed capacity fade.

After discussing the SOC independent capacity loss, we want to analyze the SOC dependence and the time dependence of the capacity fade now. For this, we subtract the curve obtained at SOC = 0 from the data points to investigate the time dependence of the SOC depending contribution to the capacity fade. We use our model in Eq. (3) with the determined $Q_{\mathrm{SEI},0}$. The anode voltage U depends on the SOC as shown in Ref. [37], where the SOC changes during storage due to capacity loss and capacity retention after check-ups. The constant factor in Eq. (3), namely $A^2 s F^2 D_{\mathrm{e}^-} c_{\mathrm{e}^-,0}/\upsilon$, serves as a single fitting variable.

The fit of the electron diffusion model equation (3) to the capacity loss depending on the SOC is shown in Fig. 2(a). Overall, the simulation

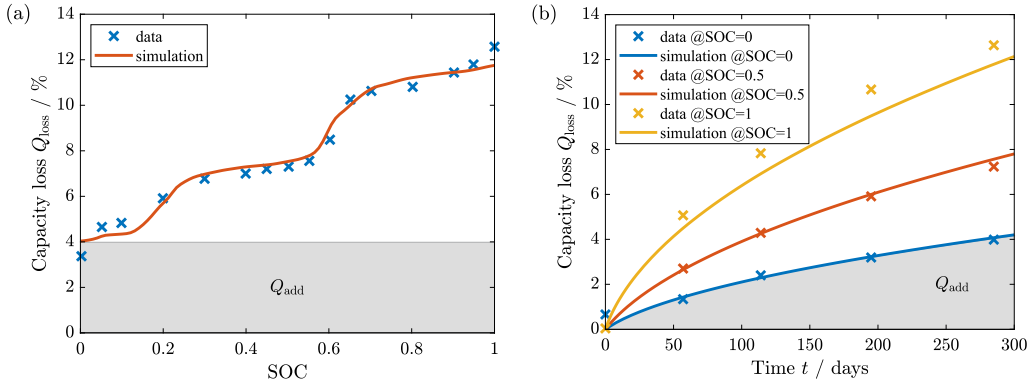

Fig. 2. Capacity loss simulated with electron diffusion fitted to the SOC depending data measured in Ref. [37]. (a) Capacity loss depending on the SOC. The plot shows a good agreement between simulation and data points. (b) Capacity loss depending on time. The agreement is excellent at low and medium SOC, whereas a minor deviation is visible at high SOC.

agrees well with the experimental data, i.e. electron diffusion can explain the SOC dependence of capacity fade. Only at very low and very high SOC, we observe major deviations that may account for additional effects.

With the same parameters, in Fig. 2(b) we compare the time dependence to the experiment. We observe an excellent agreement between the simulated time dependence and the data at low and medium SOC. The data as well as the simulation approximately show a square-root behavior in time. At high SOC, the deviation between simulation and data is more pronounced, indicating an additional contribution to capacity loss at very high SOC. This is in accordance with the deviation at high SOC observed in the SOC dependence.

We support our analysis with new data for lithium iron phosphate (LFP) cells provided by Naumann et al. [39] in the supplementary information. These additional data focus on measuring the time dependence at different states-of-charge. The capacity fade at SOC = 0 and the SOC dependence are analyzed in SI-2 and SI-3, respectively.

Altogether, we have shown that electron diffusion is able to describe the SOC dependence and the time dependence with the same parameters. Thus, electron diffusion can explain the observed behaviors of SEI growth quite accurately.

3.2. Solvent diffusion: SOC and time dependence

Next, we investigate the solvent diffusion mechanism, which competes with electron diffusion. To explain the various experimental observations, our model for solvent diffusion considers the interplay between reaction and transport limitation. In the following, we set the symmetry factor $\alpha = 0.5$, as we observe no qualitative influence of this parameter on our results (see SI-4). This choice describes the symmetric case, where the reaction overpotential influences the forward and backward reactions to the same extent. With the same procedure as before, we subtract the data at SOC = 0 from the experimental data to examine the SOC dependent capacity fade.

First, we fit the solvent diffusion model equation (9) to the SOC depending capacity fade data. The corresponding result is shown in Fig. 3(a). The simulation shows a good agreement with the SOC dependence of the observed capacity loss. The quality of the fit is similar to the one calculated for electron diffusion. This result is contrary to Ref. [20], where solvent diffusion is only described in the transport limited regime. However, Fig. 3(b) shows that with the same parameters, the simulation reproduces the time dependence only at small SOC, where the offset from SOC = 0 contributes primarily to the capacity loss. At higher SOC, the time dependence does not fit the data points. In this case, the SOC depending capacity fade, which is approximately linear in time, contributes significantly. The linearity of the capacity fade reveals that the simulation is in the reaction limited regime to capture the SOC dependence. In conclusion, matching the SOC dependence to the experiment does not reproduce the time dependence.

In comparison to the fit to the SOC dependence, which revealed the reaction limited regime, we fit the time dependence of the capacity fade next. As we assume to achieve the best accordance at medium SOC, we fit the solvent diffusion model to the capacity loss over time at SOC = 50%. As shown in Fig. 3(d), we find a perfect agreement of simulation and experiment at the fitted SOC = 50%. In contrast, at high SOC, the simulation gives the same result as at SOC = 50% and does not capture the experimental data. The deviation at high SOC is explained when regarding Fig. 3(c). With the parameters obtained from the fit to the time dependence, the simulation shows a constant contribution to capacity loss over a wide range of SOC values. The simulation does not capture the dependence of the capacity loss on the SOC at all. As we observe perfect agreement of the time dependence at SOC = 50% but no agreement of the SOC dependence, the simulation is in the transport limited regime. Thus, matching the time dependence to the experiment, the simulation does not reproduce the SOC dependence.

As both fits reveal only one observed behavior, we try to find a possible intermediate regime where the solvent diffusion mechanism captures the SOC dependence and the time dependence with the same parameters. To find this regime, we vary the reaction current and the diffusion coefficient in Eq. (9). In this parameter study, we compare the root mean square deviation between the simulation and the experimental data points describing the SOC dependence. Additionally, we fit a simple power law t^{β} to the simulated time dependence and evaluate the agreement of the time exponent β with the square-root profile, i.e. $\beta = 0.5$.

The outcome of the parameter study is depicted in Fig. 4. On the one hand, Fig. 4(a) shows the logarithm of the root mean square deviation of the simulation to the experimental data describing the SOC dependence. The smallest values depicted in dark blue refer to the best accordance of simulation and experiment. Therefore, in the given range of parameters, small values of the reaction current j_0 and large values of the diffusion coefficient D_{EC} are necessary to describe the experimentally observed SOC dependence.

On the other hand, Fig. 4(b) depicts the fitted time exponent β. Here, values around $\beta = 0.5$ are required to describe the experimentally observed time dependence, which shows approximately a square-root behavior. The corresponding values are illustrated again in dark blue. From the same range of parameters as before, now large values of the reaction current j_0 and small values of the diffusion coefficient D_{EC} are needed.

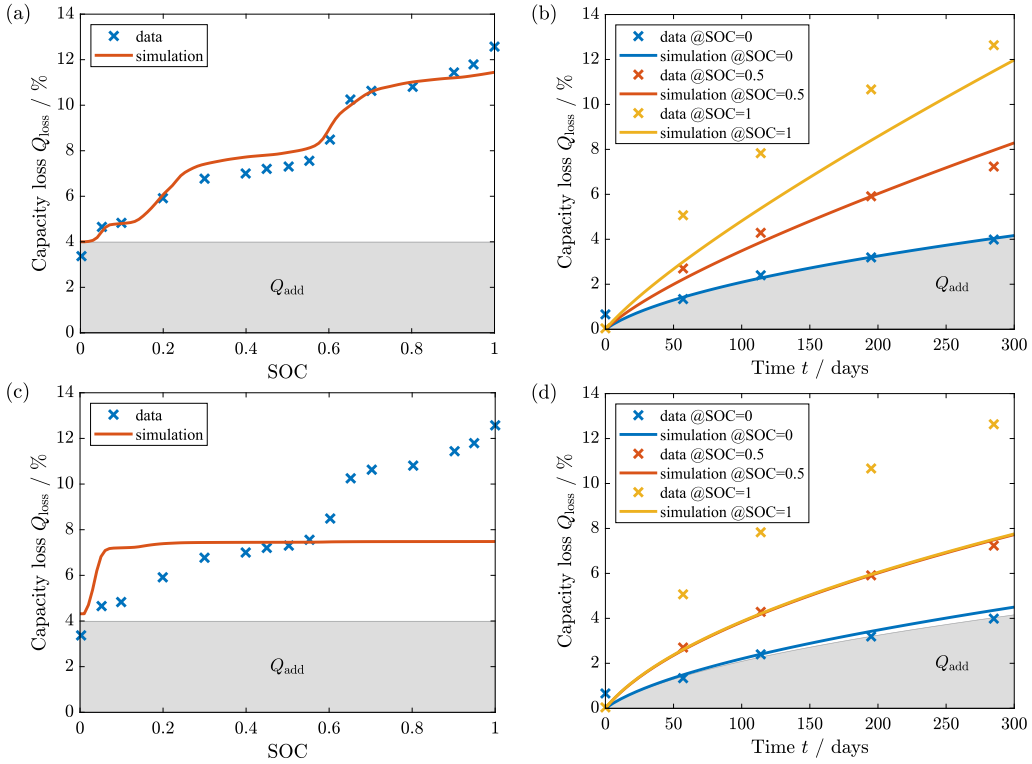

Fig. 3. Capacity loss simulated with solvent diffusion in comparison to the data measured in Ref. [37]. (a) and (b) Fit of the solvent diffusion model to the SOC dependence of capacity loss (a) Capacity loss depending on the SOC. The plot shows a good agreement between simulation and data points. (b) Capacity loss depending on time. Simulation and experiment do not match at medium and high SOC. (c) and (d) Fit of the solvent diffusion model to the time dependence of capacity loss at SOC = 50% (c) Capacity loss depending on the SOC. The simulation does not show the experimentally observed SOC dependence. (d) Capacity loss depending on time. Excellent agreement is achieved at SOC = 50% but the simulation does not reproduce the behavior at SOC = 100%.

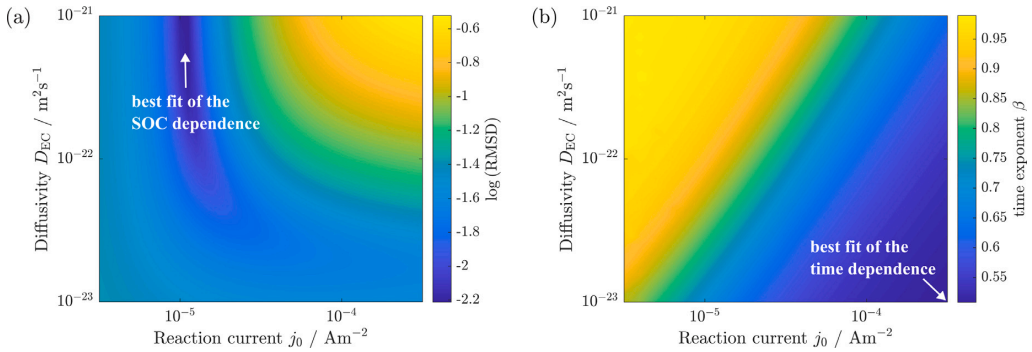

Fig. 4. Parameter study for the capacity loss simulated with solvent diffusion with a variation of the reaction current j_0 and the diffusion coefficient D_{EC}. (a) Logarithm of the root mean square deviation (RMSD) of the simulated capacity loss depending on the SOC from the experiment [37]. The smallest deviation is depicted in dark blue and reached for a small reaction current j_0 and large diffusivity D_{EC}. The best fit of the SOC dependence with the parameters used in Fig. 3(a) is highlighted. (b) Fitted time exponent β to the simulation. The experiment can be approximately described with $t^{0.5}$ depicted in dark blue. Either large values of j_0 or small values of D_{EC} are needed to achieve a good agreement with $t^{0.5}$. The best fit of the time dependence with the parameters used in Fig. 3(d) is highlighted. (For interpretation of the references to color in this figure legend, the reader is referred to the web version of this article.)

To combine both results, all sets of parameters that describe the SOC dependence do not reproduce the time dependence, and all sets of parameters that describe the time dependence do not reproduce the SOC dependence. The parameter study shows either good accordance with the SOC dependence or good accordance with the $t^{0.5}$ dependence. There exists no intermediate regime, where solvent diffusion reproduces the SOC dependence and the time dependence. As the same experiment exhibits both dependencies, the solvent diffusion

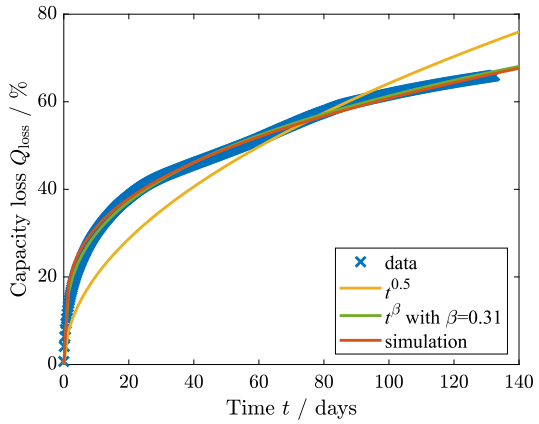

Fig. 5. Capacity loss on carbon black during storage. The experimental data from Ref. [48] show a clear deviation from $t^{0.5}$ behavior. The simulation for electron diffusion can describe the observed time behavior when self-discharge is taken into account.

mechanism fails to describe the observed SEI growth characteristics. However, solvent diffusion could be one of the reasons for the contribution to the capacity fade that is independent of the SOC. As mentioned above, we provide the analysis for the data by Naumann et al. [39] in the supplementary information (see SI-5 and SI-6).

In this section, we have shown that the diffusion of solvent molecules cannot capture the experimentally observed dependencies of capacity fade on SOC and time. An alternative approach is considering additional species like the SEI product or lithium ions inside the SEI, which diffuse through the SEI from the electrode towards the electrolyte [52,53]. However, this model requires an explanation of why the SEI product does not precipitate directly at the electrode but diffuses towards the SEI-electrolyte interface instead. Alternatively, it has to be clarified why lithium ions should limit the transport process as they can move fast through the SEI to enable battery operation. The mathematical structure of this particular description would be similar to the model of electron diffusion, as the diffusion of a species from the electrode towards the electrolyte determines the SEI growth rate.

3.3. Self-discharge: Deviation from square-root behavior

So far, we depict the SOC dependence of the capacity loss as a separate feature compared to the time dependence. Now, we want to highlight the interaction between the SOC dependence and the $t^{0.5}$ time dependence due to self-discharge. For a good demonstration of this effect, we refer to an experiment by Attia et al. measuring a particularly large capacity loss on carbon black over time [48]. The experimental data are shown in Fig. 5.

For this experiment, Attia et al. reviewed the square-root behavior in time and fitted power laws t^{β} to the experimentally observed capacity fade [48]. For storage, they observed apparent time exponents lower than 0.5, e.g. $\beta \sim 0.3$ as depicted in Fig. 5, in contrast to the usual $t^{0.5}$ behavior expected for transport limitation. However, this cannot be explained by leaving the transport limited regime, as values larger than 0.5 indicate reaction limitations [27].

As discussed before, the growth rate of the SEI depends on the anode voltage via the SOC calculated with respect to the initial capacity. However, the SOC cannot be assumed constant in time but gets effectively reduced by the amount of charge consumed due to SEI growth. This effect of self-discharge leads to a deviation of the simulated SEI growth from a simple square-root behavior in time, particularly for large capacity losses.

In contrast to the former sections, we cannot determine the contribution to the capacity loss independent of the SOC separately, as Ref. [48] provides no data at SOC = 0. However, we assume that both SOC dependent and independent parts can contribute significantly to the total capacity loss. Our assumption is supported by results from cryogenic electron microscopy of the SEI on carbon black [54]. This study reports a thin and a thick SEI layer on different particles. In addition, Ref. [53] describes two SEI growth modes, namely homogeneous and heterogeneous SEI growth. Therefore, it is reasonable to assume that two different mechanisms may lead to the observed SEI thickness. Due to our former results, we attribute the SOC dependent term to our electron diffusion model (3) and the SOC independent term to an additional mechanism. Solvent diffusion would be a candidate for this mechanism.

As motivated, we divide the total capacity loss into a contribution with nontrivial SOC dependence and a contribution with trivial SOC dependence. Here, we set $Q_{SEI,0} = 0$ to reduce the number of parameters. Fig. 5 illustrates the simulation of the capacity loss. It matches the experiment reasonably with similar quality as the simple power law fit. Therefore, we highlight that electron diffusion can well describe SEI growth as a transport limited process, i.e. $t^{0.5}$ behavior for constant voltage, when carefully considering any change in the SOC and the voltage U(SOC), respectively. Considering this self-discharge, our model for electron diffusion is able to describe deviations from the $t^{0.5}$ dependence. Our results reveal that smaller apparent exponents of the power law t^{β}, as observed in Ref. [48], are still consistent with transport limited SEI growth models. Instead, exponents larger than 0.5 imply the transition to the reaction limited regime [27].

4. Conclusions

We have investigated the SOC and time dependence of capacity fade during calendar aging and compared the electron diffusion with the solvent diffusion mechanism. The relevant transport mechanism leading to SEI growth has to capture the SOC and the time dependence with the same parameters.

We have found that the electron diffusion mechanism can reproduce the SOC dependence and the time dependence of the capacity loss simultaneously. We conclude that electron diffusion is able to describe the characteristics of the SOC dependent capacity loss. Only at very low and high SOC do additional degradation effects not captured in our model lead to deviations. Their interplay deserves further investigation.

In contrast, we have shown that solvent diffusion can reproduce either the SOC dependence or the time dependence of capacity fade. Our parameter study approves that there is no intermediate regime, which captures both dependencies with the same parameters. Thus, solvent diffusion fails to describe the observed features of the SOC dependent capacity loss.

Finally, we have emphasized the importance of the interaction between SOC dependence and time dependence of capacity fade. We have demonstrated that our model for electron diffusion captures experimentally observed deviations from the usual $t^{0.5}$ law by considering the effect of self-discharge. Consequently, smaller apparent time exponents, as reported in Ref. [48], do not contradict transport limited SEI growth. In contrast, larger exponents may indicate reaction limitations [27].

To conclude our study, we have shown that only the electron diffusion mechanism can explain the SOC and time dependence simultaneously. This mechanism can even reproduce capacity fade experiments that deviate from the square-root behavior in time. In agreement with Refs. [53,54], we have divided the total capacity loss into two contributions. However, the reason for the SOC independent capacity loss needs further investigation.

To take future calendar aging studies into account, we propose to appropriately state experimental data of capacity loss as a function of SOC and time. The check-up cycles have to be done carefully to reduce their influence on the self-discharge effect, i.e. it is important to state to which SOC the cells are charged after the check-ups. Additionally, it is crucial to provide the anode open circuit voltage curve for the investigated cells to analyze the SOC dependence of SEI growth.

CRediT authorship contribution statement

Lukas Köbbing: Methodology, Software, Validation, Formal analysis, Investigation, Writing – original draft, Visualization. **Arnulf Latz:** Conceptualization, Writing – review & editing, Supervision, Project administration, Funding acquisition. **Birger Horstmann:** Conceptualization, Methodology, Resources, Writing – review & editing, Supervision, Project administration, Funding acquisition.

Declaration of competing interest

The authors declare that they have no known competing financial interests or personal relationships that could have appeared to influence the work reported in this paper.

Data availability

Data will be made available on request.

Acknowledgments

This work was funded by the German Research Foundation (DFG) in the framework of the research training group SiMET — Simulation of Mechano-Electro-Thermal Processes in Lithium-Ion Batteries (281041241/GRK 2218).

Appendix A. Supplementary data

Supplementary material related to this article can be found online at https://doi.org/10.1016/j.jpowsour.2023.232651.

References

[1] E. Peled, The electrochemical behavior of alkali and alkaline earth metals in nonaqueous battery systems—The solid electrolyte interphase model, J. Electrochem. Soc. 126 (12) (1979) 2047–2051, http://dx.doi.org/10.1149/1.2128859, URL https://iopscience.iop.org/article/10.1149/1.2128859.

[2] E. Peled, D. Golodnitsky, G. Ardel, V. Eshkenazy, The SEI model—Application to lithium-polymer electrolyte batteries, Electrochim. Acta 40 (13–14) (1995) 2197–2204, http://dx.doi.org/10.1016/0013-4686(95)00163-9, URL https://linkinghub.elsevier.com/retrieve/pii/0013468695001639.

[3] E. Peled, D. Golodnitsky, G. Ardel, Advanced model for solid electrolyte interphase electrodes in liquid and polymer electrolytes, J. Electrochem. Soc. 144 (8) (1997) L208–L210, http://dx.doi.org/10.1149/1.1837858, URL https://iopscience.iop.org/article/10.1149/1.1837858.

[4] E. Peled, S. Menkin, Review—SEI: Past, present and future, J. Electrochem. Soc. 164 (7) (2017) A1703–A1719, http://dx.doi.org/10.1149/2.1441707jes, URL https://iopscience.iop.org/article/10.1149/2.1441707jes.

[5] M. Winter, The solid electrolyte interphase – The most important and the least understood solid electrolyte in rechargeable li batteries, Z. Phys. Chem. 223 (10–11) (2009) 1395–1406, http://dx.doi.org/10.1524/zpch.2009.6086, URL https://www.degruyter.com/document/doi/10.1524/zpch.2009.6086/html.

[6] A. Wang, S. Kadam, H. Li, S. Shi, Y. Qi, Review on modeling of the anode solid electrolyte interphase (SEI) for lithium-ion batteries, Npj Comput. Mater. 4 (1) (2018) 15, http://dx.doi.org/10.1038/s41524-018-0064-0, URL http://www.nature.com/articles/s41524-018-0064-0.

[7] B. Horstmann, F. Single, A. Latz, Review on multi-scale models of solid-electrolyte interphase formation, Curr. Opin. Electrochem. 13 (2019) 61–69, http://dx.doi.org/10.1016/j.coelec.2018.10.013, arXiv:1811.04667. URL https://linkinghub.elsevier.com/retrieve/pii/S2451910318301686.

[8] D. Aurbach, Y. Ein-Ely, A. Zaban, The surface chemistry of lithium electrodes in alkyl carbonate solutions, J. Electrochem. Soc. 141 (1) (1994) L1–L3, http://dx.doi.org/10.1149/1.2054718, URL https://iopscience.iop.org/article/10.1149/1.2054718.

[9] H.-L. Zhang, F. Li, C. Liu, J. Tan, H.-M. Cheng, New insight into the solid electrolyte interphase with use of a focused ion beam, J. Phys. Chem. B 109 (47) (2005) 22205–22211, http://dx.doi.org/10.1021/jp053311a, URL https://pubs.acs.org/doi/10.1021/jp053311a.

[10] S.J. An, J. Li, C. Daniel, D. Mohanty, S. Nagpure, D.L. Wood, The state of understanding of the lithium-ion-battery graphite solid electrolyte interphase (SEI) and its relationship to formation cycling, Carbon 105 (2016) 52–76, http://dx.doi.org/10.1016/j.carbon.2016.04.008, URL https://linkinghub.elsevier.com/retrieve/pii/S0008622316302676.

[11] D. Aurbach, B. Markovsky, M. Levi, E. Levi, A. Schechter, M. Moshkovich, Y. Cohen, New insights into the interactions between electrode materials and electrolyte solutions for advanced nonaqueous batteries, J. Power Sources 81–82 (1999) 95–111, http://dx.doi.org/10.1016/S0378-7753(99)00187-1, URL https://linkinghub.elsevier.com/retrieve/pii/S0378775399001871.

[12] D. Aurbach, Review of selected electrode–solution interactions which determine the performance of Li and Li ion batteries, J. Power Sources 89 (2) (2000) 206–218, http://dx.doi.org/10.1016/S0378-7753(00)00431-6, URL https://linkinghub.elsevier.com/retrieve/pii/S0378775300004316.

[13] F. Single, B. Horstmann, A. Latz, Dynamics and morphology of solid electrolyte interphase (SEI), Phys. Chem. Chem. Phys. 18 (27) (2016) 17810–17814, http://dx.doi.org/10.1039/C6CP02816K, URL http://xlink.rsc.org/?DOI=C6CP02816K.

[14] Y. Li, Y. Li, A. Pei, K. Yan, Y. Sun, C.-L. Wu, L.-M. Joubert, R. Chin, A.L. Koh, Y. Yu, J. Perrino, B. Butz, S. Chu, Y. Cui, Atomic structure of sensitive battery materials and interfaces revealed by cryo–electron microscopy, Science 358 (6362) (2017) 506–510, http://dx.doi.org/10.1126/science.aam6014, URL https://www.sciencemag.org/lookup/doi/10.1126/science.aam6014 https://www.science.org/doi/10.1126/science.aam6014.

[15] L. von Kolzenberg, M. Werres, J. Tetzloff, B. Horstmann, Transition between growth of dense and porous films: theory of dual-layer SEI, Phys. Chem. Chem. Phys. 24 (31) (2022) 18469–18476, http://dx.doi.org/10.1039/D2CP00188H, arXiv:2112.12628. URL http://xlink.rsc.org/?DOI=D2CP00188H.

[16] A.V. Cresce, S.M. Russell, D.R. Baker, K.J. Gaskell, K. Xu, In situ and quantitative characterization of solid electrolyte interphases, Nano Lett. 14 (3) (2014) 1405–1412, http://dx.doi.org/10.1021/nl404471v, URL https://pubs.acs.org/doi/10.1021/nl404471v.

[17] J. Zheng, H. Zheng, R. Wang, L. Ben, W. Lu, L. Chen, L. Chen, H. Li, 3D visualization of inhomogeneous multi-layered structure and Young's modulus of the solid electrolyte interphase (SEI) on silicon anodes for lithium ion batteries, Phys. Chem. Chem. Phys. 16 (26) (2014) 13229–13238, http://dx.doi.org/10.1039/C4CP01968G, URL http://xlink.rsc.org/?DOI=C4CP01968G.

[18] L.J. Bolay, T. Schmitt, S. Hein, O.S. Mendoza-Hernandez, E. Hosono, D. Asakura, K. Kinoshita, H. Matsuda, M. Umeda, Y. Sone, A. Latz, B. Horstmann, Microstructure-resolved degradation simulation of lithium-ion batteries in space applications, J. Power Sources Adv. 14 (November 2021) (2022) 100083, http://dx.doi.org/10.1016/j.powera.2022.100083, arXiv:2111.02856. URL https://linkinghub.elsevier.com/retrieve/pii/S2666248522000014.

[19] F. Single, B. Horstmann, A. Latz, Revealing SEI morphology: In-depth analysis of a modeling approach, J. Electrochem. Soc. 164 (11) (2017) E3132–E3145, http://dx.doi.org/10.1149/2.0121711jes, URL https://iopscience.iop.org/article/10.1149/2.0121711jes.

[20] F. Single, A. Latz, B. Horstmann, Identifying the mechanism of continued growth of the solid–electrolyte interphase, ChemSusChem 11 (12) (2018) 1950–1955, http://dx.doi.org/10.1002/cssc.201800077, arXiv:1812.03841. URL https://onlinelibrary.wiley.com/doi/10.1002/cssc.201800077.

[21] S.K. Heiskanen, J. Kim, B.L. Lucht, Generation and evolution of the solid electrolyte interphase of lithium-ion batteries, Joule 3 (10) (2019) 2322–2333, http://dx.doi.org/10.1016/j.joule.2019.08.018, URL https://linkinghub.elsevier.com/retrieve/pii/S2542435119304210.

[22] L. Alzate-Vargas, S.M. Blau, E.W.C. Spotte-Smith, S. Allu, K.A. Persson, J.-L. Fattebert, Insight into SEI growth in Li-ion batteries using molecular dynamics and accelerated chemical reactions, J. Phys. Chem. C 125 (34) (2021) 18588–18596, http://dx.doi.org/10.1021/acs.jpcc.1c04149, URL https://pubs.acs.org/doi/10.1021/acs.jpcc.1c04149.

[23] E.W.C. Spotte-Smith, R.L. Kam, D. Barter, X. Xie, T. Hou, S. Dwaraknath, S.M. Blau, K.A. Persson, Toward a mechanistic model of solid–electrolyte interphase formation and evolution in lithium-ion batteries, ACS Energy Lett. 7 (4) (2022) 1446–1453, http://dx.doi.org/10.1021/acsenergylett.2c00517, URL https://pubs.acs.org/doi/10.1021/acsenergylett.2c00517.

[24] S. Shi, P. Lu, Z. Liu, Y. Qi, L.G. Hector, H. Li, S.J. Harris, Direct calculation of Li-ion transport in the solid electrolyte interphase, J. Am. Chem. Soc. 134 (37) (2012) 15476–15487, http://dx.doi.org/10.1021/ja305366r.

[25] S. Shi, Y. Qi, H. Li, L.G. Hector, Defect thermodynamics and diffusion mechanisms in Li 2 CO 3 and implications for the solid electrolyte interphase in Li-Ion batteries, J. Phys. Chem. C 117 (17) (2013) 8579–8593, http://dx.doi.org/10.1021/jp310591u, URL https://pubs.acs.org/doi/10.1021/jp310591u.

[26] F.A. Soto, Y. Ma, J.M. Martinez de la Hoz, J.M. Seminario, P.B. Balbuena, Formation and growth mechanisms of solid-electrolyte interphase layers in rechargeable batteries, Chem. Mater. 27 (23) (2015) 7990–8000, http://dx.doi.org/10.1021/acs.chemmater.5b03358, URL https://pubs.acs.org/doi/10.1021/acs.chemmater.5b03358.

[27] L. Kolzenberg, A. Latz, B. Horstmann, Solid–electrolyte interphase during battery cycling: Theory of growth regimes, ChemSusChem 13 (15) (2020) 3901–3910, http://dx.doi.org/10.1002/cssc.202000867, arXiv:2004.01458. URL https://onlinelibrary.wiley.com/doi/10.1002/cssc.202000867.

[28] H.J. Ploehn, P. Ramadass, R.E. White, Solvent diffusion model for aging of lithium-ion battery cells, J. Electrochem. Soc. 151 (3) (2004) A456, http://dx.doi.org/10.1149/1.1644601, URL https://iopscience.iop.org/article/10.1149/1.1644601.

[29] R.P. Ramasamy, J.-W. Lee, B.N. Popov, Simulation of capacity loss in carbon electrode for lithium-ion cells during storage, J. Power Sources 166 (1) (2007) 266–272, http://dx.doi.org/10.1016/j.jpowsour.2006.12.086, URL https://linkinghub.elsevier.com/retrieve/pii/S0378775307000924.

[30] S. Sankarasubramanian, B. Krishnamurthy, A capacity fade model for lithium-ion batteries including diffusion and kinetics, Electrochim. Acta 70 (2012) 248–254, http://dx.doi.org/10.1016/j.electacta.2012.03.063, URL https://linkinghub.elsevier.com/retrieve/pii/S0013468612004021.

[31] M.B. Pinson, M.Z. Bazant, Theory of SEI formation in rechargeable batteries: Capacity fade, accelerated aging and lifetime prediction, J. Electrochem. Soc. 160 (2) (2013) A243–A250, http://dx.doi.org/10.1149/2.044302jes, arXiv:1210.3672. URL https://iopscience.iop.org/article/10.1149/2.044302jes.

[32] F. Hao, Z. Liu, P.B. Balbuena, P.P. Mukherjee, Mesoscale elucidation of solid electrolyte interphase layer formation in Li-ion battery anode, J. Phys. Chem. C 121 (47) (2017) 26233–26240, http://dx.doi.org/10.1021/acs.jpcc.7b09465, URL https://pubs.acs.org/doi/10.1021/acs.jpcc.7b09465.

[33] F.T. Krauss, I. Pantenburg, B. Roling, Transport of ions, molecules, and electrons across the solid electrolyte interphase: What is our current level of understanding? Adv. Mater. Interfaces 9 (8) (2022) 2101891, http://dx.doi.org/10.1002/admi.202101891, URL https://onlinelibrary.wiley.com/doi/10.1002/admi.202101891.

[34] M. Tang, S. Lu, J. Newman, Experimental and theoretical investigation of solid-electrolyte-interphase formation mechanisms on glassy carbon, J. Electrochem. Soc. 159 (11) (2012) A1775–A1785, http://dx.doi.org/10.1149/2.025211jes, URL https://iopscience.iop.org/article/10.1149/2.025211jes.

[35] S. Kranz, T. Kranz, A.G. Jaegermann, B. Roling, Is the solid electrolyte interphase in lithium-ion batteries really a solid electrolyte? Transport experiments on lithium bis(oxalato)borate-based model interphases, J. Power Sources 418 (2019) 138–146, http://dx.doi.org/10.1016/j.jpowsour.2019.01.060, URL https://linkinghub.elsevier.com/retrieve/pii/S037877531930062X.

[36] Z. Zhang, Y. Li, R. Xu, W. Zhou, Y. Li, S.T. Oyakhire, Y. Wu, J. Xu, H. Wang, Z. Yu, D.T. Boyle, W. Huang, Y. Ye, H. Chen, J. Wan, Z. Bao, W. Chiu, Y. Cui, Capturing the swelling of solid-electrolyte interphase in lithium metal batteries, Science 375 (6576) (2022) 66–70, http://dx.doi.org/10.1126/science.abi8703, URL https://www.science.org/doi/10.1126/science.abi8703.

[37] P. Keil, S.F. Schuster, J. Wilhelm, J. Travi, A. Hauser, R.C. Karl, A. Jossen, Calendar aging of lithium-ion batteries, J. Electrochem. Soc. 163 (9) (2016) A1872–A1880, http://dx.doi.org/10.1149/2.0411609jes, URL https://iopscience.iop.org/article/10.1149/2.0411609jes.

[38] P. Keil, A. Jossen, Calendar aging of NCA lithium-ion batteries investigated by differential voltage analysis and Coulomb tracking, J. Electrochem. Soc. 164 (1) (2017) A6066–A6074, http://dx.doi.org/10.1149/2.0091701jes, URL https://iopscience.iop.org/article/10.1149/2.0091701jes.

[39] M. Naumann, M. Schimpe, P. Keil, H.C. Hesse, A. Jossen, Analysis and modeling of calendar aging of a commercial LiFePO4/graphite cell, J. Energy Storage 17 (2018) 153–169, http://dx.doi.org/10.1016/j.est.2018.01.019, URL https://linkinghub.elsevier.com/retrieve/pii/S2352152X18300665.

[40] D. Werner, S. Paarmann, T. Wetzel, Calendar aging of Li-ion cells—Experimental investigation and empirical correlation, Batteries 7 (2) (2021) 28, http://dx.doi.org/10.3390/batteries7020028, URL https://www.mdpi.com/2313-0105/7/2/28.

[41] M. Broussely, S. Herreyre, P. Biensan, P. Kasztejna, K. Nechev, R. Staniewicz, Aging mechanism in Li ion cells and calendar life predictions, J. Power Sources 97–98 (2001) 13–21, http://dx.doi.org/10.1016/S0378-7753(01)00722-4, URL https://linkinghub.elsevier.com/retrieve/pii/S0378775301007224.

[42] A.J. Smith, J.C. Burns, X. Zhao, D. Xiong, J.R. Dahn, A high precision coulometry study of the SEI growth in Li/Graphite cells, J. Electrochem. Soc. 158 (5) (2011) A447, http://dx.doi.org/10.1149/1.3557892, URL https://iopscience.iop.org/article/10.1149/1.3557892.

[43] J. Wang, J. Purewal, P. Liu, J. Hicks-Garner, S. Soukazian, E. Sherman, A. Sorenson, L. Vu, H. Tataria, M.W. Verbrugge, Degradation of lithium ion batteries employing graphite negatives and nickel–cobalt–manganese oxide + spinel manganese oxide positives: Part 1, aging mechanisms and life estimation, J. Power Sources 269 (2014) 937–948, http://dx.doi.org/10.1016/j.jpowsour.2014.07.030, URL https://linkinghub.elsevier.com/retrieve/pii/S037877531401074X.

[44] L. von Kolzenberg, J. Stadler, J. Fath, M. Ecker, B. Horstmann, A. Latz, A four parameter model for the solid-electrolyte interphase to predict battery aging during operation, J. Power Sources 539 (2022) 231560, http://dx.doi.org/10.1016/j.jpowsour.2022.231560, URL https://www.sciencedirect.com/science/article/pii/S0378775322005651.

[45] J.M. Reniers, G. Mulder, D.A. Howey, Review and performance comparison of mechanical-chemical degradation models for lithium-ion batteries, J. Electrochem. Soc. 166 (14) (2019) A3189–A3200, http://dx.doi.org/10.1149/2.0281914jes, URL https://iopscience.iop.org/article/10.1149/2.0281914jes.

[46] S. Das, P.M. Attia, W.C. Chueh, M.Z. Bazant, Electrochemical kinetics of SEI growth on carbon black: Part II. Modeling, J. Electrochem. Soc. 166 (4) (2019) E107–E118, http://dx.doi.org/10.1149/2.0241904jes, URL https://iopscience.iop.org/article/10.1149/2.0241904jes.

[47] A.A. Tahmasbi, T. Kadyk, M.H. Eikerling, Statistical physics-based model of solid electrolyte interphase growth in lithium ion batteries, J. Electrochem. Soc. 164 (6) (2017) A1307–A1313, http://dx.doi.org/10.1149/2.1581706jes, URL https://iopscience.iop.org/article/10.1149/2.1581706jes.

[48] P.M. Attia, W.C. Chueh, S.J. Harris, Revisiting the t 0.5 dependence of SEI growth, J. Electrochem. Soc. 167 (9) (2020) 090535, http://dx.doi.org/10.1149/1945-7111/ab8ce4, URL https://iopscience.iop.org/article/10.1149/1945-7111/ab8ce4.

[49] M. Smeu, K. Leung, Electron leakage through heterogeneous LiF on lithium–metal battery anodes, Phys. Chem. Chem. Phys. 23 (5) (2021) 3214–3218, http://dx.doi.org/10.1039/D0CP06310J, URL http://xlink.rsc.org/?DOI=D0CP06310J.

[50] J. Pan, Q. Zhang, X. Xiao, Y.-T. Cheng, Y. Qi, Design of nanostructured heterogeneous solid ionic coatings through a multiscale defect model, ACS Appl. Mater. Interfaces 8 (8) (2016) 5687–5693, http://dx.doi.org/10.1021/acsami.5b12030, URL https://pubs.acs.org/doi/10.1021/acsami.5b12030.

[51] B. Gyenes, D.A. Stevens, V.L. Chevrier, J.R. Dahn, Understanding anomalous behavior in Coulombic efficiency measurements on Li-ion batteries, J. Electrochem. Soc. 162 (3) (2015) A278–A283, http://dx.doi.org/10.1149/2.0191503jes, URL https://iopscience.iop.org/article/10.1149/2.0191503jes.

[52] X. Jin, A. Vora, V. Hoshing, T. Saha, G. Shaver, R.E. García, O. Wasynczuk, S. Varigonda, Physically-based reduced-order capacity loss model for graphite anodes in Li-ion battery cells, J. Power Sources 342 (2017) 750–761, http://dx.doi.org/10.1016/j.jpowsour.2016.12.099, URL https://linkinghub.elsevier.com/retrieve/pii/S037877531631802X.

[53] A. Jana, A.S. Mitra, S. Das, W.C. Chueh, M.Z. Bazant, R.E. García, Physics-based, reduced order degradation model of lithium-ion batteries, J. Power Sources 545 (July) (2022) 231900, http://dx.doi.org/10.1016/j.jpowsour.2022.231900, URL https://linkinghub.elsevier.com/retrieve/pii/S0378775322008849.

[54] W. Huang, P.M. Attia, H. Wang, S.E. Renfrew, N. Jin, S. Das, Z. Zhang, D.T. Boyle, Y. Li, M.Z. Bazant, B.D. McCloskey, W.C. Chueh, Y. Cui, Evolution of the solid–electrolyte interphase on carbonaceous anodes visualized by atomic-resolution cryogenic electron microscopy, Nano Lett. 19 (8) (2019) 5140–5148, http://dx.doi.org/10.1021/acs.nanolett.9b01515, URL https://pubs.acs.org/doi/10.1021/acs.nanolett.9b01515.

Supplementary Information to "Growth of the Solid-Electrolyte Interphase: Electron Diffusion versus Solvent Diffusion"

Lukas Köbbing[a,b], Arnulf Latz[a,b,c], Birger Horstmann[a,b,c,*]

[a] *Institute of Engineering Thermodynamics, German Aerospace Center (DLR), Wilhelm-Runge-Straße 10, 89081 Ulm, Germany*
[b] *Helmholtz Institute Ulm (HIU), Helmholtzstraße 11, 89081 Ulm, Germany*
[c] *Institute of Electrochemistry, Ulm University, Albert-Einstein-Allee 47, 89081 Ulm, Germany*

1. Capacity loss at SOC=0% for Keil et al. [1]

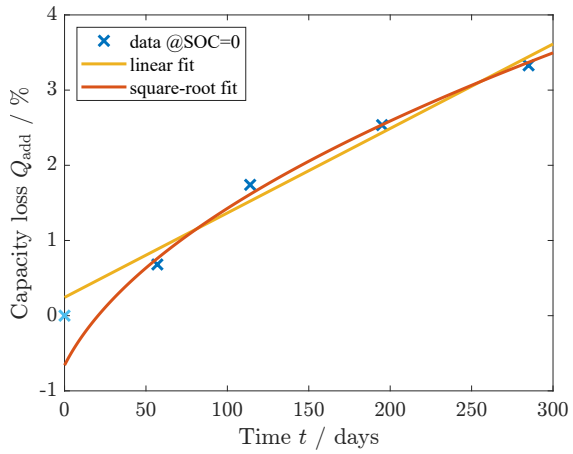

Figure SI-1: Capacity loss at SOC = 0% measured in Ref. [1]. We neglect the data point at $t = 0$ (highlighted in light blue) due to the influence of the anode overhang area that leads to an increase in the total capacity. The square-root fit describes the data points appropriately when assuming the initial capacity loss $Q_{\mathrm{SEI},0} = 1\%$.

*birger.horstmann@dlr.de

2. Capacity loss at SOC=0% for Naumann et al. [2]

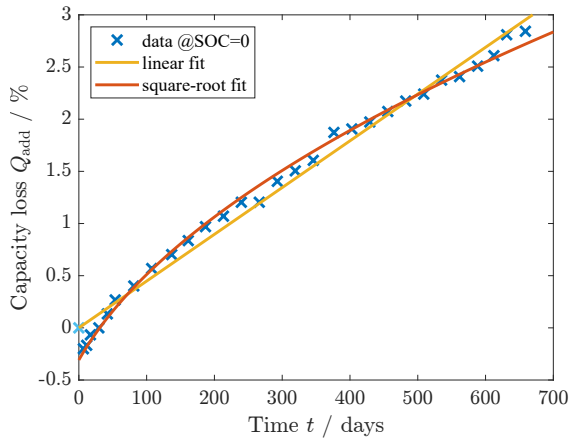

Figure SI-2: Capacity loss at SOC = 0% measured in Ref. [2]. We neglect the data point at $t = 0$ (highlighted in light blue) due to the influence of the anode overhang area that leads to an increase in the total capacity. The square-root fit describes the data points appropriately when assuming the initial capacity loss $Q_{\mathrm{SEI},0} = 1\%$.

3. Electron diffusion describing the capacity loss for Naumann et al. [2]

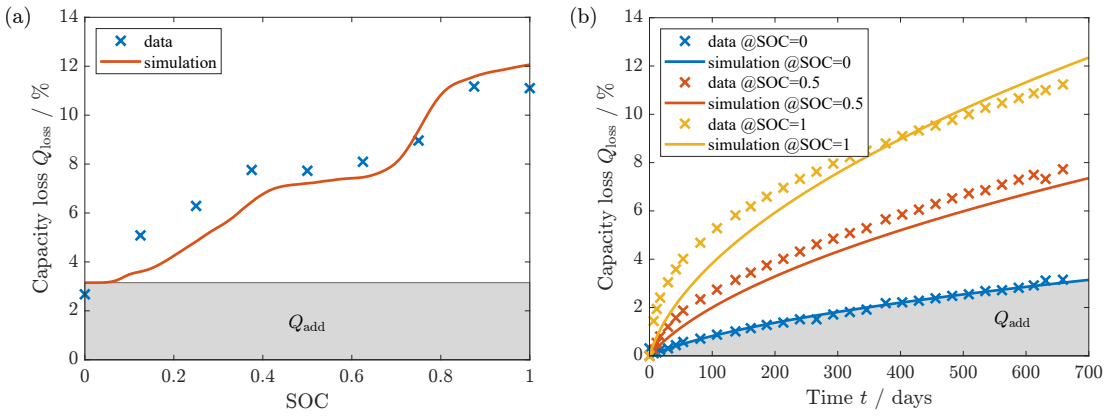

Figure SI-3: Capacity loss simulated with electron diffusion fitted to the SOC depending data measured in Ref. [2]. The focus is on measuring the time dependence at different states-of-charge. As the anode open circuit voltage is not provided for the investigated cells, we use the anode open circuit voltage measured for LFP cells in Ref. [1]. (a) Capacity loss depending on the SOC. Agreement between simulation and data is reasonable, although the exact curve for the anode open circuit voltage is not known. (b) Capacity loss depending on time. The agreement is excellent at low SOC, while at medium SOC, the general time behavior is reproduced, but the simulated values overall are too low. At high SOC, the simulation shows a large deviation from the data points.

4. Solvent diffusion describing the capacity loss for Keil et al. [1]: Variation of parameter α

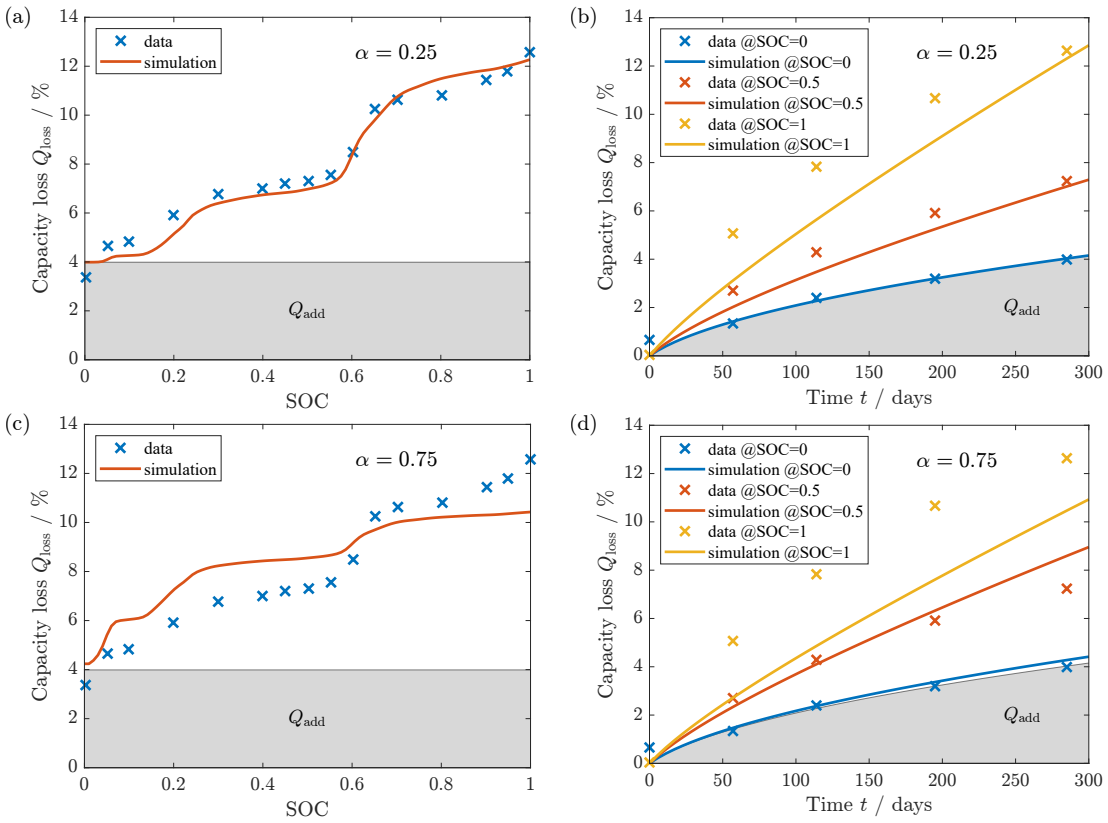

Figure SI-4: Capacity loss simulated with solvent diffusion in comparison to the data measured in Ref. [1]. Fit of the solvent diffusion model to the SOC dependence of capacity loss. (a) and (b) Parameter $\alpha = 0.25$ (a) Capacity loss depending on the SOC. The agreement between simulation and data points is reasonable. (b) Capacity loss depending on time. Simulation and experiment do not match at medium and high SOC. (c) and (d) Parameter $\alpha = 0.75$ (c) Capacity loss depending on the SOC. There is a clear deviation between the simulation and the observed data points (d) Capacity loss depending on time. Simulation and experiment do not match at medium and high SOC.

5. Solvent diffusion describing the capacity loss for Naumann et al. [2]

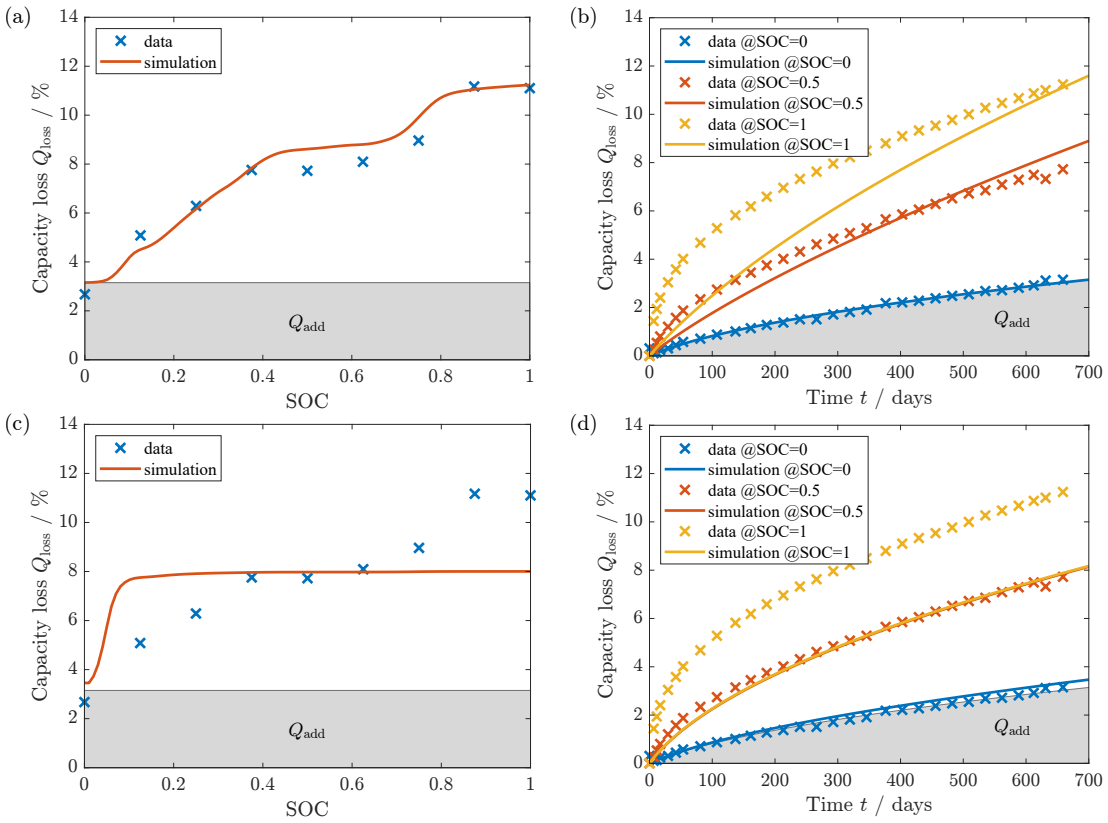

Figure SI-5: Capacity loss simulated with solvent diffusion in comparison to the data measured in Ref. [2]. (a) and (b) Fit of the solvent diffusion model to the SOC dependence of capacity loss (a) Capacity loss depending on the SOC. The agreement between simulation and data points is reasonable. (b) Capacity loss depending on time. Simulation and experiment do not match at medium and high SOC. (c) and (d) Fit of the solvent diffusion model to the time dependence of capacity loss at SOC = 50% (c) Capacity loss depending on the SOC. The observed dependence is not captured at all. (d) Capacity loss depending on time. Good agreement is achieved at SOC = 50%, but the simulation does not reproduce the behavior at SOC = 100%.

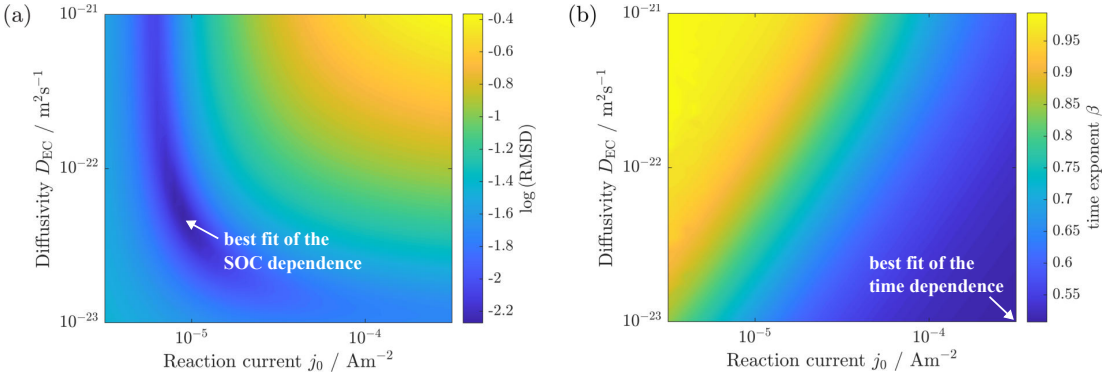

Figure SI-6: Parameter study for the capacity loss simulated with solvent diffusion with a variation of the reaction current j_0 and the diffusion coefficient D_{EC}. (a) Logarithm of the root mean square deviation of the simulated capacity loss depending on the SOC from the experiment [2]. The smallest deviation is depicted in dark blue and reached for small reaction current j_0 and medium diffusivity D_{EC}. The best fit of the SOC dependence with the parameters used in Fig. SI-5(a) is highlighted. (b) Fitted time exponent β to the simulation. The experiment can be approximately described with $t^{0.5}$ depicted in dark blue. Either large values of j_0 or small values of D_{EC} are needed to achieve a good agreement with $t^{0.5}$. The best fit of the time dependence with the parameters used in Fig. SI-5(d) is highlighted.

References

[1] P. Keil, S. F. Schuster, J. Wilhelm, J. Travi, A. Hauser, R. C. Karl, A. Jossen, Calendar Aging of Lithium-Ion Batteries, Journal of The Electrochemical Society 163 (9) (2016) A1872–A1880. doi:10.1149/2.0411609jes.
URL https://iopscience.iop.org/article/10.1149/2.0411609jes

[2] M. Naumann, M. Schimpe, P. Keil, H. C. Hesse, A. Jossen, Analysis and modeling of calendar aging of a commercial LiFePO4/graphite cell, Journal of Energy Storage 17 (2018) 153–169. doi:10.1016/j.est.2018.01.019.
URL https://doi.org/10.1016/j.est.2018.01.019https://linkinghub.elsevier.com/retrieve/pii/S2352152X18300665

Paper II

Voltage Hysteresis of Silicon Nanoparticles: Chemo-Mechanical Particle-SEI Model

Authors	Lukas Köbbing, Arnulf Latz, Birger Horstmann
Journal	Advanced Functional Materials
Year	2024
Volume (Issue)	34 (7)
Pages	2308818
DOI	10.1002/adfm.202308818
Copyright	CC BY 4.0
Copyright link	https://creativecommons.org/licenses/by/4.0/
Copyright notice	Reprinted from Ref. [173].
Preprint DOI	10.48550/arXiv.2305.17533

Author's Contribution

L. Köbbing further developed and implemented the thermodynamically consistent chemo-mechanical silicon-SEI model based on the publication by Kolzenberg et al. [63]. Particularly, L. Köbbing developed the notion of the mechanical impact of the SEI as reason for the silicon voltage hysteresis and included viscous behavior of the SEI. Furthermore, L. Köbbing analyzed the results of the chemo-mechanical model, evaluating the predicted silicon voltage hysteresis in comparison to published experimental data. The model development and analysis was supervised by B. Horstmann. In addition, L. Köbbing created the initial draft of the manuscript and the supporting information including text and figures. The writing was then thoroughly reviewed by B. Horstmann and remarked and approved by A. Latz.

RESEARCH ARTICLE

ADVANCED FUNCTIONAL MATERIALS
www.afm-journal.de

Voltage Hysteresis of Silicon Nanoparticles: Chemo-Mechanical Particle-SEI Model

*Lukas Köbbing, Arnulf Latz, and Birger Horstmann**

Silicon is a promising anode material for next-generation lithium-ion batteries. However, the volume change and the voltage hysteresis during lithiation and delithiation are two substantial drawbacks to their lifetime and performance. The reason for the voltage hysteresis in amorphous silicon nanoparticles covered by a solid-electrolyte interphase (SEI) is investigated. Concentration gradients inside the nanoscale silicon cannot produce the massive stresses necessary to cause the reported voltage hysteresis. The chemo-mechanical model shows that plastic deformation of the stiff, inorganic SEI during lithiation and delithiation reproduces the observed silicon open-circuit voltage hysteresis. Additionally, the viscous behavior of the SEI explains the difference between the voltage hysteresis observed at low currents and after relaxation. It is concluded that the visco-elastoplastic behavior of the SEI is the origin of the voltage hysteresis in silicon nanoparticle anodes. Thus, consideration of the SEI mechanics is crucial for further improvements.

1. Introduction

The improvement of lithium-ion batteries is essential for facing the pressing global challenges. Due to their high theoretical capacity, pure silicon anodes are a promising candidate for the next generation of lithium-ion batteries.[1–5] Therefore, research makes an effort to investigate this advantageous and abundant material.

Silicon confronts research with two challenging features on the way to commercial silicon anodes. The first is the significant expansion and constriction with a volume change of up to 300% during lithiation and delithiation, respectively. The deformation leads to the cracking of large silicon particles and the formation of networks with nanometer-sized silicon particles.[6] However, no cracking occurs below a critical particle diameter of ≈150 nm.[7] Due to the superior mechanical stability, recent research concentrates on investigating nano-structured silicon anodes.[8–12] Additionally, experiments observe a volume hysteresis, that is, a difference in the silicon particle or anode volume between lithiation and delithiation.[13–16]

The second major issue is the voltage hysteresis of silicon anodes observed in experiments for various silicon structures, namely thin films,[13,17–23] nanowires,[24,25] and nanoparticles.[26–29] The voltage hysteresis considerably reduces energy efficiency and leads to detrimental heat generation during cycling.[30] Thus, the hysteresis phenomenon is a very important challenge for the commercialization of silicon-anode lithium-ion batteries. Most literature reports the hysteresis of pseudo-open-circuit voltages at currents smaller than C/10. However, even for the open-circuit voltage measured by the galvanostatic intermittent titration technique (GITT) after relaxation periods, a reduced, but still significant voltage hysteresis remains.[20,28,29] We emphasize that the measurements reveal a clear difference in the size of the voltage hysteresis observed for small currents and after relaxation periods.

Phase transformations can explain a voltage hysteresis for crystalline silicon or the first cycle of amorphous silicon anodes.[31–34] However, also amorphous silicon anodes show a voltage hysteresis after the first cycle. In this case, the literature commonly considers plastic flow of silicon as the reason for the hysteresis phenomenon. In thin-film silicon electrodes, massive stresses arise naturally due to the restricted expansion in the in-plane direction.[22,35,36] For micron-sized silicon particles or high applied currents, the slow diffusion in silicon can lead to concentration gradients during lithiation and delithiation, inducing a voltage hysteresis.[37–39] Nevertheless, the reason for substantial stresses inside amorphous silicon nanoparticles during slow lithiation and delithiation remains unclear.

Similarly to other anode materials, the solid-electrolyte interphase (SEI) naturally covers silicon particles. The SEI protects the anode from the electrolyte[40,41] and grows via electron transport from the anode through the SEI.[42,43] Additionally, between the silicon particle and the SEI, there is a native silicon oxide layer

L. Köbbing, A. Latz, B. Horstmann
Institute of Engineering Thermodynamics
German Aerospace Center (DLR)
Wilhelm-Runge-Straße 10, 89081 Ulm, Germany
E-mail: birger.horstmann@dlr.de
L. Köbbing, A. Latz, B. Horstmann
Helmholtz Institute Ulm (HIU)
Helmholtzstraße 11, 89081 Ulm, Germany
A. Latz, B. Horstmann
Institute of Electrochemistry
Ulm University
Albert-Einstein-Allee 47, 89081 Ulm, Germany

The ORCID identification number(s) for the author(s) of this article can be found under https://doi.org/10.1002/adfm.202308818

DOI: 10.1002/adfm.202308818

ADVANCED SCIENCE NEWS
www.advancedsciencenews.com

ADVANCED FUNCTIONAL MATERIALS
www.afm-journal.de

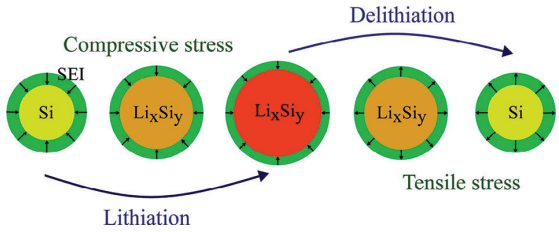

Figure 1. Scheme of the radial stress inside the SEI during lithiation and delithiation of a silicon nanoparticle.

influencing the interface between particle and SEI.[44] Research invests much effort into characterizing and improving the SEI on silicon anodes.[45–51] Due to the considerable volume changes of silicon anodes, the plasticity and cracking of the SEI on silicon deserve particular interest.[52–56]

As the SEI deforms due to the chemical expansion and shrinkage of the particle, considerable strains and stresses occur inside the SEI. Certain studies even claim that the compressive stress of the SEI acting on the particle might be beneficial to avoid particle cracking.[4,57,58] Further, we note that a carbon coating on top of the silicon particle reduces the observed voltage hysteresis of the silicon anode.[27] The reason might be a different SEI composition on carbon and silicon. In conclusion, we propose that the composition and stress of the SEI have a crucial impact on the lithiation behavior and, particularly, on the voltage hysteresis of silicon particles.

In this paper, we consider a visco-elastoplastic SEI model based on non-equilibrium thermodynamics.[59] We evaluate the influence of the stress generated by the SEI on the lithiation and delithiation behavior of an amorphous silicon nanoparticle. Our model can faithfully reproduce the broadly recognized but empirical Plett model. Furthermore, it allows to investigate the reason for the difference between the voltage hysteresis for small currents and GITT data points. Finally, we discuss the influence of the mechanical parameters of the SEI and the silicon nanoparticle on the silicon voltage hysteresis.

2. Theory

When the silicon anode particle expands and contracts, distinct strains emerge inside the SEI as illustrated in **Figure 1**. Elastic deformations lead to significant stresses in tangential and radial directions. The radial stress component impacts the stress inside the particle, which crucially influences the silicon potential. We discuss a chemo-mechanical silicon particle model and a visco-elastoplastic SEI model.

2.1. Silicon Particle Model

Our silicon particle model is based on the work of Kolzenberg et al. complemented by plasticity.[56,60] During lithiation and delithiation, the silicon particle experiences significant expansion and shrinkage, respectively. The deformation tensor $\mathbf{F} = \partial\vec{x}/\partial\vec{X}_0$ describes the transformation from the undeformed Lagrangian frame to the deformed Eulerian frame.[61] We use the large deformation approach to describe the deformation inside the silicon particle.[62] Therefore, the total deformation $\mathbf{F}$ consisting of a chemical deformation $\mathbf{F}_{ch}$, an elastic deformation $\mathbf{F}_{el}$, and a plastic deformation $\mathbf{F}_{pl}$ reads

$$\mathbf{F} = \mathbf{F}_{pl}\mathbf{F}_{el}\mathbf{F}_{ch} \tag{1}$$

The chemical deformation $\mathbf{F}_{ch}$ is described by the concentration of lithium $c_{Li,0}$ inside the silicon particle in the Lagrangian frame according to

$$\mathbf{F}_{ch} = \lambda_{ch}\mathbf{Id} = (1 + \nu_{Li}c_{Li,0})^{1/3}\mathbf{Id} \tag{2}$$

where ν_{Li} is the molar volume of lithium inside silicon.

The lithiation behavior and the mechanical deformations are derived in our model based on non-equilibrium thermodynamics. Our model builds up on the free energy according to the first law of thermodynamics. In Supporting Information, we discuss non-negativity of the entropy production $\mathcal{R} \geq 0$ in our model stated in Equation (S12), Supporting Information, which means accordance with the second law.

The free energy density $\rho_0\varphi$ of the silicon anode consists of a chemical contribution depending on the lithium concentration and a mechanical contribution due to elastic deformation. The free energy of the silicon anode reads

$$\rho_0\varphi = -\int_0^{c_{Li}} FU_0\left(c'_{Li}\right)\mathrm{d}c'_{Li} + \frac{1}{2}\left(\lambda_{Si}\left(\mathrm{tr}\left(\mathbf{E}_{el}\right)\right)^2 + 2G_{Si}\,\mathrm{tr}\left(\mathbf{E}_{el}^2\right)\right) \tag{3}$$

with the Faraday constant F and the ideal open-circuit voltage of silicon U_0. The elastic strain tensor $\mathbf{E}_{el}$ in Equation (3) is defined by

$$\mathbf{E}_{el} = \frac{1}{2}\left(\mathbf{F}_{el}^{T}\mathbf{F}_{el} - \mathbf{Id}\right) \tag{4}$$

The first and second Lamé constants read $\lambda_{Si} = 2G_{Si}\nu_{Si}/(1-2\nu_{Si})$ and $G_{Si} = E_{Si}/2(1+\nu_{Si})$, where ν_{Si} is the Poisson ratio of silicon. The elastic deformation $\mathbf{F}_{el}$ depends on the Piola–Kirchhoff stress $\mathbf{P}$ inside the particle determined by the constitutive equation

$$\mathbf{P} = 2\mathbf{F}\frac{\partial\rho_0\varphi}{\partial\mathbf{C}} = \lambda_{ch}^{-2}\mathbf{F}\mathbf{F}_{pl}^{-T}\mathbf{F}_{pl}^{-1}\left(\lambda_{Si}\,\mathrm{tr}(\mathbf{E}_{el})\mathbf{Id} + 2G_{Si}\mathbf{E}_{el}\right) \tag{5}$$

where $\mathbf{C}$ is the right Cauchy–Green tensor $\mathbf{C} = \mathbf{F}^{T}\mathbf{F}$. The Piola–Kirchhoff stress is related to the Cauchy stress σ as $\mathbf{P} = J\sigma\mathbf{F}^{-T}$ with $J = \det\mathbf{F}$. The Piola–Kirchhoff stress $\mathbf{P}$ defined in Equation (5) has to fulfill the momentum balance in the Lagrangian frame

$$0 = \nabla_0 \cdot \mathbf{P} \tag{6}$$

In addition to the elastic deformation, the particle deforms plastically when reaching the von Mises yield criterion

$$f = \frac{\frac{3}{2}|\mathbf{M}^{dev}|^2}{\sigma_{Y,Si}^2} - 1 \leq 0 \tag{7}$$

ADVANCED SCIENCE NEWS
www.advancedsciencenews.com

ADVANCED FUNCTIONAL MATERIALS
www.afm-journal.de

where $\mathbf{M}^{\text{dev}} = \mathbf{M} - 1/3\,\text{tr}\,\mathbf{M}$ is the deviatoric part of the Mandel stress $\mathbf{M} = \mathbf{F}_{\text{rev}}^{\text{T}}\sigma\mathbf{F}_{\text{rev}}^{-\text{T}}$ with the reversible part of the deformation $\mathbf{F}_{\text{rev}} = \mathbf{F}_{\text{el}}\mathbf{F}_{\text{ch}}$. The yield stress σ_{Y} depends on the material and reveals how much stress the particle can withstand with reversible deformations. The plastic flow $\mathbf{L}_{\text{pl}} = \dot{\mathbf{F}}_{\text{pl}}\mathbf{F}_{\text{pl}}^{-1}$ is calculated by

$$\mathbf{L}_{\text{pl}} = \phi\frac{\partial f}{\partial \mathbf{M}} \tag{8}$$

where the plastic multiplier ϕ is determined from the consistency condition $\dot{f} = 0$.

The defining equation for the lithiation and delithiation of a silicon particle reads

$$\dot{c}_{\text{Li},0} = -\nabla_0 \cdot \vec{N}_{\text{Li},0} \tag{9}$$

with the lithium flux $\vec{N}_{\text{Li},0} = -L\nabla_0\mu_{\text{Li}}$ and the electro–chemo–mechanical potential μ_{Li}. The mobility is determined by $L = D_{\text{Li}}(\partial\mu_{\text{Li}}/\partial c_{\text{Li},0})^{-1}$ with D_{Li} the diffusion coefficient of lithium in silicon. At the boundary of the particle $r = R$, the lithium flux $\vec{N}_{\text{Li},0}(R)$ is determined by the applied (de)lithiation rate.

The lithium concentration and the stress inside the particle influence the electro–chemo–mechanical potential of lithium according to the constitutive equation

$$\mu_{\text{Li}} = \frac{\partial\rho_0\varphi}{\partial c_{\text{Li},0}} = -FU_0 - \frac{v_{\text{Li}}}{3\lambda_{\text{ch}}^3}\mathbf{P} : \mathbf{F} \tag{10}$$

The chemical potential at the outer border of the anode determines the measurable silicon open-circuit voltage (OCV) by $U = -\mu_{\text{Li}}/F$. Thus, the OCV reads

$$U = U_0 + \frac{v_{\text{Li}}}{3F\lambda_{\text{ch}}^3}\mathbf{P} : \mathbf{F} \tag{11}$$

We determine the ideal open-circuit voltage U_0 as the mean value of the open-circuit voltages measured via GITT during lithiation and delithiation in ref. [28]. However, stress inside the particle crucially affects the open-circuit voltage during lithiation and delithiation.

2.2. SEI Model

Inside the SEI, there is no chemical deformation, as no lithiation of the SEI is possible. Therefore, the SEI only deforms elastically and plastically

$$\mathbf{F}_{\text{SEI}} = \mathbf{F}_{\text{SEI,pl}}\mathbf{F}_{\text{SEI,el}} \tag{12}$$

In our visco-elastoplastic SEI model, elastoplastic deformations and viscous flow contribute to the total stress. The stress due to elastoplastic deformations is defined similarly to Equation (5) as

$$\begin{aligned}\mathbf{P}_{\text{SEI,el}} &= 2\mathbf{F}_{\text{SEI}}\frac{\partial\rho_{0,\text{SEI}}\varphi_{\text{SEI}}}{\partial\mathbf{C}_{\text{SEI}}} \\ &= \mathbf{F}_{\text{SEI}}\mathbf{F}_{\text{SEI,pl}}^{-\text{T}}\mathbf{F}_{\text{SEI,pl}}^{-1}\left(\lambda_{\text{SEI}}\,\text{tr}(\mathbf{E}_{\text{SEI,el}})\mathbf{Id} + 2G_{\text{SEI}}\mathbf{E}_{\text{SEI,el}}\right)\end{aligned} \tag{13}$$

with the strain tensor $\mathbf{E}_{\text{SEI, el}}$, the right Cauchy–Green tensor $\mathbf{C}_{\text{SEI}}$, and the Lamé constants λ_{SEI} and G_{SEI} defined analog to the particle model. The free energy density of the SEI is defined according to merely the mechanical contribution in Equation (3).

Plastic flow can occur inside the SEI similarly to the particle when reaching the von Mises yield criterion

$$f_{\text{SEI}} = \frac{\frac{3}{2}|\mathbf{M}_{\text{SEI,el}}^{\text{dev}}|^2}{\sigma_{\text{Y,SEI}}^2} - 1 \le 0 \tag{14}$$

leading to the plastic flow

$$\mathbf{L}_{\text{SEI,pl}} = \phi_{\text{SEI}}\frac{\partial f_{\text{SEI}}}{\partial\mathbf{M}_{\text{SEI,el}}} \tag{15}$$

The consistency condition $\dot{f}_{\text{SEI}} = 0$ determines again the value of the plastic multiplier ϕ_{SEI}. We emphasize that plastic flow in the SEI is driven by the deviatoric part of the elastoplastic stress contribution $\mathbf{M}_{\text{SEI,el}}^{\text{dev}}$.

In addition to the elastoplastic model discussed in ref. [56], we consider stress generated by the viscous flow of the SEI. The viscous Cauchy stress is defined as

$$\sigma_{\text{SEI,visc}} = \eta_{\text{SEI}}\dot{\mathbf{E}}_{\text{SEI}} \tag{16}$$

with the viscosity of the SEI η_{SEI}. Radial symmetry in our system ensures $\dot{\mathbf{E}}_{\text{SEI}} = \mathbf{F}_{\text{SEI}}^{\text{T}}\dot{\mathbf{F}}_{\text{SEI}}$. Therefore, the viscous Piola–Kirchhoff stress corresponding to Equation (16) reads

$$\mathbf{P}_{\text{SEI,visc}} = J_{\text{SEI}}\eta_{\text{SEI}}\dot{\mathbf{F}}_{\text{SEI}} \tag{17}$$

with $J_{\text{SEI}} = \det\mathbf{F}_{\text{SEI}}$.

We describe the SEI as a power-law shear thinning material. Therefore, the viscosity decreases with increasing strain rate

$$\eta_{\text{SEI}}\left(\dot{\mathbf{E}}_{\text{SEI}}\right) = \eta_{\text{SEI},0}\dot{\mathbf{E}}_{\text{SEI}}^{n-1} \tag{18}$$

where $\eta_{\text{SEI, 0}}$ is a constant value and $n < 1$ is the shear-thinning exponent.

In our model, we consider the viscous behavior in parallel to the elastoplastic model. Thus, the sum of the elastic and viscous contributions describes the total Piola–Kirchhoff stress as

$$\mathbf{P}_{\text{SEI}} = \mathbf{P}_{\text{SEI,el}} + \mathbf{P}_{\text{SEI,visc}} \tag{19}$$

Analog to the particle model, the momentum balance

$$0 = \nabla_0 \cdot \mathbf{P}_{\text{SEI}} \tag{20}$$

determines the stress inside the SEI.

Finally, we emphasize that our model describes the SEI mechanics on a continuum level. The visco-elastoplastic behavior is not a single-crystal property but results from subsequent partial SEI fracture and healing.[56] This approach is valid for small currents, where the SEI fractures only partially and healing is fast compared to the lithiation timescale.

ADVANCED SCIENCE NEWS
www.advancedsciencenews.com

ADVANCED FUNCTIONAL MATERIALS
www.afm-journal.de

2.3. Particle-SEI Interface

At the interface between the anode particle and SEI, we assume a perfect sticking of the SEI on top of the silicon particle. Therefore, the stresses inside the particle and SEI interact at the interface. Precisely, the radial component of the Cauchy stress has to be equal in particle and SEI at the boundary. Due to the radial symmetry, this also implies the equivalence of the radial part of the Piola–Kirchhoff stress at the interface

$$\mathbf{P}_{\mathrm{rr}}|_{r=R} = \mathbf{P}_{\mathrm{SEI,rr}}|_{r=R} \tag{21}$$

Inside the particle, the chemical contribution dominates the total deformation. In contrast, the SEI deforms only elastically and plastically. Thus, mechanical deformations of the SEI have to afford the large deformation implied by the particle. These deformations result in significant strains and stresses inside the SEI. Consequently, the stress inside the SEI can substantially affect the stress and lithiation behavior of the silicon particle.

2.4. Material Parameters

The literature states values of Young's modulus of the SEI E_{SEI} between only a few hundreds of MPa and values greater than 100 GPa. For a better overview, we divide the reported values into the categories: soft with $E_{\mathrm{SEI}} < 1\,\mathrm{GPa}$,[63–67] medium with $1\,\mathrm{GPa} \leqslant E_{\mathrm{SEI}} < 10\,\mathrm{GPa}$,[63,66,68–72] stiff with $10\,\mathrm{GPa} \leqslant E_{\mathrm{SEI}} < 100\,\mathrm{GPa}$,[53,68–70,73–75] and very stiff SEI with $E_{\mathrm{SEI}} \geqslant 100\,\mathrm{GPa}$.[68,75] In general, references report lower values of Young's modulus for thicker SEI layers. In contrast, the initial SEI or the inner, inorganic SEI layer reveals higher values of Young's modulus. Due to the small scale, the measurement values of the inner SEI might underestimate the corresponding Young's modulus, as the measured point might be in the transition zone between the inner and the outer SEI. Further, the literature reports a size effect of Young's modulus on the nanoscale for different materials. Structures on the nanometer level typically reveal a higher Young's modulus compared to bulk values.[76–80] Therefore, we use $E_{\mathrm{SEI}} = 100\,\mathrm{GPa}$ for the SEI in our studies.

Experiments attempt to determine the viscosity of the SEI but face severe difficulties due to the small length scale of interest. Recently, research has advanced in estimating the viscosity value of the outer, organic SEI layer.[67,75] However, the inner, inorganic SEI layer is known to be much stiffer than the outer layer. We assume this coincides with a considerably higher viscosity of the inner layer. Consequently, reasonable values of the viscosity of the inner SEI are between $\eta = 10^7\,\mathrm{Pa\,s}$ measured for pitch, a highly viscous polymer,[81] and $\eta = 10^{15}\,\mathrm{Pa\,s}$ measured for silicon oxide.[82–84] We estimate the shear-thinning exponent to be $n = 0.15$ from ref. [85].

Measurements for Young's modulus of silicon show a wide range of values.[86,87] For amorphous macroscopic silicon, literature reports values around 90[88,89] and 125 GPa.[90,91] Crystalline silicon nanowires reveal values between 50 and 250 GPa.[87,92] At the nanoscale, we expect that the values of Young's modulus of amorphous and crystalline silicon will approach each other as crystalline phases inside nanoparticles gain more importance. In comparison to nanowires, nanoparticles may even show more pronounced surface effects leading to higher values of Young's modulus. Therefore, we use $E_{\mathrm{Si}} = 200\,\mathrm{GPa}$ in our simulations.

If not mentioned explicitly, we use the parameters presented in Table S1, Supporting Information.

2.5. Computational Details

We implement our model in MATLAB using a finite difference approach. We solve the partial differential Equations (6), (8), (9), (15), and (20) with the solver ode15i by discretizing the radial dimension. The principal variables inside the particle are the lithium concentration $c_{\mathrm{Li},0}$, the deformed radius r, and the radial component of the plastic deformation $\mathbf{F}_{\mathrm{pl,rr}}$ of each element. Inside the SEI domain, the principal variables are the deformed radius r_{SEI} and the radial component of the plastic deformation $\mathbf{F}_{\mathrm{SEI,pl,rr}}$ of each SEI element.

3. Results and Discussion

Based on our chemo-mechanical model, we evaluate the influence of the mechanics of the silicon particle and its covering interphase on the voltage hysteresis of silicon anodes in this section. Although we term the covering layer SEI throughout this paper, our model also describes a particle covered by a silicon oxide layer.

Without the impact of the SEI, we can create three different scenarios presented in Sections S2–S4, Supporting Information reasoning the experimental voltage hysteresis. First, literature often considers silicon thin-film anodes, where the expansion and contraction are restricted to the normal direction of the film as illustrated in Figure S1, Supporting Information. This leads to significant stresses and plastic flow, resulting in a voltage hysteresis shown in Figure S2, Supporting Information. Second, in a real multi-particle electrode, the expansion of a single particle is constrained. We model this situation with a simplified particle confined by a fixed wall (see Figure S3, Supporting Information). As depicted in Figure S4, Supporting Information, considerable stresses and a voltage hysteresis occur only during the first lithiation due to permanent plastic deformation. Third, massive stresses generated by concentration gradients can arise in silicon particles without constraints due to the slow diffusion process. However, Figure S5, Supporting Information shows that no voltage hysteresis is visible for silicon nanoparticles cycled at C/20. Only currents as large as 1C create substantial concentration gradients and a voltage hysteresis in silicon nanoparticles without constraints. We emphasize that these concentration gradients vanish after relaxation and cannot explain the open-circuit voltage hysteresis.

Consequently, plastic flow due to slow diffusion or constrained particles cannot reproduce the voltage hysteresis observed in GITT measurements with a silicon nanoparticle anode. Thus, we investigate the influence of the SEI on the stress and potential inside the silicon particle.

3.1. Open-Circuit Voltage Hysteresis

In our model, we consider the SEI as a visco-elastoplastic material. Inside the particle, a substantial amount of the total

ADVANCED SCIENCE NEWS
www.advancedsciencenews.com

ADVANCED FUNCTIONAL MATERIALS
www.afm-journal.de

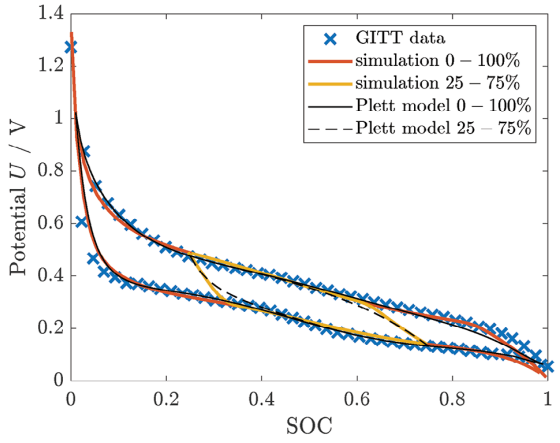

Figure 2. Open-circuit voltage hysteresis generated by a visco-elastoplastic SEI with $E_{Si} = 200$ GPa and $E_{SEI} = 100$ GPa in comparison to GITT measurement.[28] A complete cycle and a partial cycle are depicted for the simulation and the Plett model.

deformation is the chemical contribution due to the change in lithium concentration. In contrast, the SEI merely shows mechanical deformations. As the deformation of the SEI has to adjust to the deformation of the particle, considerable strains occur naturally inside the SEI. Assuming a high Young's modulus of the SEI, strains inside the SEI cause significant stresses. As discussed, the radial component of the stress inside the SEI at the particle-SEI interface determines the radial stress component inside the particle at the interface. For currents as small as C/20, the radial stress component of the SEI is the main reason for the stress inside the particle. The particle stress distributes uniformly, reasoning vanishing deviatoric stress. Therefore, plastic flow will not occur inside the particle. Nevertheless, the substantial stresses inside the particle can generate a voltage hysteresis.

In our simulation, we determine the open-circuit voltage after a relaxation period to reproduce GITT measurements. **Figure 2** depicts the open-circuit voltage for lithiation and delithiation simulated with our visco-elastoplastic SEI model depending on the state-of-charge (SOC). Notably, the simulation reveals a significant voltage hysteresis. Furthermore, our results agree well with the experimentally observed voltage hysteresis.[28] Only for very low and very high SOC does the experiment show a steeper decrease and increase, respectively, compared to the simulation. We attribute this to the use of the mean value of the lithiation and delithiation GITT voltages as the ideal open-circuit voltage curve. However, the situation is asymmetric at the endpoints of lithiation and delithiation. Before swapping the current direction, the stress stays constant but changes gradually after. Therefore, the ideal open-circuit voltage will differ from the mean value of the lithiation and delithiation open-circuit voltages at very low and very high SOC.

The standard fitting model to describe transitions between the lithiation and delithiation voltages is the Plett model.[93–95] We briefly present the equations describing the Plett model in Section S5, Supporting Information. In Figure 2, we depict our simulation of a complete cycle and a partial cycle between 25% and 75% in comparison to the behavior of the Plett model. The illustration reveals that our physical model is in reasonable accordance with the phenomenological Plett model.

Before discussing the evolution of the stresses inside particle and SEI in detail, we attempt to illustrate the physical mechanism of stress-potential coupling leading to the hysteresis behavior. During lithiation, the silicon particle expands continuously. To withstand the expansion, the SEI has to deform mechanically, generating a compressive stress acting on the particle. This compression increases the energy needed to insert more lithium inside the particle. Therefore, the chemo-mechanical potential of lithium inside the silicon particle increases, leading to a decrease in the anode OCV (Equation (11)). The additional energy necessary for the lithiation is transformed into pressure-volume work of particle and SEI. When the system behaves purely elastically, this energy is completely regained during the delithiation such that no hysteresis behavior occurs. However, plasticity inside the model causes irreversible deformation of the SEI and energy dissipation. During delithiation, the plastically expanded SEI induces tensile stress in the particle. This increases the energy necessary to extract lithium from the particle. Thus, the chemo-mechanical potential of lithium decreases, leading to an increase in the anode OCV. In total, plasticity of the SEI causes the OCV hysteresis. The energy dissipated due to plastic deformations is equivalent to the area between the hysteresis branches of the OCV curve.

After the illustrative description of the hysteresis, we discuss the stress behavior in detail. In our model, the radial stress component of the SEI impacts the stress inside the particle and implicitly generates the voltage hysteresis of the silicon nanoparticle. In **Figure 3**a, we illustrate the stress components inside the SEI at the particle-SEI interface. During lithiation, the particle expands, and the SEI deforms purely elastically until reaching the yield criterion. As the particle surface area increases, the SEI has to stretch in the tangential direction leading to tensile tangential stress (yellow). This tangential expansion leads to a constriction in the SEI thickness and compressive radial stress (red). Upon meeting the yield criterion, the SEI starts to flow plastically. The tangential stress shows a significant kink at the transition between elastic and plastic deformation. In the purely plastic regime, the stress components change only slightly. The radial component stays compressive, and the tangential tensile. Switching to delithiation, the SEI immediately leaves the plastic regime and deforms purely elastically again. The tensile tangential stress reduces, and compressive stress occurs. Simultaneously, compressive radial stress reduces, and tensile stress occurs. Reaching the plastic limit, the compressive tangential stress and the tensile radial stress stay almost constant until the end of the delithiation process. Eventually, the radial stress and the tangential stress of the SEI show a hysteresis behavior due to path-dependent plastic deformations.

The maximum stress in the system results from the yield condition, which determines the maximum deviatoric stress independent of the particle size. However, expressing Equation (6) in spherical coordinates indicates that the radial stress component increases with the ratio of SEI thickness and particle radius. Nevertheless, the particle size of interest is around the optimum size for silicon nanoparticles in terms of degradation found in ref. [55]. That means smaller particles with a higher specific surface area are covered by a thinner SEI compared to larger particles. We

ADVANCED SCIENCE NEWS
www.advancedsciencenews.com

ADVANCED FUNCTIONAL MATERIALS
www.afm-journal.de

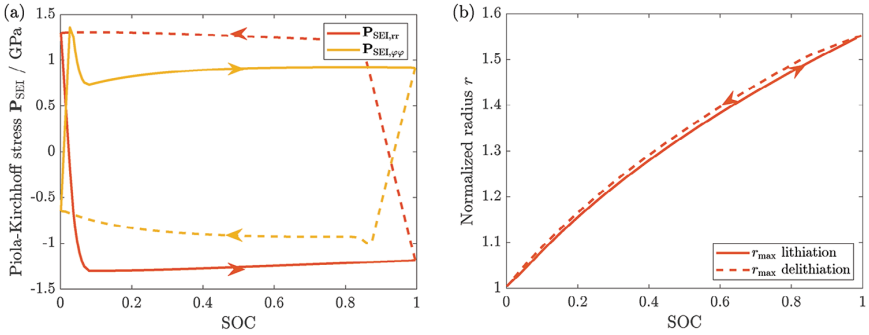

Figure 3. Stress and size effects of a visco-elastoplastic SEI covering a silicon particle with $E_{Si} = 200$ GPa and $E_{SEI} = 100$ GPa. Lithiation is depicted with solid and delithiation with dashed lines. a) Hysteresis of the stress components inside the SEI at the SEI-particle interface. b) Hysteresis of the particle radius generated by the impact of the visco-elastoplastic SEI.

conclude that a change in particle size has only a minor influence on the size of the OCV hysteresis in the realm of interest.

As the stresses inside particle and SEI influence the particle deformations, the stress hysteresis induces a hysteresis phenomenon in the deformation tensor. This leads to a hysteresis behavior in the radius and volume of the particle. In Figure 3b, we depict the particle radius depending on the SOC, revealing a clear hysteresis effect. The particle radius shows larger values for delithiation than for lithiation at the same SOC. The simulation result matches qualitatively the volume hysteresis reported for silicon anodes.[13–16]

3.2. Voltage Hysteresis During Cycling

The literature states a significant difference between the voltage hysteresis of silicon anodes for small currents and the open-circuit voltage hysteresis measured with GITT. As discussed at the beginning of Section 3, we cannot attribute this to concentration gradients inside the particle. Instead, we assign the potential difference to the viscous behavior of the SEI. As the literature provides no value for the viscosity of the inner SEI, we fit the viscosity to the experimental data.

To investigate the influence of viscous SEI behavior on the voltage during slow cycling, we simulate the GITT measurement procedure with alternating C/20 current steps and relaxation periods. We show the simulated voltage together with the voltage measured during the GITT experiment.[28] in **Figure 4**a. The simulated voltage profile shows a good agreement with the experiment. The fitted viscosity value in Figure 4a is $\eta_{SEI,0} = 15\,\text{GPa}\,\text{s}^n$. Only the potential difference between the two observed hysteresis phenomena stays approximately constant in the experiment but slightly decreases with increasing SOC in the simulation. The declining strain rate of the SEI for higher SOC causes the observed decrease of the viscous contribution in the simulation. More pronounced shear thinning behavior could reduce the deviation between simulation and experiment.

In Figure 4b, we depict the simulation of a single lithiation pulse with a subsequent rest period in comparison to an experimental GITT pulse.[29] The voltage curve demonstrates the transition between the lithiation potential and the measured GITT data points and vice versa. During the lithiation step, the simulation exhibits a slower decay from the rest potential to the lithiation potential compared to the experiment. Therefore, the timescale of the simulated lithiation step with the applied parameters is larger than the experimental value. For the subsequent

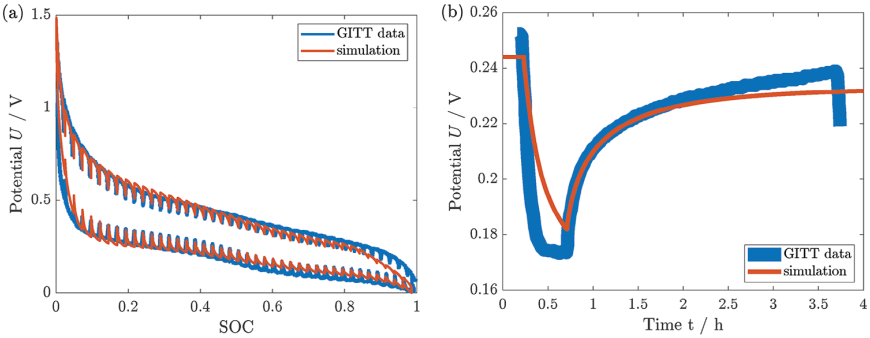

Figure 4. Impact of visco-elastoplastic SEI on the silicon potential with $E_{Si} = 200$ GPa and $E_{SEI} = 100$ GPa. a) Simulation of the voltage hysteresis generated by a visco-elastoplastic SEI during a GITT procedure in comparison to the measurement.[28] b) Simulation of lithiation pulse and rest period in comparison to a single GITT pulse.[29]

ADVANCED SCIENCE NEWS
www.advancedsciencenews.com

ADVANCED FUNCTIONAL MATERIALS
www.afm-journal.de

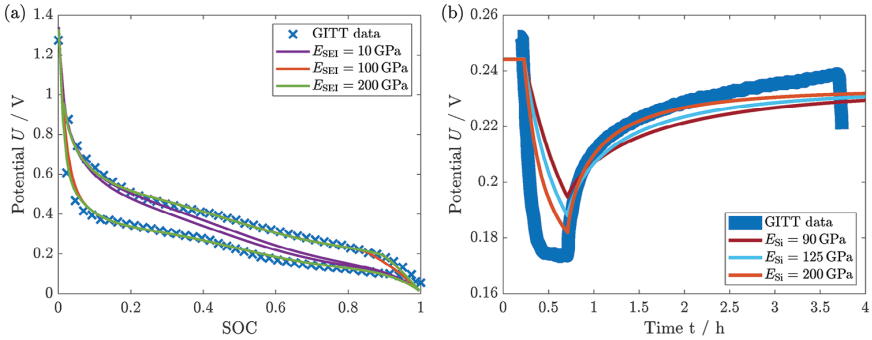

Figure 5. Effect of Young's modulus of the SEI and the silicon nanoparticle on the voltage hysteresis. a) Impact of Young's modulus of the SEI on the shape of the silicon voltage hysteresis with E_{Si} = 200 GPa in comparison to experimental data.[28] b) Influence of Young's modulus of the silicon nanoparticle on the transition voltage profile with E_{SEI} = 100 GPa in comparison to a single GITT pulse.[29]

rest period, our simulation and the experiment reveal similar timescales. However, the experiment reveals an additional longer timescale as the voltage is not constant after 3 h of relaxation. A more sophisticated rheological model describing the viscoelastoplastic behavior could improve the timescales by the cost of additional parameters. Further, we will evaluate the influence of Young's modulus on the simulated timescales of GITT pulses in Section 3.3.

In Supporting Information, we compare shear-thinning viscosity with Newtonian behavior. As illustrated in Figure S6a, Supporting Information, Newtonian behavior leads to a more pronounced decrease of the viscous contribution to the voltage hysteresis with increasing SOC, which disagrees with the experiment. Therefore, we consider the power-law shear thinning model in our studies. However, due to the constant value of the viscosity, we can compare the Newtonian viscosity to the range of values presented in Section 2.4. The value $\eta_{SEI} = 1.25 \times 10^{14}$ Pa s found for the Newtonian viscosity agrees with the range of 10^7 Pa s $< \eta_{SEI} < 10^{15}$ Pa s discussed as reasonable in Section 2.4. The accordance indicates the suitability of considering viscous behavior to explain the amplified hysteresis observed during cycling. Furthermore, the high fitting value of the viscosity matches the assumption of a stiff inner SEI layer.

Regarding the timescales, Newtonian viscosity and power-law shear-thinning viscosity reveal similar transition times during the GITT pulse depicted in S6b, Supporting Information. Thus, the choice of shear-thinning or Newtonian behavior does not significantly influence the transition profile between the different potential curves.

3.3. Variation of Mechanical Parameters and Size

As the exact mechanical parameters of the SEI are ambiguous in experiments, we provide a parameter study to estimate the influence of Young's modulus E_{SEI}. In **Figure 5**a, we compare the open-circuit voltage hysteresis simulated for three different values of Young's modulus. For a small Young's modulus of the SEI, the simulated voltage hysteresis is small, and its shape does not match the experiment. In contrast, there is a reasonable agreement between simulation and experiment for medium and high values. In particular, the simulation with the value used throughout this study, E_{SEI} = 100 GPa, matches the experimental data well. Nonetheless, the maximum value E_{SEI} = 200 GPa even shows a slightly more accurate agreement. This indicates that Young's modulus of the SEI is often underestimated and the nanoscale effect discussed in Section 2.4 induces a further increase.

In Figure S7a, Supporting Information illustrates the timescale of a single lithiation pulse and relaxation for the medium and high parameter values of E_{SEI}. Overall, the simulated timescales are comparable with the ones observed in the experiment. Increasing Young's modulus of the SEI leads to a slightly faster transition. However, the influence of Young's modulus of the SEI on the revealed timescale is essentially negligible.

Therefore, we analyze the mechanical properties of the silicon nanoparticle and its impact on the transition times. Due to the increase of Young's modulus reported at the nanoscale,[76–80] we vary Young's modulus of the silicon nanoparticle for constant Young's modulus of the SEI. We compare the literature values of Young's modulus for bulk amorphous silicon of 90–125 GPa[88–91] with the modulus for silicon estimated at the nanoscale of 200 GPa from refs. [87, 92]. In Figure 5b, we depict the voltage of a simulated GITT pulse for the variation of Young's modulus of silicon. The highest value E_{Si} = 200 GPa shows the best agreement with the experiment for the transition profile. The voltage relaxation for the lower values of E_{Si} is slightly too slow. Nevertheless, the lower values are still able to qualitatively describe the GITT data. The variation reveals that a value for Young's modulus of the silicon nanoparticle, which is approximately a factor two higher than the literature bulk value, can best reproduce the timescale of the experiment. This indicates the importance of considering nanoscale effects for the mechanical description.

At the same time, we investigate the influence of Young's modulus of the silicon nanoparticle on the shape and size of the voltage hysteresis in Supporting Information. Figure S7b, Supporting Information reveals that Young's modulus of silicon has only a minor influence on the voltage hysteresis in our model.

Therefore, the parameter study shows that high values of Young's modulus of the silicon nanoparticle and the SEI achieve

ADVANCED SCIENCE NEWS
www.advancedsciencenews.com

ADVANCED FUNCTIONAL MATERIALS
www.afm-journal.de

the best agreement between the chemo-mechanical simulation and experimental data. This indicates the importance of nanoscale effects on the silicon voltage hysteresis.

Additionally, we investigate the influence of Poisson's ratio of the SEI and the silicon particle on the voltage hysteresis in Supporting Information. Figure S8, Supporting Information shows that a variation of Poisson's ratio of SEI and particle does not change the size and shape of the voltage hysteresis. According to Figure S9, Supporting Information, the value of Poisson's ratio of SEI and silicon influences the transition time during a single GITT pulse. Generally, higher values of Poisson's ratio show an accelerated transition profile. We rationalize this observation based on our model understanding. Poisson's ratio couples the radial and tangential force components and thus affects the time scale of relaxation. Universal energy conservation, however, determines the size of the voltage hysteresis.

Despite mechanical parameters, the size of the particle-SEI system may also impact the observable voltage hysteresis. Thus, we analyze the influence of the SEI thickness L_{SEI}, the particle radius R, and their ratio L_{SEI}/R in Supporting Information. Figure S10a, Supporting Information reveals an increase in the mean voltage difference between delithiation and lithiation OCV for increasing SEI thicknesses. In contrast, Figure S10b, Supporting Information shows a decrease in the voltage difference for increasing particle radius. Combining these results, Figure S11, Supporting Information reveals a linear increase in the mean voltage difference depending on the ratio of SEI thickness and particle radius. We expect this ratio to stay roughly constant in typical experiments as first there exists an optimum particle size in the order of $R = 50\,\mathrm{nm}$[55] and second large particles tend to break into smaller ones.[7]

4. Conclusions

To conclude, the slow diffusion process or particle constriction inside electrodes cannot cause the voltage hysteresis observed for silicon nanoparticle anodes. However, the expansion of silicon nanoparticles leads to an impact of the SEI or the silicon oxide layer on the stress and potential inside the anode. We propose a visco-elastoplastic silicon-SEI model, which can for the first time explain the open-circuit voltage hysteresis of a silicon nanoparticle anode measured with GITT. The plasticity of the SEI leads to different stresses inside the particle during lithiation and delithiation, inducing the observed voltage hysteresis. In addition, our SEI model qualitatively reproduces the volume hysteresis of silicon anodes. Furthermore, the viscous SEI behavior describes the difference between the voltage hysteresis observed for cycling at low currents and the open-circuit voltage from GITT after a relaxation period. A variation of Young's modulus of the SEI reveals its crucial influence on the shape of the voltage hysteresis. The results indicate a stiff inner SEI layer with a Young's modulus in the order of $E_{\mathrm{SEI}} = 100\,\mathrm{GPa}$. Consequently, our work suggests that a soft SEI will mitigate the voltage hysteresis of silicon nano-anodes.

Supporting Information

Supporting Information is available from the Wiley Online Library or from the author.

Acknowledgements

Lukas Köbbing gratefully acknowledges funding and support by the German Research Foundation (DFG) within the research training group SiMET under project number 281041241/GRK2218.

Open access funding enabled and organized by Projekt DEAL.

Conflict of Interest

The authors declare no conflict of interest.

Data Availability Statement

The data that support the findings of this study are available from the corresponding author upon reasonable request.

Keywords

battery aging, lithium-ion batteries, plastic flow, solid-electrolyte interphase mechanics, silicon anode, solid-electrolyte interphase, voltage hysteresis

Received: July 28, 2023
Revised: October 23, 2023
Published online: November 5, 2023

[1] X. Zuo, J. Zhu, P. Müller-Buschbaum, Y.-J. Cheng, *Nano Energy* **2017**, *31*, 113.
[2] M. Kim, Z. Yang, I. Bloom, *J. Electrochem. Soc.* **2021**, *168*, 010523.
[3] C. Zhang, F. Wang, J. Han, S. Bai, J. Tan, J. Liu, F. Li, *Small Struct.* **2021**, *2*, 2100009.
[4] L. Sun, Y. Liu, R. Shao, J. Wu, R. Jiang, Z. Jin, *Energy Storage Mater.* **2022**, *46*, 482.
[5] J. Lin, X. Zhang, E. Fan, R. Chen, F. Wu, L. Li, *Energy Environ. Sci.* **2023**, *16*, 745.
[6] M. Wetjen, S. Solchenbach, D. Pritzl, J. Hou, V. Tileli, H. A. Gasteiger, *J. Electrochem. Soc.* **2018**, *165*, A1503.
[7] X. H. Liu, L. Zhong, S. Huang, S. X. Mao, T. Zhu, J. Y. Huang, *ACS Nano* **2012**, *6*, 1522.
[8] J. Chakraborty, C. P. Please, A. Goriely, S. J. Chapman, *Int. J. Solids Struct.* **2015**, *54*, 66.
[9] P. Stein, Y. Zhao, B.-X. Xu, *J. Power Sources* **2016**, *332*, 154.
[10] Y. Yang, W. Yuan, W. Kang, Y. Ye, Q. Pan, X. Zhang, Y. Ke, C. Wang, Z. Qiu, Y. Tang, *Sustainable Energy Fuels* **2020**, *4*, 1577.
[11] Z. Xiao, C. Wang, L. Song, Y. Zheng, T. Long, *J. Solid State Electrochem.* **2022**, *26*, 1125.
[12] L. Zhang, M. Al-Mamun, L. Wang, Y. Dou, L. Qu, S. X. Dou, H. K. Liu, H. Zhao, *Cell Rep. Phys. Sci.* **2022**, *3*, 100811.
[13] I. Yoon, D. P. Abraham, B. L. Lucht, A. F. Bower, P. R. Guduru, *Adv. Energy Mater.* **2016**, *6*, 1600099.
[14] J. Duay, K. W. Schroder, S. Murugesan, K. J. Stevenson, *ACS Appl. Mater. Interfaces* **2016**, *8*, 17642.
[15] B. Jerliu, E. Hüger, L. Dörrer, B. K. Seidlhofer, R. Steitz, M. Horisberger, H. Schmidt, *Phys. Chem. Chem. Phys.* **2018**, *20*, 23480.
[16] K. Dong, H. Markötter, F. Sun, A. Hilger, N. Kardjilov, J. Banhart, I. Manke, *ChemSusChem* **2019**, *12*, 261.
[17] L. Baggetto, J. Oudenhoven, T. van Dongen, J. Klootwijk, M. Mulder, R. Niessen, M. de Croon, P. Notten, *J. Power Sources* **2009**, *189*, 402.
[18] V. A. Sethuraman, M. J. Chon, M. Shimshak, V. Srinivasan, P. R. Guduru, *J. Power Sources* **2010**, *195*, 5062.

ADVANCED SCIENCE NEWS
www.advancedsciencenews.com

ADVANCED FUNCTIONAL MATERIALS
www.afm-journal.de

[19] V. A. Sethuraman, V. Srinivasan, A. F. Bower, P. R. Guduru, *J. Electrochem. Soc.* **2010**, *157*, A1253.
[20] V. A. Sethuraman, V. Srinivasan, J. Newman, *J. Electrochem. Soc.* **2013**, *160*, A394.
[21] M. W. Verbrugge, D. R. Baker, X. Xiao, Q. Zhang, Y.-T. Cheng, *J. Phys. Chem. C* **2015**, *119*, 5341.
[22] B. Lu, Y. Song, Q. Zhang, J. Pan, Y.-T. Cheng, J. Zhang, *Phys. Chem. Chem. Phys.* **2016**, *18*, 4721.
[23] D. R. Baker, M. W. Verbrugge, X. Xiao, *J. Appl. Phys.* **2017**, *122*, 165102.
[24] C. K. Chan, H. Peng, G. Liu, K. McIlwrath, X. F. Zhang, R. A. Huggins, Y. Cui, *Nat. Nanotechnol.* **2008**, *3*, 31.
[25] H. Wu, G. Chan, J. W. Choi, I. Ryu, Y. Yao, M. T. McDowell, S. W. Lee, A. Jackson, Y. Yang, L. Hu, Y. Cui, *Nat. Nanotechnol.* **2012**, *7*, 310.
[26] R. Chandrasekaran, T. F. Fuller, *J. Electrochem. Soc.* **2011**, *158*, A859.
[27] P. Bernard, J. P. Alper, C. Haon, N. Herlin-Boime, M. Chandesris, *J. Power Sources* **2019**, *435*, 226769.
[28] K. Pan, F. Zou, M. Canova, Y. Zhu, J.-H. Kim, *J. Power Sources* **2019**, *413*, 20.
[29] K. Pan, Ph.D. thesis, Ohio State University, Columbus, OH **2020**.
[30] M. T. McDowell, S. W. Lee, W. D. Nix, Y. Cui, *Adv. Mater.* **2013**, *25*, 4966.
[31] H. Yang, S. Huang, X. Huang, F. Fan, W. Liang, X. H. Liu, L.-Q. Chen, J. Y. Huang, J. Li, T. Zhu, S. Zhang, *Nano Lett.* **2012**, *12*, 1953.
[32] Z. Cui, F. Gao, J. Qu, *J. Mech. Phys. Solids* **2013**, *61*, 293.
[33] Y. Zhao, P. Stein, Y. Bai, M. Al-Siraj, Y. Yang, B.-X. Xu, *J. Power Sources* **2019**, *413*, 259.
[34] Y. Jiang, G. Offer, J. Jiang, M. Marinescu, H. Wang, *J. Electrochem. Soc.* **2020**, *167*, 130533.
[35] A. Bower, P. Guduru, V. Sethuraman, *J. Mech. Phys. Solids* **2011**, *59*, 804.
[36] C. V. Di Leo, E. Rejovitzky, L. Anand, *Int. J. Solids Struct.* **2015**, *67-68*, 283.
[37] R. Chandrasekaran, A. Magasinski, G. Yushin, T. F. Fuller, *J. Electrochem. Soc.* **2010**, *157*, A1139.
[38] K. Zhao, M. Pharr, S. Cai, J. J. Vlassak, Z. Suo, *J. Am. Ceram. Soc.* **2011**, *94*, s226.
[39] Z. Cui, F. Gao, J. Qu, *J. Mech. Phys.Solids* **2012**, *60*, 1280.
[40] B. Horstmann, J. Shi, R. Amine, M. Werres, X. He, H. Jia, F. Hausen, I. Cekic-Laskovic, S. Wiemers-Meyer, J. Lopez, D. Galvez-Aranda, F. Baakes, D. Bresser, C. Su, Y. Xu, W. Xu, P. Jakes, R.-A. Eichel, E. Figgemeier, U. Krewer, J. M. Seminario, P. B. Balbuena, C. Wang, S. Passerini, Y. Shao-Horn, M. Winter, K. Amine, R. Kostecki, A. Latz, *Energy Environ. Sci.* **2021**, *14*, 5289.
[41] B. Horstmann, F. Single, A. Latz, *Curr. Opin. Electrochem.* **2019**, *13*, 61.
[42] L. Kolzenberg, A. Latz, B. Horstmann, *ChemSusChem* **2020**, *13*, 3901.
[43] L. Köbbing, A. Latz, B. Horstmann, *J. Power Sources* **2023**, *561*, 232651.
[44] C. Cao, I. I. Abate, E. Sivonxay, B. Shyam, C. Jia, B. Moritz, T. P. Devereaux, K. A. Persson, H.-G. Steinrück, M. F. Toney, *Joule* **2019**, *3*, 762.
[45] M. B. Pinson, M. Z. Bazant, *J. Electrochem. Soc.* **2013**, *160*, A243.
[46] M. Nie, D. P. Abraham, Y. Chen, A. Bose, B. L. Lucht, *J. Phys. Chem. C* **2013**, *117*, 13403.
[47] M. Wetjen, D. Pritzl, R. Jung, S. Solchenbach, R. Ghadimi, H. A. Gasteiger, *J. Electrochem. Soc.* **2017**, *164*, A2840.
[48] Y. Zhang, N. Du, D. Yang, *Nanoscale* **2019**, *11*, 19086.
[49] J. Kim, O. B. Chae, B. L. Lucht, *J. Electrochem. Soc.* **2021**, *168*, 030521.
[50] X. Zhang, S. Weng, G. Yang, Y. Li, H. Li, D. Su, L. Gu, Z. Wang, X. Wang, L. Chen, *Cell Rep. Phys. Sci.* **2021**, *2*, 100668.
[51] A. Dopilka, Y. Gu, J. M. Larson, V. Zorba, R. Kostecki, *ACS Appl. Mater. Interfaces* **2023**, *15*, 6755.
[52] R. Kumar, P. Lu, X. Xiao, Z. Huang, B. W. Sheldon, *ACS Appl. Mater. Interfaces* **2017**, *9*, 28406.
[53] M. Tanaka, J. B. Hooper, D. Bedrov, *ACS Appl. Energy Mater.* **2018**, *1*, 1858.
[54] K. Guo, R. Kumar, X. Xiao, B. W. Sheldon, H. Gao, *Nano Energy* **2020**, *68*, 104257.
[55] M. Y. Jin, K. Guo, X. Xiao, M. W. Verbrugge, H. Gao, B. W. Sheldon, *Adv. Funct. Mater.* **2021**, *31*, 2010640.
[56] L. Kolzenberg, A. Latz, B. Horstmann, *Batteries Supercaps* **2022**, *5*, 202100216.
[57] Q. Li, X. Liu, X. Han, Y. Xiang, G. Zhong, J. Wang, B. Zheng, J. Zhou, Y. Yang, *ACS Appl. Mater. Interfaces* **2019**, *11*, 14066.
[58] J. Chen, X. Fan, Q. Li, H. Yang, M. R. Khoshi, Y. Xu, S. Hwang, L. Chen, X. Ji, C. Yang, H. He, C. Wang, E. Garfunkel, D. Su, O. Borodin, C. Wang, *Nat. Energy* **2020**, *5*, 386.
[59] M. Schammer, B. Horstmann, A. Latz, *J. Electrochem. Soc.* **2021**, *168*, 026511.
[60] G. F. Castelli, L. von Kolzenberg, B. Horstmann, A. Latz, W. Dörfler, *Energy Technol.* **2021**, *9*, 2000835.
[61] G. Holzapfel, *Nonlinear Solid Mechanics: A Continuum Approach for Engineering*, Wiley, New York **2000**.
[62] M. E. Gurtin, E. Fried, L. Anand, *The Mechanics and Thermodynamics of Continua*, Cambridge University Press, Cambridge **2010**.
[63] J. Zheng, H. Zheng, R. Wang, L. Ben, W. Lu, L. Chen, L. Chen, H. Li, *Phys. Chem. Chem. Phys.* **2014**, *16*, 13229.
[64] V. Kuznetsov, A.-H. Zinn, G. Zampardi, S. Borhani-Haghighi, F. La Mantia, A. Ludwig, W. Schuhmann, E. Ventosa, *ACS Appl. Mater. Interfaces* **2015**, *7*, 23554.
[65] I. Yoon, S. Jurng, D. P. Abraham, B. L. Lucht, P. R. Guduru, *Energy Storage Mater.* **2020**, *25*, 296.
[66] M. Gu, A. M. Rao, J. Zhou, B. Lu, *Energy Environ. Sci.* **2023**, *16*, 1166.
[67] Y. Chen, W. Wu, S. Gonzalez-munoz, L. Forcieri, C. Wells, S. P. Jarvis, F. Wu, R. Young, A. Dey, M. Isaacs, M. Nagarathinam, R. G. Palgrave, N. Tapia-ruiz, O. V. Kolosov, *Nat. Commun.* **2023**, *14*, 1321.
[68] H. Shin, J. Park, S. Han, A. M. Sastry, W. Lu, *J. Power Sources* **2015**, *277*, 169.
[69] I. A. Shkrob, J. F. Wishart, D. P. Abraham, *J. Phys. Chem. C* **2015**, *119*, 14954.
[70] Y. He, H. Hu, K. Zhang, S. Li, J. Chen, *J. Mater. Sci.* **2017**, *52*, 2836.
[71] Y. Kamikawa, K. Amezawa, K. Terada, *J. Phys. Chem. C* **2020**, *124*, 22488.
[72] Y. Liu, X. Xu, O. O. Kapitanova, P. V. Evdokimov, Z. Song, A. Matic, S. Xiong, *Adv. Energy Mater.* **2022**, *12*, 2103589.
[73] Q. Zhang, X. Xiao, W. Zhou, Y.-T. Cheng, M. W. Verbrugge, *Adv. Energy Mater.* **2015**, *5*, 1401398.
[74] H. Zhang, D. Wang, C. Shen, *Appl. Surf. Sci.* **2020**, *507*, 145059.
[75] Y. Chai, W. Jia, Z. Hu, S. Jin, H. Jin, H. Ju, X. Yan, H. Ji, L.-J. Wan, *Chin. Chem. Lett.* **2021**, *32*, 1139.
[76] C. Q. Chen, Y. Shi, Y. S. Zhang, J. Zhu, Y. J. Yan, *Phys. Rev. Lett.* **2006**, *96*, 075505.
[77] A. Mathur, J. Erlebacher, *Appl. Phys. Lett.* **2007**, *90*, 061910.
[78] R. Agrawal, B. Peng, E. E. Gdoutos, H. D. Espinosa, *Nano Lett.* **2008**, *8*, 3668.
[79] J. He, C. M. Lilley, *Nano Lett.* **2008**, *8*, 1798.
[80] Y. Chen, Q. Gao, Y. Wang, X. An, X. Liao, Y.-W. Mai, H. H. Tan, J. Zou, S. P. Ringer, C. Jagadish, *Nano Lett.* **2015**, *15*, 5279.
[81] R. Edgeworth, B. J. Dalton, T. Parnell, *Eur. J. Phys.* **1984**, *5*, 198.
[82] P. Sutardja, W. G. Oldham, *IEEE Trans. Electron Devices* **1989**, *36*, 2415.
[83] V. Senez, D. Collard, B. Baccus, M. Brault, J. Lebailly, *J. Appl. Phys.* **1994**, *76*, 3285.
[84] M. I. Ojovan, *Adv. Condens. Matter Phys.* **2008**, *2008*, 817829.
[85] W. S. LePage, Y. Chen, E. Kazyak, K.-H. Chen, A. J. Sanchez, A. Poli, E. M. Arruda, M. D. Thouless, N. P. Dasgupta, *J. Electrochem. Soc.* **2019**, *166*, 2A89.
[86] C. L. Allred, X. Yuan, M. Z. Bazant, L. W. Hobbs, *Phys. Rev. B* **2004**, *70*, 134113.

ADVANCED SCIENCE NEWS
www.advancedsciencenews.com

ADVANCED FUNCTIONAL MATERIALS
www.afm-journal.de

[87] M. Nasr Esfahani, B. E. Alaca, *Adv. Eng. Mater.* **2019**, *21*, 1900192.
[88] M. D. Kluge, J. R. Ray, *Phys. Rev. B* **1988**, *37*, 4132.
[89] V. Shenoy, P. Johari, Y. Qi, *J. Power Sources* **2010**, *195*, 6825.
[90] S. I. Tan, B. S. Berry, B. L. Crowder, *Appl. Phys. Lett.* **1972**, *20*, 88.
[91] M. Szabadi, P. Hess, A. J. Kellock, H. Coufal, J. E. E. Baglin, *Phys. Rev. B* **1998**, *58*, 8941.
[92] D.-M. Tang, C.-L. Ren, M.-S. Wang, X. Wei, N. Kawamoto, C. Liu, Y. Bando, M. Mitome, N. Fukata, D. Golberg, *Nano Lett.* **2012**, *12*, 1898.
[93] G. L. Plett, *J. Power Sources* **2004**, *134*, 262.
[94] C. P. Graells, M. S. Trimboli, G. L. Plett, in *2020 IEEE Transportation Electrification Conf. & Expo (ITEC)*, Vol. *1*, IEEE, Piscataway, NJ **2020**, pp. 175–180.
[95] D. Wycisk, M. Oldenburger, M. G. Stoye, T. Mrkonjic, A. Latz, *J. Energy Storage* **2022**, *52*, 105016.

ADVANCED FUNCTIONAL MATERIALS

Supporting Information

for *Adv. Funct. Mater.*, DOI 10.1002/adfm.202308818

Voltage Hysteresis of Silicon Nanoparticles: Chemo-Mechanical Particle-SEI Model

*Lukas Köbbing, Arnulf Latz and Birger Horstmann**

Reprinted from Ref. [173].

Supporting Information: Voltage Hysteresis of Silicon Nanoparticles: Chemo-Mechanical Particle-SEI Model

Lukas Köbbing
Institute of Engineering Thermodynamics, German Aerospace Center (DLR), Wilhelm-Runge-Straße 10, 89081 Ulm, Germany and Helmholtz Institute Ulm (HIU), Helmholtzstraße 11, 89081 Ulm, Germany

Arnulf Latz and Birger Horstmann*
Institute of Engineering Thermodynamics, German Aerospace Center (DLR), Wilhelm-Runge-Straße 10, 89081 Ulm, Germany Helmholtz Institute Ulm (HIU), Helmholtzstraße 11, 89081 Ulm, Germany and Institute of Electrochemistry, Ulm University, Albert-Einstein-Allee 47, 89081 Ulm, Germany

SI. THERMODYNAMIC CONSISTENT THEORY

For the general derivation of the thermodynamic theory, we follow Kolzenberg et al. [1] and additionally introduce viscous behavior. We consider the first Piola-Kirchhoff stress $\mathbf{P}$ as the sum of the stress due to elastic deformation $\mathbf{P}_{\mathrm{el}}$ and the stress due to viscous behavior $\mathbf{P}_{\mathrm{visc}}$

$$\mathbf{P} = \mathbf{P}_{\mathrm{el}} + \mathbf{P}_{\mathrm{visc}}. \tag{S1}$$

The general momentum balance with momentum $\vec{g}$ reads

$$\rho_0 \dot{\vec{g}} = \nabla_0 \cdot \mathbf{P} + \rho_0 \vec{b}, \tag{S2}$$

where ρ_0 is the host density in the undeformed Lagrange frame and $\vec{b}$ are body forces. The time derivative of the total energy density e is described by

$$\rho_0 \dot{e} = \rho_0 \vec{v}\,\vec{b} + \nabla_0 \cdot \left(\mathbf{P}^{\mathrm{T}} \vec{v}\right), \tag{S3}$$

where $\vec{v}$ is the velocity of the host material. Next, we use the product rule $\nabla_0 \cdot \left(\mathbf{P}^{\mathrm{T}} \vec{v}\right) = \vec{v} \nabla_0 \cdot \mathbf{P} + \mathbf{P} : \nabla_0 \vec{v}$ and recognize that $\dot{\mathbf{F}} = \nabla_0 \vec{v}$. The internal energy u then changes according to $\dot{u} = \dot{e} - \vec{v}\dot{\vec{g}}$ as

$$\rho_0 \dot{u} = \mathbf{P} : \dot{\mathbf{F}}. \tag{S4}$$

The second law of thermodynamics imposes a non-negative dissipation rate $\mathcal{R} \geq 0$. The generic entropy balance reads

$$\rho_0 T \dot{s} = -\nabla T \vec{N}_{\mathrm{S},0} + \mathcal{R} \tag{S5}$$

with the entropy flux $\vec{N}_{\mathrm{S},0}$. We rewrite Eq. (S5) with the free energy φ using the Legendre transformation of the internal energy $\varphi = u - Ts$ as

$$\mathcal{R} = -\rho_0 \dot{\varphi} + \mathbf{P} : \dot{\mathbf{F}} + \nabla_0 T \vec{N}_{\mathrm{S},0} \geq 0. \tag{S6}$$

We state the total time derivative of the free energy of a mobile species in an elastic material as

$$\rho_0 \dot{\varphi} = \mu_{\mathrm{Li}} \dot{c}_{\mathrm{Li},0} + \frac{1}{2} \mathbf{T}_{\mathrm{rev}} : \dot{\mathbf{C}}_{\mathrm{rev}}. \tag{S7}$$

Here, $\mathbf{T}_{\mathrm{rev}}$ is the reversible second Piola-Kirchhoff stress tensor only due to elastic deformation. The chemical potential μ_{Li} and the reversible second Piola-Kirchhoff stress tensor are defined as

$$\mu_{\mathrm{Li}} = \frac{\partial(\rho_0 \varphi)}{\partial c_{\mathrm{Li},0}} \tag{S8}$$

$$\mathbf{T}_{\mathrm{rev}} = 2 \frac{\partial(\rho_0 \varphi)}{\partial \mathbf{C}_{\mathrm{rev}}}. \tag{S9}$$

* birger.horstmann@dlr.de

Combining the dissipation equation Eq. (S6) with the balance of the free energy Eq. (S7) gives

$$\mathcal{R} = -\mu_{\mathrm{Li}}\dot{c}_{\mathrm{Li},0} - \frac{1}{2}\mathbf{T}_{\mathrm{rev}} : \dot{\mathbf{C}}_{\mathrm{rev}} + \mathbf{P} : \dot{\mathbf{F}} + \nabla_0 T \vec{N}_{\mathrm{S},0} \geq 0. \tag{S10}$$

The mechanical power density is composed of a reversible part due to elastic deformation, an irreversible part due to plastic flow, and a dissipation part due to viscous behavior

$$\mathbf{P} : \dot{\mathbf{F}} = \frac{1}{2}\mathbf{T}_{\mathrm{rev}} : \dot{\mathbf{C}}_{\mathrm{rev}} + \mathbf{M} : \mathbf{L}_{\mathrm{pl}} + \mathbf{P}_{\mathrm{visc}} : \dot{\mathbf{F}}, \tag{S11}$$

where $\mathbf{M} = \mathbf{C}_{\mathrm{rev}}\mathbf{T}_{\mathrm{rev}}$ is the Mandel stress and $\mathbf{L}_{\mathrm{pl}} = \dot{\mathbf{F}}_{\mathrm{pl}}\mathbf{F}_{\mathrm{pl}}^{-1}$ is the plastic velocity gradient. Finally, we obtain an expression for the dissipation rate that guarantees non-negative entropy production

$$\mathcal{R} = -\vec{N}_{\mathrm{S},0}\nabla_0\mu_{\mathrm{Li}} + \mathbf{M} : \mathbf{L}_{\mathrm{pl}} + \mathbf{P}_{\mathrm{visc}} : \dot{\mathbf{F}} \geq 0. \tag{S12}$$

Non-negativity of the first two terms in Eq. (S12) is shown in Ref. [1], and non-negativity of the last term results from our viscosity model.

SII. ELASTOPLASTIC THIN-FILM SILICON ANODE

Many articles discuss the voltage hysteresis in thin-film silicon anodes due to plasticity of silicon [2–9]. In this setup, silicon is deposited as a film on a current collector. This current collector restricts the expansion to the normal direction of the plane. In-plane expansion is completely prohibited by the current collector as illustrated in Fig. S1. As depicted in Fig. S2(a), large stresses occur during lithiation already for small SOC due to the restricted expansion. For slow lithiation, they are almost independent of the lithiation current. After a regime of elastic deformation, the silicon film deforms plastically at a constant Piola-Kirchhoff stress. During delithiation, the silicon shrinks elastically first and then again plastically. The plastic flow inside the silicon anode leads to dissipation and an observable voltage hysteresis in silicon thin-film electrodes as shown in Fig. S2(b).

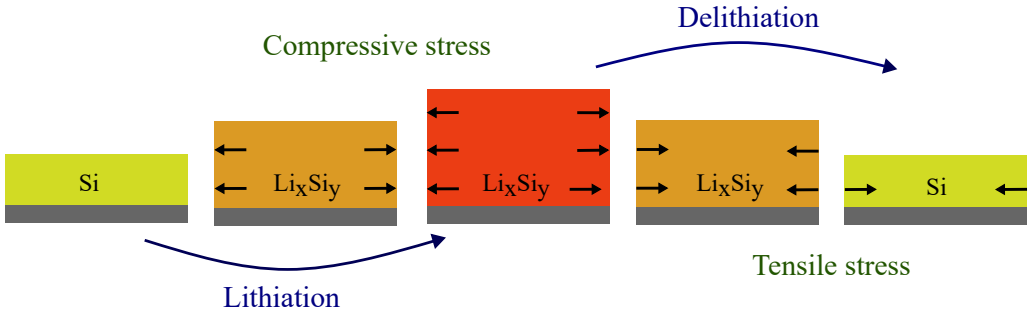

FIG. S1. Scheme of the stress inside a thin-film silicon anode during lithiation and delithiation.

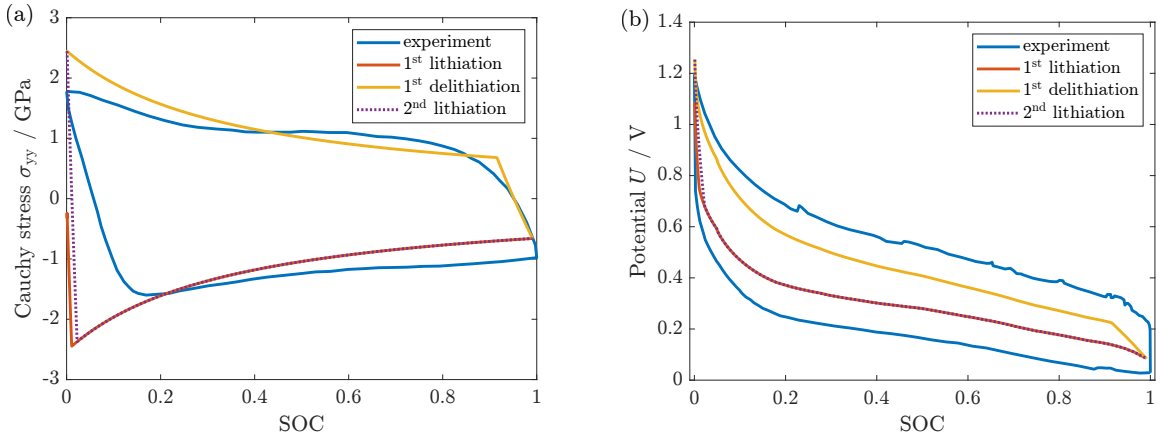

FIG. S2. Simulation of thin-film silicon anode in comparison to experiment [3]. The parameters are taken from this reference. The diffusion coefficient is $D_{\mathrm{Li}} = 1 \times 10^{-13}\,\mathrm{m}^2/\mathrm{s}$, the film thickness is $d = 250\,\mathrm{nm}$, and the current is C/4. The remaining parameters are taken from Table S1. (a) Stress hysteresis generated by restricted expansion. The simulation can reasonably reproduce the experimental data. (b) Stress hysteresis due to large stresses. The simulation underestimates the size of the hysteresis but reproduces its shape.

SIII. ELASTOPLASTIC SILICON PARTICLE WITH CONSTRAINTS

As seen for silicon thin films, a restricted expansion leads to large stresses. Thus, we investigate the stress of a simplified silicon nanoparticle, which is restricted by a rigid border in two directions. With this setup, we model the situation of silicon nanoparticles inside an electrode, where other electrode particles restrict the expansion. When the particle gets in contact with the wall during lithiation, large stresses arise and plastic flow starts to occur almost immediately. As illustrated in Fig. S3, this irreversibly deforms the particle, squeezing in the direction where free expansion is possible. After a short delithiation period, the plastically deformed particle detaches from the wall and stresses vanish due to the free expansion. Therefore, a significant stress and voltage hysteresis is visible for the first cycle in Fig. S4. However, for the subsequent lithiation and delithiation cycles, no plastic flow will occur, and the particle shows no stress or voltage hysteresis.

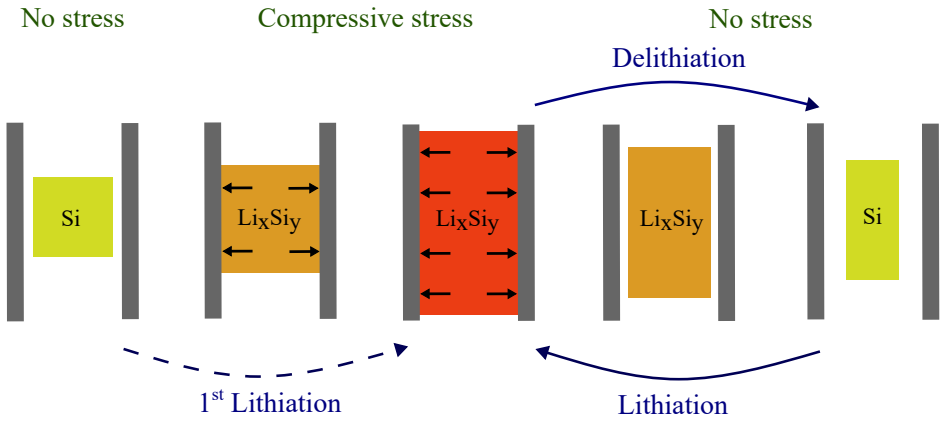

FIG. S3. Scheme of the stress inside a constrained silicon anode during first lithiation and subsequent lithiation and delithiation.

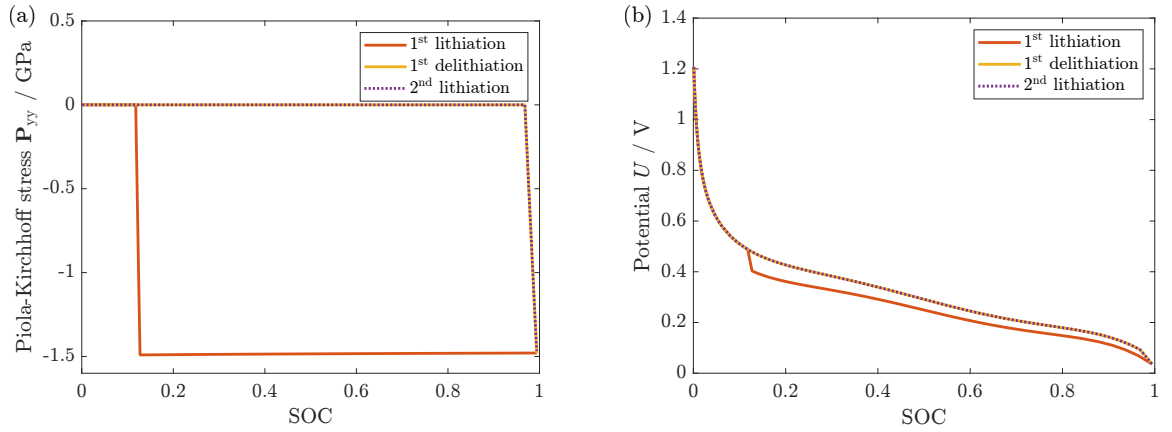

FIG. S4. Simulation of simplified nanoparticle with constraints at low C-rate. The size of the nanoparticle is 100 nm, and the distance between the fixed walls is 110 nm. (a) Stress generated by the restricted expansion. The stress vanishes when the particle is not in contact with the constraints. (b) Potential simulated for the constrained nanoparticle. A voltage hysteresis occurs only for the first cycle.

SIV. ELASTOPLASTIC SILICON PARTICLE WITHOUT CONSTRAINTS OR SEI

In silicon nanoparticles without SEI and any borders, stress can only arise due to concentration gradients generated by the slow diffusion of lithium inside the silicon particle. To prevent underestimating the concentration gradients, we choose a small value of the diffusion coefficient of lithium in silicon reported in the literature, $D_{\mathrm{Li}} = 10^{-17}\,\mathrm{m^2 s^{-1}}$ [10]. We simulate slow lithiation and delithiation with C/20 of a silicon nanoparticle with radius $R = 50\,\mathrm{nm}$. The results shown in black in Fig. S5 reveal only a minor hysteresis in the stress and a vanishing voltage hysteresis. Therefore, slow diffusion can not explain the voltage hysteresis observed for silicon nanoparticles at C-rates as low as C/20.

To enhance the effect of concentration gradients, we increase the current to 1C. Figure S5 depicts the results for fast cycling as colored lines. Only for this high current do we find a significant stress and voltage hysteresis.

We illustrate the outcome of the simulation in Fig. S5 in comparison to the open-circuit voltage hysteresis observed via GITT measurement. Our simulation does not show a stress or voltage hysteresis after relaxation. However, we depict the experimental open-circuit voltage hysteresis in order to estimate the size of the simulated voltage hysteresis. We find that even for fast cycling with 1C the observed hysteresis is smaller than the experimental voltage hysteresis observed after relaxation.

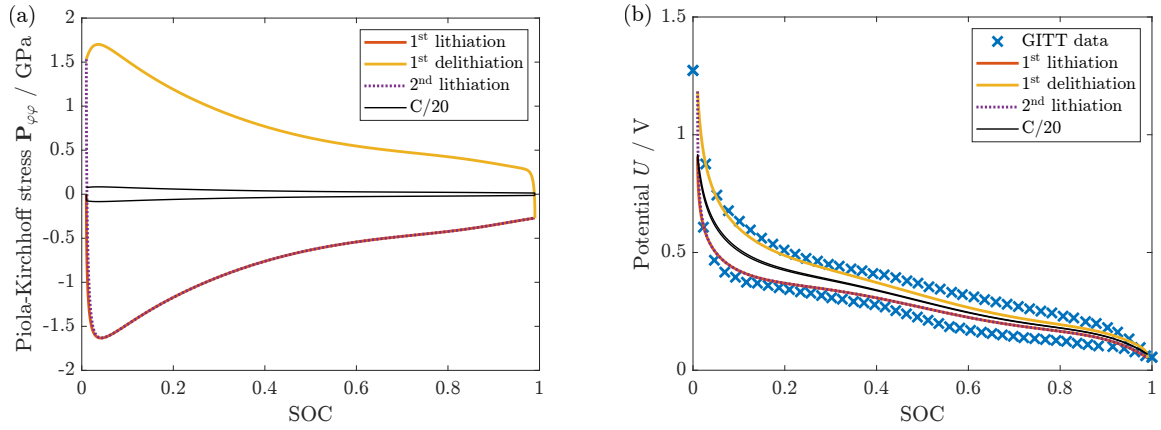

FIG. S5. Simulation of a freely expanding elastoplastic silicon nanoparticle for fast cycling with 1C (colored lines) in comparison to slow cycling with C/20 (black lines). (a) Stress hysteresis generated by concentration gradients. (b) Simulated voltage hysteresis compared to experimental GITT data [11].

SV. PLETT MODEL

The Plett model [12–14] considers the measured potential as the sum of the mean open-circuit voltage $U_0(\mathrm{SOC})$, half of the width of the voltage hysteresis measured between lithiation and delithiation $H(\mathrm{SOC})$, and the hysteresis state $h(\mathrm{SOC})$ defined between -1 and 1 as

$$U = U_0(\mathrm{SOC}) + H(\mathrm{SOC}) \cdot h(\mathrm{SOC}). \tag{S13}$$

The Plett model defines the transition between the potential curves observed for lithiation and delithiation. It is a phenomenological model described by the differential equation

$$\frac{dh(\mathrm{SOC})}{d\mathrm{SOC}} = -k(\mathrm{SOC}) \left(1 + \mathrm{sgn}\left(\frac{d\mathrm{SOC}}{dt}\right) h(\mathrm{SOC})\right). \tag{S14}$$

The velocity of the transition between the two hysteresis paths is determined by the parameter k, which depends on the SOC. As a simple relation, we set $k(\mathrm{SOC}) = 40/(1 + 4 \cdot \mathrm{SOC})$.

SVI. SEI WITH NEWTONIAN VISCOSITY

For the description of the viscosity of the SEI in our study, we apply a power-law shear-thinning behavior. Here, we evaluate the influence of Newtonian behavior, where the viscosity does not depend on the strain rate. Figure S6(a) reveals, that the size of the viscous contribution to the hysteresis decreases in our simulation with increasing SOC. The decline is produced by a decreasing strain rate, as the volume increases linearly with SOC. In comparison, the shear-thinning reduces this change in the hysteresis size and agrees better with the experimental data. According to Fig. S6(b), the Newtonian behavior possesses a similar timescale compared to the shear-thinning model used in our studies.

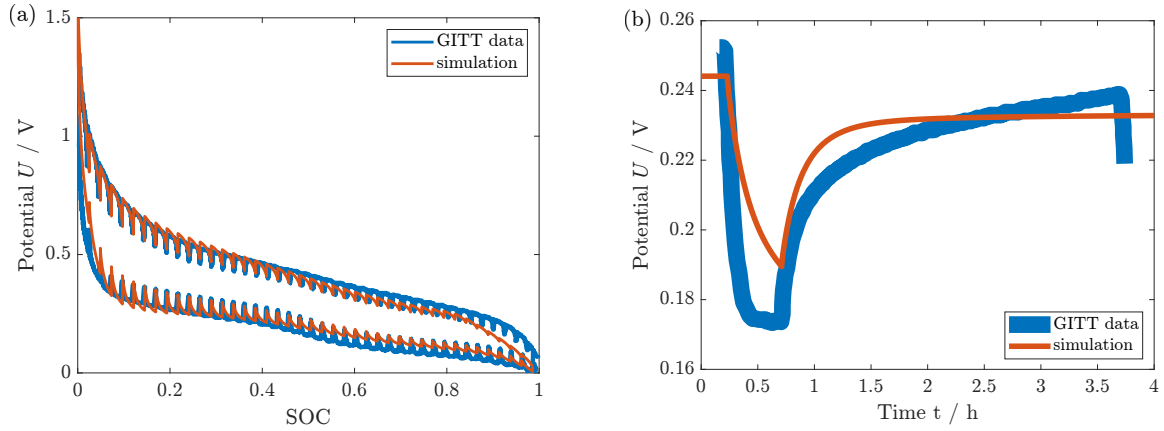

FIG. S6. Impact of Newtonian visco-elastoplastic SEI with viscosity $\eta_{\mathrm{SEI}} = 1.25 \times 10^{14}$ Pa s on the silicon potential. (a) Voltage hysteresis generated by a Newtonian visco-elastoplastic SEI for small currents and after relaxation in comparison to GITT measurement [11]. (b) Simulation of lithiation pulse and rest time in comparison to a single GITT pulse [15].

SVII. ADDITIONAL FIGURES FOR PARAMETER STUDY OF YOUNG'S MODULUS

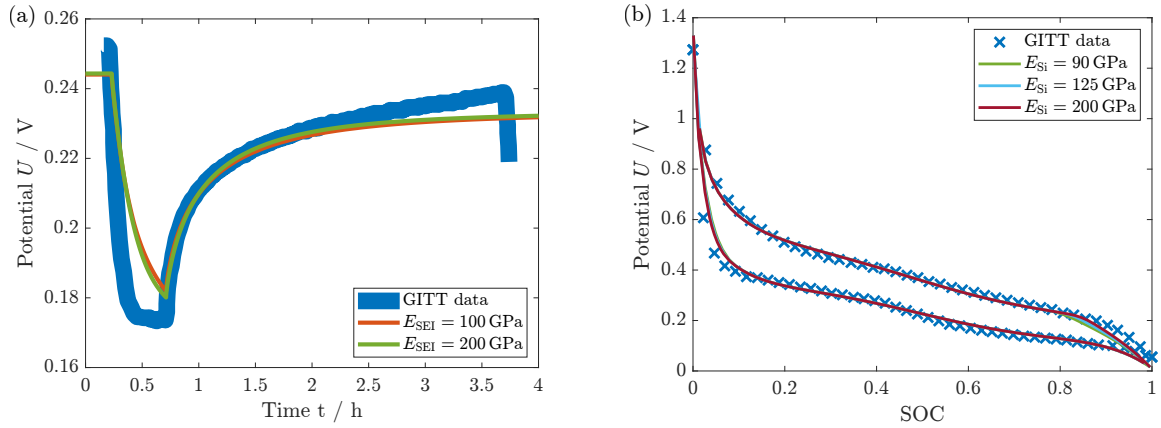

FIG. S7. Variation of Young's modulus of the SEI and the silicon particle due to nanoscale effects. (a) Variation of E_{SEI} for constant E_{Si}. Simulation of a single GITT pulse in comparison to experimental data [15]. As the lowest value $E_{SEI} = 10\,GPa$ does not reproduce the voltage hysteresis, we cannot include this parameter in the figure. (b) Variation of E_{Si} for constant E_{SEI}. Simulation of the voltage hysteresis in comparison to experimental data [11].

SVIII. PARAMETER STUDY OF POISSON'S RATIO

Here, we investigate the influence of Poisson's ratio of the SEI and the silicon particle on the voltage hysteresis. Fig. S8 shows that a variation of Poisson's ratio of SEI and particle does not change the size and shape of the voltage hysteresis. According to Fig. S9, the value of Poisson's ratio of SEI and silicon influences the transition time during a single GITT pulse. Generally, higher values of Poisson's ratio show an accelerated transition profile. This observation is in accordance with our model understanding. Poisson's ratio couples the radial and tangential force components influencing the time scale of the relaxation process. In contrast, universal energy conservation affects the size of the observed voltage hysteresis.

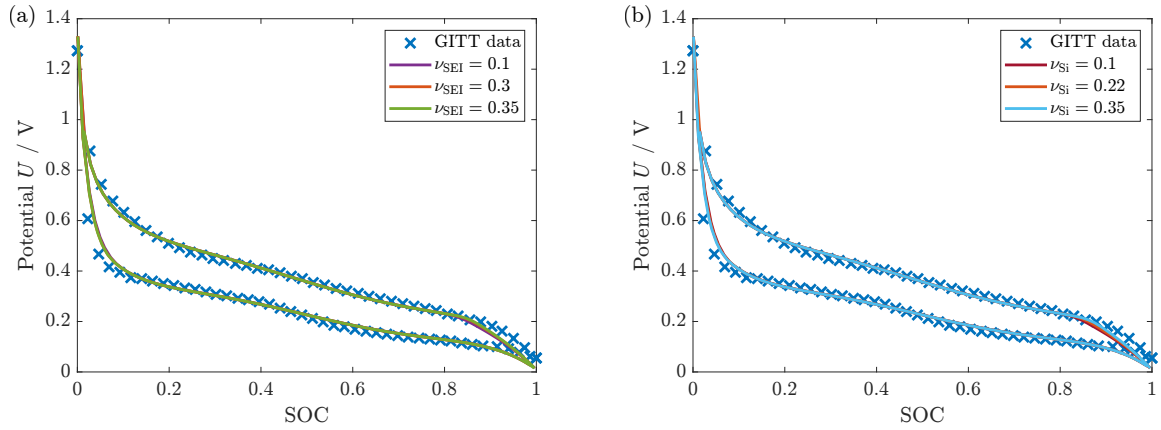

FIG. S8. Simulation of the voltage hysteresis for a variation of Poisson's ratio of the SEI and the silicon particle in comparison to experimental data [11]. (a) Variation of ν_{SEI}. (b) Variation of ν_{Si}. The variations of Poisson's ratio of SEI and silicon particle show a negligible influence on the OCV hysteresis.

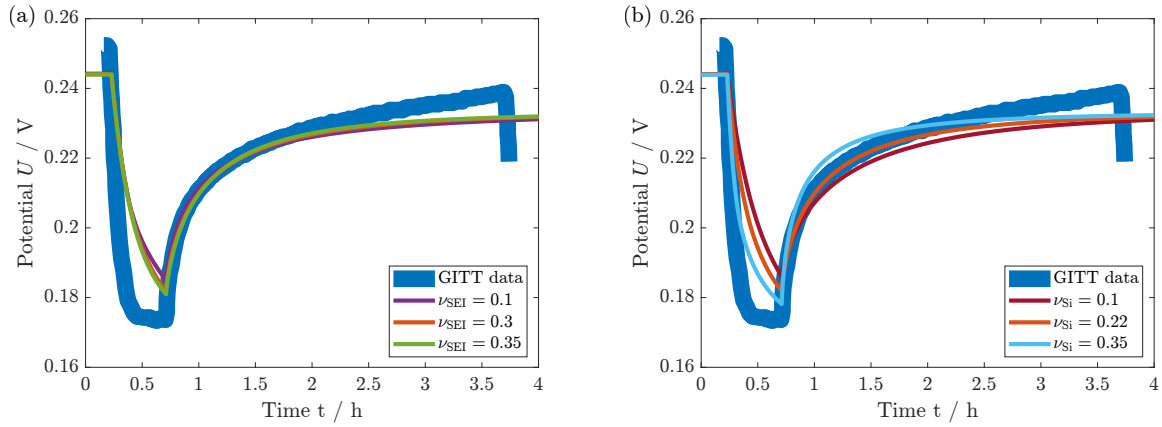

FIG. S9. Simulation of a single GITT pulse for a variation of Poisson's ratio of the SEI and the silicon particle in comparison to experimental data [15]. (a) Variation of ν_{SEI}. (b) Variation of ν_{Si}. Generally, higher Poisson's ratios show a faster transition.

SIX. PARAMETER STUDY OF THE SYSTEM'S SIZE

We analyze the influence of the SEI thickness L_{SEI}, the particle radius R, and their ratio L_{SEI}/R. Therefore, we determine the mean open-circuit voltage difference $\Delta\bar{U}$ between the mean relaxed delithiation voltage $\bar{U}^{\mathrm{GITT}}_{\mathrm{delithiation}}$ and lithiation voltage $\bar{U}^{\mathrm{GITT}}_{\mathrm{lithiation}}$ in our simulation as

$$\Delta\bar{U} = \bar{U}^{\mathrm{GITT}}_{\mathrm{delithiation}} - \bar{U}^{\mathrm{GITT}}_{\mathrm{lithiation}}. \tag{S15}$$

Fig. S10(a) reveals an increase in the mean voltage difference between delithiation and lithiation OCV for increasing SEI thicknesses. In contrast, Fig. S10(b) shows a decrease in the voltage difference for increasing particle radius. Combining these results, Fig. S11 reveals a linear increase in the mean voltage difference depending on the ratio of SEI thickness and particle radius.

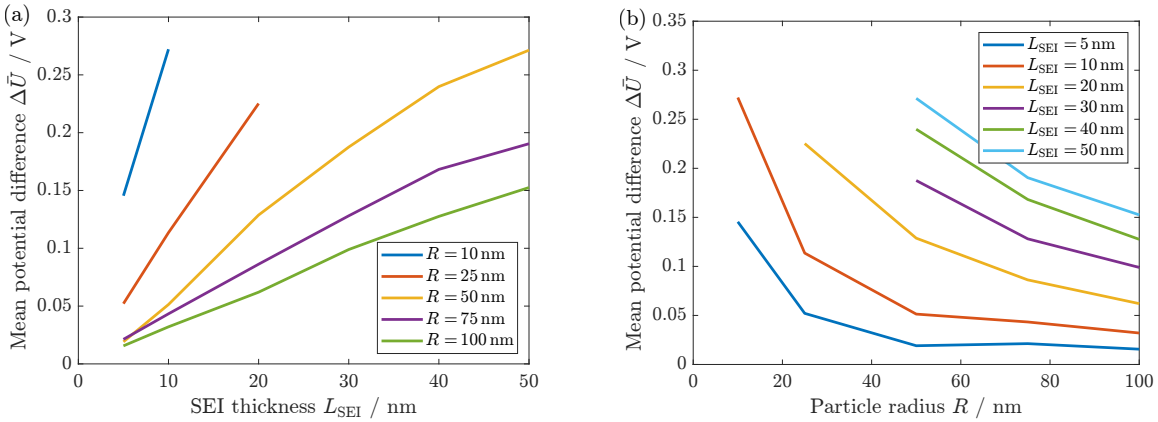

FIG. S10. Mean potential difference between delithiation and lithiation OCV depending on the system's size. (a) Dependence on the SEI thickness L_{SEI}. (b) Dependence on the particle radius R.

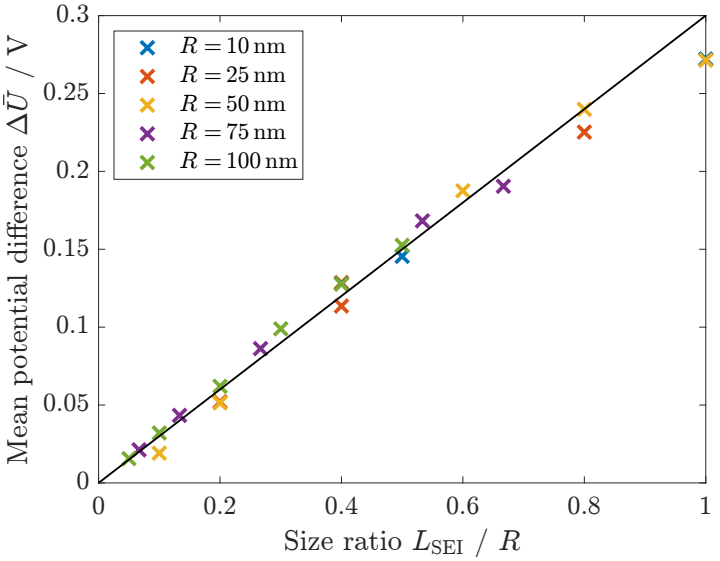

FIG. S11. Mean potential difference between delithiation and lithiation OCV curve depending on the size ratio of the SEI thickness L_{SEI} and the particle radius R.

SX. PARAMETERS

Parameter	Value		Reference
Silicon			
Nanoparticle radius R	50	nm	estimated [11]
Solid state diffusion coefficient in silicon D_{Li}	1×10^{-17}	m^2/s	[10]
Young's modulus E_{Si}	200	GPa	estimated [16, 17]
Poisson's ratio ν_{Si}	0.22		[18]
Yield stress $\sigma_{\mathrm{Y,Si}}$	3	GPa	fit
Maximum lithium concentration in Si $c_{\mathrm{Li,max}}$	311×10^3	$\mathrm{mol}/\mathrm{m}^3$	[19]
Lithium molar volume in Si v_{Li}	9×10^{-6}	$\mathrm{m}^3/\mathrm{mol}$	[20]
Charging rate	1/20	C	[11]
SEI			
SEI thickness L_{SEI}	20	nm	estimated [21]
Young's modulus E_{SEI}	100	GPa	estimated [22, 23]
Poisson's ratio ν_{SEI}	0.3		[22]
Yield stress $\sigma_{\mathrm{Y,SEI}}$	2.5	GPa	fit
Newtonian viscosity η_{SEI}	125×10^{12}	Pa s	fit
Shear-thinning viscosity $\eta_{\mathrm{SEI},0}$	15×10^9	$\mathrm{Pa\,s}^n$	fit
Shear-thinning exponent n	0.15		estimated [24]
Universal constants and other parameters			
Temperature T	298	K	
Faraday constant F	96 485	C/mol	
Universal gas constant R_{gas}	8.314	J/(mol K)	

TABLE S1. List of the simulation parameters.

[1] L. Kolzenberg, A. Latz, and B. Horstmann, Chemo-Mechanical Model of SEI Growth on Silicon Electrode Particles, Batteries & Supercaps **5**, 1 (2022).
[2] L. Baggetto, J. Oudenhoven, T. van Dongen, J. Klootwijk, M. Mulder, R. Niessen, M. de Croon, and P. Notten, On the electrochemistry of an anode stack for all-solid-state 3D-integrated batteries, Journal of Power Sources **189**, 402 (2009).
[3] V. A. Sethuraman, M. J. Chon, M. Shimshak, V. Srinivasan, and P. R. Guduru, In situ measurements of stress evolution in silicon thin films during electrochemical lithiation and delithiation, Journal of Power Sources **195**, 5062 (2010).
[4] V. A. Sethuraman, V. Srinivasan, A. F. Bower, and P. R. Guduru, In Situ Measurements of Stress-Potential Coupling in Lithiated Silicon, Journal of The Electrochemical Society **157**, A1253 (2010).
[5] V. A. Sethuraman, V. Srinivasan, and J. Newman, Analysis of Electrochemical Lithiation and Delithiation Kinetics in Silicon, Journal of The Electrochemical Society **160**, A394 (2013).
[6] M. W. Verbrugge, D. R. Baker, X. Xiao, Q. Zhang, and Y.-T. Cheng, Experimental and Theoretical Characterization of Electrode Materials that Undergo Large Volume Changes and Application to the Lithium–Silicon System, The Journal of Physical Chemistry C **119**, 5341 (2015).
[7] I. Yoon, D. P. Abraham, B. L. Lucht, A. F. Bower, and P. R. Guduru, In Situ Measurement of Solid Electrolyte Interphase Evolution on Silicon Anodes Using Atomic Force Microscopy, Advanced Energy Materials **6**, 1600099 (2016).
[8] B. Lu, Y. Song, Q. Zhang, J. Pan, Y.-T. Cheng, and J. Zhang, Voltage hysteresis of lithium ion batteries caused by mechanical stress, Physical Chemistry Chemical Physics **18**, 4721 (2016).
[9] D. R. Baker, M. W. Verbrugge, and X. Xiao, An approach to characterize and clarify hysteresis phenomena of lithium-silicon electrodes, Journal of Applied Physics **122**, 165102 (2017).
[10] J. Li, X. Xiao, F. Yang, M. W. Verbrugge, and Y.-T. Cheng, Potentiostatic Intermittent Titration Technique for Electrodes Governed by Diffusion and Interfacial Reaction, The Journal of Physical Chemistry C **116**, 1472 (2012).
[11] K. Pan, F. Zou, M. Canova, Y. Zhu, and J.-H. Kim, Systematic electrochemical characterizations of Si and SiO anodes for high-capacity Li-Ion batteries, Journal of Power Sources **413**, 20 (2019).
[12] G. L. Plett, Extended Kalman filtering for battery management systems of LiPB-based HEV battery packs, Journal of Power Sources **134**, 262 (2004).
[13] C. P. Graells, M. S. Trimboli, and G. L. Plett, Differential hysteresis models for a silicon-anode Li-ion battery cell, in *2020 IEEE Transportation Electrification Conference & Expo (ITEC)*, Vol. 1 (IEEE, 2020) pp. 175–180.
[14] D. Wycisk, M. Oldenburger, M. G. Stoye, T. Mrkonjic, and A. Latz, Modified Plett-model for modeling voltage hysteresis in lithium-ion cells, Journal of Energy Storage **52**, 105016 (2022).
[15] K. Pan, *Dissertation*, Ph.D. thesis, Ohio State University (2020).
[16] M. Nasr Esfahani and B. E. Alaca, A Review on Size-Dependent Mechanical Properties of Nanowires, Advanced Engineering Materials **21**, 1900192 (2019).
[17] D.-M. Tang, C.-L. Ren, M.-S. Wang, X. Wei, N. Kawamoto, C. Liu, Y. Bando, M. Mitome, N. Fukata, and D. Golberg, Mechanical Properties of Si Nanowires as Revealed by in Situ Transmission Electron Microscopy and Molecular Dynamics Simulations, Nano Letters **12**, 1898 (2012).
[18] V. Shenoy, P. Johari, and Y. Qi, Elastic softening of amorphous and crystalline Li–Si Phases with increasing Li concentration: A first-principles study, Journal of Power Sources **195**, 6825 (2010).
[19] A. Verma, A. A. Franco, and P. P. Mukherjee, Mechanistic Elucidation of Si Particle Morphology on Electrode Performance, Journal of The Electrochemical Society **166**, A3852 (2019).
[20] R. Koerver, W. Zhang, L. de Biasi, S. Schweidler, A. O. Kondrakov, S. Kolling, T. Brezesinski, P. Hartmann, W. G. Zeier, and J. Janek, Chemo-mechanical expansion of lithium electrode materials – on the route to mechanically optimized all-solid-state batteries, Energy & Environmental Science **11**, 2142 (2018).
[21] J. Zheng, H. Zheng, R. Wang, L. Ben, W. Lu, L. Chen, L. Chen, and H. Li, 3D visualization of inhomogeneous multi-layered structure and Young's modulus of the solid electrolyte interphase (SEI) on silicon anodes for lithium ion batteries, Phys. Chem. Chem. Phys. **16**, 13229 (2014).
[22] H. Shin, J. Park, S. Han, A. M. Sastry, and W. Lu, Component-/structure-dependent elasticity of solid electrolyte interphase layer in Li-ion batteries: Experimental and computational studies, Journal of Power Sources **277**, 169 (2015).
[23] Y. Chai, W. Jia, Z. Hu, S. Jin, H. Jin, H. Ju, X. Yan, H. Ji, and L.-J. Wan, Monitoring the mechanical properties of the solid electrolyte interphase (SEI) using electrochemical quartz crystal microbalance with dissipation, Chinese Chemical Letters **32**, 1139 (2021).
[24] W. S. LePage, Y. Chen, E. Kazyak, K.-H. Chen, A. J. Sanchez, A. Poli, E. M. Arruda, M. D. Thouless, and N. P. Dasgupta, Lithium Mechanics: Roles of Strain Rate and Temperature and Implications for Lithium Metal Batteries, Journal of The Electrochemical Society **166**, A89 (2019).

Paper III

Slow Voltage Relaxation of Silicon Nanoparticles with a Chemo-Mechanical Core-Shell Model

Authors	Lukas Köbbing, Yannick Kuhn, Birger Horstmann
Journal	ACS Applied Materials & Interfaces
Year	2024
Volume (Issue)	16 (49)
Pages	67609–67619
DOI	10.1021/acsami.4c12976
Copyright	CC BY 4.0
Copyright link	https://creativecommons.org/licenses/by/4.0/
Copyright notice	Reprinted from Ref. [174].
Preprint DOI	10.48550/arXiv.2408.01106

Author's Contribution

L. Köbbing further developed and implemented the thermodynamically consistent chemo-mechanical silicon-SEI model based on the publication by Kolzenberg et al. [63] and Paper II [173]. Particularly, L. Köbbing identified suitability of the Garofalo viscosity law, incorporated the model for the SEI, and derived a reduced chemo-mechanical hysteresis model. Furthermore, L. Köbbing analyzed the results of the chemo-mechanical model, evaluating the predicted silicon voltage relaxation in comparison to published experimental data. The model development and analysis was supervised by B. Horstmann. Y. Kuhn identified the logarithmic trend in the experimental voltage relaxation. In addition, L. Köbbing created the initial draft of the manuscript and the supporting information including text and figures. The writing was then thoroughly reviewed by Y. Kuhn and B. Horstmann.

ACS APPLIED MATERIALS & INTERFACES

www.acsami.org
Research Article

Slow Voltage Relaxation of Silicon Nanoparticles with a Chemo-Mechanical Core−Shell Model

Lukas Köbbing, Yannick Kuhn, and Birger Horstmann*

Cite This: ACS Appl. Mater. Interfaces 2024, 16, 67609−67619

ABSTRACT: Silicon presents itself as a high-capacity anode material for lithium-ion batteries with a promising future. The high ability for lithiation comes along with massive volume changes and a problematic voltage hysteresis, causing reduced efficiency, detrimental heat generation, and a complicated state-of-charge estimation. During slow cycling, amorphous silicon nanoparticles show a larger voltage hysteresis than after relaxation periods. Interestingly, the voltage relaxes for at least several days, which has not been physically explained so far. We apply a chemo-mechanical continuum model in a core−shell geometry interpreted as a silicon particle covered by the solid-electrolyte interphase to account for the hysteresis phenomena. The silicon core (de)lithiates during every cycle while the covering shell is chemically inactive. The visco-elastoplastic behavior of the shell explains the voltage hysteresis during cycling and after relaxation. We identify a logarithmic voltage relaxation, which fits with the established Garofalo law for viscosity. Our chemo-mechanical model describes the observed voltage hysteresis phenomena and outperforms the empirical Plett model. In addition to our full model, we present a reduced model to allow for easy voltage profile estimations. The presented results support the mechanical explanation of the silicon voltage hysteresis with a core−shell model and encourage further efforts into the investigation of the silicon anode mechanics.

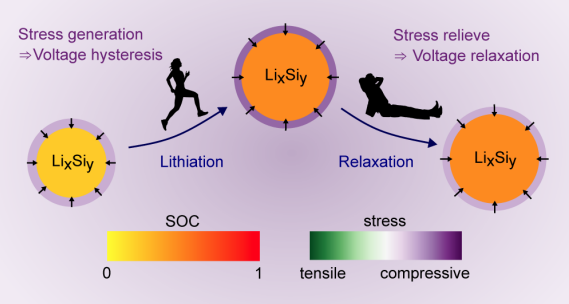

KEYWORDS: *lithium-ion batteries, solid-electrolyte interphase (SEI), silicon anode, voltage relaxation, voltage hysteresis, chemo-mechanical core−shell model, SEI mechanics, Garofalo viscosity*

1. INTRODUCTION

For the enhancement of next-generation lithium-ion batteries, research and industry consider the application of pure silicon anodes.[1−3] Silicon is a popular choice as it is an abundant and cheap material. Anodes made of silicon possess a high theoretical capacity, leading to a massive volume expansion of up to 300% during lithiation and respective shrinkage during delithiation.[4] The massive deformations induce significant stresses inside the anode material, causing fracture of large silicon particles above a critical diameter of 150 nm.[5] Larger silicon particles suffer from cracks, particle pulverization, and are prone to losing contact with the current collector.[6] Anodes made of silicon nanoparticles promise a higher stability and cycle life compared to anodes with larger silicon particles. Thus, research and industry focus on the behavior of nanostructured silicon anodes.[7]

A severe challenge for the commercialization of silicon anodes is the handling and possible reduction of the voltage hysteresis observed in various experiments.[8−11] Silicon anodes reveal a different voltage during slow lithiation compared to delithiation, reducing efficiency and causing detrimental heat generation.[12,13] Experiments observe this hysteresis phenomenon of amorphous silicon anodes in thin-film geometries, micron-sized particles, and nanoparticles.

Literature discusses different reasons for the voltage hysteresis: mechanics and plastic flow of silicon in thin-film geometries,[14,15] concentration gradients due to slow diffusion in micrometer-sized particles,[16−18] phase transformation in the very first cycle,[19] and slow reaction kinetics.[20] As demonstrated in our previous paper,[21] these hypotheses are not able to explain the observed voltage hysteresis in GITT experiments with anodes based on amorphous silicon nanoparticles. Therefore, we developed a new chemo-mechanical core−shell model with the plastic flow of the shell,[21] which explains the observed OCV hysteresis. The enlarged hysteresis during slow cycling is modeled with viscous behavior of the shell. Our previous model can describe the short-term voltage relaxation during GITT measurements for at most 1 h.

Received: August 2, 2024
Revised: October 21, 2024
Accepted: October 24, 2024
Published: November 26, 2024

https://doi.org/10.1021/acsami.4c12976
ACS Appl. Mater. Interfaces 2024, 16, 67609−67619

ACS Applied Materials & Interfaces www.acsami.org Research Article

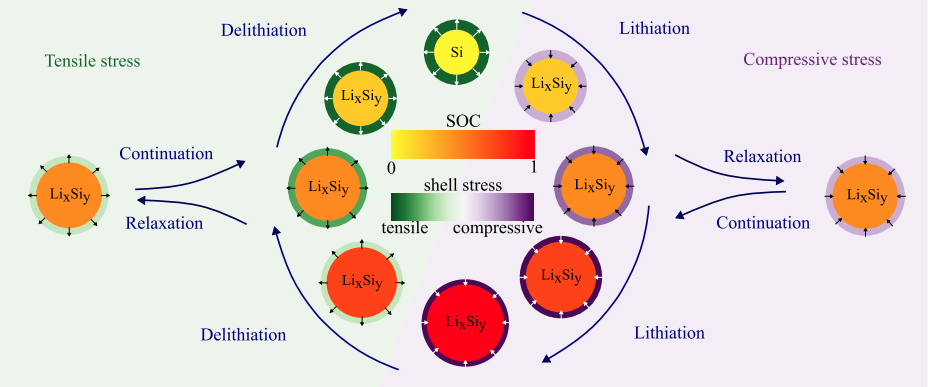

Figure 1. Scheme of volume changes and shell stress during lithiation, delithiation, and relaxation periods.

Recent experimental results unveil a slow, nonexponential voltage relaxation behavior for at least 300 h, which was so far neither experimentally observed nor theoretically explained on this extended time scale.[11] Particularly, the observed slow relaxation process once again rules out a diffusional origin with exponential relaxation behavior. Moreover, although the slow voltage relaxation is in line with the mid-term experimental findings of Sethuraman et al.,[20] their theoretical explanation with reaction kinetics in the Tafel regime requires unreasonable parameter values for the exchange current density and the transfer coefficients. Thus, the novel long-term relaxation measurements strongly support our mechanical explanation. In this article, we propose a viscosity model that fits the experimental results. Our chemo-mechanical consideration as a core−shell model provides a consistent picture of the silicon hysteresis and its dynamics over several time scales.

The core−shell model can be interpreted as a silicon nanoparticle covered by the solid-electrolyte interphase (SEI). The SEI arises on anode particles due to electrolyte decomposition,[22−26] driven via the electron diffusion mechanism.[27,28] Moreover, the native silicon oxide layer[29−31] or artificial coatings[10] can contribute to the SEI and influence the lithiation behavior of silicon, even for solid electrolytes.[32] Supporting the impact of the SEI, the inner SEI is reported to be robust[33−35] and beneficial for the mechanical integrity of the silicon anode.[1,36,37] This mechanism can also explain the hysteresis of larger silicon particles due to particle pulverization, causing nanoparticles surrounded by freshly formed SEI.[6,38]

An alternative interpretation is the occurrence of active silicon nanodomains in larger silicon particles surrounded by chemically inactive regions. Literature reports the existence of silicon nanodomains for amorphous silicon under high pressure,[39] for crystalline silicon,[40] and generically for silicon oxide particles.[41,42] In general, the presence of nanodomains is independent of the anode geometry.

This manuscript builds on our previous explanation of the voltage hysteresis of silicon nanoparticles by the chemo-mechanical core−shell coupling.[21] However, this manuscript focuses on the examination and interpretation of the long-term voltage relaxation process of silicon anodes, considering an adequate viscosity model. We explain the basic principles of our chemo-mechanical core−shell model in Section 2. Furthermore, we introduce the Garofalo viscosity model necessary because of the large stresses arising inside the shell and discuss its behavior in the core−shell system with an analytical approximation and a reduced model. In Section 3, we describe the recent experiments performed by Wycisk et al.,[11] which we analyze in detail in Section 4. In conclusion, we present a consistent description of the observed slow voltage relaxation, hysteresis shape, C-rate dependence, and voltage transition profiles.

2. THEORY

Our theoretical framework describes the behavior of a core−shell system, where the silicon particle as core can lithiate and delithiate while the shell is chemically inactive and deforms only mechanically as illustrated in Figure 1. We have presented the foundations of the chemo-mechanical core−shell model used in this study in our previous publications.[21,35] In the following, we summarize the most important assumptions and equations. Further, we highlight advancements compared to our previous works.

2.1. Chemo-Mechanical Core−Shell Model. The silicon particle core deforms due to the chemical lithiation and delithiation $\mathbf{F}_{\mathrm{core,ch}}$, elastic deformation $\mathbf{F}_{\mathrm{core,el}}$, and plastic deformation $\mathbf{F}_{\mathrm{core,pl}}$ when reaching the yield criterion. The large deformation approach determines the total deformation $\mathbf{F}_{\mathrm{core}}$ as

$$\mathbf{F}_{\mathrm{core}} = \mathbf{F}_{\mathrm{core,pl}}\mathbf{F}_{\mathrm{core,el}}\mathbf{F}_{\mathrm{core,ch}} \tag{1}$$

The concentration of lithium atoms $c_{\mathrm{Li},0}$ inside the silicon particle expressed in the undeformed Lagrangian frame determines the chemical deformation

$$\mathbf{F}_{\mathrm{core,ch}} = \lambda_{\mathrm{ch}}\mathbf{Id} = (1 + \nu_{\mathrm{Li}}c_{\mathrm{Li},0})^{1/3}\mathbf{Id} \tag{2}$$

with ν_{Li} the molar volume of lithium inside silicon.

The strain tensors $\mathbf{E}_{\mathrm{core,k}}$ read

$$\mathbf{E}_{\mathrm{core,k}} = \frac{1}{2}(\mathbf{F}_{\mathrm{core,k}}^{\mathrm{T}}\mathbf{F}_{\mathrm{core,k}} - \mathbf{Id}) \tag{3}$$

where the subscript k indicates the kind of deformation, which is either the total deformation or one of the mentioned deformation contributions from eq 1.

The Cauchy stress $\boldsymbol{\sigma}$ describes the stress in the deformed Euler frame and the Piola−Kirchhoff stress $\mathbf{P} = J\boldsymbol{\sigma}\mathbf{F}^{-\mathrm{T}}$ describes the stress in the undeformed Lagrangian frame with $J = \det \mathbf{F}$. The Piola−Kirchhoff stress due to elastoplastic deformation reads

https://doi.org/10.1021/acsami.4c12976
ACS Appl. Mater. Interfaces 2024, 16, 67609−67619

$$\mathbf{P}_{\mathrm{core}} = \lambda_{\mathrm{ch}}^{-2}\mathbf{F}_{\mathrm{core}}\mathbf{F}_{\mathrm{core,pl}}^{-\mathrm{T}}\mathbf{F}_{\mathrm{core,pl}}^{-1} \left(\lambda_{\mathrm{core}}\,\mathrm{tr}(\mathbf{E}_{\mathrm{core,el}})\mathbf{Id} + 2G_{\mathrm{core}}\mathbf{E}_{\mathrm{core,el}}\right) \tag{4}$$

with the first Lamé constant λ_{core} and the second Lamé constant G_{core}.

Due to the chemo-mechanical coupling, the stress inside the particle affects the voltage as

$$U = U_0 + \frac{\nu_{\mathrm{Li}}}{3F\lambda_{\mathrm{ch}}^3}\mathbf{P}_{\mathrm{core}}\colon \mathbf{F}_{\mathrm{core}} \tag{5}$$

with the true open-circuit voltage (OCV) of silicon U_0 and the Faraday constant F.

The differential equations of interest inside the particle are the continuity equation for the time derivative of the lithium concentration $\dot{c}_{\mathrm{Li},0}$, the momentum balance, and the equation for the plastic flow rate $\dot{\mathbf{F}}_{\mathrm{core,pl}}$,

$$\dot{c}_{\mathrm{Li},0} = -\nabla_0\cdot\vec{N}_{\mathrm{Li},0} \tag{6}$$

$$0 = \nabla_0\cdot\mathbf{P}_{\mathrm{core}} \tag{7}$$

$$\dot{\mathbf{F}}_{\mathrm{core,pl}}\mathbf{F}_{\mathrm{core,pl}}^{-1} = \phi_{\mathrm{core}}\frac{\partial f_{\mathrm{core}}}{\partial \mathbf{M}_{\mathrm{core}}} \tag{8}$$

For the lithiation equation, we define the lithium flux $\vec{N}_{\mathrm{Li},0} = -L\nabla_0\mu_{\mathrm{Li}}$, the electro-chemo-mechanical potential $\mu_{\mathrm{Li}} = -FU$, the mobility $L = D_{\mathrm{Li}}(\partial\mu_{\mathrm{Li}}/\partial c_{\mathrm{Li},0})^{-1}$, and the diffusion coefficient D_{Li}. At the particle boundary, the (de)lithiation rate determines the lithium flux $\vec{N}_{\mathrm{Li},0}(R_{\mathrm{core}})$. For the plastic flow, the von Mises yield criterion $f_{\mathrm{core}} = \frac{3}{2}\left|\mathbf{M}_{\mathrm{core}}^{\mathrm{dev}}\right|^2/\sigma_{\mathrm{Y,core}}^2 - 1 \le 0$ determines plasticity with $\mathbf{M}_{\mathrm{core}}^{\mathrm{dev}} = \mathbf{M}_{\mathrm{core}} - 1/3\,\mathrm{tr}\,\mathbf{M}_{\mathrm{core}}$ the deviatoric part of the adapted Mandel stress $\mathbf{M}_{\mathrm{core}} = \mathbf{F}_{\mathrm{core,rev}}^{\mathrm{T}}\boldsymbol{\sigma}_{\mathrm{core}}\mathbf{F}_{\mathrm{core,rev}}^{-\mathrm{T}}$, the reversible deformation $\mathbf{F}_{\mathrm{core,rev}} = \mathbf{F}_{\mathrm{core,el}}\mathbf{F}_{\mathrm{core,ch}}$, and the yield stress $\sigma_{\mathrm{Y,core}}$. The consistency condition $\dot{f}_{\mathrm{core}} = 0$ determines the plastic multiplier ϕ_{core}.

For the shell behavior, we assume that the shell deforms only mechanically, namely elastically and plastically,

$$\mathbf{F}_{\mathrm{shell}} = \mathbf{F}_{\mathrm{shell,pl}}\mathbf{F}_{\mathrm{shell,el}} \tag{9}$$

leading to massive mechanical strains and stresses when experiencing the significant volume change of the silicon particle during cycling. Analogous to the particle, eq 3 determines the strain tensors $\mathbf{E}_{\mathrm{shell,k}}$ inside the shell.

In addition to the elastoplastic stress $\mathbf{P}_{\mathrm{shell,el}}$ determined analogously to eq 4, we consider the viscous behavior of the shell. To describe large viscous stresses during cycling on the one hand and small viscous stresses during relaxation on the other hand, we use the Garofalo law or inverse hyperbolic sine law

$$\mathbf{P}_{\mathrm{shell,visc}} = J_{\mathrm{shell}}\sigma_{\mathrm{ref}}\cdot\mathrm{asinh}(\tau\dot{\mathbf{E}}_{\mathrm{shell}})\mathbf{F}_{\mathrm{shell}}^{-\mathrm{T}} \tag{10}$$

calculated component-wise and presented initially in ref.43. The parameter σ_{ref} describes as a reference stress the magnitude of viscous stress at a certain strain rate. The parameter τ describes the time constant of the system and the dependence on the strain rate. In this study, we use the Garofalo viscosity model stated in eq 10 instead of a standard Newtonian model or a shear-thinning model[21] to account more adequately for the complexity of the mechanical behavior. The particular functional dependence of the Garofalo law is reasoned in ref.44 by a change in the energy landscape due to mechanical deformations and lattice distortions. Furthermore, positive entropy production is guaranteed analogously to the derivation in ref.21, as the inverse hyperbolic sine is positive for positive arguments and negative for negative ones.

The differential equations of interest inside the shell are the momentum balance and the equation for plastic flow,

$$0 = \nabla_0\cdot(\mathbf{P}_{\mathrm{shell,el}} + \mathbf{P}_{\mathrm{shell,visc}}) \tag{11}$$

$$\dot{\mathbf{F}}_{\mathrm{shell,pl}}\mathbf{F}_{\mathrm{shell,pl}}^{-1} = \phi_{\mathrm{shell}}\frac{\partial f_{\mathrm{shell}}}{\partial \mathbf{M}_{\mathrm{shell,el}}} \tag{12}$$

The yield criterion $f_{\mathrm{shell}} = \frac{3}{2}\left|\mathbf{M}_{\mathrm{shell,el}}^{\mathrm{dev}}\right|^2/\sigma_{\mathrm{Y,shell}}^2 - 1 \le 0$ is determined by the deviatoric part $\mathbf{M}_{\mathrm{shell,el}}^{\mathrm{dev}}$ of the adapted elastic Mandel stress $\mathbf{M}_{\mathrm{shell,el}} = \mathbf{F}_{\mathrm{shell,el}}^{\mathrm{T}}\boldsymbol{\sigma}_{\mathrm{shell,el}}\mathbf{F}_{\mathrm{shell,el}}^{-\mathrm{T}}$ and the plastic multiplier ϕ_{shell} results from the consistency condition $\dot{f}_{\mathrm{shell}} = 0$.

Note that we model the mechanical deformations on a continuum scale. Thus, the visco-elastoplastic behavior is not necessarily an intrinsic property of a single material domain. Instead, interfaces and grain boundaries of multiple crystal domains can determine the continuum mechanics. Hence, the described visco-elastoplasticity can be a consequence of repeated partial cracking and healing, as discussed for the SEI in ref.35. This description is reasonable because the literature does not observe significant fracture of the inner SEI layer on silicon.[33−35]

We assume that the surfaces of the silicon core and the shell stick tightly together, meaning that the radial part of the stress coincides

$$\mathbf{P}_{\mathrm{core,rr}}\big|_{r=R_{\mathrm{core}}} = \mathbf{P}_{\mathrm{shell,rr}}\big|_{r=R_{\mathrm{core}}} \tag{13}$$

when evaluated at the core−shell interface $r = R_{\mathrm{core}}$. Due to the merely mechanical deformation of the shell, significant stresses arise inside the shell, impacting the silicon particle stress and voltage.

As presented in ref.21, the expansion of the silicon particle during lithiation leads to a mechanical reaction of the shell, namely, first elastic and then plastic deformation. The strains inside the shell generate significant compressive stress acting on the silicon particle as visualized in Figure 1. Additionally, viscous behavior increases the total compressive stress during lithiation depending on the strain rate. During the subsequent delithiation, tensile stress originates from elastic and plastic deformations as well as viscosity, which causes a stress hysteresis inside the shell, impacting the voltage of the silicon particle according to eq 5. Hence, the visco-elastoplastic behavior of the shell describes the voltage hysteresis observed for silicon nanoparticles.

2.2. Analytical Approximation for the Voltage Relaxation. To gain an analytical approximation for the voltage relaxation, we investigate the behavior of the presented chemo-mechanical core−shell model in a simplified setup. Thus, we analyze all local variables at the interface accounting for the central role of the interface coupling. In the following,

https://doi.org/10.1021/acsami.4c12976
ACS Appl. Mater. Interfaces 2024, 16, 67609−67619

we discuss several assumptions paving the way to a simplified analytical expression.

First, we choose the simplified description that during relaxation the silicon particle behaves purely elastically according to Hooke's law

$$\sigma_{ev} = E_{core} \cdot \mathbf{E}_{core,ev,rr} \tag{14}$$

with Young's modulus E_{core} and the elastic radial strain of the core $\mathbf{E}_{core,ev,rr}$ due to viscous stress of the shell.

Furthermore, we consider only the viscous stress contribution inside the shell as the elastic stress of the shell stays constant, i.e.,

$$\boldsymbol{\sigma}_{shell,visc} = \sigma_{ref} \cdot \mathrm{asinh}(\tau \dot{\mathbf{E}}_{shell}) \tag{15}$$

The time evolution of the radial stress component in the silicon particle resulting from the time derivative of eq 14 states

$$\frac{d\sigma_{ev}}{dt} = E_{core} \cdot \dot{\mathbf{E}}_{core,ev,rr} \tag{16}$$

The silicon core deforms only elastically during relaxation of viscous shell stress and isotropically, thus

$$\dot{\mathbf{E}}_{core,ev} \approx \dot{\mathbf{F}}_{core,ev} \approx \frac{\dot{\mathbf{E}}_{core}}{\lambda_{ch}} \approx \frac{\dot{\mathbf{E}}_{core}}{\lambda_{ch}^2} \tag{17}$$

and

$$\dot{\mathbf{E}}_{core,ev,rr} = \dot{\mathbf{E}}_{core,ev,\varphi\varphi} = \frac{\dot{\mathbf{E}}_{core,\varphi\varphi}}{\lambda_{ch}^2} \tag{18}$$

The radial and tangential stresses are related by the momentum balance as

$$\boldsymbol{\sigma}_{shell,\varphi\varphi} = -\alpha\lambda_{ch}^3 \boldsymbol{\sigma}_{shell,rr} \tag{19}$$

with the parameter $\alpha = \frac{1}{2}\left(\frac{R_{core}}{L_{shell}} - 1\right)$ defined by the core radius R_{core} and the shell thickness L_{shell}.

Using eqs 13, 15, 16 and 19, we find the differential equation for the radial stress component

$$\frac{d\sigma_{ev}}{dt} = E_{core} \cdot \frac{\dot{\mathbf{E}}_{core,\varphi\varphi}}{\lambda_{ch}^2} \tag{20}$$

$$= \frac{E_{core}}{\tau\lambda_{ch}^2} \sinh\left(\frac{\boldsymbol{\sigma}_{shell,visc,\varphi\varphi}}{\sigma_{ref}}\right) \tag{21}$$

$$= -\frac{E_{core}}{\tau\lambda_{ch}^2} \sinh\left(\frac{\alpha\lambda_{ch}^3\sigma_{ev}}{\sigma_{ref}}\right) \tag{22}$$

We solve the simplified differential equation in eq 22 analytically to describe the whole time dependence with a single analytical solution

$$\sigma_{ev} = \frac{2\sigma_{ref}}{\alpha\lambda_{ch}^3} \cdot \mathrm{atanh}\left(C \cdot \exp\left(-\frac{E_{core}\alpha\lambda_{ch}}{\tau\sigma_{ref}}t\right)\right) \tag{23}$$

where the constant C can be determined from the boundary condition at time $t = 0$ with $\sigma_{ev}(t = 0) = \sigma_0$.

For the calculation of the stress effect on the silicon voltage according to eq 5, we approximate the deformation of the silicon particle core as purely chemical, $\mathbf{F}_{core} = \mathbf{F}_{core,ch} = \lambda_{ch}\mathbf{Id}$, and we assume isotropic stress distribution inside the particle $\mathbf{P}_{core,ev} = \lambda_{ch}^2\sigma_{ev}\mathbf{Id}$. Therefore, the impact of the stress on the voltage according to eq 5 simplifies to $\Delta U_{ev} = \nu_{Li}\sigma_{ev}/F$ in the reduced model and the voltage relaxation reads

$$\Delta U_{ev} = \frac{2\nu_{Li}\sigma_{ref}}{\alpha F\lambda_{ch}^3} \mathrm{atanh}\left(C \exp\left(-\frac{E_{core}\alpha\lambda_{ch}}{\tau\sigma_{ref}}t\right)\right) \tag{24}$$

To understand the origin and the regimes of the convoluted functional behavior in eq 20, we analyze the relaxation behavior in the limits of large and low stress magnitudes in Section SI. Due to the importance of the long-term relaxation, here we present only the large stress limit. In the limit of large compressive stress, the differential eq 22 simplifies to

$$\frac{d\sigma_{ev}}{dt} = -\frac{E_{core}}{\tau\lambda_{ch}^2} \cdot \left(-\frac{1}{2}\right) \exp\left(-\frac{\alpha\lambda_{ch}^3\sigma_{ev}}{\sigma_{ref}}\right) \tag{25}$$

The analytical solution for this differential equation is

$$\sigma_{ev} = \frac{\sigma_{ref}}{\alpha\lambda_{ch}^3} \cdot \ln\left(\frac{E_{core}\alpha\lambda_{ch}}{2\tau\sigma_{ref}}t + C_{exp}\right) \tag{26}$$

with the integration constant C_{exp} determined from the boundary condition.

Thus, the voltage relaxation according to the Garofalo viscosity

$$\Delta U_{ev} = \frac{\nu_{Li}\sigma_{ref}}{\alpha F\lambda_{ch}^3} \cdot \ln\left(\frac{E_{core}\alpha\lambda_{ch}}{2\tau\sigma_{ref}}t + C_{exp}\right) \tag{27}$$

reveals logarithmic behavior in the large stress limit.

2.3. Reduced Model Equations. Complementary to our full model presented in Section 2.1, we derive a reduced model with the key features in Section SII. The reduced model describes the elastic stress contribution of the core at the interface between core and shell due to elastoplastic behavior of the shell σ_{ee} and due to viscous behavior of the shell σ_{ev}.

The system of equations defining the reduced chemo-mechanical hysteresis model reads

$$\frac{dSOC}{dt} = \frac{\dot{c}_{Li,0}}{c_{Li,max}} = \pm\frac{C_{rate}}{3600\ s} \tag{28}$$

$$\frac{d\Delta U_{ee}}{dt} = \begin{cases} -E_{shell}\dfrac{2\nu_{Li}^2}{3F\lambda_{ch}^7}\dot{c}_{Li,0}, & \text{if } f_{red} < 0 \\ \dfrac{\alpha\sigma_{Y,shell}\nu_{Li}^2}{F(1+\alpha\lambda_{ch}^3)^2}|\dot{c}_{Li,0}|, & \text{otherwise} \end{cases} \tag{29}$$

$$\frac{d\Delta U_{ev}}{dt} = -\frac{E_{core}\nu_{Li}}{\tau F\lambda_{ch}^2} \sinh\left(\frac{\alpha\lambda_{ch}^3 F\Delta U_{ev}}{\sigma_{ref}\nu_{Li}}\right) \tag{30}$$

$$-\frac{E_{core}\nu_{Li}^2}{3F\lambda_{ch}^3}\dot{c}_{Li,0} \tag{31}$$

with the parameter $\alpha = \frac{1}{2}\left(\frac{R_{core}}{L_{shell}} - 1\right)$ and the yield condition for plastic flow for the reduced model

$$f_{red} = -\mathrm{sgn}(\dot{c}_{Li,0})(1+\alpha\lambda_{ch}^3)\frac{F\Delta U_{ee}}{\nu_{Li}\sigma_{Y,shell}} - 1 < 0 \tag{32}$$

The equations defining the reduced model describe the silicon anode voltage as $U = U_{mean} + \Delta U_{ee} + \Delta U_{ev}$. Eq 28

https://doi.org/10.1021/acsami.4c12976
ACS Appl. Mater. Interfaces 2024, 16, 67609−67619

ACS Applied Materials & Interfaces www.acsami.org Research Article

states the change of SOC for lithiation (+) and delithiation (−). The upper case in eq 29 describes the voltage evolution caused by elastic behavior of the silicon core due to elastic behavior of the shell. The lower case describes elastic core stress due to plastic behavior of the shell. The first term in eq 30 considers the viscous shell stress relaxation. The second term considers viscous shell stress increase because of silicon volume changes.

In Figure 2, we depict the voltage profile predicted by the reduced model for a GITT procedure with (de)lithiation steps

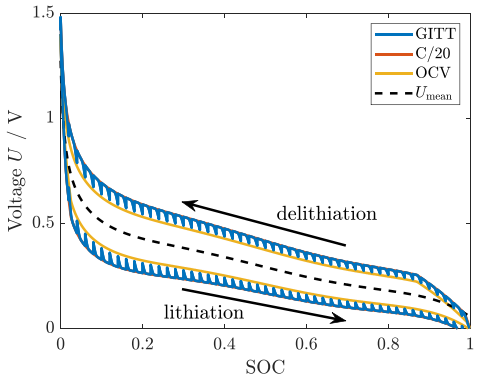

Figure 2. Voltages according to the presented reduced model during GITT, C/20 cycling, and after 12 h relaxation periods. The dashed black line depicts the mean experimental OCV measured for a silicon anode in ref.8.

of ΔSOC = 0.02 with C/20 and relaxation periods of 3 h. Furthermore, the figure shows the voltage during C/20 cycling and after 12 h relaxation periods. The dashed black line depicts the fitted mean experimental OCV curve U_{mean} between the measured lithiation and delithiation voltage after 3 h rest period for a pure silicon anode from ref.8 used as true OCV curve for the simulations. Note that the mean experimental OCV does not coincide with the mean value of the simulated OCV curves in the extreme SOC regimes due to an asymmetric stress situation discussed in detail in Section 4.3.

3. COMPUTATIONAL AND EXPERIMENTAL DETAILS

3.1. Simulation Setup. Our simulations describe the behavior of a silicon nanoparticle anode with a single-particle model. We implement our model in MATLAB using a finite-difference approach by discretizing the radial dimension. To solve the set of differential eqs 6−8, 11 and 12, we use the solver ode15i. The variables inside the silicon core are the concentration of lithium $c_{Li,0}$, the deformed radius r_{core}, and the radial component of the plastic deformation $\mathbf{F}_{core,pl,rr}$ of each silicon core element. The variables inside the shell are the deformed radius r_{shell} and the radial component of the plastic deformation $\mathbf{F}_{shell,pl,rr}$ of each shell element.

3.2. Material Parameters. We adopt the parameters from our previous publication[21] and adapt where necessary. Particularly, we consider a stiff, inorganic (SEI) shell with Young's modulus of E_{shell} = 100 GPa compatible with experiments.[45,46] The viscosity of the (inner SEI) shell is considered as a fit value and may range from $\eta = 10^7$ Pa s for a highly viscous polymer[47] to $\eta = 10^{15}$ Pa s for silicon oxide.[48−50]

3.3. Experimental Setup. The experiments analyzed in this study have been performed and published by Wycisk et al.[11] at Mercedes following discussions with the authors of this manuscript. The publication discusses full-cell voltage measurements with an NMC811 cathode and anodes with varying contents of silicon active material. Here, we constrain solely to the experimental results discussing anodes with pure silicon active material. The silicon anode consists of silicon nanoparticles attached to a conductive carbon network discussed as "silicon−carbon composite granules" in ref.51. We summarize the experimental and our simulation protocols in Section SIII but refer to the experimental publication for the experimental details.[11]

Throughout this manuscript, we consider voltages from the anode perspective and calculate voltage differences to the mean OCV, $U - U_{mean}$. For comparison, the voltage difference for the performed full-cell measurements is calculated as $U - U_{mean} = -(U_{full} - U_{full,mean})$.

4. RESULTS AND DISCUSSION

4.1. Experimental Results: Logarithmic Voltage Relaxation. First, we analyze the long-time relaxation experiment performed by Wycisk et al.[11] following the

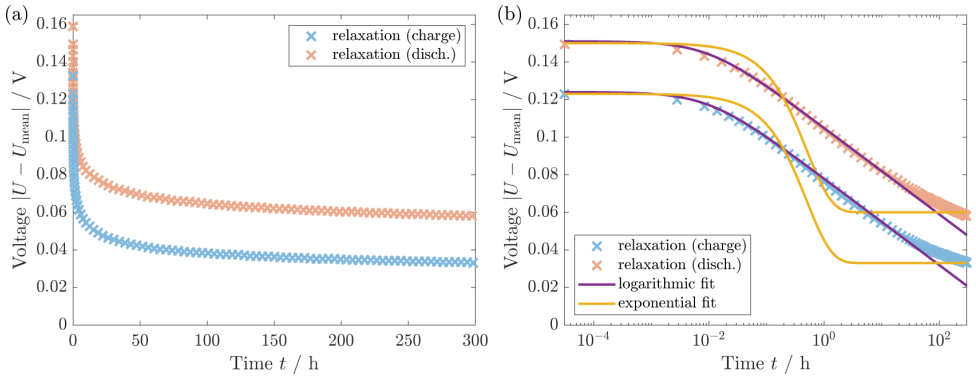

Figure 3. (a) Experimental voltage relaxation of silicon at SOC = 0.3 over 300 h after a charge and discharge period (protocol SIII A).[11] (b) The semilogarithmic plot unveils the logarithmic voltage relaxation behavior.

https://doi.org/10.1021/acsami.4c12976
ACS Appl. Mater. Interfaces 2024, 16, 67609−67619

ACS Applied Materials & Interfaces www.acsami.org Research Article

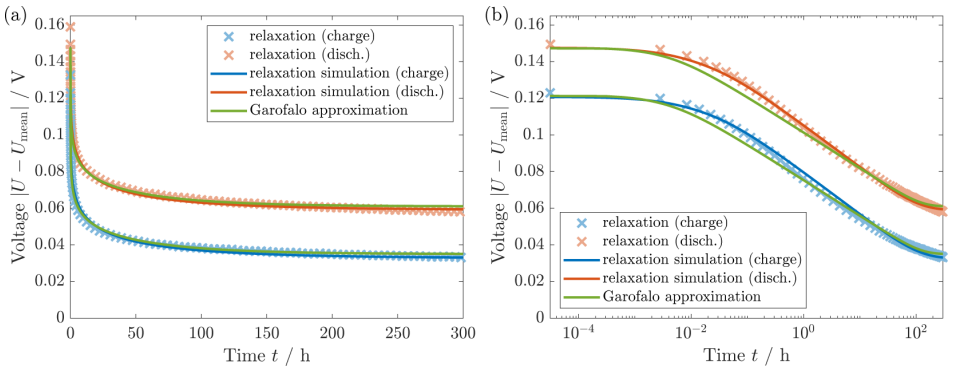

Figure 4. (a) Voltage relaxation of silicon at SOC = 0.3 over 300 h (protocol SIII A). Comparison of simulation, experiment,[11] and the analytical Garofalo approximation. (b) The semilogarithmic plot shows agreement of the various curves.

protocol described in Section SIII A. In Figure 3, we depict the voltage relaxation at the same SOC measured once in charge and once in discharge direction.

Interestingly, the authors of ref.11 find that even after 300 h of rest, the voltage depicted in Figure 3a is not completely relaxed. Therefore, the true OCV value deviates from the relaxed voltage after 300 h and strongly deviates from standard GITT measurements with only a few hours of voltage relaxation. The authors of ref.11 exclude degradation or self-discharge due to the similar voltage relaxation profiles after the charge and discharge period. However, the mean value of the relaxed voltage after 300 h varies from the mean OCV measured with GITT for C/20 and 12 h rest periods. Therefore, the relaxed voltages after lithiation and delithiation reveal different values with a deviation of 0.03 V. The difference can occur on the one hand due to cell-to-cell deviations of the experimental cells. On the other hand, a minor drift in the absolute SOC estimation of only 2% is already sufficient to create such a small voltage difference.

Here, we investigate the voltage relaxation profile in detail again. In Figure 3b, we show the voltage relaxation over time as a semilogarithmic plot. Apparently, the voltage relaxation profile does not follow a typical exponential relaxation behavior, as illustrated in yellow. We identify a linear regime in the semilogarithmic plot and fit a logarithmic function to the experimental data. The logarithmic fit agrees with the experimental data in a wide range of times $t < 20$ h. Only for times larger than 20 h, the voltage relaxation slightly diminishes, leaving the logarithmic regime. This is expected as logarithmic behavior would diverge for large times. The logarithmic voltage relaxation found in the experiment agrees with the experimentally observed voltage relaxation of silicon thin-film electrodes in ref.[20].

Regarding the hysteresis hypotheses in literature, the experimentally identified logarithmic voltage relaxation is in stark contrast to diffusional effects. Overpotentials due to diffusion would reveal an exponential voltage relaxation behavior, which cannot reproduce the experimental data as illustrated in Figure 3b. Moreover, reaction kinetics as the reason for the voltage hysteresis and relaxation would require unreasonable parameter values of the exchange current density and the anodic and cathodic transfer coefficients α_a, $\alpha_c \gg 1$.[20] Therefore, the observed logarithmic voltage relaxation provides clear support for the mechanical origin of the silicon voltage hysteresis.

4.2. Simulation Results: Slow Voltage Relaxation. As discussed in Section 2.1, the silicon OCV hysteresis results from elastoplastic stress generated by the shell, and the enlarged voltage hysteresis during cycling results from viscous shell stress acting on the particle core.[21] A simple Newtonian viscosity model, $\sigma_{shell} = \eta_{shell}\dot{E}_{shell}$, with constant viscosity η_{shell} would imply exponential voltage relaxation behavior during rest contrasting the experimental observations. Due to the large stresses inside the shell, the Newtonian model is not suitable for describing the viscous behavior. Instead, for large stresses, the strain rate is known to depend exponentially on the stress, leading to a logarithmic stress relaxation behavior. Therefore, we use the established Garofalo law given in eq 10 to describe both regimes.

Using the Garofalo model, Figure 4 depicts our simulation results in comparison to the experimental data. The parameters are given in Table S1. We shift our simulations to match the observed voltage after relaxation. The simulations reproduce the voltage relaxation profiles after the charge and discharge period. In particular, the simulation using the Garofalo law describes both the logarithmic relaxation regime as well as the decreasing relaxation after 20 h. The agreement confirms the explanation of the silicon voltage hysteresis by a visco-elastoplastic shell behavior.

To validate our simulation results, Figure 4 compares our simulation and the experiment to the analytical approximation presented in Section 2.2. The analytical approximation for the voltage relaxation with Garofalo law viscosity reveals a similar logarithmic relaxation regime followed by a slowed relaxation. Thus, the specific trends observed for our simulation and the analytical approximation agree while the actual values deviate slightly. Nevertheless, as the analytical approach relies on several assumptions and approximations, the similarity of the voltage profile supports our simulation results.

4.3. OCV and Cycling Voltage Hysteresis. Silicon anodes are generally known to show a significant voltage hysteresis. In Figure 5, we depict the experimental OCV hysteresis after relaxation and the enlarged voltage hysteresis during slow cycling.[11] We describe the protocol in Section SIII B. To check the consistency of our model with the experimental voltage hysteresis, Figure 5 shows the simulation of the anode voltage during slow cycling and the OCV after relaxation depending on the SOC for the parameters obtained from the voltage relaxation behavior. The illustrated voltages describe the influence on the silicon anode voltage. Hence, the

https://doi.org/10.1021/acsami.4c12976
ACS Appl. Mater. Interfaces 2024, 16, 67609−67619

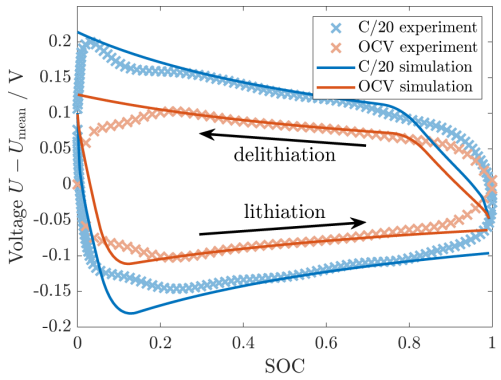

Figure 5. C/20 and open-circuit voltage hysteresis after 12 h relaxation in simulation and experiment (protocol SIII B).[11]

voltage decreases during lithiation due to compressive stress and increases during delithiation due to tensile stress. The simulation results in Figure 5 reveal a significant OCV hysteresis resulting from the elastoplastic contribution. Furthermore, the simulation shows an enlarged hysteresis during cycling caused by viscous stress.

The comparison of the cycling and relaxed voltages reveals a good agreement between simulation and experiment in a wide SOC regime. However, our simulation and the experiment deviate slightly at both extremes, SOC < 0.2 and SOC > 0.8. This disagreement results at least partially from the determination of the true, stress-free OCV curve as the mean between lithiation and delithiation OCV. At very high SOC, the elastoplastically generated compressive stress during lithiation is fully developed, while the tensile stress during the following delithiation has to build up gradually after the change of direction. Analogously, the tensile stress during delithiation is fully developed, while the compressive stress during the following lithiation has to build up gradually after the change of direction at low SOC. Therefore, the mean value between the lithiation and delithiation OCV at both extremes is not stress-free. Its consideration as true, stress-free OCV in the simulation leads to an apparent deviation. In the Supporting Information, we discuss a corrected OCV curve assuming a constant hysteresis size in the extreme SOC regimes. Figure S3 reveals a better agreement between simulation and experiment in the extreme SOC regimes compared to Figure 5. Note that the stress asymmetry in the extreme SOC regimes is generated by the elastoplastic behavior of the shell responsible for the OCV hysteresis. The asymmetry does not result from the viscous behavior, causing the enlarged hysteresis during slow cycling and the voltage relaxation.

In our previous publication,[21] we compared our simulation to the GITT measurement performed for a silicon half cell by Pan et al.[8,9] The cells differ significantly from the cells investigated by Wycisk et al.[11] due to a presumably different silicon raw material and electrolyte composition. Nevertheless, we compare our new model and the parameters obtained from the voltage relaxation[11] to the GITT measurement[8,9] in Section SV. Figure S4 shows a reasonable match of simulation and experiment considering the full GITT procedure as well as a single GITT pulse. The agreement confirms the applicability of our chemo-mechanical model to GITT measurements with different cells.

4.4. C-Rate Dependence of Voltage Hysteresis. The experimental data obtained by Wycisk et al.[11] also cover the C-rate dependence of the voltage difference between the cycling voltage and the relaxed voltage after 12 h at SOC = 0.5 following the protocol given in Section SIII C. As displayed in Figure 6, the data reveal a linear dependence of the voltage on

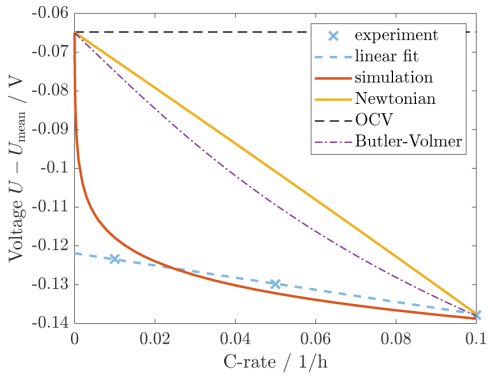

Figure 6. C-rate dependence of voltage hysteresis at SOC = 0.5 in simulation and experiment (protocol SIII C).[11]

the C-rate. However, extrapolating this linear dependence to zero current results in a significant voltage offset compared to the OCV after infinite relaxation time. This offset would imply an enlarged hysteresis even for infinitely slow cycling, which is unexpected. Therefore, the authors conclude that the voltage will depart from the linear trend at particularly low C-rates.

The Newtonian viscosity model has a linear relation between the strain rate and the viscous stress. Hence, the size of the additional voltage hysteresis is linearly dependent on the C-rate as illustrated in yellow in Figure 6. However, the Newtonian model explains no voltage offset, and the slope disagrees with the experiment when matching the hysteresis size at C/10.

In comparison to the experimental and the Newtonian C-rate dependence, Figure 6 also depicts the simulated C-rate dependence. The inverse hyperbolic sine in eq 10 determines the C-rate dependence of the viscous stress and, consequently, the C-rate dependence of the additional voltage hysteresis during cycling. Thus, the simulation reveals a nonlinear dependence of the voltage on the current. Nonetheless, after a swift increase of the voltage at current rates smaller C/100, the increase slows down, approaching an almost linear trend with small curvature. Although the three experimental data points follow the linear trend exactly, we assume that our simulation is in reasonable agreement with the experiment and additionally describes the transition to vanishing voltage at zero current. We expect that more experimental data points particularly at low C-rates might indicate a curvature and deviation from the linear trend.

Concerning diffusion and reaction overpotentials as alternative hysteresis hypotheses stated in literature, diffusion overpotentials inhere a linear dependence on the C-rate without offset, coinciding with the curve for Newtonian viscosity (yellow) in Figure 6. Further, reaction overpotentials expressed by the Butler–Volmer equation with typical symmetry factor $\alpha = 0.5$ show only a slight curvature (purple) in Figure 6. Considering a parameter variation, Figure S5 demonstrates that unreasonable anodic transfer coefficients

https://doi.org/10.1021/acsami.4c12976
ACS Appl. Mater. Interfaces 2024, 16, 67609−67619

$\alpha_a > 2$ are necessary to approach the experimentally observed C-rate dependence. Therefore, neither diffusion nor reaction overpotentials can reasonably reproduce the experimentally observed dependence on the C-rate. This demonstrates once again the insufficiency of transport and reaction overpotentials for explaining the silicon voltage hysteresis, thereby promoting our chemo-mechanical explanation.

4.5. Voltage Transition Profiles. Another interesting behavior is the silicon anode voltage profile of transitions between cycling and rest periods. In the following, we discuss the features of different transitions and compare our simulation to the experimental data from ref.11 wherever possible.

First, we investigate the transition profile between lithiation and delithiation according to protocol SIII D. In Figure 7, we show the delithiation with either C/10, C/20, or GITT procedure after a continuous lithiation and rest period. For reference, the figure also includes the simulated and measured lithiation and delithiation OCV curves from Figure 5, which almost coincide in the depicted regime $0.3 < \mathrm{SOC} < 0.5$. All experimental data[11] reveal a smooth transition between the lithiation and delithiation voltage. The slope of the voltage profiles is large directly after the change of direction and slows down gradually when approaching the delithiation voltage.

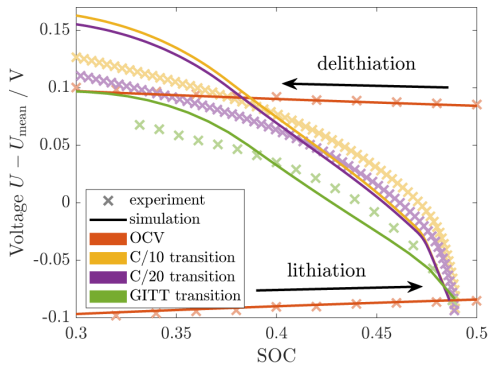

Figure 7. Voltage transition from lithiation to delithiation in simulation and experiment (protocol SIII D).[11]

The numerical results are depicted in Figure 7 compared to the experiment. When switching the current direction from lithiation to delithiation, the simulated voltage profiles for C/10 (yellow) and C/20 (purple) currents reveal three regimes. Immediately after the change of direction, the voltage shows a steep increase for a small span of $\Delta\mathrm{SOC} \approx 0.01$ attributed to the rapid buildup of viscous stress. Afterward, for a range of $\Delta\mathrm{SOC} \approx 0.1$, a constant, moderate voltage slope demonstrates the decrease of compressive elastic stress and the subsequent increase in tensile elastic stress. In the third regime, the slope slows down, and the voltage approaches a maximum value when reaching the yield criterion for plasticity. The higher current C/10 shows a slightly faster voltage transition compared to the lower current C/20. For the GITT transition curve (green), the relaxation of viscous stress during the rest periods suppresses the viscous regime after the change of direction. Contrary to the simulation, the experimental curves do not reveal clearly defined regimes but are in line with the general trend of a rapid voltage increase after the change of direction followed by an attenuated transition to the delithiation voltage curve. The much smoother experimental results compared to our simulation are expected as we consider only a single-particle model but the detailed features average out in the multi-particle experiment. Thus, we conclude that our simulation result agrees reasonably with the experimental measurement.

In Section SVII, we evaluate the behavior of an interrupted lithiation pulse for different C-rates and at different SOC values. All voltage profiles in Figures S6 and S7 show a steep slope at the beginning of the pulses, revealing the increase in viscous stress followed by a slower convergence to the lithiation voltage, indicating elastoplastic behavior. The similar voltage profiles for different C-rates indicate that the voltage transition needs a certain amount of charge throughput or SOC change ΔSOC in accordance with the experimental results from ref.11 for a blended graphite-silicon anode. Additionally, the voltage profiles at different SOC values in Figure S6 show that the general trends of the chemo-mechanical simulation agree with the ones of the experiment. However, all experimental curves show an overshoot instead of a smooth convergence to the lithiation voltage, which is not visible in our simulations. In terms of mechanics, this overshoot might result from a thixotropic behavior of the shell as discussed in the Supporting Information.

Another voltage hysteresis effect measured for silicon anodes is a pronounced relaxation during rest observed for higher applied currents.[11,S2] Higher C-rates show an increased voltage

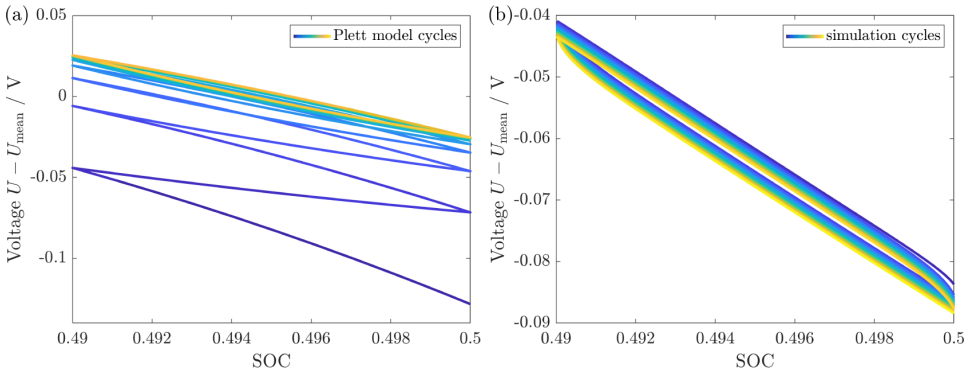

Figure 8. Voltage for alternating lithiation and delithiation pulses with $\Delta\mathrm{SOC} = 1\%$ (protocol SIII F) for (a) the phenomenological Plett model and (b) our chemo-mechanical simulation.

https://doi.org/10.1021/acsami.4c12976
ACS Appl. Mater. Interfaces 2024, 16, 67609−67619

hysteresis during cycling in agreement with our viscosity model. However, this dependence surprisingly inverts after relaxation. This phenomenon is not captured in our chemo-mechanical single-particle model. Therefore, we support the interpretation as a multi-particle effect[11] and add a mechanical explanation. For fast charging, the silicon particles inside the anode will lithiate more inhomogeneously, causing enhanced plastic flow of the shell around particles with a higher lithiation level. During the subsequent rest period, the silicon particles with initially higher lithiation degrees delithiate slightly. The shrinkage of those particles reduces the remaining compressive stress, while the stress in the particles with initially lower lithiation levels can not exceed the yield stress for plastic flow. Hence, this multi-particle effect can reduce the mean stress hysteresis inside the silicon anode and, consequently, the voltage hysteresis after relaxation.

Finally, we estimate the voltage transition behavior for alternating short lithiation and delithiation pulses following protocol SIII F. The silicon voltage hysteresis is often described empirically with the Plett model presented in Section SVIII.[53−55] In Figure 8a, we depict the behavior for alternating pulses with $\Delta SOC = 0.01$ predicted by the empirical Plett model with the parameters adjusted to fit the experimental voltage hysteresis. The Plett model does not reveal a constant hysteresis behavior during 10 subsequent cycles but rather approaches the mean OCV within the first cycles and then describes a hysteresis around it. Additionally, the Plett model is not able to account for a relaxation phase without a change in SOC. In contrast, Figure 8b shows the simulation of alternating pulses, which reveal a permanent hysteresis during 10 subsequent cycles. Only the very first pulse initially shows a slightly different behavior with an enlarged hysteresis size because of a different stress state in the initial situation after the 12 h relaxation period. We know that experiments show a permanent hysteresis behavior upon alternate lithiation and delithiation pulses in line with our simulation result. Thus, we conclude that our chemo-mechanical core−shell model outperforms the empirical Plett model in the description of voltage hysteresis phenomena.

5. CONCLUSIONS

Detailed analysis of the silicon voltage hysteresis experiments performed by Wycisk et al.[11] reveals a slow, non-exponential voltage relaxation. We identify a logarithmic voltage relaxation for a wide range of times and a transition to exponential relaxation for larger times due to the divergence of the logarithmic behavior. With a chemo-mechanical core−shell model, we have illustrated that the visco-elastoplastic shell behavior following the Garofalo law or inverse hyperbolic sine law for viscosity can accurately describe the voltage relaxation of a silicon anode over the whole time span. Our simulations also reproduce the observed voltage hysteresis and GITT measurement with the parameters obtained from the relaxation experiment. Our core−shell model can be interpreted as silicon nanoparticles covered by SEI but can also portray active silicon nanodomains within larger silicon particles.

Additionally, the Garofalo viscosity model can approach the experimentally observed C-rate dependence of the cycling voltage hysteresis. The inverse hyperbolic sine behaves approximately linear in a wide span of C-rates but shows a kink and reveals vanishing additional voltage hysteresis at zero current. Therefore, the Garofalo law viscosity model fits much better to the C-rate dependence than Newtonian viscosity, which reveals a proportional relation between the voltage and the applied C-rate.

With a focus on the voltage transition behavior between lithiation and delithiation, the presented chemo-mechanical model can adequately describe the general trends of an initially fast voltage transition followed by an attenuated convergence to the delithiation voltage curve. The interplay of viscous, elastic, and plastic contributions to the simulated voltage explains this voltage profile. Furthermore, our model reasonably describes the lithiation behavior after a rest period. Thus, our chemo-mechanical core−shell model outperforms the empirical Plett model regarding physical understanding as well as the description of the various features of the hysteresis phenomenon.

The overall accordance of our simulations to experimental results supports our chemo-mechanical explanation of the voltage hysteresis presented initially in ref.21. The description of the viscous behavior using the Garofalo law is more suitable than linear Newtonian viscosity because of the large stresses reached inside the shell. In conclusion, we have demonstrated that our physical model presents a consistent picture of the various features of the silicon voltage hysteresis phenomenon.

■ ASSOCIATED CONTENT

Supporting Information

The Supporting Information is available free of charge at https://pubs.acs.org/doi/10.1021/acsami.4c12976.

Analytical approximation for the voltage relaxation in the extremestress regimes; derivation of reduced model; detailed experimental and simulation protocols; corrected open-circuit voltage (OCV) curve; comparison with GITT measurement; C-rate dependence of reaction overpotentials; voltage profiles of lithiation pulses; Plett model; parameters (PDF)

■ AUTHOR INFORMATION

Corresponding Author

Birger Horstmann − *Institute of Engineering Thermodynamics, German Aerospace Center (DLR), Ulm 89081, Germany; Helmholtz Institute Ulm (HIU), Ulm 89081, Germany; Faculty of Natural Sciences, Ulm University, Ulm 89081, Germany;* orcid.org/0000-0002-1500-0578; Email: birger.horstmann@dlr.de

Authors

Lukas Köbbing − *Institute of Engineering Thermodynamics, German Aerospace Center (DLR), Ulm 89081, Germany; Helmholtz Institute Ulm (HIU), Ulm 89081, Germany;* orcid.org/0000-0002-1806-6732

Yannick Kuhn − *Institute of Engineering Thermodynamics, German Aerospace Center (DLR), Ulm 89081, Germany; Helmholtz Institute Ulm (HIU), Ulm 89081, Germany*

Complete contact information is available at: https://pubs.acs.org/10.1021/acsami.4c12976

Notes

The authors declare no competing financial interest.

■ ACKNOWLEDGMENTS

Lukas Köbbing gratefully acknowledges funding and support by the European Union's Horizon Europe within the research initiative Battery 2030+ via the OPINCHARGE project under

https://doi.org/10.1021/acsami.4c12976
ACS Appl. Mater. Interfaces 2024, 16, 67609−67619

the grant agreement number 101104032 and by the German Research Foundation (DFG) within the research training group SiMET under project number 281041241/GRK2218. The authors appreciate fruitful discussions with Dominik Wycisk, Felix Schwab, Martin Werres, Raphael Schoof, and Arnulf Latz.

REFERENCES

(1) Sun, L.; Liu, Y.; Shao, R.; Wu, J.; Jiang, R.; Jin, Z. Recent progress and future perspective on practical silicon anode-based lithium ion batteries. *Energy Storage Mater.* **2022**, *46*, 482−502.
(2) Zuo, X.; Zhu, J.; Müller-Buschbaum, P.; Cheng, Y.-J. Silicon based lithium-ion battery anodes: A chronicle perspective review. *Nano Energy* **2017**, *31*, 113−143.
(3) Feng, K.; Li, M.; Liu, W.; Kashkooli, A. G.; Xiao, X.; Cai, M.; Chen, Z. Silicon-Based Anodes for Lithium-Ion Batteries: From Fundamentals to Practical Applications. *Small* **2018**, *14* (8), 1702737.
(4) Beaulieu, L. Y.; Eberman, K. W.; Turner, R. L.; Krause, L. J.; Dahn, J. R. Colossal Reversible Volume Changes in Lithium Alloys. *Electrochem. Solid-State Lett.* **2001**, *4*, A137.
(5) Liu, X. H.; Zhong, L.; Huang, S.; Mao, S. X.; Zhu, T.; Huang, J. Y. Size-Dependent Fracture of Silicon Nanoparticles During Lithiation. *ACS Nano* **2012**, *6*, 1522−1531.
(6) Wetjen, M.; Solchenbach, S.; Pritzl, D.; Hou, J.; Tileli, V.; Gasteiger, H. A. Morphological Changes of Silicon Nanoparticles and the Influence of Cutoff Potentials in Silicon-Graphite Electrodes. *J. Electrochem. Soc.* **2018**, *165*, A1503−A1514.
(7) Kilchert, F.; Schammer, M.; Latz, A.; Horstmann, B. Silicon Nanowires as Anodes for Lithium-Ion Batteries: Full Cell Modeling. *Energy Technol.* **2024**, *12* (6), 2400206.
(8) Pan, K.; Zou, F.; Canova, M.; Zhu, Y.; Kim, J.-H. Systematic electrochemical characterizations of Si and SiO anodes for high-capacity Li-Ion batteries. *J. Power Sources* **2019**, *413*, 20−28.
(9) Pan, K. *A Systematic Methodology for Characterization and Prediction of Performance of Si-based Materials for Li-ion Batteries*; The Ohio State University, 2020.
(10) Bernard, P.; Alper, J. P.; Haon, C.; Herlin-Boime, N.; Chandesris, M. Electrochemical analysis of silicon nanoparticle lithiation − Effect of crystallinity and carbon coating quantity. *J. Power Sources* **2019**, *435*, 226769.
(11) Wycisk, D.; Mertin, G. K.; Oldenburger, M.; von Kessel, O.; Latz, A. Challenges of open-circuit voltage measurements for silicon-containing Li-Ion cells. *J. Energy Storage* **2024**, *89*, 111617.
(12) McDowell, M. T.; Lee, S. W.; Nix, W. D.; Cui, Y. 25th Anniversary Article: Understanding the Lithiation of Silicon and Other Alloying Anodes for Lithium-Ion Batteries. *Adv. Mater.* **2013**, *25*, 4966−4985.
(13) Wycisk, D.; Mertin, G. K.; Oldenburger, M.; Latz, A. Analysis of heat generation due to open-circuit voltage hysteresis in lithium-ion cells. *J. Energy Storage* **2023**, *61*, 106817.
(14) Sethuraman, V. A.; Chon, M. J.; Shimshak, M.; Srinivasan, V.; Guduru, P. R. In situ measurements of stress evolution in silicon thin films during electrochemical lithiation and delithiation. *J. Power Sources* **2010**, *195*, 5062−5066.
(15) Lu, B.; Song, Y.; Zhang, Q.; Pan, J.; Cheng, Y.-T.; Zhang, J. Voltage hysteresis of lithium ion batteries caused by mechanical stress. *Phys. Chem. Chem. Phys.* **2016**, *18*, 4721−4727.
(16) Chandrasekaran, R.; Magasinski, A.; Yushin, G.; Fuller, T. F. Analysis of Lithium Insertion/Deinsertion in a Silicon Electrode Particle at Room Temperature. *J. Electrochem. Soc.* **2010**, *157*, A1139.
(17) Zhao, K.; Pharr, M.; Cai, S.; Vlassak, J. J.; Suo, Z. Large Plastic Deformation in High-Capacity Lithium-Ion Batteries Caused by Charge and Discharge. *J. Am. Ceram. Soc.* **2011**, *94* (s1), s226−s235.
(18) Cui, Z.; Gao, F.; Qu, J. A finite deformation stress-dependent chemical potential and its applications to lithium ion batteries. *J. Mech. Phys. Solids* **2012**, *60*, 1280−1295.
(19) McDowell, M. T.; Lee, S. W.; Harris, J. T.; Korgel, B. A.; Wang, C.; Nix, W. D.; Cui, Y. In Situ TEM of Two-Phase Lithiation of Amorphous Silicon Nanospheres. *Nano Lett.* **2013**, *13*, 758−764.
(20) Sethuraman, V. A.; Srinivasan, V.; Newman, J. Analysis of Electrochemical Lithiation and Delithiation Kinetics in Silicon. *J. Electrochem. Soc.* **2013**, *160*, A394−A403.
(21) Köbbing, L.; Latz, A.; Horstmann, B. Voltage Hysteresis of Silicon Nanoparticles: Chemo-Mechanical Particle-SEI Model. *Adv. Funct. Mater.* **2024**, *34*, 2308818.
(22) Verma, P.; Maire, P.; Novák, P. A review of the features and analyses of the solid electrolyte interphase in Li-ion batteries. *Electrochim. Acta* **2010**, *55*, 6332−6341.
(23) Peled, E.; Menkin, S. Review—SEI: Past, Present and Future. *J. Electrochem. Soc.* **2017**, *164*, A1703−A1719.
(24) Horstmann, B.; Single, F.; Latz, A. Review on multi-scale models of solid-electrolyte interphase formation. *Curr. Opin. Electrochem.* **2019**, *13*, 61−69.
(25) Zhang, X.; Weng, S.; Yang, G.; Li, Y.; Li, H.; Su, D.; Gu, L.; Wang, Z.; Wang, X.; Chen, L. Interplay between solid-electrolyte interphase and (in)active LixSi in silicon anode. *Cell Rep. Phys. Sci.* **2021**, *2*, 100668.
(26) Nie, M.; Abraham, D. P.; Chen, Y.; Bose, A.; Lucht, B. L. Silicon Solid Electrolyte Interphase (SEI) of Lithium Ion Battery Characterized by Microscopy and Spectroscopy. *J. Phys. Chem. C* **2013**, *117*, 13403−13412.
(27) Köbbing, L.; Latz, A.; Horstmann, B. Growth of the solid-electrolyte interphase: Electron diffusion versus solvent diffusion. *J. Power Sources* **2023**, *561*, 232651.
(28) von Kolzenberg, L.; Latz, A.; Horstmann, B. Solid−Electrolyte Interphase During Battery Cycling: Theory of Growth Regimes. *ChemSuschem* **2020**, *13*, 3901−3910.
(29) Schroder, K. W.; Dylla, A. G.; Harris, S. J.; Webb, L. J.; Stevenson, K. J. Role of Surface Oxides in the Formation of Solid−Electrolyte Interphases at Silicon Electrodes for Lithium-Ion Batteries. *ACS Appl. Mater. Interfaces* **2014**, *6*, 21510−21524.
(30) Cao, C.; Abate, I. I.; Sivonxay, E.; Shyam, B.; Jia, C.; Moritz, B.; Devereaux, T. P.; Persson, K. A.; Steinrück, H.-G.; Toney, M. F. Solid Electrolyte Interphase on Native Oxide-Terminated Silicon Anodes for Li-Ion Batteries. *Joule* **2019**, *3*, 762−781.
(31) Schnabel, M.; Harvey, S. P.; Arca, E.; Stetson, C.; Teeter, G.; Ban, C.; Stradins, P. Surface SiO 2 Thickness Controls Uniform-to-Localized Transition in Lithiation of Silicon Anodes for Lithium-Ion Batteries. *ACS Appl. Mater. Interfaces* **2020**, *12*, 27017−27028.
(32) Huo, H.; Jiang, M.; Bai, Y.; Ahmed, S.; Volz, K.; Hartmann, H.; Henss, A.; Singh, C. V.; Raabe, D.; Janek, J. Chemo-mechanical failure mechanisms of the silicon anode in solid-state batteries. *Nat. Mater.* **2024**, *23*, 543−551.
(33) Guo, K.; Kumar, R.; Xiao, X.; Sheldon, B. W.; Gao, H. Failure progression in the solid electrolyte interphase (SEI) on silicon electrodes. *Nano Energy* **2020**, *68*, 104257.
(34) Lee, J.; Jeong, J.-Y.; Ha, J.; Kim, Y.-T.; Choi, J. Understanding solid electrolyte interface formation on graphite and silicon anodes in lithium-ion batteries: Exploring the role of fluoroethylene carbonate. *Electrochem. Commun.* **2024**, *163*, 107708.
(35) von Kolzenberg, L.; Latz, A.; Horstmann, B. Chemo-Mechanical Model of SEI Growth on Silicon Electrode Particles. *Batteries Supercaps* **2022**, *5*, No. e202100216.
(36) Li, Q.; Liu, X.; Han, X.; Xiang, Y.; Zhong, G.; Wang, J.; Zheng, B.; Zhou, J.; Yang, Y. Identification of the Solid Electrolyte Interface on the Si/C Composite Anode with FEC as the Additive. *ACS Appl. Mater. Interfaces* **2019**, *11*, 14066−14075.
(37) Chen, J.; et al. Electrolyte design for LiF-rich solid−electrolyte interfaces to enable high-performance microsized alloy anodes for batteries. *Nat. Energy* **2020**, *5*, 386−397.
(38) He, Y.; et al. Progressive growth of the solid−electrolyte interphase towards the Si anode interior causes capacity fading. *Nat. Nanotechnol.* **2021**, *16*, 1113−1120.
(39) Deringer, V. L.; Bernstein, N.; Csányi, G.; Ben Mahmoud, C.; Ceriotti, M.; Wilson, M.; Drabold, D. A.; Elliott, S. R. Origins of

https://doi.org/10.1021/acsami.4c12976
ACS Appl. Mater. Interfaces 2024, 16, 67609−67619

structural and electronic transitions in disordered silicon. *Nature* **2021**, *589*, 59−64.
(40) Chevrier, V. L.; Liu, L.; Le, D. B.; Lund, J.; Molla, B.; Reimer, K.; Krause, L. J.; Jensen, L. D.; Figgemeier, E.; Eberman, K. W. Evaluating Si-Based Materials for Li-Ion Batteries in Commercially Relevant Negative Electrodes. *J. Electrochem. Soc.* **2014**, *161*, A783−A791.
(41) Kitada, K.; Pecher, O.; Magusin, P. C. M. M.; Groh, M. F.; Weatherup, R. S.; Grey, C. P. Unraveling the Reaction Mechanisms of SiO Anodes for Li-Ion Batteries by Combining in Situ 7 Li and ex Situ 7 Li/ 29 Si Solid-State NMR Spectroscopy. *J. Am. Chem. Soc.* **2019**, *141*, 7014−7027.
(42) Wang, J.; Wang, X.; Liu, B.; Lu, H.; Chu, G.; Liu, J.; Guo, Y.-G.; Yu, X.; Luo, F.; Ren, Y.; Chen, L.; Li, H. Size effect on the growth and pulverization behavior of Si nanodomains in SiO anode. *Nano Energy* **2020**, *78*, 105101.
(43) Garofalo, F.; Richmond, O.; Domis, W. F.; von Gemmingen, F.Strain-Time, Rate-Stress and Rate-Temperature Relations during Large Deformations in Creep*Proceedings of The Institution of Mechanical Engineers, Conference Proceedings*Sage196331−39
(44) Stang, E. T. Constitutive Modeling of Creep in Leaded and Lead-Free Solder Alloys Using Constant Strain-Rate Tensile Testing. In *Master of Science in Mechanical Engineering*; Wright State University, 2018.
(45) Shin, H.; Park, J.; Han, S.; Sastry, A. M.; Lu, W. Component-/structure-dependent elasticity of solid electrolyte interphase layer in Li-ion batteries: Experimental and computational studies. *J. Power Sources* **2015**, *277*, 169−179.
(46) Chai, Y.; Jia, W.; Hu, Z.; Jin, S.; Jin, H.; Ju, H.; Yan, X.; Ji, H.; Wan, L.-J. Monitoring the mechanical properties of the solid electrolyte interphase (SEI) using electrochemical quartz crystal microbalance with dissipation. *Chin. Chem. Lett.* **2021**, *32*, 1139−1143.
(47) Edgeworth, R.; Dalton, B. J.; Parnell, T. The pitch drop experiment. *Euro. J. Phy.* **1984**, *5*, 198−200.
(48) Sutardja, P.; Oldham, W. Modeling of stress effects in silicon oxidation. *IEEE Trans. Electron Devices* **1989**, *36*, 2415−2421.
(49) Senez, V.; Collard, D.; Baccus, B.; Brault, M.; Lebailly, J. Analysis and application of a viscoelastic model for silicon oxidation. *J. Appl. Phys.* **1994**, *76*, 3285−3296.
(50) Ojovan, M. I. Viscosity and Glass Transition in Amorphous Oxides. *Adv. Condensed Matter Phys.* **2008**, *2008*, 1−23.
(51) Schwan, J.; Nava, G.; Mangolini, L. Critical barriers to the large scale commercialization of silicon-containing batteries. *Nanoscale Adv.* **2020**, *2*, 4368−4389.
(52) Durdel, A.; Friedrich, S.; Hüsken, L.; Jossen, A. Modeling Silicon-Dominant Anodes: Parametrization, Discussion, and Validation of a Newman-Type Model. *Batteries* **2023**, *9*, 558.
(53) Plett, G. L. Extended Kalman filtering for battery management systems of LiPB-based HEV battery packs. *J. Power Sources* **2004**, *134*, 262−276.
(54) Graells, C. P.; Trimboli, M. S.; Plett, G. L. Differential hysteresis models for a silicon-anode Li-ion battery cell. *2020 IEEE Transportation Electrification Conference & Expo (ITEC)*; IEEE, 2020, 175180.
(55) Wycisk, D.; Oldenburger, M.; Stoye, M. G.; Mrkonjic, T.; Latz, A. Modified Plett-model for modeling voltage hysteresis in lithium-ion cells. *J. Energy Storage* **2022**, *52*, 105016.

https://doi.org/10.1021/acsami.4c12976
ACS Appl. Mater. Interfaces 2024, 16, 67609−67619

Supporting Information: Slow Voltage Relaxation of Silicon Nanoparticles with a Chemo-Mechanical Core-Shell Model

Lukas Köbbing, Yannick Kuhn, and Birger Horstmann*
Institute of Engineering Thermodynamics, German Aerospace Center (DLR), Wilhelm-Runge-Straße 10, 89081 Ulm, Germany
Helmholtz Institute Ulm (HIU), Helmholtzstraße 11, 89081 Ulm, Germany and
Faculty of Natural Sciences, Ulm University, Albert-Einstein-Allee 47, 89081 Ulm, Germany

SI. ANALYTICAL APPROXIMATION FOR THE VOLTAGE RELAXATION IN THE EXTREME STRESS REGIMES

The time evolution of the general stress relaxation behavior during rest is derived in the manuscript as

$$\frac{\mathrm{d}\sigma_{\mathrm{ev}}}{\mathrm{d}t} = -E_{\mathrm{core}}\frac{1}{\tau\lambda_{\mathrm{ch}}^2}\sinh\left(\frac{\alpha\lambda_{\mathrm{ch}}^3\sigma_{\mathrm{ev}}}{\sigma_{\mathrm{ref}}}\right) \tag{S1}$$

with the analytical solution

$$\sigma_{\mathrm{ev}} = \frac{2\sigma_{\mathrm{ref}}}{\alpha\lambda_{\mathrm{ch}}^3}\cdot\operatorname{atanh}\left(C\cdot\exp\left(-\frac{E_{\mathrm{core}}\alpha\lambda_{\mathrm{ch}}}{\tau\sigma_{\mathrm{ref}}}t\right)\right). \tag{S2}$$

To understand the origin and the regimes of the convoluted functional behavior in Equation (S2), we analyze the relaxation behavior in the limits of low and large stress magnitudes in the following.

First, to solve the differential equation (S1) analytically in the limit of large compressive stress, i.e.

$$\frac{\sigma_{\mathrm{ev}}}{\sigma_{\mathrm{ref}}} \ll -1, \tag{S3}$$

the hyperbolic sine can be approximated by

$$\sinh x = \frac{1}{2}\left(\mathrm{e}^{x} - \mathrm{e}^{-x}\right) \approx -\frac{1}{2}\mathrm{e}^{-x}. \tag{S4}$$

Thus, the differential equation in the large compressive stress regime reads

$$\frac{\mathrm{d}\sigma_{\mathrm{ev}}}{\mathrm{d}t} = -\frac{E_{\mathrm{core}}}{\tau\lambda_{\mathrm{ch}}^2}\cdot\left(-\frac{1}{2}\right)\exp\left(-\frac{\alpha\lambda_{\mathrm{ch}}^3\sigma_{\mathrm{ev}}}{\sigma_{\mathrm{ref}}}\right). \tag{S5}$$

The analytical solution for this differential equation is

$$\sigma_{\mathrm{ev}} = \frac{\sigma_{\mathrm{ref}}}{\alpha\lambda_{\mathrm{ch}}^3}\cdot\ln\left(\frac{E_{\mathrm{core}}\alpha\lambda_{\mathrm{ch}}}{2\tau\sigma_{\mathrm{ref}}}t + C_{\mathrm{exp}}\right). \tag{S6}$$

Using the chemo-mechanical coupling $\Delta U = v_{\mathrm{Li}}\sigma/F$, the voltage relaxation reads

$$\Delta U_{\mathrm{ev}} = \frac{v_{\mathrm{Li}}\sigma_{\mathrm{ref}}}{\alpha F\lambda_{\mathrm{ch}}^3}\cdot\ln\left(\frac{E_{\mathrm{core}}\alpha\lambda_{\mathrm{ch}}}{2\tau\sigma_{\mathrm{ref}}}t + C_{\mathrm{exp}}\right). \tag{S7}$$

The integration constant C_{exp} has to be determined from the boundary condition as

$$C_{\mathrm{exp}} = \exp\left(\frac{\alpha\lambda_{\mathrm{ch}}^3\sigma_0}{\sigma_{\mathrm{ref}}}\right). \tag{S8}$$

* birger.horstmann@dlr.de

Second, to solve the differential equation analytically in the low compressive stress limit with

$$-1 < \frac{\sigma_{\mathrm{ev}}}{\sigma_{\mathrm{ref}}} \leq 0 \tag{S9}$$

we approximate the hyperbolic sine as

$$\sinh x = \frac{1}{2}\left(\mathrm{e}^{x} - \mathrm{e}^{-x}\right) \approx x. \tag{S10}$$

Therefore, the differential equation (S1) in the low compressive stress limit reads

$$\frac{\mathrm{d}\sigma_{\mathrm{ev}}}{\mathrm{d}t} = -\frac{E_{\mathrm{core}}}{\tau} \cdot \frac{\alpha\lambda_{\mathrm{ch}}\sigma_{\mathrm{ev}}}{\sigma_{\mathrm{ref}}}. \tag{S11}$$

This equation describes Newtonian viscosity with $\eta = \tau\sigma_{\mathrm{ref}}$. The analytical solution states

$$\sigma_{\mathrm{ev}} = C_{\mathrm{lin}} \cdot \exp\left(-\frac{E_{\mathrm{core}}\alpha\lambda_{\mathrm{ch}}}{\tau\sigma_{\mathrm{ref}}}t\right). \tag{S12}$$

The voltage relaxation reads

$$\Delta U_{\mathrm{ev}} = \frac{v_{\mathrm{Li}}C_{\mathrm{lin}}}{F} \cdot \exp\left(-\frac{E_{\mathrm{core}}\alpha\lambda_{\mathrm{ch}}}{\tau\sigma_{\mathrm{ref}}}t\right). \tag{S13}$$

This time, the constant C_{lin} has to be determined from the boundary condition at the time entering the low compressive stress limit.

Thus, the general solution describes logarithmic behavior in the large stress limit but exponential relaxation behavior in the low stress limit. We depict the approximations for the large and low stress limits in Figure S1 in comparison to the general approximation and the experimental data from Ref. [1].

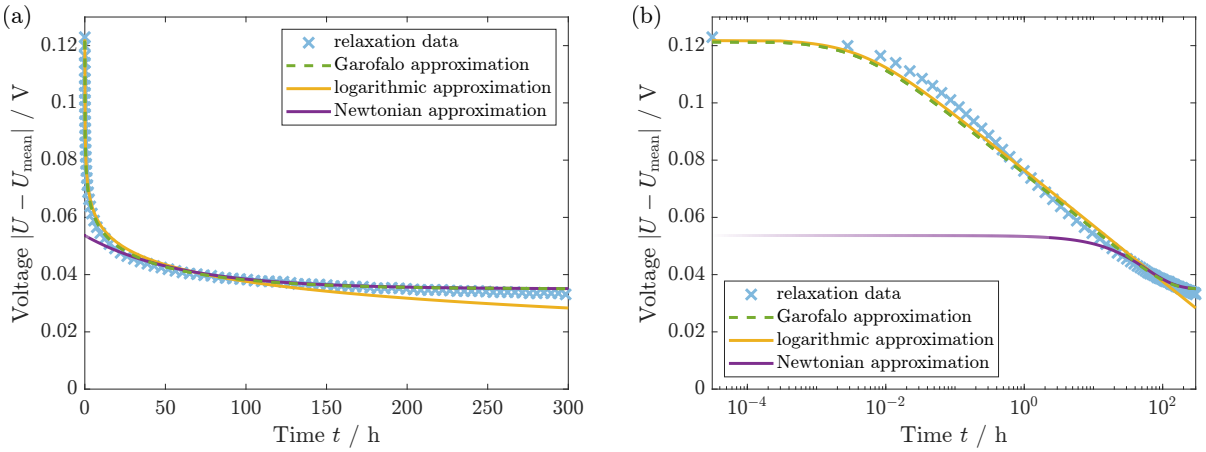

Figure S1. (a) Voltage relaxation of silicon described by the analytical approximations in comparison to the experiment [1]. (b) Semi-logarithmic plot of approximations and experiment [1].

SII. DERIVATION OF REDUCED MODEL

First, we assume volume conservation of the shell

$$1 = J_{\text{shell}} = \mathbf{F}_{\text{shell,rr}}\mathbf{F}^2_{\text{shell},\varphi\varphi}. \tag{S14}$$

The tangential deformation of the shell is determined by the total expansion of the particle dominated by the chemical deformation

$$\mathbf{F}_{\text{shell,rr}} = \mathbf{F}^{-2}_{\text{shell},\varphi\varphi} \approx \lambda^{-2}_{\text{ch}} = \left(1 + v_{\text{Li}} c_{\text{Li},0}\right)^{-\frac{2}{3}}. \tag{S15}$$

The strain rate reads

$$\dot{\mathbf{E}}_{\text{shell,rr}} = \mathbf{F}_{\text{shell,rr}}\dot{\mathbf{F}}_{\text{shell,rr}} = \mathbf{F}^{-2}_{\text{shell},\varphi\varphi}\left(\dot{\mathbf{F}^{-2}_{\text{shell},\varphi\varphi}}\right) = -2\mathbf{F}^{-5}_{\text{shell},\varphi\varphi}\dot{\mathbf{F}}_{\text{shell},\varphi\varphi} \approx -2\lambda^{-6}_{\text{ch}}\dot{\mathbf{E}}_{\text{core,rr}} \tag{S16}$$

using isotropic deformation inside the silicon particle core $\mathbf{E}_{\text{core,rr}} = \mathbf{E}_{\text{core},\varphi\varphi}$. In the elastic regime, the elastic stress contribution from the shell reads

$$\boldsymbol{\sigma}_{\text{shell,el,rr}} = E_{\text{shell}}\mathbf{E}_{\text{shell,rr}}. \tag{S17}$$

The elastic stress is mainly generated during cycling by the chemical deformation rate

$$\dot{\mathbf{E}}_{\text{shell,rr}} = -2\lambda^{-5}_{\text{ch}}\dot{\lambda}_{\text{ch}} = -\frac{2v_{\text{Li}}}{3\lambda^{7}_{\text{ch}}}\dot{c}_{\text{Li},0}. \tag{S18}$$

The time evolution of the elastic stress inside the particle due to the elastic stress of the shell reads

$$\dot{\sigma}_{\text{ee}} = \dot{\boldsymbol{\sigma}}_{\text{shell,el,rr}} = -E_{\text{shell}}\frac{2v_{\text{Li}}}{3\lambda^{7}_{\text{ch}}}\dot{c}_{\text{Li},0}. \tag{S19}$$

The yield criterion is given by the deviatoric Mandel stress. Due to the constant shell volume, Mandel stress equals Cauchy stress

$$\mathbf{M}^{\text{dev}}_{\text{shell,el}} = \mathbf{M}_{\text{shell,el}} - \frac{1}{3}\operatorname{tr}\mathbf{M}_{\text{shell,el}} = \boldsymbol{\sigma}_{\text{shell,el}} - \frac{1}{3}\operatorname{tr}\boldsymbol{\sigma}_{\text{shell,el}} \tag{S20}$$

and

$$\left|\mathbf{M}^{\text{dev}}_{\text{shell,el}}\right|^2 = \left(\frac{2}{3}\left(\boldsymbol{\sigma}_{\text{shell,el,rr}} - \boldsymbol{\sigma}_{\text{shell,el},\varphi\varphi}\right)\right)^2 + 2\left(-\frac{1}{3}\left(\boldsymbol{\sigma}_{\text{shell,el,rr}} - \boldsymbol{\sigma}_{\text{shell,el},\varphi\varphi}\right)\right)^2 = \frac{2}{3}\left(\boldsymbol{\sigma}_{\text{shell,el,rr}} - \boldsymbol{\sigma}_{\text{shell,el},\varphi\varphi}\right)^2. \tag{S21}$$

The empirical relation from our simulations $\mathbf{P}_{\text{shell,rr}} \approx -\frac{2L_{\text{shell}}/R_{\text{core}}}{1-L_{\text{shell}}/R_{\text{core}}}\mathbf{P}_{\text{shell},\varphi\varphi}$ implies $\boldsymbol{\sigma}_{\text{shell},\varphi\varphi} = -\frac{1}{2}(R_{\text{core}}/L_{\text{shell}} - 1)\lambda^3_{\text{ch}}\boldsymbol{\sigma}_{\text{shell,rr}}$ and the yield condition

$$f = \frac{\frac{3}{2}\left|\mathbf{M}^{\text{dev}}_{\text{shell,el}}\right|^2}{\sigma^2_{\text{Y,shell}}} - 1 = \frac{\left(\boldsymbol{\sigma}_{\text{shell,el,rr}}(1 + \frac{1}{2}(R_{\text{core}}/L_{\text{shell}} - 1)\lambda^3_{\text{ch}})\right)^2}{\sigma^2_{\text{Y,shell}}} - 1 \leq 0. \tag{S22}$$

When the yield criterion is reached, plastic flow determines the deformation and the stress follows the yield surface

$$\dot{\sigma}_{\text{ee}} = \dot{\boldsymbol{\sigma}}_{\text{shell,el,rr}} = \sigma_{\text{Y,shell}}\left(1 + \frac{1}{2}\left(\frac{R_{\text{core}}}{L_{\text{shell}}} - 1\right)\lambda^3_{\text{ch}}\right)^{-2}\frac{1}{2}\left(\frac{R_{\text{core}}}{L_{\text{shell}}} - 1\right)v_{\text{Li}}\left|\dot{c}_{\text{Li},0}\right|. \tag{S23}$$

For the viscous part of the stress, we take the time evolution of the elastic silicon core stress due to viscous stress of the shell

$$\dot{\sigma}_{\text{ev}} = E_{\text{core}}\dot{\mathbf{E}}_{\text{core,ev,rr}}. \tag{S24}$$

We describe the deformation of the silicon particle with a multiplicative approach

$$\mathbf{F}_{\text{core}} = \mathbf{F}_{\text{core,el}}\mathbf{F}_{\text{core,ch}} = \mathbf{F}_{\text{core,ee}}\mathbf{F}_{\text{core,ev}}\mathbf{F}_{\text{core,ch}} \approx \mathbf{F}_{\text{core,ev}}\mathbf{F}_{\text{core,ch}}. \tag{S25}$$

Therefore, the elastic strain rate due to viscosity reads

$$\dot{\mathbf{E}}_{\mathrm{core,ev}} = \mathbf{F}_{\mathrm{core,ev}}\dot{\mathbf{F}}_{\mathrm{core,ev}} \approx \dot{\mathbf{F}}_{\mathrm{core,ev}} \approx \frac{\dot{\mathbf{F}}_{\mathrm{core}}}{\lambda_{\mathrm{ch}}} - \frac{\dot{\mathbf{F}}_{\mathrm{core,ch}}}{\lambda_{\mathrm{ch}}}. \tag{S26}$$

The viscous stress contribution is determined by the Garofalo law

$$\boldsymbol{\sigma}_{\mathrm{shell,visc}} = \sigma_{\mathrm{ref}}\,\mathrm{asinh}\left(\tau\dot{\mathbf{E}}_{\mathrm{shell}}\right). \tag{S27}$$

Thus, the stress evolution reads

$$\begin{aligned}
\dot{\sigma}_{\mathrm{ev}} &= E_{\mathrm{core}}\dot{\mathbf{E}}_{\mathrm{core,ev,rr}} && \text{(S28)}\\
&= E_{\mathrm{core}}\left(\frac{\dot{\mathbf{F}}_{\mathrm{core,rr}}}{\lambda_{\mathrm{ch}}} - \frac{\dot{\mathbf{F}}_{\mathrm{core,ch}}}{\lambda_{\mathrm{ch}}}\right) && \text{(S29)}\\
&\approx E_{\mathrm{core}}\left(\frac{\dot{\mathbf{E}}_{\mathrm{shell},\varphi\varphi}}{\lambda_{\mathrm{ch}}^2} - \frac{\dot{\lambda}_{\mathrm{ch}}}{\lambda_{\mathrm{ch}}}\right) && \text{(S30)}\\
&= E_{\mathrm{core}}\frac{1}{\tau\lambda_{\mathrm{ch}}^2}\sinh\left(\frac{\boldsymbol{\sigma}_{\mathrm{shell,visc},\varphi\varphi}}{\sigma_{\mathrm{ref}}}\right) - E_{\mathrm{core}}\frac{v_{\mathrm{Li}}}{3\lambda_{\mathrm{ch}}^3}\dot{c}_{\mathrm{Li},0} && \text{(S31)}\\
&= -E_{\mathrm{core}}\frac{1}{\tau\lambda_{\mathrm{ch}}^2}\sinh\left(\frac{\frac{1}{2}\left(\frac{R_{\mathrm{core}}}{L_{\mathrm{shell}}}-1\right)\lambda_{\mathrm{ch}}^3\sigma_{\mathrm{ev}}}{\sigma_{\mathrm{ref}}}\right) - E_{\mathrm{core}}\frac{v_{\mathrm{Li}}}{3\lambda_{\mathrm{ch}}^3}\dot{c}_{\mathrm{Li},0}. && \text{(S32)}
\end{aligned}$$

With the chemo-mechanical coupling $\Delta U = v_{\mathrm{Li}}\sigma/F$, the system of equations reads

$$\frac{\mathrm{d}\,\mathrm{SOC}}{\mathrm{d}t} = \frac{\dot{c}_{\mathrm{Li},0}}{c_{\mathrm{Li,max}}} = \pm\frac{C_{\mathrm{rate}}}{3600}\frac{1}{\mathrm{s}} \tag{S33}$$

$$\frac{\mathrm{d}\,\Delta U_{\mathrm{ee}}}{\mathrm{d}t} = \begin{cases} -E_{\mathrm{shell}}\dfrac{2v_{\mathrm{Li}}^2}{3F\lambda_{\mathrm{ch}}^7}\dot{c}_{\mathrm{Li},0}, & \text{if } -\mathrm{sgn}\left(\dot{c}_{\mathrm{Li},0}\right)\left(1+\alpha\lambda_{\mathrm{ch}}^3\right)\dfrac{F\Delta U_{\mathrm{ee}}}{v_{\mathrm{Li}}} < \sigma_{\mathrm{Y,shell}} \\ \sigma_{\mathrm{Y,shell}}\dfrac{\alpha v_{\mathrm{Li}}^2}{F\left(1+\alpha\lambda_{\mathrm{ch}}^3\right)^2}\left|\dot{c}_{\mathrm{Li},0}\right|, & \text{otherwise} \end{cases} \tag{S34}$$

$$\frac{\mathrm{d}\,\Delta U_{\mathrm{ev}}}{\mathrm{d}t} = -E_{\mathrm{core}}\frac{v_{\mathrm{Li}}}{\tau F\lambda_{\mathrm{ch}}^2}\sinh\left(\frac{\alpha\lambda_{\mathrm{ch}}^3}{\sigma_{\mathrm{ref}}}\frac{F\Delta U_{\mathrm{ev}}}{v_{\mathrm{Li}}}\right) - E_{\mathrm{core}}\frac{v_{\mathrm{Li}}^2}{3F\lambda_{\mathrm{ch}}^3}\dot{c}_{\mathrm{Li},0}. \tag{S35}$$

To simplify the equations, we define the parameter $\alpha = \frac{1}{2}\left(\frac{R_{\mathrm{core}}}{L_{\mathrm{shell}}} - 1\right)$.

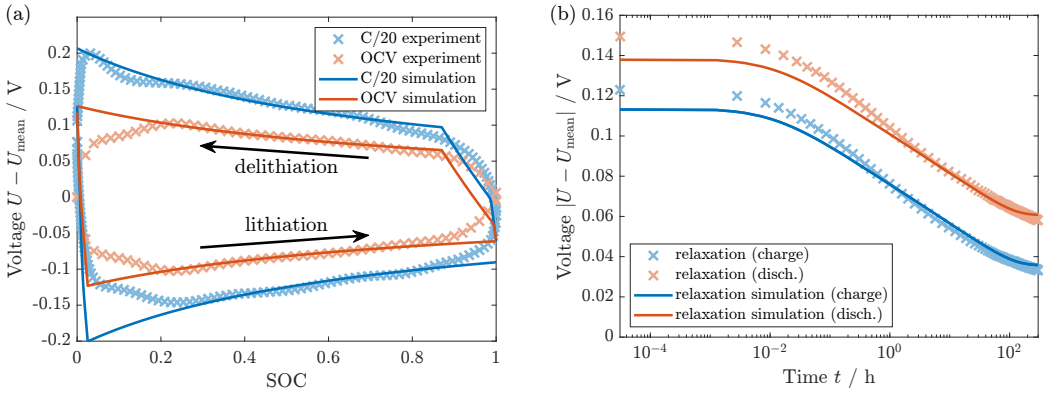

Figure S2. Results of reduced model equations in comparison to the experimental data [1]. (a) Voltage Hysteresis for C/20 current and OCV after 12 h relaxation period. (b) Voltage relaxation for 300 h after C/10 lithiation at SOC = 0.3.

SIII. DETAILED EXPERIMENTAL AND SIMULATION PROTOCOLS

In the following, we summarize the experimental and our simulation protocols but refer to the experimental publication for the experimental details [1]. We relate the measured and simulated voltages consistently to the mean value of the charging and discharging OCV obtained in Section SIII B.

A. Long-term relaxation

For the long-term relaxation experiment, the authors of Ref. [1] charge the cell with C/10 up to 30 % state-of-charge (SOC) and allow it to relax under open-circuit conditions for 300 h. Afterward, they charge the cell up to 60 % SOC, discharge to 30 % SOC, and observe the relaxation again. Thus, the authors of Ref. [1] measure the voltage relaxation at the same SOC once in charge and once in discharge direction. We apply the same protocol for our simulation of the long-term relaxation.

B. Cycling and open-circuit voltage hysteresis

Additionally, the authors of Ref. [1] measure the voltage hysteresis during slow cycling with C/20 and the OCV hysteresis between 0 % and 100 % SOC. The OCV hysteresis is obtained by the galvanostatic intermittent titration technique (GITT). The GITT protocol consists of subsequent (dis)charging steps with 2 % SOC and relaxation periods of 12 h. We simulate the cycling voltage with C/20 and the OCV after 12 h relaxation.

C. C-rate dependence of voltage hysteresis

For the C-rate dependence, the authors of Ref. [1] measure the voltage difference for varying currents during continuous charging and the relaxed voltage after 12 h at 50 % SOC. To calculate the voltage related to the mean OCV, we use the voltage after 12 h relaxation at 50 % SOC for C/20 obtained in Section SIII B. We apply the same protocol for our simulation of the C-rate dependence.

D. Voltage transition profiles

To measure the transition profile between lithiation and delithiation, the authors of Ref. [1] charge the cell up to SOC = 0.49 with C/10 current with a following relaxation time of 12 h. Subsequently, they discharge with either C/10, C/20, or GITT steps of ΔSOC = 0.01 with C/10 and 12 h relaxation. We apply the same protocol for our simulation of the voltage transition.

E. Voltage profiles for interrupted lithiation

The authors of Ref. [1] measure the behavior of an interrupted lithiation pulse for different SOC values with C/20 and a rest period of 12 h. We apply the same protocol for our simulation of an interrupted simulation pulse. Furthermore, we simulate the behavior of an interrupted lithiation pulse for different C-rates after a rest period of 12 h at SOC = 0.5.

F. Voltage profiles for alternating pulses

Finally, we simulate the voltage transition behavior for alternating pulses. We lithiate the silicon anode up to 50 % SOC with a subsequent relaxation period of 12 h. Then, we apply ten sequences of alternating delithiation and lithiation pulses with ΔSOC = 0.01.

SIV. CORRECTED OPEN-CIRCUIT VOLTAGE (OCV) CURVE

For simplicity and reduction of the degrees of freedom, we take the mean value of the measured OCV curves after 12 h as true OCV in our manuscript, $U_{\mathrm{mean}} = 1/2(U_{\mathrm{OCV,lithiation}} + U_{\mathrm{OCV,delithiation}})$. Nevertheless, the symmetry between lithiation and delithiation is broken at the extreme SOC values. At high SOC, elastoplastic compressive stress is fully developed during lithiation. In contrast, this compressive stress has to be reduced, and tensile stress has to build up gradually after the change in direction. At low SOC, tensile stress is fully developed during delithiation. In contrast, this tensile stress has to be reduced, and compressive stress has to build up gradually after the change in direction. To account for and estimate the significance of this effect, we define a corrected OCV curve as

$$U_{\mathrm{OCV,corr}}(\mathrm{SOC}) = \begin{cases} U_{\mathrm{OCV,delithiation}}(\mathrm{SOC}) - (U_{\mathrm{OCV,delithiation}}(0.2) - U_{\mathrm{mean}}(0.2))\,, & \text{if SOC} < 0.2 \\ U_{\mathrm{mean}}(\mathrm{SOC}), & \text{if } 0.2 \leq \mathrm{SOC} \leq 0.8 \\ U_{\mathrm{OCV,lithiation}}(\mathrm{SOC}) - (U_{\mathrm{OCV,lithiation}}(0.8) - U_{\mathrm{mean}}(0.8))\,, & \text{if SOC} > 0.8. \end{cases} \tag{S36}$$

The corrected OCV curve equals the mean OCV curve in the regime $0.2 \leq \mathrm{SOC} \leq 0.8$. In the extreme SOC regimes, we assume that the distance between the OCV curve in the direction of fully developed stress and the true OCV stays constant. The corrected OCV curve is depicted in Figure S3(a) compared to the mean OCV curve used in our manuscript. We depict our simulation results compared to the experimental data [1] related to the corrected OCV in Figure S3(b). In comparison to Fig. 5 in our manuscript with the experiment related to the mean OCV, our simulation shows an improved agreement with the experiment related to the corrected OCV curve. Thus, a corrected OCV should be considered when a superior agreement between simulation and experiment is indispensable. Nonetheless, we use the simple approach with the mean OCV throughout our manuscript.

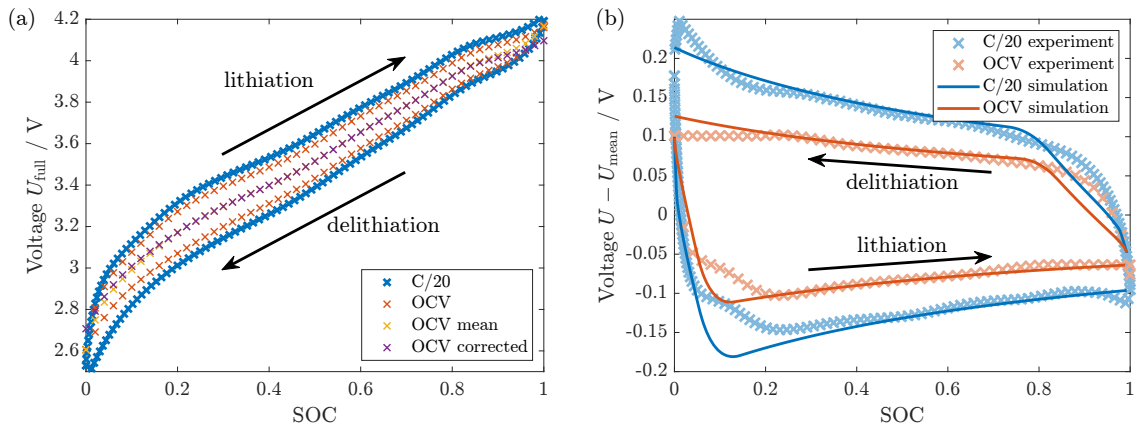

Figure S3. (a) Mean OCV and corrected OCV in comparison to the experimental data [1]. (b) Chemo-mechanical simulation of the voltage hysteresis in comparison to the experimental data related to the corrected OCV curve [1].

SV. COMPARISON WITH GITT MEASUREMENT

Here, we compare our chemo-mechanical core-shell model with the galvanostatic intermittent titration technique (GITT) measurements from Pan et al. [2, 3] for silicon anode half-cells. We use the parameters stated in Table S1 gained in our manuscript from the voltage relaxation measured for silicon anode full cells [1]. Fig. S4(a) reveals a reasonable agreement between the simulated GITT voltage curve and the experimental curve [2]. Fig. S4(b) shows the comparison of our simulation and the experiment for a single GITT pulse. The voltage profiles for the current phase and the relaxation period look similar, while the difference between lithiation voltage and relaxed voltage is smaller for the simulation compared to the data. Particularly, the simulation predicts smaller voltage relaxations for delithiation at high SOC and for lithiation at low SOC values. This deviation results from a slightly too slow voltage transition directly after change of direction predicted by the model compared to the experiment. Additionally, the relaxation appears smaller than it is due to the large slope of the voltage curves in the respective regimes. The deviation of the absolute voltage values is expected as the exact parameters are gained from the relaxation experiment performed with different cells.

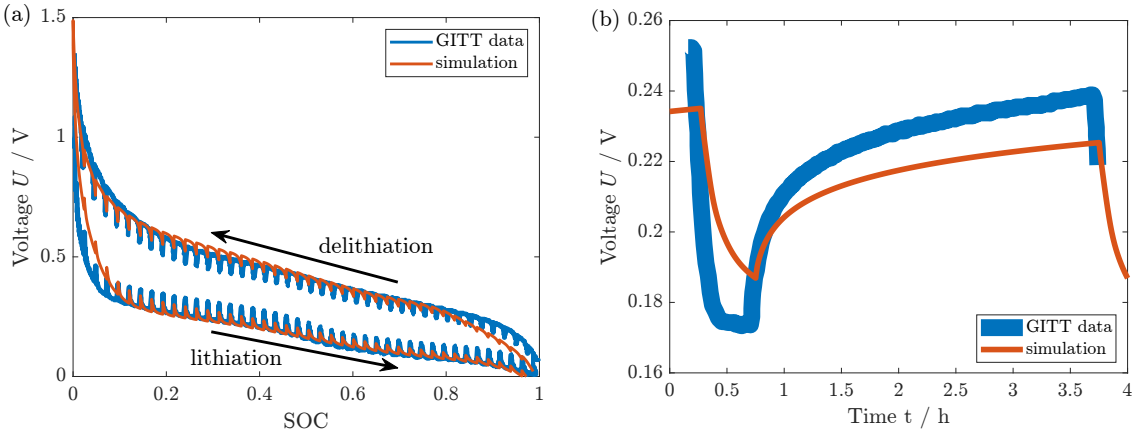

Figure S4. (a) Simulation of GITT procedure with the model and parameters obtained for the long-term relaxation experiment from Ref. [1] in comparison to the experimental data presented in Ref. [2]. (b) Simulation of the voltage transition of a single GITT pulse in comparison to the experimental data presented in Ref. [3].

SVI. C-RATE DEPENDENCE OF REACTION OVERPOTENTIALS

Contrary to our chemo-mechanical model, reaction kinetics are considered in literature as explanation hypothesis for the voltage hysteresis of silicon anodes [4]. For comparison with our model, we evaluate the C-rate dependence of reaction overpotentials in the following.

The relation between the current density j and the reaction overpotential ΔU is commonly described by the Butler-Volmer equation

$$j = -j_0 \left[\exp\left(\frac{\alpha_a F \Delta U}{R_{\text{gas}} T} \right) - \exp\left(-\frac{\alpha_c F \Delta U}{R_{\text{gas}} T} \right) \right] \tag{S37}$$

with the exchange current density j_0 as well as the anodic and cathodic transfer coefficients α_a and α_c. The remaining parameters are the Faraday constant F, the universal gas constant R_{gas} and the temperature T.

Typically for charge-transfer reactions in lithium-ion batteries, the transfer coefficients are assumed to be $\alpha_a = \alpha$ and $\alpha_c = 1 - \alpha$ with $\alpha = 0.5$. Slight deviations of $\alpha = 0.5$ are possible but less common. Values of $\alpha_a, \alpha_c > 1$ are considered to be physically unreasonable.

Figure S5 depicts the C-rate dependence of the reaction overpotentials predicted by the Butler-Volmer equation for different sets of parameters. The exchange current density j_0 is adjusted to meet the OCV at vanishing current and the experimental voltage measured at C/10. The plot shows that typical parameters of $\alpha = 0.5$ can not explain the observed C-rate dependence. In contrast, unreasonable parameter values $\alpha_a > 2$ are necessary to approach the experimental C-rate dependence. Therefore, reaction overpotentials are not able to explain the observed C-rate dependence with reasonable parameter values.

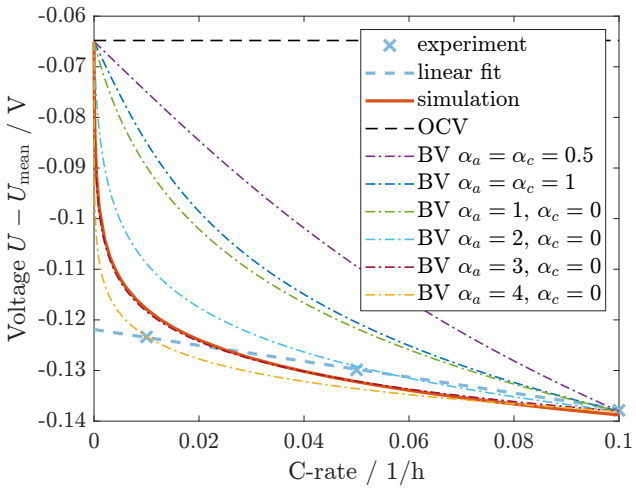

Figure S5. C-rate dependence of Butler-Volmer reaction overpotentials for various reasonable and unreasonable parameters in comparison to experimental data [1].

SVII. VOLTAGE PROFILES OF LITHIATION PULSES

We simulate the voltage profile according to our chemo-mechanical core-shell model during a lithiation after a rest period of 12 h following protocol SIII E. Fig. S6 shows the voltage transition for an interrupted lithiation pulse with C/20 at different SOC values in comparison to a continuous lithiation (dashed lines). The initial voltage difference decreases, and the transition to the lithiation voltage gets slower for higher SOC values. For comparison, we show the experimental result [1] (lighter colors). For the experiment, the initial voltage difference decreases slightly, and the voltage transition shows a slight retardation for higher SOC values. Thus, the general trends of our chemo-mechanical simulation agree with the ones of the experiment. However, all experimental curves show an overshoot instead of a smooth convergence to the lithiation voltage, which is not visible in our simulations.

Such a voltage overshoot during the transition from a rest period to lithiation is measured in Ref. [1] consistently for different C-rates, SOC values, and Si contents in the anode. In terms of mechanics, this overshoot might result from a thixotropic behavior of the shell. Thixotropy means that the viscosity of a material reduces during a deformation period but increases again during a rest period. This increase in viscosity is due to a reorganization of particles or grains inside the material. Assuming the thixotropic behavior of the shell can result in an initially steeper voltage transition and an overshoot analogous to the experimental data shown in Figure S6.

Fig. S7(a) depicts the behavior of an interrupted lithiation pulse for different C-rates after a rest period of 12 h at SOC = 0.5. All curves show a steep slope at the beginning attributed to viscous stress. For $\Delta\mathrm{SOC} > 0.01$, it is followed by a slower convergence to the lithiation voltage attributed to elastoplastic behavior. A purely elastic regime is not visible in this scenario, as elastic stress is not significantly relieved during relaxation in contrast to a transition between lithiation and delithiation. The similar slope of the voltage profiles for different C-rates indicates that the voltage transition is dependent on the charge throughput as measured by Wycisk et al. [1] for a blended graphite-silicon anode with 20 % silicon in the low-SOC regime, where silicon is the active component. In contrast, Figure S7(b) reveals that the time dependence of the voltage transition differs strongly for different currents.

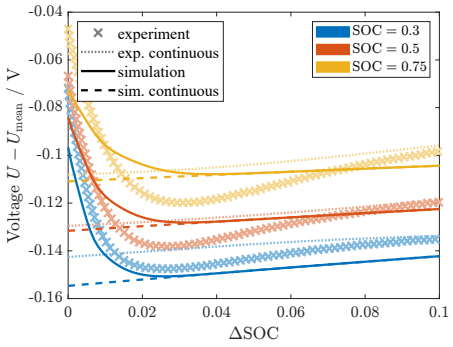

Figure S6. Simulated voltage profile of a lithiation pulse at different SOC after a rest period and the voltage during continuous lithiation depending on the change in SOC in comparison to experimental data [1].

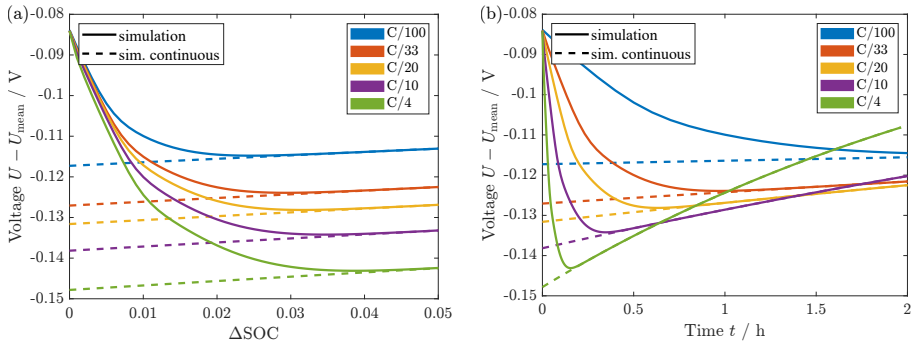

Figure S7. Simulated voltage profile of a lithiation pulse with different C-rates after a rest period and the voltage during continuous lithiation. (a) Voltage profile depending on the change in SOC. (b) Voltage profile depending on the elapsed time.

SVIII. PLETT MODEL

The phenomenological Plett model [5–7] can describe the hysteresis phenomenon and transitions between the voltage curves observed for lithiation and delithiation. According to the Plett model, the measured voltage is the mean open-circuit voltage $U_{\mathrm{mean}}(\mathrm{SOC})$ changed by half of the width of the voltage hysteresis measured between lithiation and delithiation $H(\mathrm{SOC})$ times the hysteresis state $h(\mathrm{SOC})$ defined between -1 and 1 as

$$U = U_{\mathrm{mean}}(\mathrm{SOC}) + H(\mathrm{SOC}) \cdot h(\mathrm{SOC}). \tag{S38}$$

The voltage considering the hysteresis behavior results from the differential equation

$$\frac{dh(\mathrm{SOC})}{d\mathrm{SOC}} = -k(\mathrm{SOC}) \left(1 + \mathrm{sgn}\left(\frac{d\mathrm{SOC}}{dt}\right) h(\mathrm{SOC})\right). \tag{S39}$$

The parameter k determines the slope of the transition between the two hysteresis states, which can in principle depend on the SOC. As a simple relation, we set $k(\mathrm{SOC}) = k_0 = 40$.

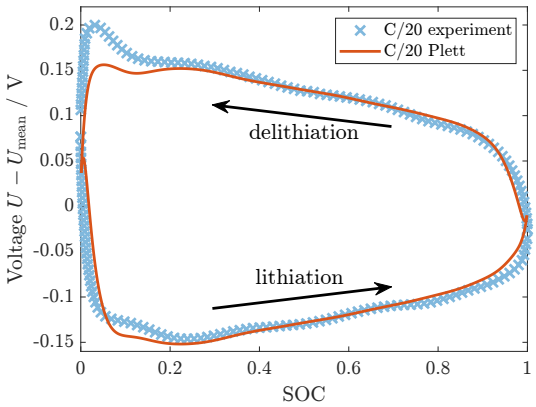

Figure S8. Voltage hysteresis described by the empirical Plett model in comparison to experimental data [1].

SIX. PARAMETERS

Parameter	Value		Reference
Silicon core			
Nanoparticle radius R_{core}	50	nm	estimated [2]
Solid state diffusion coefficient in silicon D_{Li}	$1 \cdot 10^{-17}$	m^2/s	[8]
Young's modulus E_{core}	200	GPa	estimated [9, 10]
Poisson's ratio ν_{core}	0.22		[11]
First Lamé constant $\lambda_{\mathrm{core}} = 2G_{\mathrm{core}}\nu_{\mathrm{core}}/(1-2\nu_{\mathrm{core}})$	64	GPa	calculated
Second Lamé constant $G_{\mathrm{core}} = E_{\mathrm{core}}/2(1+\nu_{\mathrm{core}})$	82	GPa	calculated
Yield stress $\sigma_{\mathrm{Y,core}}$	3	GPa	fit
Theoretical maximum lithium concentration in Si core $c_{\mathrm{Li,max}}$	$311 \cdot 10^3$	$\mathrm{mol}/\mathrm{m}^3$	[12]
Lithium concentration in Si core at SOC = 0	0.1	$c_{\mathrm{Li,max}}$	estimated
Lithium concentration in Si core at SOC = 1	0.9	$c_{\mathrm{Li,max}}$	estimated
Lithium molar volume in Si core v_{Li}	$9 \cdot 10^{-6}$	$\mathrm{m}^3/\mathrm{mol}$	[13]
SEI shell			
Shell thickness L_{shell}	20	nm	estimated [14]
Young's modulus E_{shell}	100	GPa	estimated [15, 16]
Poisson's ratio ν_{shell}	0.3		[15]
First Lamé constant $\lambda_{\mathrm{shell}} = 2G_{\mathrm{shell}}\nu_{\mathrm{shell}}/(1-2\nu_{\mathrm{shell}})$	58	GPa	calculated
Second Lamé constant $G_{\mathrm{shell}} = E_{\mathrm{shell}}/2(1+\nu_{\mathrm{shell}})$	38	GPa	calculated
Yield stress $\sigma_{\mathrm{Y,shell}}$	2.0	GPa	fit
Newtonian viscosity η_{shell}	$135 \cdot 10^{12}$	Pa s	fit
Viscous reference stress σ_{ref}	133	MPa	fit
Viscous time constant τ	$3 \cdot 10^8$	s	fit
Universal constants and other parameters			
Temperature T	298	K	
Faraday constant F	96 485	C/mol	
Universal gas constant R_{gas}	8.314	J/(mol K)	

TABLE S1. List of the simulation parameters.

[1] D. Wycisk, G. K. Mertin, M. Oldenburger, O. von Kessel, and A. Latz, Challenges of open-circuit voltage measurements for silicon-containing Li-Ion cells, Journal of Energy Storage **89**, 111617 (2024).
[2] K. Pan, F. Zou, M. Canova, Y. Zhu, and J.-H. Kim, Systematic electrochemical characterizations of Si and SiO anodes for high-capacity Li-Ion batteries, Journal of Power Sources **413**, 20 (2019).
[3] K. Pan, *A Systematic Methodology for Characterization and Prediction of Performance of Si-based Materials for Li-ion Batteries*, Ph.D. thesis, Ohio State University (2020).
[4] V. A. Sethuraman, V. Srinivasan, and J. Newman, Analysis of Electrochemical Lithiation and Delithiation Kinetics in Silicon, Journal of The Electrochemical Society **160**, A394 (2013).
[5] G. L. Plett, Extended Kalman filtering for battery management systems of LiPB-based HEV battery packs, Journal of Power Sources **134**, 262 (2004).
[6] C. P. Graells, M. S. Trimboli, and G. L. Plett, Differential hysteresis models for a silicon-anode Li-ion battery cell, in *2020 IEEE Transportation Electrification Conference & Expo (ITEC)*, Vol. 1 (IEEE, 2020) pp. 175–180.
[7] D. Wycisk, M. Oldenburger, M. G. Stoye, T. Mrkonjic, and A. Latz, Modified Plett-model for modeling voltage hysteresis in lithium-ion cells, Journal of Energy Storage **52**, 105016 (2022).
[8] J. Li, X. Xiao, F. Yang, M. W. Verbrugge, and Y.-T. Cheng, Potentiostatic Intermittent Titration Technique for Electrodes Governed by Diffusion and Interfacial Reaction, The Journal of Physical Chemistry C **116**, 1472 (2012).
[9] M. Nasr Esfahani and B. E. Alaca, A Review on Size-Dependent Mechanical Properties of Nanowires, Advanced Engineering Materials **21**, 1900192 (2019).
[10] D.-M. Tang, C.-L. Ren, M.-S. Wang, X. Wei, N. Kawamoto, C. Liu, Y. Bando, M. Mitome, N. Fukata, and D. Golberg, Mechanical Properties of Si Nanowires as Revealed by in Situ Transmission Electron Microscopy and Molecular Dynamics Simulations, Nano Letters **12**, 1898 (2012).
[11] V. Shenoy, P. Johari, and Y. Qi, Elastic softening of amorphous and crystalline Li–Si Phases with increasing Li concentration: A first-principles study, Journal of Power Sources **195**, 6825 (2010).
[12] A. Verma, A. A. Franco, and P. P. Mukherjee, Mechanistic Elucidation of Si Particle Morphology on Electrode Performance, Journal of The Electrochemical Society **166**, A3852 (2019).
[13] R. Koerver, W. Zhang, L. de Biasi, S. Schweidler, A. O. Kondrakov, S. Kolling, T. Brezesinski, P. Hartmann, W. G. Zeier, and J. Janek, Chemo-mechanical expansion of lithium electrode materials – on the route to mechanically optimized all-solid-state batteries, Energy & Environmental Science **11**, 2142 (2018).
[14] J. Zheng, H. Zheng, R. Wang, L. Ben, W. Lu, L. Chen, L. Chen, and H. Li, 3D visualization of inhomogeneous multi-layered structure and Young's modulus of the solid electrolyte interphase (SEI) on silicon anodes for lithium ion batteries, Phys. Chem. Chem. Phys. **16**, 13229 (2014).
[15] H. Shin, J. Park, S. Han, A. M. Sastry, and W. Lu, Component-/structure-dependent elasticity of solid electrolyte interphase layer in Li-ion batteries: Experimental and computational studies, Journal of Power Sources **277**, 169 (2015).
[16] Y. Chai, W. Jia, Z. Hu, S. Jin, H. Jin, H. Ju, X. Yan, H. Ji, and L.-J. Wan, Monitoring the mechanical properties of the solid electrolyte interphase (SEI) using electrochemical quartz crystal microbalance with dissipation, Chinese Chemical Letters **32**, 1139 (2021).

Paper IV

Elliptical Silicon Nanowire Covered by the SEI in a 2D Chemo-Mechanical Simulation

Authors	Raphael Schoof,[+] Lukas Köbbing,[+] Arnulf Latz, Birger Horstmann, Willy Dörfler
Journal	Batteries & Supercaps
Year	2025
Volume (Issue)	8 (5)
Pages	e202400604
DOI	10.1002/batt.202400604
Copyright	CC BY 4.0
Copyright link	https://creativecommons.org/licenses/by/4.0/
Copyright notice	Reprinted from Ref. [62].
Preprint DOI	10.48550/arXiv.2409.07991
+	R. Schoof and L. Köbbing contributed equally.

Author's Contribution

R. Schoof further developed and implemented the chemo-mechanical silicon-SEI model numerically efficiently in the two-dimensional geometry. In collaboration with R. Schoof, L. Köbbing continuously analyzed and evaluated preliminary and final results, elaborating the physical interpretation and identifying relevant parameter scenarios as well as interesting consequences of the elliptical geometry and the mechanical impact of the SEI. For the publication, L. Köbbing wrote the Introduction, Results and Discussion, Summary and Conclusion, and Appendices. R. Schoof wrote the Abstract, Theory, and Numerical Approach, and illustrated the results in the figures shown in the manuscript and appendix. L. Köbbing and R. Schoof jointly revised the manuscript, which was then reviewed and remarked by B. Horstmann, A. Latz, and W. Dörfler.

Check for updates

Batteries & Supercaps

Research Article
doi.org/10.1002/batt.202400604

Chemistry Europe
European Chemical Societies Publishing

www.batteries-supercaps.org

Elliptical Silicon Nanowire Covered by the SEI in a 2D Chemo-Mechanical Simulation

Raphael Schoof[+],*[a] Lukas Köbbing[+],*[b, c] Arnulf Latz,[b, c, d] Birger Horstmann,[b, c, d] and Willy Dörfler[a]

Understanding the mechanical interplay between silicon anodes and their surrounding solid-electrolyte interphase (SEI) is essential to improve the next generation of lithium-ion batteries. We model and simulate a 2D elliptical silicon nanowire with SEI via a thermodynamically consistent chemo-mechanical continuum ansatz using a higher order finite element method in combination with a variable-step, variable-order time integration scheme. Considering a soft viscoplastic SEI for three half cycles, we see at the minor half-axis the largest stress magnitude at the silicon nanowire surface, leading to a concentration anomaly. This anomaly is caused by the shape of the nanowire itself and not by the SEI. Also for the tangential stress of the SEI, the largest stress magnitudes are at this point, which can lead to SEI fracture. However, for a stiff SEI, the largest stress magnitude inside the nanowire occurs at the major half-axis, causing a reduced concentration distribution in this area. The largest tangential stress of the SEI is still at the minor half-axis. In total, we demonstrate the importance of considering the mechanics of the anode and SEI in silicon anode simulations and encourage further numerical and model improvements.

Introduction

Silicon anodes can present the next vital step towards improved lithium-ion batteries with higher capacity.[1–5] Nevertheless, the significant ability for lithiation causes massive volume changes during cycling, hindering the commercialization of pure silicon anodes.[6,7] The substantial deformations lead to mechanical instabilities of anode particles larger than 150 nm and cause particle fracture and pulverization.[8,9] Consequently, hopes are pinned on nanostructured silicon anodes[10–12] and silicon nanowires in particular.[13–15]

Due to electrolyte instability in contact with anode particles, the solid-electrolyte interphase (SEI) forms on silicon anodes, reasonably passivating the electrolyte from further decomposition.[16–19] However, the SEI continues to grow during storage and battery operation via electron transport from the anode towards the electrolyte.[20–22] On silicon anodes, the SEI and its mechanical behavior merit special attention as the massive volume changes of the anode challenge the stability of the SEI.[23,24] Nonetheless, the inner SEI is reported to stay intact during cycling.[25] Thus, it is important to consider the stress generated inside the SEI and its implication for silicon anodes in simulations of the silicon-SEI system.[26–28]

Our previous works discussed the silicon-SEI system with spherical symmetry.[24,26,27,29] Additionally, we performed 2D simulations of the nanowire only[30–32] and restricted expansion by a rigid obstacle.[33] As literature reports the importance of non-symmetric geometries on the mechanical properties during cycling[34] in contrast to a spherical setup,[35] we investigate the mechanics of an elliptical silicon nanowire covered by SEI in this manuscript. Therefore, we straightforwardly adapt our 1D radial symmetric setup for the chemical and elastic silicon core as well as the elastic and viscoplastic SEI shell to the 2D elliptical nanowire. Our variable-step, variable-order time integration scheme is combined with a higher order finite element method. In total, we simulate three half cycles, meaning a first lithiation is followed by delithiation and a second lithiation. We provide extensive investigations of the mechanical characteristics and concentration distribution for the coupled silicon-SEI structure.

The remaining of this manuscript is structured as follows: in "Theory", we present the key details of our continuum modeling, followed by a brief summary of our numerical procedure in "Numerical Approach". The focus of this work is "Results and Discussion", in which we present our extensive numerical results and discussions. We conclude with a summary and a short outlook in "Summary and Conclusion".

[a] *R. Schoof,[+] Prof. Dr. W. Dörfler*
Karlsruhe Institute of Technology (KIT), Institute for Applied and Numerical Mathematics, Englerstraße 2, 76131 Karlsruhe, Germany
E-mail: raphael.schoof@kit.edu

[b] *L. Köbbing,[+] Prof. Dr. A. Latz, Prof. Dr. B. Horstmann*
German Aerospace Center (DLR),
Wilhelm-Runge-Straße 10, 89081 Ulm, Germany
E-mail: lukas.koebbing@dlr.de

[c] *L. Köbbing,[+] Prof. Dr. A. Latz, Prof. Dr. B. Horstmann*
Helmholtz Institute Ulm (HIU),
Helmholtzstraße 11, 89081 Ulm, Germany

[d] *Prof. Dr. A. Latz, Prof. Dr. B. Horstmann*
Faculty of Natural Sciences, Ulm University,
Albert-Einstein-Allee 47, 89081 Ulm, Germany

[+] *These authors contributed equally.*

Supporting information for this article is available on the WWW under https://doi.org/10.1002/batt.202400604

Batteries & Supercaps

Research Article
doi.org/10.1002/batt.202400604

Chemistry Europe
European Chemical Societies Publishing

Theory

We follow Ref. [29] and briefly recap our chemo-mechanically coupled model for the *silicon-SEI* approach. This ansatz is based on the thermodynamically consistent theory by Refs. [24, 26, 29–31, 36, 37].

We use a purely elastic (Lagrangian) logarithmic Hencky strain for the finite deformation model of the electrode nanowire, whereas we apply a viscoplastic approach for the SEI. For a purely elastic particle without SEI, the typically used Lagrangian strain or Green–St–Venant strain leads to similar results compared to the Hencky strain.[31,38] The deformation Φ relates the reference (Lagrangian) configuration $\Omega_0 \subset \mathbb{R}^3$ to the current (Eulerian) configuration Ω. A silicon core subdomain and a SEI shell subdomain are identified in each frame, indicated with the subscript C and S, respectively. In this work, we consider a quarter section of an elliptical nanowire, resulting from symmetry assumptions along both half-axes as well as free expansion and vanishing stresses in the third direction. At the half-axes, we impose a non-displacement condition in tangential direction. A sketch of the considered domain with the underlying computational grid is depicted in Figure 1.

Finite Deformation

The deformation gradient $\mathbf{F} = \mathbf{Id} + \boldsymbol{\nabla}_0 \boldsymbol{u}$ with the identity tensor $\mathbf{Id}$ and the displacement vector $\boldsymbol{u}$ can be split up multiplicatively into three parts: $\mathbf{F}=\mathbf{F}_{ch}\mathbf{F}_{el}\mathbf{F}_{pl}$, the chemical, elastic, and plastic deformation, respectively, compare Sect. 10.4 in Ref. [39], Sect. 8.2.2 in Ref. [40] and Ref. [41].

In the silicon core domain, we consider only reversible deformations $\mathbf{F}=\mathbf{F}_{ch}\mathbf{F}_{el}=\mathbf{F}_{rev}$. The elastic part results from mechanical stresses and the chemical part from changes of the lithium concentration during lithiation and delithiation as $\mathbf{F}_{ch} = \lambda_{ch}\mathbf{Id} = \sqrt[3]{1 + v_{pmv} c_{max} \bar{c}}\,\mathbf{Id}$ with the partial molar volume v_{pmv} of lithium inside silicon, the normalized lithium concentration $\bar{c} = c/c_{max} \in [0, 1]$ of the lithium concentration $c \in [0, c_{max}]$ with respect to the maximal concentration c_{max} in the reference configuration. The chemical deformation causes a volume expansion during lithiation of approximately 300% and dominates the total deformation of the silicon core. In the SEI domain, no chemical deformation occurs: $\mathbf{F} = \mathbf{F}_{el}\mathbf{F}_{pl}$. We omit the index C or S for reasons of better readability if it is clear from the context which part is referred to.

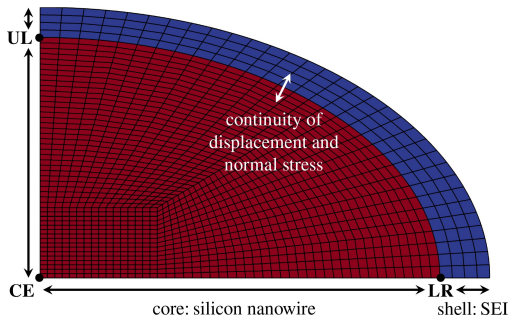

Figure 1. Sketch of the silicon nanowire core (red) covered by the SEI shell (blue) with the underlying time-constant computational grid and the points **LR** (lower right), **UL** (upper left) and **CE** (center) for further investigations. The white double arrow indicates the continuity of the displacement and the normal stress at the core-shell interface.

Free Energy

We consider all model equations in the reference configuration at constant temperature and state the Helmholtz free energy $\psi(\bar{c}, \boldsymbol{\nabla}_0 \boldsymbol{u}, \mathbf{F}_{pl}) = \psi_{ch}(\bar{c}) + \psi_{el}(\bar{c}, \boldsymbol{\nabla}_0 \boldsymbol{u}, \mathbf{F}_{pl})$ resulting in $\psi(\bar{c}, \boldsymbol{\nabla}_0 \boldsymbol{u}_C) = \psi_{ch}(\bar{c}) + \psi_{el}(\bar{c}, \boldsymbol{\nabla}_0 \boldsymbol{u}_C)$ and $\psi(\boldsymbol{\nabla}_0 \boldsymbol{u}_S, \mathbf{F}_{pl}) = \psi_{el}(\boldsymbol{\nabla}_0 \boldsymbol{u}_S, \mathbf{F}_{pl})$ for the respective silicon core and SEI shell domain. With the mass density ρ_0 of silicon in the reference configuration the chemical and elastic free energy densities can be defined as:

$$\rho_0 \psi_{ch}(\bar{c}) = -c_{max} \int_0^{\bar{c}} F\, U_{OCV}(z)\, \mathrm{d}z$$

with an experimental open-circuit voltage (OCV) curve U_{OCV}[24,26,31,33] and the Faraday constant F as well as:

$$\rho_0 \psi_{el}(\bar{c}, \boldsymbol{\nabla}_0 \boldsymbol{u}, \mathbf{F}_{pl}) = \frac{1}{2} \mathbf{E}_{el}(\bar{c}, \boldsymbol{\nabla}_0 \boldsymbol{u}, \mathbf{F}_{pl}) \,:\, \mathbb{C}[\mathbf{E}_{el}]$$

with $\mathbf{F}_{pl} = \mathbf{Id}$ for silicon, the elastic strain tensor $\mathbf{E}_{el}$, and the constant, isotropic stiffness fourth-order tensor $\mathbb{C}$ as $\mathbb{C}[\mathbf{E}_{el}] = \lambda \mathrm{tr}(\mathbf{E}_{el})\mathbf{Id} + 2G\mathbf{E}_{el}$. Here, $\lambda = 2G\nu/(1-2\nu)$ and $G = E/(2(1+\nu))$ are the first and second Lamé constants, respectively, depending further on Young's modulus E and Poisson's ratio ν. In Table S1 in the Supporting Information, we give the parameters for silicon and SEI. The (Lagrangian) logarithmic Hencky strain tensor $\mathbf{E}_{el}$ is given as:

$$\mathbf{E}_{el} = \ln(\mathbf{U}_{el}) = \ln\left(\sqrt{\mathbf{C}_{el}}\right) = \sum_{\alpha=1}^{3} \ln\left(\sqrt{\eta_{el,\alpha}}\right) \boldsymbol{r}_{el,\alpha} \otimes \boldsymbol{r}_{el,\alpha}$$

with the eigenvalues $\eta_{el,\alpha}$ and eigenvectors $\boldsymbol{r}_{el,\alpha}$ of $\mathbf{U}_{el}$. The tensor $\mathbf{U}_{el}$ is the unique, symmetric and positive definite right stretch part of the unique polar decomposition of $\mathbf{F}_{el} = \mathbf{R}_{el}\mathbf{U}_{el}$, see Sect. 2.6 in Ref. [42].

Chemistry

The lithium concentration changes during lithiation and delithiation inside the reference silicon core domain $\Omega_{0,C}$ can be stated via a generalized diffusivity equation:[24,43,44]

$$\partial_t c = -\boldsymbol{\nabla}_0 \cdot \boldsymbol{N}. \tag{1}$$

The lithium flux $\boldsymbol{N} = -D(\partial_c \mu)^{-1} \boldsymbol{\nabla}_0 \mu$ with the diffusion coefficient D for lithium in silicon is applied for an isotropic case. The chemical potential μ can be derived as the partial derivative of the free energy density with respect to the concentration c:[24,26,31,33,36]

$$\begin{aligned} \mu &= \partial_c(\rho_0 \psi) = \mu_{ch} + \mu_{el} \\ &= -F U_{OCV} - \frac{v_{pmv}}{3\lambda_{ch}^3} \mathrm{tr}(\mathbb{C}[\mathbf{E}_{el}]). \end{aligned} \tag{2}$$

Therefore, the total lithium flux $\boldsymbol{N} = \boldsymbol{N}_{ch} + \boldsymbol{N}_{el}$ can be divided into the lithium concentration-driven diffusive flux component $\boldsymbol{N}_{ch} = -D(\partial_c \mu)^{-1} \boldsymbol{\nabla}_0 \mu_{ch}$ and the stress-driven convective flux component $\boldsymbol{N}_{el} = -D(\partial_c \mu)^{-1} \boldsymbol{\nabla}_0 \mu_{el}$, respectively. A uniform and constant external flux N_{ext} in the Lagrangian domain with either positive or negative sign (for lithiation or delithiation, respectively) is applied at the surface of the silicon core. This boundary condition corresponds to cycling with a constant current and assumes a homogeneous current distribution. The value of the external flux depends on the specific surface, i.e., the surface-to-volume ratio as we have

discussed in Ref. [30] and App. A.3.2 in Ref. [45]. This external flux is measured with regard to the charging rate (C-rate) connecting the state of charge (SOC) to the simulation time via the external lithium flux and the initial concentration $\mathrm{SOC}(t) = \bar{c}_0 + N_{\mathrm{ext}} t$. Further information about the SOC, the C-rate, and N_{ext} can be found in Refs. [24, 30, 31] and the references cited therein.

Elastic and Inelastic Deformation

We solve the momentum balance equation[24,30,31,33] in the silicon core domain and the SEI shell domain:

$$\mathbf{0} = \boldsymbol{\nabla}_0 \cdot \mathbf{P}_{\mathrm{C}}(\bar{c}, \boldsymbol{\nabla}_0 \boldsymbol{u}_{\mathrm{C}}), \ \mathbf{0} = \boldsymbol{\nabla}_0 \cdot \mathbf{P}_{\mathrm{S}}(\boldsymbol{\nabla}_0 \boldsymbol{u}_{\mathrm{S}}, \mathbf{F}_{\mathrm{pl}}) \tag{3}$$

for the respective deformation. The first Piola–Kirchhoff tensor $\mathbf{P}$ is thermodynamically consistently derived as:

$$\mathbf{P} = 2\mathbf{F}\partial_{\mathbf{C}}(\rho_0 \psi) = \mathbf{F}\left(\mathbf{F}_{\mathrm{el}}^{\mathrm{T}}\mathbf{F}_{\mathrm{el}}\right)^{-1}\left(\mathbf{F}_{\mathrm{pl}}^{-1}\right)^{\mathrm{T}}\mathbf{F}_{\mathrm{pl}}^{-1}\mathbb{C}[\mathbf{E}_{\mathrm{el}}],$$

see Refs. [24, 26, 31, 33]. With the first Piola–Kirchhoff tensor $\mathbf{P}$ we state the related symmetric Cauchy stress $\boldsymbol{\sigma}$ in the current configuration as $\boldsymbol{\sigma} = \mathbf{P}\mathbf{F}^{\mathrm{T}}/\det(\mathbf{F})$, see Sect. 3.1 in Ref. [42].

In this work, we rely on the rate-dependent plastic approach.[29,31] Therefore, we introduce the scalar yield stress σ_{Y} and the evolution equation of the scalar accumulated equivalent inelastic strain $\varepsilon_{\mathrm{pl}}^{\mathrm{eq}} \geq 0$ as:

$$\dot{\varepsilon}_{\mathrm{pl}}^{\mathrm{eq}} = \begin{cases} 0, & \left\|\mathbf{M}^{\mathrm{dev}}\right\| \leq \sigma_{\mathrm{Y}} \\ \dot{\varepsilon}_0 \left(\frac{\left\|\mathbf{M}^{\mathrm{dev}}\right\| - \sigma_{\mathrm{Y}}}{\sigma_{\mathrm{Y}}*}\right)^{\beta}, & \left\|\mathbf{M}^{\mathrm{dev}}\right\| > \sigma_{\mathrm{Y}} \end{cases},$$

which replace the typical Karush–Kuhn-Tucker (KKT) conditions for the plastic approach, compare Sect. 1.7 in Ref. [46] and Refs. [29, 31, 41]. The deviatoric Mandel stress $\mathbf{M}^{\mathrm{dev}} = \mathbf{M} - 1/3\mathrm{tr}(\mathbf{M})\mathbf{Id}$ is computed via the Mandel stress $\mathbf{M} = \partial_{\mathbf{E}_{\mathrm{el}}}(\rho_0 \psi_{\mathrm{el}}) = \mathbb{C}_{\mathrm{S}}[\mathbf{E}_{\mathrm{el}}]$ in the SEI domain. The remaining values are the positive-valued stress-dimensioned constant $\sigma_{\mathrm{Y}}*$, the reference tensile stress $\dot{\varepsilon}_0$, and the measure of the strain rate sensitivity of the material β which are given in Table S1. Furthermore, we rescale the yield stress with the factor $\sqrt{2/3}$ due to consistency with the one dimensional tensile test, see Sect. 2.3.1 in Ref. [46]. Finally, we use a projector formulation to map the stresses onto the set of admissible stresses, stated for our viscoplastic approach in Ref. [31]. This procedure is also known as static condensation.[47,48] Therefore, $\mathbf{F}_{\mathrm{pl}}$ and $\varepsilon_{\mathrm{pl}}^{\mathrm{eq}}$ are applied as internal variables. This procedure has the advantage that the nonlinear system of partial differential equations does not need to be extended by the plastic part of the deformation gradient, in contrast to Refs. [26, 24].

Numerical Approach

Again, we follow Ref. [29] and state only the most important details. All in all, after non-dimensionalization and omitting the accentuation for the non-dimensionalization, we solve for given $\mathbf{F}_{\mathrm{pl}}$ and $\varepsilon_{\mathrm{pl}}^{\mathrm{eq}}$ the continuity equation in Eq. (1), the chemical potential equation in Eq. (2), and the momentum balance equations in Eq. (3). As a result, we obtain the concentration c, the chemical potential μ, and the silicon core displacement $\boldsymbol{u}_{\mathrm{C}}$ as well as the SEI shell displacement $\boldsymbol{u}_{\mathrm{S}}$. Therefore, we imply boundary conditions at the interface between the silicon core and the SEI shell domain: $\boldsymbol{u}_{\mathrm{C}} = \boldsymbol{u}_{\mathrm{S}}$ and $\mathbf{P}_{\mathrm{C}} \cdot \boldsymbol{n} = \mathbf{P}_{\mathrm{S}} \cdot \boldsymbol{n}$ with the normal vector $\boldsymbol{n} = \boldsymbol{n}_{\mathrm{C}}$. At the outer boundary of the SEI, we have no stresses meaning $\mathbf{P}_{\mathrm{S}} \cdot \boldsymbol{n}_{\mathrm{S}} = \mathbf{0}$. Furthermore, we impose initial conditions $c(0, \cdot) = c_0$, $\mathbf{F}_{\mathrm{pl}}(0, \cdot) = \mathbf{Id}$ and $\varepsilon_{\mathrm{pl}}^{\mathrm{eq}}(0, \cdot) = 0$. Note that we perform all calculations in the undeformed Lagrangian frame, which considers volume expansion via the deformation gradient tensor $\mathbf{F}$. We have shown the transformation to the deformed Eulerian frame, e.g., in Ref. [33].

For the numerical solution of the nonlinear system of partial differential equations, we choose an admissible mesh for the computational domain, use the isoparametric Lagrangian finite element method, see Chapt. III §2 in Ref. [49], derive a weak formulation and a spatial and temporal discretization.[29] For the spatial discretization, we apply a fourth order finite element approach using a uniform and time-constant mesh in the reference configuration, displayed in Figure 1. Note that the original set of equations is derived in 3D, however, all equations are also mathematically valid in 2D.[30,31] The temporal discretization is realized with a variable-step, variable-order time integration scheme using the numerical differential formulation (NDF) of linear multistep methods.[50–52] The temporal discretization of the internal variables are treated with an implicit exponential map. For a detailed procedure of the temporal integration for $\mathbf{F}_{\mathrm{pl}}$ and $\varepsilon_{\mathrm{pl}}^{\mathrm{eq}}$, we refer to Ref. [31]. In each time step, the nonlinear system is solved using the Newton–Raphson method and the adaptive scheme for the time presented as Algorithm 1 in Ref. [30].

We start with the constant initial concentration $\bar{c}_0 = 0.02$ and $\mu_0 = \partial_c \rho \psi_{\mathrm{ch}}(\bar{c}_0)$. The initial time step size is 10^{-8} h, the maximal time step size 10^{-3} h and temporal relative and absolute tolerances $2 \cdot 10^{-4}$ and $2 \cdot 10^{-7}$, respectively. The grid has around $87 \cdot 10^3$ degrees of freedom. Additional zero-displacement boundary conditions are applied on the major half-axis with $u_y = 0$ and on the minor half-axis with $u_x = 0$. The Newton update is computed with an LU-decomposition from the UMFPACK package [53, Version 5.7.8] and shared memory with OpenMP Version 4.5 is enabled for assembling the Newton method. Our implementation is based on the open-source finite element library *deal.II*.[54] All simulations are performed on a single node at the BwUniCluster2.0 with GCC 12.1.[55]

Results and Discussion

Due to the importance of mechanics and the silicon anode geometry, we investigate the chemo-mechanical coupling of an elliptical silicon nanowire covered by the SEI in a 2D setup. We discuss the stresses occurring inside the silicon anode and the SEI in comparison to a symmetric nanowire. Additionally, we examine the lithium concentration distribution and gradients during lithiation and delithiation influenced by mechanics. To assess the impact of the SEI, we compare the chemo-mechanical results for a silicon anode covered by a soft and a stiff SEI layer.

During cycling, the lithium concentration inside the silicon nanowire changes. An increase in the lithium concentration results in a chemical expansion of the anode, while a decrease leads to a shrinkage. Inhomogeneous lithium distribution inside the silicon implies inhomogeneous volume changes that have to be accommodated by mechanical deformations. These mechanical strains inside the lithiated silicon generate stresses. While the silicon can deform chemically and elastically, the SEI features elastic and viscoplastic material behavior. During

Batteries & Supercaps | Research Article
doi.org/10.1002/batt.202400604
Chemistry Europe
European Chemical Societies Publishing

cycling, the SEI layer has to adjust to the volume changes of the silicon anode. As the SEI can only deform mechanically, expansion and shrinkage of the silicon anode lead to significant mechanical strains, creating stresses inside the SEI as well. The stresses inside silicon and SEI are coupled due to the interface condition of equal stress in normal direction.

Silicon Nanowire with Soft SEI

First, we investigate the behavior of an elliptical silicon nanowire covered by a soft SEI layer. The ratio of the minor to the major half-axis is 0.6:1. The SEI thickness is one eighth of the silicon core length. We simulate three half cycles (1st lithiation, 1st delithiation, and 2nd lithiation) with a rate of 1*C*. The simulation parameters are stated in Table S1. We begin our discussion with the mechanics inside the silicon anode and the SEI layer and continue with the examination of the lithium concentration distribution. Especially, we consider the quantities of interest at the lower right of the major half-axis (point **LR**), at the upper left of the minor half-axis (point **UL**), and at the center of the silicon (point **CE**), respectively. The interfacial points (**LR** and **UL**) and the central point (**CE**) are illustrated in Figure 1.

Mechanical Behavior

Concerning the mechanics inside the silicon anode, lithiation from the outside leads to concentration gradients and inhomogeneous volume changes. The volume mismatch generates compressive stress at the outer boundary of the nanowire and tensile stress at the center. During delithiation, lithium flux out of the anode leads to tensile stress at the outer boundary and compressive stress at the center. To investigate the mechanics in detail, we illustrate the simulated stresses for the elliptical silicon nanowire covered by a soft SEI layer in Figure 2. We depict the stress distribution during lithiation at 30% SOC for the normal component σ_n in Figure 2(a) and the tangential component σ_t in Figure 2(b). Both stress distributions reveal the general trend of tensile stress at the center and compressive stress at the outer boundary of the silicon nanowire. The largest compressive stresses appear in normal direction at the end of the major half-axis at point **LR** and in tangential direction at the end of the minor half-axis at point **UL**. The largest tensile stresses appear in normal direction along the major half-axis and in tangential direction along the minor half-axis, each close to the center. Therefore, possible plasticity[31] and fracture might occur along the minor half-axis.

We depict the time evolution of the stress inside silicon during three half cycles for the normal component in Figure 2(c) and for the tangential component in Figure 2(d). The evolution of the stress components during the first lithiation reveals permanent compressive stress at points **UL** and **LR**, with significantly larger stress magnitudes for the tangential component. The normal stress in Figure 2(c) always shows the largest magnitude at the major half-axis at point **LR**, and the tangential stress in Figure 2(d) shows the largest magnitude at the minor half-axis at point **UL**. During the subsequent delithiation, tensile stresses arise at the outer boundary, showing the largest magnitudes at the same points as before. The normal stress during the second lithiation in Figure 2(c) deviates from the first lithiation in the beginning due to a different initial state, but the stresses continuously approach the ones during the first

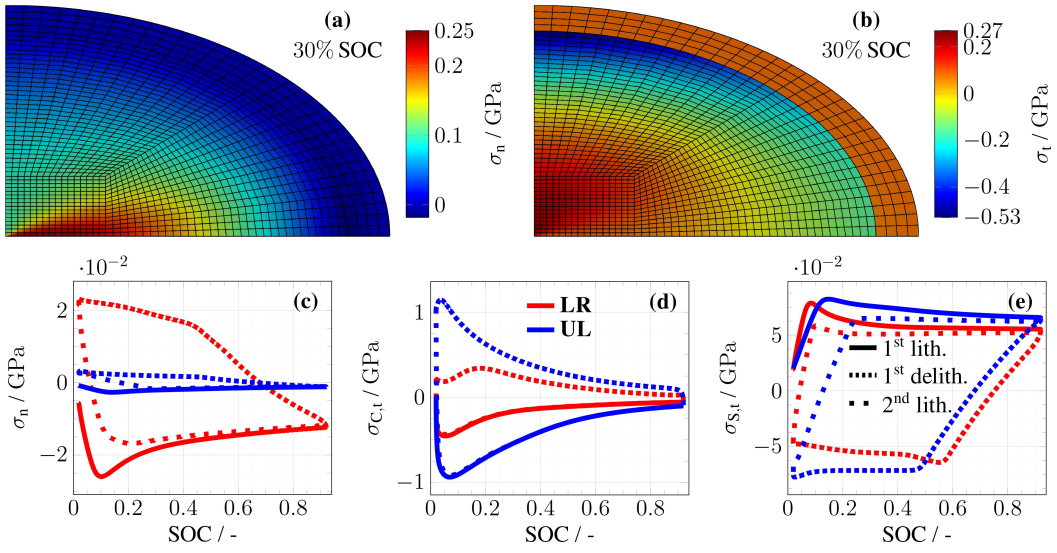

Figure 2. Cauchy stresses for the elliptical silicon nanowire with a soft SEI in the undeformed Lagrangian frame. Distribution of (a) normal and (b) tangential Cauchy stress inside the silicon core and the SEI shell during lithiation at 30% SOC. Evolution of Cauchy stress at the points **LR** and **UL** during three half cycles for (c) normal, (d) tangential core, and (e) tangential shell stress.

Batteries & Supercaps

Research Article
doi.org/10.1002/batt.202400604

Chemistry Europe
European Chemical Societies Publishing

lithiation. The tangential stress during the second lithiation in Figure 2(d) coincides with the first lithiation. The largest stress magnitudes during cycling occur at low SOC in particular in tangential direction at the end of the minor half-axis at point **UL**. This supports our previous finding that the elliptical silicon nanowire might be prone to plasticity[31] and fracture in this regime.

To highlight the influence of the elliptical geometry, we compare our simulation results to the case of a symmetric silicon nanowire with the same capacity in Figure S1. Due to the symmetry, the stresses at points **UL** and **LR** are equal. The stress magnitudes of the normal and tangential stress components at the outer boundary in the symmetric case are always in between the stress values at point **UL** and **LR** for the elliptical case. Therefore, the largest stresses reached during cycling in the symmetric case stay smaller than the ones for the elliptical case. Consequently, the symmetric silicon nanowires are mechanically more stable than elliptical silicon nanowires with the same capacity.

Next, we discuss the mechanics of the SEI shell during cycling. The Cauchy stress in normal direction in silicon and SEI is coupled at the interface. At the outer boundary of the SEI, the stress in normal direction vanishes. Therefore, we focus on the description of the tangential component of the SEI stress depicted in Figure 2(e). During lithiation, the volume expansion of the nanowire leads to tensile tangential stress inside the SEI. The tangential stress magnitude at the minor half-axis at point **UL** is slightly larger compared to point **LR**. This can be expected as the curvature of the SEI is smallest at the end of the minor half-axis. Thus, the SEI might be prone to fracture at point **UL**. During delithiation, the tangential stress inside the SEI is compressive and the maximum value is reached again at point **UL**. During the second lithiation, the size of the stress overshoot reduces and the stress converges to that one of the first lithiation. Compared to the symmetric nanowire, we observe the same trend for the stresses inside the SEI shell as for the silicon core. The stress magnitudes are in between the stresses at points **UL** and **LR**. Consequently, the maximum value is smaller for the symmetric case, meaning a superior mechanical stability of the SEI. To investigate the influence of viscosity, we vary the parameter for the plastic strain rate $\dot{\varepsilon}_0$ in Figure S3. A smaller value retards plastic flow, leading to a larger stress overshoot and larger stress magnitudes in general. Nevertheless, the shape of the stress profiles does not change significantly upon variation of $\dot{\varepsilon}_0$.

Lithiation Behavior

After the mechanical description, we investigate the lithium concentration inside the elliptical silicon nanowire. During lithiation, the lithium flux points from the outside into the interior of the silicon anode. Thus, we expect that the concentration at the outer boundary of the anode exceeds the concentration at the center, as shown for the symmetrical nanowire covered by SEI in Figure S2. During delithiation, we expect a decreased lithium concentration at the outer boundary compared to the center. We show our simulation results for the lithium concentration in Figure 3. The lithium distribution inside the elliptical silicon nanowire during lithiation is illustrated in Figure 3(a) to (c) for 5%, 30%, and 90% SOC. As expected, the lithium concentration increases in general from the outside. The lithium distribution reveals the highest concentration at the end of the major half-axis at point **LR**. At this point, the elliptical geometry has the highest local surface-to-volume ratio. The local surface determines the lithium intake into the anode and the local volume determines the lithium distribution below this surface. Thus, a high local surface-to-volume ratio results in a

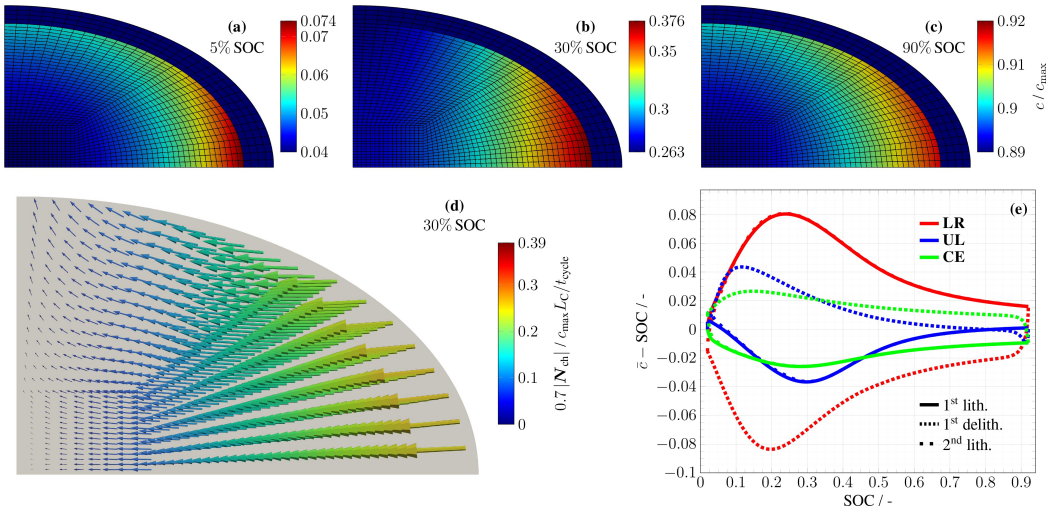

Figure 3. Lithium concentration for the elliptical silicon nanowire with a soft SEI in the undeformed Lagrangian frame. Distribution of the lithium concentration inside silicon during lithiation at (a) 5%, (b) 30%, and (c) 90% SOC. (d) Concentration-driven diffusive lithium flux $\boldsymbol{N}_{\mathrm{ch}}$ scaled with 0.7. (e) Deviation of the lithium concentration from the mean at the points **LR**, **UL**, and **CE** during three half cycles.

Batteries & Supercaps

Research Article
doi.org/10.1002/batt.202400604

Chemistry Europe
European Chemical Societies Publishing

faster lithium concentration increase, compare Sect. 2.2.3 in Ref. [56]. Contrary to our expectation, the lithium concentration at the end of the minor half-axis at point **UL** is lower than the concentration at the center point **CE** during lithiation at 30% SOC. For a better illustration of this concentration anomaly, we depict the concentration-driven diffusive lithium flux $\boldsymbol{N}_{ch}$ during lithiation at 30% SOC in Figure 3(d), indicating negatively scaled concentration gradients. Along the major half-axis, lithium diffusion points towards the center of the ellipse, as expected. However, along the minor half-axis, diffusion points towards the outer boundary of the nanowire, revealing the concentration depletion at point **UL**. While the arrows indicating the direction of lithium diffusion partially point towards the outer boundary, the more pronounced stress-driven convective lithium flux $\boldsymbol{N}_{el}$ depicted in Figure S4(a) points towards the interior. This ensures that the total flux $\boldsymbol{N}$ always points towards the interior of the silicon core during lithiation.

To confirm the appearance of the concentration anomaly, we examine the deviation of the lithium concentration from the mean during cycling in Figure 3(e). As expected during lithiation, the concentration at point **LR** is always larger, and at point **CE** smaller than the mean concentration. During delithiation, this concentration distribution is inverse. However, the concentration at point **UL** is smaller than the mean concentration and even smaller than the concentration in the center **CE** during lithiation in a wider SOC regime between 15% and 45% SOC. The concentration anomaly at point **UL** also appears during delithiation as concentration excess between 35% and 5% SOC and the second lithiation again as depletion. Thus, the concentration anomaly at point **UL** is no simulation artifact in a narrow SOC range during the first lithiation but significant and robust during cycling.

The concentration anomaly also appears during slow cycling with C/20 and inside an elliptical silicon nanowire without SEI as shown in Figure S6. Thus, we exclude kinetic limitations or the mechanical impact of the SEI on the silicon core as reasons for the concentration anomaly. Instead, we attribute this effect to a mechanical origin inside the elliptical silicon nanowire. During lithiation, the lithium concentration increases the fastest at point **LR** at the end of the major half-axis due to the highest surface-to-volume ratio. The significant increase causes pronounced volume expansion, leading to compressive stress along the outer boundary of the nanowire. This compressive stress is largest at point **UL** at the end of the minor half-axis due to the smaller curvature at this point. The substantial compressive stress affects the chemo-mechanical potential and hinders further lithium concentration increase at point **UL**. During delithiation, the fastest decrease in concentration appears at point **LR**, generating tensile stress, especially at point **UL**. The substantial tensile stress impedes lithium concentration decrease at point **UL**, generating a local concentration excess. Investigating a purely chemical 2D elliptical silicon nanowire without mechanical coupling, such a concentration anomaly does not occur. Thus, the concentration anomaly during cycling results from the chemo-mechanical interplay inside the silicon nanowire significantly influenced by the elliptical geometry.

Silicon Nanowire with Stiff SEI

After discussing the soft SEI, we want to investigate the influence of a stiff SEI layer on the mechanics and the lithiation behavior of an elliptical silicon nanowire as discussed for a spherical nanoparticle in Ref. [26]. Therefore, we increase the value of Young's modulus and the yield stress of the SEI shell by a factor of 100 compared to the soft SEI, i.e. $E = 90$ GPa and $\sigma_Y = \sigma_Y^* = 4.95$ GPa.

Mechanical Behavior

The increase in the mechanical parameters immediately evokes elevated stresses inside the SEI. We depict the stress distribution in Figure 4(a) for the normal component and in Figure 4(b) for the tangential component at 30% SOC during lithiation. Analog to the soft SEI scenario, the largest compressive stress in the SEI in normal direction occurs at the major half-axis at point **LR** and the largest tensile stress in tangential direction appears at the minor half-axis at point **UL** due to the local curvature effects. Therefore, possible cracking of the SEI might occur again at point **UL** due to the largest tangential stresses.

The time evolution during cycling of the normal stress in Figure 4(c) and the tangential stress in Figure 4(e) confirms this observation. During delithiation, we observe the largest tensile stress in normal direction inside the SEI at the major half-axis at point **LR** and the largest compressive stress in tangential direction at the minor half-axis at point **UL** accordingly. The stresses during the second lithiation approach the stresses during the first lithiation but deviate due to the viscoplastic behavior. The comparison to the soft SEI case reveals a stress increase inside the SEI for both components by approximately a factor of 100, representing the increase in the mechanical parameters.

The stress inside the silicon nanowire is affected by the stiff SEI layer due to the mechanical coupling of the silicon core and the SEI shell. We depict the normal stress component inside silicon and SEI during lithiation at 30% SOC in Figure 4(a). The illustration reveals that the normal stresses at the interface are equal as imposed by the boundary condition. The stress distribution shows significantly larger compressive stresses within the whole silicon nanowire except a small region along the minor half-axis close to the center, where tensile stresses appear. Compared to the soft SEI, the most significant normal compressive stress occurs again at the end of the major half-axis at point **LR** due to the largest curvature and pronounced impact of the SEI. The tangential stress component inside silicon depicted in Figure 4(b) is indirectly affected by the different SEI mechanics. The stress distribution reveals compressive stresses within the whole silicon nanowire with the largest stress magnitude at the end of the major half-axis at point **LR**. This is in contrast to the case with the soft SEI, where the largest compressive stress occurs at the end of the minor half-axis at point **UL** and where tensile stresses occur in a larger region around the center.

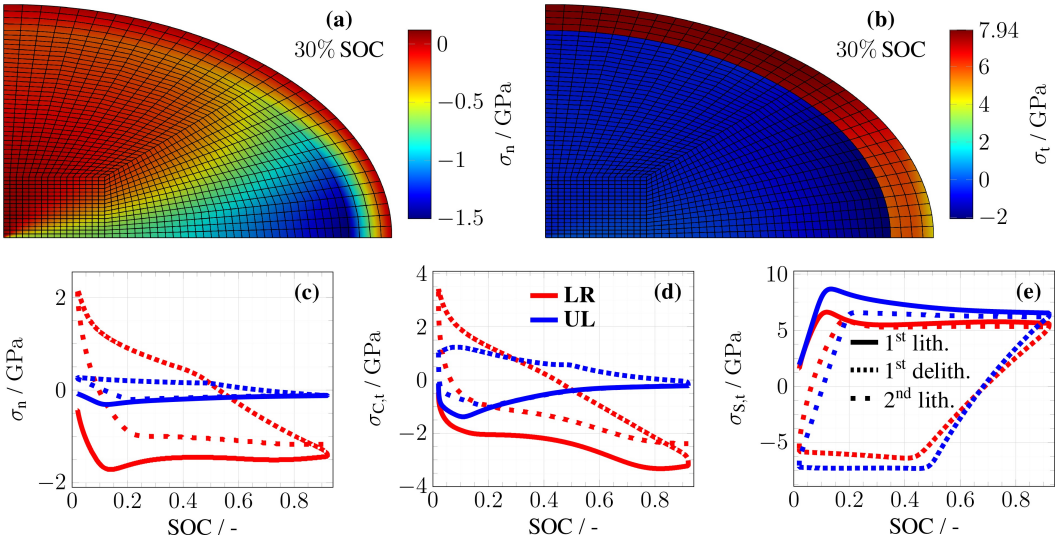

Figure 4. Cauchy stresses for the elliptical silicon nanowire with a stiff SEI in the undeformed Lagrangian frame. Distribution of (a) normal and (b) tangential Cauchy stress inside the silicon core and the SEI shell during lithiation at 30% SOC. Evolution of Cauchy stress at the points **LR** and **UL** during three half cycles for (c) normal, (d) tangential core, and (e) tangential shell stress.

We depict the stress evolution within the silicon core during cycling in the normal direction in Figure 4(c) and in the tangential direction in Figure 4(d). As discussed for the SEI mechanics, the normal stress inside silicon at the boundary is approximately 100 times larger compared to the soft SEI scenario with a similar shape of the stress profile. The tangential stress inside silicon is compressive during lithiation and changes to tensile stress during delithiation analog to the soft SEI case. However, the largest tangential stress magnitudes appear at point **LR** in contrast to the scenario with the soft SEI, where the largest tangential stress magnitude appears at point **UL**. Thus, the maximum stress magnitudes inside silicon occur at the same point **LR** for the normal and tangential component due to the impact of the stiff SEI shell, which is most significant at this point due to the largest curvature. This effect emphasizes the importance of the mechanical interplay between the silicon core and the SEI shell. Due to the larger stress magnitudes inside the core, the silicon nanowire might be more prone to plasticity and cracking for the stiff SEI shell in comparison to the soft SEI scenario.

Lithiation Behavior

Next, we discuss the influence of the stiff SEI mechanics on the lithiation behavior of the silicon nanowire core. We depict the lithium concentration distribution during lithiation in Figure 5 at (a) 5%, (b) 30%, and (c) 90% SOC. The illustration reveals that upon the start of the lithiation, lithium concentration increases at the outer boundary of the silicon core, proceeding gradually towards the center as expected. Nevertheless, this trend is broken during further lithiation, and a concentration anomaly occurs at the end of the major half-axis at point **LR**. The concentration-driven diffusive lithium flux $\boldsymbol{N}_{ch}$ during lithiation at 30% SOC depicted as arrows in Figure 5(d) indicates the negatively scaled concentration gradient and confirms the concentration depletion at point **LR**. This is in contrast to the concentration anomaly found for the soft SEI case at the end of the minor half-axis at point **UL**, where no anomaly occurs for the stiff SEI case. Instead, the anomaly appears at the point with the largest curvature and the most significant stress magnitude generated by the stiff SEI. Again, the stress-driven convective lithium flux $\boldsymbol{N}_{el}$ depicted in Figure S4(b) guarantees that the total lithium flux $\boldsymbol{N}$ always points towards the interior of the silicon core during lithiation. This confirms the importance of the chemo-mechanical interplay and the severe influence of the stiff SEI shell on the lithiation behavior of the silicon nanowire core. The stiff SEI shell acts similarly to a rigid obstacle hindering local volume expansion and, consequently, lithiation as discussed in Ref. [33].

We depict the evolution of the lithium concentration in Figure 5(e) to estimate the robustness of the mechanical impact during cycling. During the first lithiation, the decrease in concentration at point **LR** exists in the whole SOC range. During the subsequent delithiation, this decrease in concentration reduces continuously, and an increase in concentration, meaning an anomaly, appears for SOC values smaller than 20%. During the second lithiation, a concentration anomaly appears for SOC values larger than 30%. The second lithiation deviates significantly from the first lithiation due to the viscoplastic behavior of the SEI shell. Nevertheless, the concentration anomaly caused by the mechanical impact of the stiff SEI shell is a robust effect appearing during every cycle.

Batteries & Supercaps

Research Article
doi.org/10.1002/batt.202400604

Chemistry Europe
European Chemical Societies Publishing

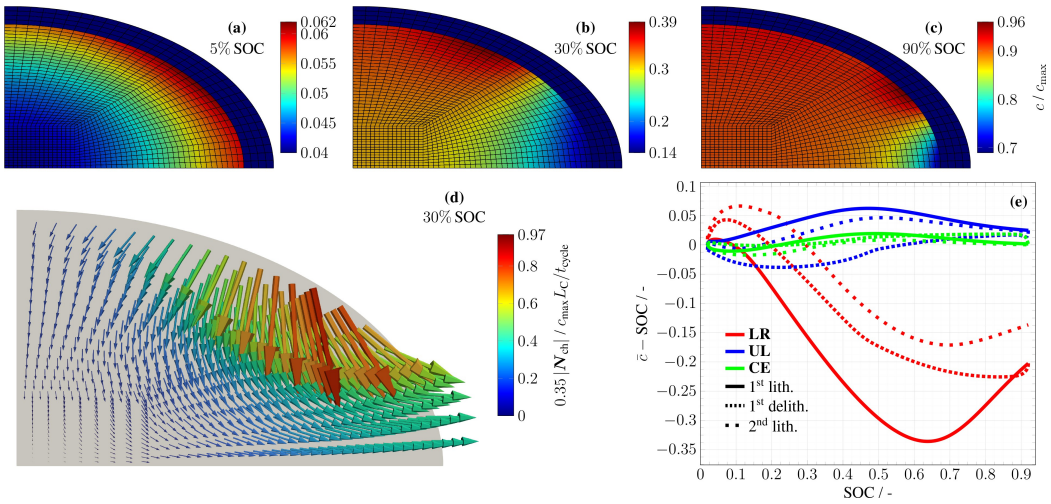

Figure 5. Lithium concentration for the elliptical silicon nanowire with a stiff SEI in the undeformed Lagrangian frame. Distribution of the lithium concentration inside silicon during lithiation at (a) 5%, (b) 30%, and (c) 90% SOC. (d) Concentration-driven diffusive lithium flux $\boldsymbol{N}_{\mathrm{ch}}$ scaled with 0.35. (e) Deviation of the lithium concentration from the mean at the points **LR**, **UL**, and **CE** during three half cycles.

The stiff SEI mechanics influences the chemo-mechanical potential inside silicon. Due to the viscoplastic behavior, the stiff SEI shell generates a stress hysteresis during cycling, causing a voltage hysteresis as depicted in Figure S7. Thus, the hysteresis effect discussed in Refs. [26,27] for a spherical silicon particle covered by a stiff SEI shell also occurs for elliptical nanowires. This demonstrates the importance of mechanical considerations for silicon cores and SEI shells in simulations dealing with silicon anodes as battery active material.

Regarding the battery performance, the larger stress magnitudes inside the silicon core for the stiff SEI case compared to the soft case may lead to plasticity and fracture of the silicon nanowire. The reduced mechanical stability of the silicon anode can negatively influence the battery lifetime. Moreover, the voltage hysteresis caused by the stiff SEI layer significantly reduces the battery efficiency. Therefore, the soft SEI might be more beneficial from a battery performance perspective. Concerning SEI cracking and accelerated SEI growth, the soft SEI might adapt better to the silicon deformations without cracking. However, the behavior is determined by the yield stress and cracking strength rather than only Young's modulus.

Summary and Conclusions

In this study, we have systematically investigated the mechanical behavior and lithiation characteristics of an elliptical silicon nanowire core covered by a viscoplastic SEI shell with a 2D chemo-mechanical simulation. We have compared the influence of a soft and stiff SEI shell on the system and discussed the effect of the elliptical geometry. We base our model and numerical simulation on a higher order finite element method with a variable-step, variable-order time integration scheme extended straightforwardly from the 1D radial symmetric case.[29]

Concerning the mechanics, the silicon and soft SEI system shows the largest stress magnitudes in tangential direction at the end of the minor half-axis at point **UL**, where the curvature is minor. The normal component of the stress shows the largest magnitude at the end of the major half-axis at point **LR**, however, with significantly smaller values compared to the tangential stresses. For the stiff SEI case, the system reaches the largest stress magnitudes at the end of the major half-axis at point **LR**, where the curvature is major and the mechanical impact of the SEI is dominant. Thus, the stress magnitudes are significantly higher compared to the soft SEI case. Only the tangential stress component inside the SEI is larger at the point with the smallest curvature **UL**, where the SEI is prone to cracking. Symmetric silicon nanowires with the same capacity and corresponding SEI shell are mechanically more stable than elliptical nanowires.

The mechanics of the elliptical geometry significantly influences the lithiation behavior of the silicon nanowire. Generally, the lithium concentration is increased at the outer boundary during lithiation and decreased during delithiation, with the fastest concentration changes at the end of the major half-axis at point **LR** due to the largest surface-to-volume ratio at this point. For the soft SEI case, the concentration distribution reveals a deviation from this trend at the end of the minor half-axis at point **UL**. This concentration anomaly also appears during slow cycling and without SEI. Therefore, the mechanics of the elliptical silicon nanowire causes this effect. For the stiff SEI case, in contrast, a concentration anomaly occurs at the end of the major half-axis at point **LR**. The SEI influences the lithiation behavior more dominantly at this point due to the

Batteries & Supercaps

Research Article
doi.org/10.1002/batt.202400604

Chemistry Europe
European Chemical Societies Publishing

pronounced curvature. In total, the soft SEI has only a minor effect on the silicon nanowire, while the stiff SEI significantly impacts the lithiation behavior.

As shown in Refs. [57–59], inhomogeneous lithiation on particle scale is also responsible for considerable overpotential fluctuations on electrode scale. Our results demonstrate that inclusion of mechanical effects not only predicts mechanical degradation but also influences electrochemically induced degradation due to the mechanically induced overpotential fluctuations.

To conclude, we have demonstrated the importance of the chemo-mechanical coupling, the geometry, and the SEI on the silicon anode behavior during cycling. Based on our work, further simulations could include plasticity of the silicon nanowire, fracture modes inside silicon and SEI, or SEI growth. From a numerical perspective, an adaptive spatial grid algorithm could optimize the simulation.

Author Contributions

R. Schoof: Conceptualization, Methodology, Software, Validation, Formal analysis, Investigation, Data Curation, Writing – Original Draft, Visualization. **L. Köbbing**: Conceptualization, Methodology, Validation, Formal analysis, Investigation, Writing – Original Draft, Visualization. **A. Latz**: Resources, Writing – Review & Editing, Project administration, Funding acquisition. **B. Horstmann**: Resources, Writing – Review & Editing, Supervision. **W. Dörfler**: Resources, Writing – Review & Editing, Supervision, Project administration, Funding acquisition.

Acknowledgements

The authors thank L. von Kolzenberg for fruitful discussions about modeling silicon particles and G. F. Castelli for the software basis as well as A. Dyck, J. Niermann and T. Böhlke for their contribution on efficient (visco-) plastic modeling. R. S. and L. K. acknowledge financial support by the German Research Foundation (DFG) through the Research Training Group 2218 SiMET – Simulation of Mechano-Electro-Thermal processes in Lithium-ion Batteries, project number 281041241. L. K. and B. H. acknowledge financial support by the European Union's Horizon Europe within the research initiative Battery 2030+ via the OPINCHARGE project under the grant agreement number 101104032. The authors acknowledge support by the state of Baden-Württemberg through bwHPC. Open Access funding enabled and organized by Projekt DEAL.

Conflict of Interests

The authors declare that they have no known competing financial interests or personal relationships that could have appeared to influence the work in this paper.

Data Availability Statement

The data that support the findings of this study are available from the corresponding author upon reasonable request.

Keywords: silicon-SEI mechanics · stress distribution · lithiation characteristics · chemo-mechanical simulation · 2D elliptical nanowire

[1] M. N. Obrovac, V. L. Chevrier, *Chem. Rev.* **2014**, *114*, 11444, 10.1021/cr500207g.
[2] L. Sun, Y. Liu, R. Shao, J. Wu, R. Jiang, Z. Jin, *Energy Storage Mater.* **2022**, *46*, 482, 10.1016/j.ensm.2022.01.042.
[3] X. Zuo, J. Zhu, P. Müller-Buschbaum, Y.-J. Cheng, *Nano Energy* **2017**, *31*, 113, 10.1016/j.nanoen.2016.11.013.
[4] K. Feng, M. Li, W. Liu, A. G. Kashkooli, X. Xiao, M. Cai, Z. Chen, *Small* **2018**, *14*, 10.1002/smll.201702737.
[5] Y. Li, Q. Li, J. Chai, Y. Wang, J. Du, Z. Chen, Y. Rui, L. Jiang, B. Tang, *ACS Materials Lett.* **2023**, *5*, 2948, 10.1021/acsmaterialslett.3c00253.
[6] L. Y. Beaulieu, K. W. Eberman, R. L. Turner, L. J. Krause, J. R. Dahn, *Electrochem. Solid-State Lett.* **2001**, *4*, A137, 10.1149/1.1388178.
[7] N. Kim, Y. Kim, J. Sung, J. Cho, *Nat. Energy* **2023**, *8*, 921, 10.1038/s41560-023-01333-5.
[8] X. H. Liu, L. Zhong, S. Huang, S. X. Mao, T. Zhu, J. Y. Huang, *ACS Nano* **2012**, *6*, 1522, 10.1021/nn204476h.
[9] M. Wetjen, S. Solchenbach, D. Pritzl, J. Hou, V. Tileli, H. A. Gasteiger, *J. Electrochem. Soc.* **2018**, *165*, A1503, 10.1149/2.1261807jes.
[10] X. Su, Q. Wu, J. Li, X. Xiao, A. Lott, W. Lu, B. W. Sheldon, J. Wu, *Adv. Energy Mater.* **2014**, *4*, 1, 10.1002/aenm.201300882.
[11] Y. Yang, W. Yuan, W. Kang, Y. Ye, Y. Yuan, Z. Qiu, C. Wang, X. Zhang, Y. Ke, Y. Tang, *Nanoscale* **2020**, *12*, 7461, 10.1039/C9NR10652A.
[12] L. Xu, *J. Phys. Conf. Ser.* **2023**, *2608*, 012001, 10.1088/1742-6596/2608/1/012001.
[13] C. K. Chan, H. Peng, G. Liu, K. McIlwrath, X. F. Zhang, R. A. Huggins, Y. Cui, *Nat. Nanotechnol.* **2008**, *3*, 31, 10.1038/nnano.2007.411.
[14] Y. Yang, W. Yuan, W. Kang, Y. Ye, Q. Pan, X. Zhang, Y. Ke, C. Wang, Z. Qiu, Y. Tang, *Sustain. Energy Fuels* **2020**, *4*, 1577, 10.1039/C9SE01165J.
[15] F. Kilchert, M. Schammer, A. Latz, B. Horstmann, *Energy Technol.* **2024**, *12*, 2400206, 10.1002/ente.202400206.
[16] B. Horstmann, F. Single, A. Latz, *Curr. Opin. Electrochem.* **2019**, *13*, 61, 10.1016/j.coelec.2018.10.013.
[17] X. Zhang, S. Weng, G. Yang, Y. Li, H. Li, D. Su, L. Gu, Z. Wang, X. Wang, L. Chen, *Cell Rep. Phys. Sci.* **2021**, *2*, 100668, 10.1016/j.xcrp.2021.100668.
[18] H. Adenusi, G. A. Chass, S. Passerini, K. V. Tian, G. Chen, *Adv. Energy Mater.* **2023**, *13*, 10.1002/aenm.202203307.
[19] A. Wang, S. Kadam, H. Li, S. Shi, Y. Qi, *npj Comput. Mater.* **2018**, *4*, 10.1038/s41524-018-0064-0.
[20] L. von Kolzenberg, A. Latz, B. Horstmann, *ChemSusChem* **2020**, *13*, 3901, 10.1002/cssc.202000867.
[21] L. Köbbing, A. Latz, B. Horstmann, *J. Power Sources* **2023**, *561*, 232651, 10.1016/j.jpowsour.2023.232651.
[22] Y.-X. Yao, J. Wan, N.-Y. Liang, C. Yan, R. Wen, Q. Zhang, *J. Am. Chem. Soc.* **2023**, *145*, 8001, 10.1021/jacs.2c13878.
[23] Y. Zhang, N. Du, D. Yang, *Nanoscale* **2019**, *11*, 19086, 10.1039/C9NR05748J.
[24] L. von Kolzenberg, A. Latz, B. Horstmann, *Batteries & Supercaps* **2022**, *5*, 1, 10.1002/batt.202100216.
[25] K. Guo, R. Kumar, X. Xiao, B. W. Sheldon, H. Gao, *Nano Energy* **2020**, *68*, 104257, 10.1016/j.nanoen.2019.104257.
[26] L. Köbbing, A. Latz, B. Horstmann, *Adv. Funct. Mater.* **2024**, *34*, 2308818, 10.1002/adfm.202308818.
[27] L. Köbbing, Y. Kuhn, B. Horstmann, *ACS Appl. Mater. Interfaces* **2024**, *16*, 67609, 10.1021/acsami.4c12976.
[28] D. Wycisk, G. K. Mertin, M. Oldenburger, O. von Kessel, A. Latz, *J. Energy Storage* **2024**, *89*, 111617, 10.1016/j.est.2024.111617.
[29] R. Schoof, G. F. Castelli, W. Dörfler, *Examples Counterexamples* **2024**, *6*, 100157, 10.1016/j.exco.2024.100157.
[30] G. F. Castelli, L. von Kolzenberg, B. Horstmann, A. Latz, W. Dörfler, *Energy Technol.* **2021**, *9*, 2000835, 10.1002/ente.202000835.
[31] R. Schoof, J. Niermann, A. Dyck, T. Böhlke, W. Dörfler, *Comput. Mech.* **2024**, 10.1007/s00466-024-02499-9.

Batteries & Supercaps

Research Article
doi.org/10.1002/batt.202400604

Chemistry Europe
European Chemical Societies Publishing

[32] R. Schoof, G. F. Castelli, W. Dörfler, Parallelization of a Finite Element Solver for Chemo-Mechanical Coupled Anode and Cathode Particles in Lithium-Ion Batteries, in T. Kvamsdal, K. M. Mathisen, K.-A. Lie, M. G. Larson (Editors), *8th European Congress on Computational Methods in Applied Sciences and Engineering (ECCOMAS Congress 2022)*, CIMNE, Barcelona **2022** 10.23967/eccomas.2022.106.
[33] R. Schoof, G. F. Castelli, W. Dörfler, *Comput. Math. Appl.* **2023**, *149*, 135, 10.1016/j.camwa.2023.08.027.
[34] M. Tanaka, J. B. Hooper, D. Bedrov, *ACS Appl. Energ. Mater.* **2018**, *1*, 1858, 10.1021/acsaem.8b00344.
[35] J. Ding, X. Li, L. Gong, P. Tan, *Advanced Powder Materials* **2024**, *3*, 100200, 10.1016/j.apmate.2024.100200.
[36] R. Schoof, L. Flür, F. Tuschner, W. Dörfler, *Springer Proc. Math. Stat.* **2024**, accepted: 15. 03. 2024.
[37] M. Schammer, B. Horstmann, A. Latz, *J. Electrochem. Soc.* **2021**, *168*, 026511, 10.1149/1945-7111/abdddf.
[38] T. Zhang, M. Kamlah, *J. Electrochem. Soc.* **2018**, *165*, A1997, 10.1149/2.0141810jes.
[39] A. Bertram, *Elasticity and Plasticity of Large Deformations: Including Gradient Materials*, Springer Nature Switzerland AG, Cham, 4 edition **2021**, 10.1007/978-3-030-72328-6.
[40] J. Lubliner, *Plasticity theory*, Pearson Education, Inc., New York **2006**, 10.1115/1.2899459.
[41] C. V. Di Leo, E. Rejovitzky, L. Anand, *Int. J. Solids Struct.* **2015**, *67–68*, 283, 10.1016/j.ijsolstr.2015.04.028.
[42] G. A. Holzapfel, *Nonlinear Solid Mechanics*, John Wiley & Sons, Ltd., Chichester **2010**.
[43] L. Anand, *J. Mech. Phys. Solids* **2012**, *60*, 1983, 10.1016/j.jmps.2012.08.001.
[44] C. V. Di Leo, *Chemo-mechanics of lithium-ion battery electrodes*, Ph.D. thesis, Massachusetts Institute of Technology (MIT) **2015**, https://hdl.handle.net/1721.1/100119.
[45] R. Schoof, *Modellierung und Simulation chemisch-mechanisch gekoppelter Prozesse in Batterie-Aktivmaterialpartikeln*, Dissertation, Karlsruhe Institut für Technologie (KIT) **2024**, https://publikationen.bibliothek.kit.edu/1000176102.
[46] J. C. Simo, T. J. R. Hughes, *Computational inelasticity*, Interdisciplinary applied mathematics, Springer, New York **1998**.
[47] E. L. Wilson, *Int. J. Numer. Methods Eng.* **1974**, *8*, 198, 10.1002/nme.1620080115.
[48] D. A. Di Pietro, A. Ern, *Comput. Methods Appl. Mech. Engrg.* **2015**, *283*, 1, 10.1016/j.cma.2014.09.009.
[49] D. Braess, *Finite Elements*, Cambridge University Press, Cambridge, third edition **2007**, 10.1007/978-3-540-72450-6.
[50] M. W. Reichelt, L. F. Shampine, J. Kierzenka, MATLAB ode15s **1997**, copyright 1984–2020 The MathWorks, Inc.
[51] L. F. Shampine, M. W. Reichelt, *SIAM J. Sci. Comput.* **1997**, *18*, 1, 10.1137/S1064827594276424.
[52] L. F. Shampine, M. W. Reichelt, J. A. Kierzenka, *SIAM Rev.* **1999**, *41*, 538, 10.1137/S003614459933425X.
[53] T. A. Davis, *ACM Trans. Math. Software* **2004**, *30*, 196, 10.1145/992200.992206.
[54] D. Arndt, W. Bangerth, M. Bergbauer, M. Feder, M. Fehling, J. Heinz, T. Heister, L. Heltai, M. Kronbichler, M. Maier, P. Munch, J.-P. Pelteret, B. Turcksin, D. Wells, S. Zampini, *J. Numer. Math.* **2023**, *31*, 231, 10.1515/jnma-2023-0089.
[55] WIKI bw HPC Team, *BwUniCluster 2.0 Hardware and Architecture* **2024**, https://wiki.bwhpc.de/e/BwUniCluster_2.0_Hardware_and_Architecture.
[56] M. Huttin, *Phase-field modeling of the influence of mechanical stresses on charging and discharging processes in lithium ion batteries*, Ph.D. thesis, Karlsruher Institut für Technologie (KIT), Karlsruhe **2014**, 10.5445/IR/1000039883.
[57] I. Traskunov, A. Latz, *Electrochim. Acta* **2021**, *379*, 138144, 10.1016/j.electacta.2021.138144.
[58] I. Traskunov, A. Latz, *Energy Technol.* **2021**, *9*, 16, 10.1002/ente.202000861.
[59] I. Traskunov, A. Latz, *Electrochim. Acta* **2022**, *434*, 141248, 10.1016/j.electacta.2022.141248.

Manuscript received: September 13, 2024
Revised manuscript received: January 24, 2025
Accepted manuscript online: January 24, 2025
Version of record online: ■■, ■■

RESEARCH ARTICLE

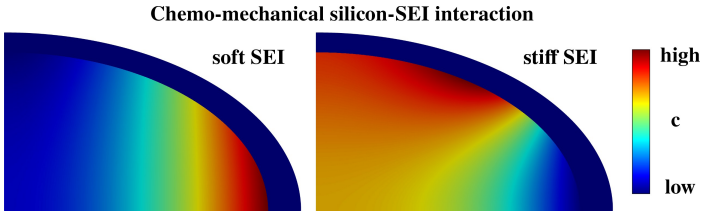

Silicon anodes are a promising next-generation anode material, for which consideration of the chemo-mechanical interaction is crucial. This publication investigates an elliptical silicon nanowire with surrounded SEI comparing a soft and stiff SEI scenario. Particularly, we examine the occurring stress distribution within the nanowire and the SEI as well as the mechanical influence on the lithium concentration distribution in the silicon nanowire.

R. Schoof, L. Köbbing*, Prof. Dr. A. Latz, Prof. Dr. B. Horstmann, Prof. Dr. W. Dörfler*

1 – 11

Elliptical Silicon Nanowire Covered by the SEI in a 2D Chemo-Mechanical Simulation

Batteries & Supercaps

Supporting Information

Elliptical Silicon Nanowire Covered by the SEI in a 2D Chemo-Mechanical Simulation

Raphael Schoof,* Lukas Köbbing,* Arnulf Latz, Birger Horstmann, and Willy Dörfler

Reprinted from Ref. [62].

Supporting Information to "Elliptical Silicon Nanowire Covered by the SEI in a 2D Chemo-Mechanical Simulation"

Raphael Schoof,*,+,[a] Lukas Köbbing,*,+,[b,c] Arnulf Latz,[b,c,d] Birger Horstmann,[b,c,d] Willy Dörfler[a]

SI. Symmetric Nanowire with Soft SEI

For comparison, we investigate the stresses and the lithiation characteristics of a symmetric silicon nanowire during cycling. We choose the radius as $L_{\mathrm{C}} = 38.73 \cdot 10^{-9}\,\mathrm{m}$ to obtain the same capacity as for the elliptical nanowire and the thickness of the SEI is chosen as an eighth of the core length as $L_{\mathrm{S}} = 4.84 \cdot 10^{-9}\,\mathrm{m}$.

We depict the stress distribution during lithiation at 30% SOC for the normal and tangential component in Figure S1(a) and (b). Inside the silicon core, both components show compressive stresses close to the outer boundary and tensile stresses close to the center. Inside the SEI, the normal stress is compressive close to the nanowire and vanishes at the outer boundary. The tangential component is tensile inside the whole SEI shell.

We show the evolution of the stress components at the interface during three half-cycles in Figure S1(c), (d), and (e). During lithiation, the normal component and the tangential component inside the silicon core show compressive stress, while the tangential component inside the SEI shell shows tensile stress. Stresses are opposite during delithiation. During the second lithiation, the normal stress inside the silicon and the tangential stress inside the SEI converge gradually to the stress during the first lithiation. The tangential stress inside the silicon during the second lithiation coincides with the first lithiation for the whole SOC range. The stress magnitude is always smaller than the maximum magnitude in the elliptical case.

In Figure S2(a), we depict the concentration distribution within the symmetric silicon nanowire during lithiation at 30% SOC. The concentration increases from the outer boundary during lithiation and no concentration anomaly occurs. The deviation of the lithium concentration at the outer boundary and the center from the mean during cycling is shown in Figure S2(b). As expected, during lithiation, the lithium concentration at the outer boundary exceeds the mean, while the concentration at the center is smaller than the mean. The concentration profiles are vice versa during delithiation, as expected.

[a] R. Schoof, Prof. Dr. W. Dörfler
Karlsruhe Institute of Technology (KIT), Institute for Applied and Numerical Mathematics, Englerstraße 2, 76131 Karlsruhe, Germany
E-mail: raphael.schoof@kit.edu

[b] L. Köbbing, Prof. Dr. A. Latz, Prof. Dr. B. Horstmann
German Aerospace Center (DLR), Wilhelm-Runge-Straße 10, 89081 Ulm, Germany
E-mail: lukas.koebbing@dlr.de

[c] L. Köbbing, Prof. Dr. A. Latz, Prof. Dr. B. Horstmann
Helmholtz Institute Ulm (HIU), Helmholtzstraße 11, 89081 Ulm, Germany

[d] Prof. Dr. A. Latz, Prof. Dr. B. Horstmann
Faculty of Natural Sciences, Ulm University, Albert-Einstein-Allee 47, 89081 Ulm, Germany

[+] These authors contributed equally.

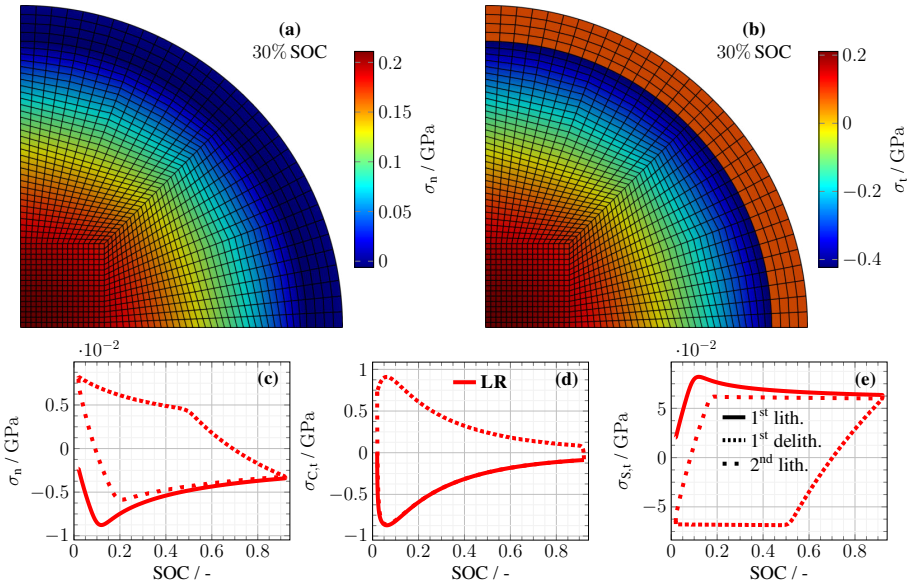

Figure S1. Cauchy stresses for the symmetric silicon nanowire with a soft SEI. Distribution of (a) normal and (b) tangential Cauchy stress inside the silicon core and the SEI shell during lithiation at 30% SOC. Evolution of Cauchy stress at the interface during three half cycles for (c) normal, (d) tangential core, and (e) tangential shell stress.

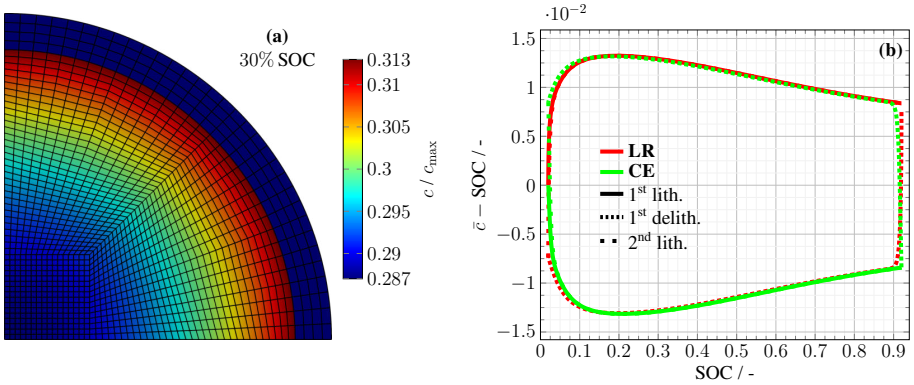

Figure S2. Lithium concentration for the symmetric silicon nanowire with a soft SEI. (a) Distribution of the lithium concentration inside silicon during lithiation at 30% SOC. (b) Deviation of the lithium concentration from the mean at the interface **LR** and the center **CE** during three half cycles.

SII. Variation of Plastic Strain Rate $\dot{\varepsilon}_0$

To estimate the influence of the viscoplastic behavior, we vary the plastic strain rate $\dot{\varepsilon}_0$ for the soft SEI. For higher values, plastic flow starts quickly upon reaching the yield condition, while it starts only slowly for smaller values. We depict the normal component of the stress inside the SEI shell in Figure S3(a) and the tangential component in Figure S3(b). The magnitude of both stress components and the size of the stress overshoot increase with decreasing plastic strain rate $\dot{\varepsilon}_0$. This is expected due to the retarded plastic flow for low plastic strain rates $\dot{\varepsilon}_0$. Nevertheless, the stress profiles reveal a similar shape for all tested values. For our simulations, we take the medium parameter $\dot{\varepsilon}_0 = 10^{-5}\,\mathrm{s}^{-1}$.

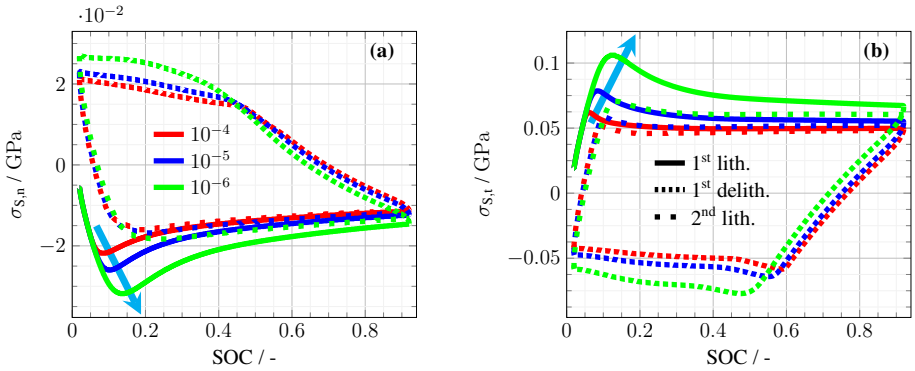

Figure S3. Variation of the plastic strain rate $\dot{\varepsilon}_0$ for the soft SEI. Evolution of the Cauchy stress inside the SEI during cycling for (a) the normal and (b) the tangential stress component.

SIII. Stress-Driven Lithium Flux $\boldsymbol{N}_{\mathrm{el}}$

We depict the stress-driven convective lithium flux $\boldsymbol{N}_{\mathrm{el}}$ during lithiation at 30% SOC in Figure S4 to complement the illustrations of the concentration-driven diffusive lithium flux $\boldsymbol{N}_{\mathrm{ch}}$ in Figure 3(d) and Figure 5(d). For the soft SEI case shown in Figure S4(a), the stress-driven lithium flux everywhere points towards the interior of the silicon core. The largest magnitude of the stress-driven flux occurs at point **UL**, where the largest stress values and stress gradients exist. For the stiff SEI case shown in Figure S4(b), the stress-driven lithium flux mostly points towards the interior of the silicon core. The largest magnitude of the stress-driven flux and a significant deviation from center-directed flux occurs at the outer boundary in a larger region around point **LR**, where the largest stress values and stress gradients exist. Combining both flux components, the total lithium flux always points towards the interior of the silicon core during lithiation for the soft SEI as well as for the stiff SEI.

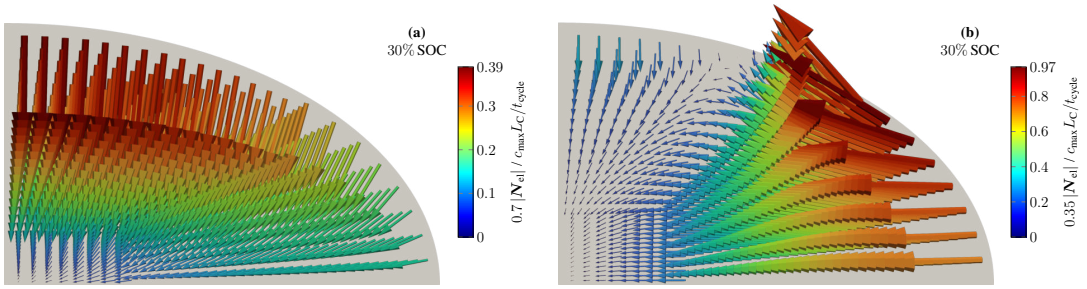

Figure S4. Stress-driven convective lithium flux $\boldsymbol{N}_{\mathrm{el}}$ for (a) the soft SEI case and (b) the stiff SEI case with different scaling for the fluxes.

SIV. Silicon Nanowire without SEI and C/20

We briefly investigate the stress and lithiation characteristics of an elliptical silicon nanowire without SEI during slow cycling with C/20 to estimate the influence of the SEI and the C-rate. The stress distribution in normal direction during lithiation at 30% SOC is depicted in Figure S5(a). The normal component vanishes at the outer boundary due to the surface condition and shows tensile stress throughout the nanowire. The largest stress magnitude is achieved close to the center along the major half-axis. We display the tangential stress component in Figure S5(b). The tangential component shows compressive stress at the outer boundary, with the largest magnitude occurring at the end of the minor half-axis at point **UL**. The tangential stress is tensile in a region around the center. In Figure S5(c), we depict the evolution of the tangential Cauchy stress during cycling at the points **LR** and **UL**. The curves reveal compressive stress during lithiation and tensile stress during delithiation. The largest stress magnitudes occur at the end of the minor half-axis at point **UL** for the whole SOC range. The stress distribution and evolution during slow cycling is similar to the soft SEI case and cycling with 1 C. Only the magnitude of the stresses is smaller in general due to the reduced C-rate.

In Figure S6, we display the lithium concentration distribution during lithiation at (a) 5%, (b) 30%, and (c) 90% SOC. The concentration shows the largest values at the end of the major half-axis at point **LR** due to the highest surface-to-volume ratio at this point. At 30% SOC, the distribution shows a concentration depletion at the end of the minor half-axis at point **UL**. The negatively scaled concentration gradient during lithiation at 30% SOC in Figure S6(d) indicates the chemical diffusion component of the lithium flux and illustrates the anomaly at point **UL**. In Figure S6(e), we depict the deviation of the lithium concentration at the points **LR**, **UL**, and **CE** from the mean during cycling. The evolution reveals the pronounced concentration increase/decrease at point **LR** during lithiation/delithiation. Furthermore, the evolution reveals the concentration anomaly at point **UL** during

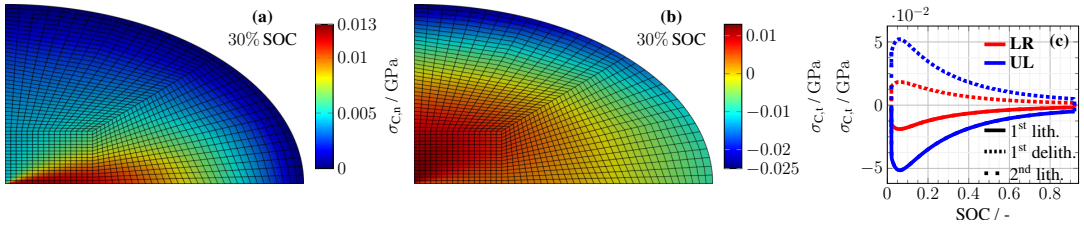

Figure S5. Cauchy stresses for the elliptical silicon nanowire without SEI during cycling with C/20. Distribution of (a) normal and (b) tangential Cauchy stress inside the silicon core during lithiation at 30% SOC. (c) Evolution of the tangential Cauchy stress at the points **LR** and **UL** during three half cycles.

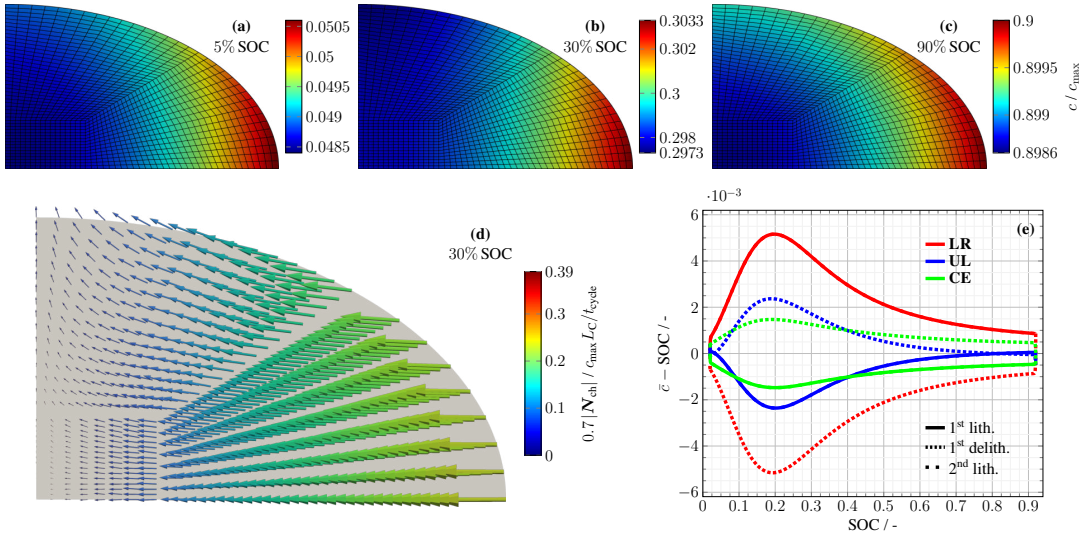

Figure S6. Concentration for silicon nanowire only with C/20. Lithium concentration for the elliptical silicon nanowire without SEI during cycling with C/20. Distribution of the lithium concentration inside silicon during lithiation at (a) 5%, (b) 30%, and (c) 90% SOC. (d) Concentration-driven diffusive lithium flux $\boldsymbol{N}_{ch}$ scaled with 0.7. (e) Deviation of the lithium concentration from the mean at the points **LR**, **UL**, and **CE** during three half cycles.

cycling between 10% and 40% SOC. In total, the lithiation characteristics during slow cycling without SEI are similar to standard cycling with SEI. Only the magnitude of the concentration deviations is significantly reduced due to the smaller C-rate.

SV. Voltage Hysteresis

To estimate the mechanical impact of the SEI shell on the lithiation behavior of the silicon nanowire, we compare the voltage during slow cycling with C/20 with the soft and the stiff SEI shell. Due to numerical reasons, we adjust the plastic strain rate to $\dot{\varepsilon}_0 = 10^{-6}\,\mathrm{s}^{-1}$. For both cases depicted in Figure S7, the voltages at point **LR** and **UL** are equivalent, revealing chemo-mechanical equilibrium during slow cycling. For the soft SEI case displayed in Figure S7(a), also the voltages during lithiation and delithiation coincide. In contrast, Figure S7(b) reveals that a voltage hysteresis arises for the stiff SEI case. This is in agreement with our explanation of the voltage hysteresis for spherical silicon nanoparticles covered by a stiff SEI shell presented in Refs. [1, 2].

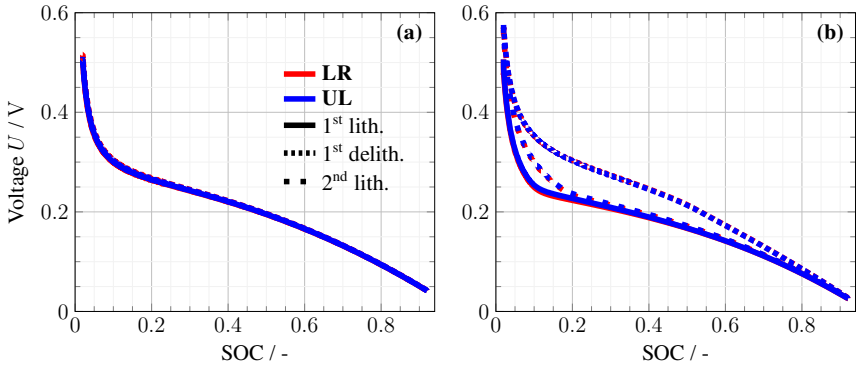

Figure S7. Voltage for the elliptical silicon nanowire covered by SEI during slow cycling with C/20 for (a) soft and (b) stiff SEI.

SVI. Table with Parameters

The simulation parameters and constants are summarized in Table S1. Additionally, we follow Ref. [3] and use $U_{\max} = 0.5\,\mathrm{V}$ and $U_{\min} = 0.05\,\mathrm{V}$ as maximal and minimal voltage for the lithiation and delithiation. Therefore, we choose $\bar{c}_0 = 0.02$ as constant initial concentration and 0.9 h as duration of one half cycle. The applied OCV curve

$$U_{\mathrm{OCV}}(\bar{c}) = \frac{-0.2453\,\bar{c}^3 - 0.00527\,\bar{c}^2 + 0.2477\,\bar{c} + 0.006457}{\bar{c} + 0.002493} \tag{S1}$$

is delivered by Ref. [4].

Table S1. Model parameters for the numerical experiments [3, 5, 6].

Description	Symbol	Value	Unit	Dimensionless
Universal gas constant	R_{gas}	8.314	$\mathrm{J\,mol^{-1}\,K^{-1}}$	1
Faraday constant	F	96485	$\mathrm{J\,V^{-1}\,mol^{-1}}$	1
Operation temperature	T	298.15	K	1
		Silicon		
Core length scale	L_{C}	$50 \cdot 10^{-9}$	m	1
Cycle time	t_{cycle}	3600	s	1
Diffusion coefficient	D	$1 \cdot 10^{-17}$	$\mathrm{m^2\,s^{-1}}$	14.4
OCV curve	U_{OCV}	Equation (S1)	V	$F/R_{\mathrm{gas}}T \cdot$ (S1)
Young's modulus	E_{C}	$90.13 \cdot 10^{9}$	Pa	116.74
Partial molar volume	v_{pmv}	$10.96 \cdot 10^{-6}$	$\mathrm{m^3\,mol^{-1}}$	3.41
Maximal concentration	$c_{\max}$	$311.47 \cdot 10^{3}$	$\mathrm{mol\,m^{-3}}$	1
Initial concentration	c_0	$6.23 \cdot 10^{3}$	$\mathrm{mol\,m^{-3}}$	$2 \cdot 10^{-2}$
Poisson's ratio	ν_{C}	0.22	–	0.22
		SEI		
Shell length scale	L_{S}	$6.25 \cdot 10^{-9}$	m	0.125
Young's modulus	E_{S}	$900 \cdot 10^{6}$	Pa	1.17
Poisson's ratio	ν_{S}	0.25	–	0.25
Yield stress	σ_{Y}	$49.5 \cdot 10^{6}$	Pa	0.052
Strain measurement	β	2.94	–	2.94
Stress constant	σ_{Y^*}	$49.5 \cdot 10^{6}$	Pa	0.052
Tensile plastic strain rate	$\dot{\varepsilon}_0$	$1.0 \cdot 10^{-5}$	$\mathrm{s^{-1}}$	0.036

References

[1] L. Köbbing, A. Latz, B. Horstmann, *Adv. Funct. Mater.* **2024**, *34*, 2308818, DOI 10.1002/adfm.202308818.
[2] L. Köbbing, Y. Kuhn, B. Horstmann, *ACS Appl. Mater. Interfaces* **2024**, *16*, 67609–67619, DOI 10.1021/acsami.4c12976.
[3] L. von Kolzenberg, A. Latz, B. Horstmann, *Batter. Supercaps* **2022**, *5*, 1–12, DOI 10.1002/batt.202100216.
[4] C. K. Chan, H. Peng, G. Liu, K. McIlwrath, X. F. Zhang, R. A. Huggins, Y. Cui, *Nat. Nanotechnol.* **2007**, *3*, 31–35, DOI 10.1038/nnano.2007.411.
[5] R. Schoof, J. Niermann, A. Dyck, T. Böhlke, W. Dörfler, *Comput. Mech.* **2024**, DOI 10.1007/s00466-024-02499-9.
[6] C. V. Di Leo, E. Rejovitzky, L. Anand, *Int. J. Solids Struct.* **2015**, *67-68*, 283–296, DOI 10.1016/j.ijsolstr.2015.04.028.

Lukas Köbbing

Curriculum Vitae

lukas.koebbing@dlr.de
linkedin.com/in/lukas-koebbing

Education

since 11/2020 **Ph.D. student**, *German Aerospace Center (DLR), Helmholtz Institute Ulm (HIU), and Ulm University*, Ulm, Germany.
Thesis: "Understanding Growth and Performance Drawbacks of the Solid-Electrolyte Interphase in Lithium-Ion Batteries"
Projects: DFG research training group "SiMET - Simulation of Mechano-Electro-Thermal Processes in Lithium-Ion Batteries" and Horizon Europe project "OPINCHARGE - OPerando analyses and modelling of INterface dynamics and CHARGE transport in lithium-ion batteries"

2019 – 2020 **Master of Science in Physics**, *University of Bonn*, Bonn, Germany.
Master thesis: "Quantum thermalization of charge and spin in the isolated Fermi-Hubbard model"

2017 **Semester abroad**, *University of Glasgow*, Glasgow, Scotland.

2015 – 2019 **Bachelor of Science in Physics**, *University of Bonn*, Bonn, Germany.
Bachelor thesis: "Topological insulators"

Peer-Reviewed Publications

2025 **Elliptical Silicon Nanowire Covered by the SEI in a 2D Chemo-Mechanical Simulation**
Schoof, R., Köbbing, L., Latz, A., Horstmann, B. & Dörfler, W. *Batteries & Supercaps* **2025**, 8 (5), e202400604, https://doi.org/10.1002/batt.202400604.

2024 **Slow Voltage Relaxation of Silicon Nanoparticles with a Chemo-Mechanical Core-Shell Model**
Köbbing, L., Kuhn, Y. & Horstmann, B. *ACS Applied Materials & Interfaces* **2024**, 16 (49), 67609–67619, https://doi.org/10.1021/acsami.4c12976.

2024 **Voltage Hysteresis of Silicon Nanoparticles: Chemo-Mechanical Particle-SEI Model**
Köbbing, L., Latz, A., & Horstmann, B. *Advanced Functional Materials* **2024**, 34 (7), 2308818, https://doi.org/10.1002/adfm.202308818.

2023 **Growth of the Solid-Electrolyte Interphase: Electron Diffusion versus Solvent Diffusion**
Köbbing, L., Latz, A., & Horstmann, B. *Journal of Power Sources* **2023**, 561, 232651. https://doi.org/10.1016/j.jpowsour.2023.232651.

Conference Contributions

2025 **Chemo-Mechanical Core-Shell Model Explaining the Silicon Voltage Hysteresis and Long-Term Relaxation**
Köbbing, L., Kuhn, Y., Latz, A., and Horstmann, B. *21st Symposium on Modeling and Experimental Validation of Electrochemical Energy Technologies (ModVal2025)*, Karlsruhe, Germany, 10. – 12. March 2025, Talk.

2024 **Explaining the Voltage Hysteresis and Slow Relaxation of Silicon Nanoparticles with a Chemo-Mechanical Particle-SEI Model**
Köbbing, L., Latz, A., and Horstmann, B. *Pacific Rim Meeting on Electrochemical and Solid State Science*, Honolulu, USA, 06. – 11. October 2024, Poster.

2024 **Understanding the Silicon Voltage Hysteresis by considering the impact of the Solid-Electrolyte Interphase (SEI)**
Köbbing, L., Latz, A., and Horstmann, B. *Advanced Battery Power*, Münster, Germany, 09. – 11. April 2024, Poster.

2024 **Elucidating the Silicon Voltage Hysteresis by Mechanical Coupling of Anode Particles and the SEI**
Köbbing, L., Latz, A., and Horstmann, B. *Spring Meeting of the Deutsche Physikalische Gesellschaft (DPG)*, Berlin, Germany, 17. – 22. March 2024, Talk.

2023 **Continued SEI Growth and its Impact on the Silicon Potential Hysteresis**
Köbbing, L., Latz, A., and Horstmann, B. *74th Annual Meeting of the International Society of Electrochemistry*, Lyon, France, 03. – 08. September 2023, Talk.

2023 **Description of the Silicon Voltage Hysteresis with a Visco-Elastoplastic SEI Model**
Köbbing, L., Latz, A., and Horstmann, B. *HIU Biennial Meeting*, Ulm, Germany, 11. – 12. July 2023, Talk.

2023 **Modeling of the Solid-Electrolyte Interphase: Transport Mechanisms and Mechanics**
Köbbing, L., Latz, A., and Horstmann, B. *243rd Meeting of the Electrochemical Society*, Boston, USA, 28. May – 02. June 2023, Talk.

2022 **How Does the Solid-Electrolyte Interphase Grow? Transport Mechanisms, Mechanics and Interfaces**
Köbbing, L., von Kolzenberg, L., Latz, A., and Horstmann, B. *Workshop on Computational Modeling of Batteries*, Reisensburg, Germany, 23. – 26. October 2022, Poster.

2022 **Theory and Modeling of Transport, Interfaces and Mechanics inside the Solid Electrolyte Interphase**
Köbbing, L., Horstmann, B., and Latz, A. *International Meeting on Lithium Batteries*, Sydney, Australia, 26. June – 01. July 2022, Poster.

2022 **Theory and Simulation of Transport and Mechanics of a Polycrystalline SEI**
Köbbing, L., Latz, A., and Horstmann, B. *31st Topical Meeting of the International Society of Electrochemistry*, Aachen, Germany, 15. – 19. May 2022, Poster.

2022 **Modeling and Simulation of Transport, Interfaces and Mechanics inside the SEI**
Köbbing, L., Horstmann, B., and Latz, A. *18th Symposium on Modeling and Experimental Validation of Electrochemical Energy Technologies (ModVal2022)*, Hohenkammer, Germany, 14. – 16. March 2022, Poster.

Journalistic Publication

2024 **Batterien wie Sand am Meer**
Köbbing, L., Latz, A., & Horstmann, B. *Physik Jorunal* **2024**, 23 (5), 28-34, https://pro-physik.de/zeitschriften/physik-journal/2024-5/,
Preprint: https://elib.dlr.de/204279/.

Awards

2022 **Poster Prize** at the Conference *"18th Symposium on Modeling and Experimental Validation of Electrochemical Energy Technologies (ModVal2022)"*, Hohenkammer near Munich, Germany.

2019 **Bachelor Prize** of the *Foundation of Physics and Astronomy in Bonn*.

2017 **Scholarship Erasmus** for the semester abroad.

Place, Date

Lukas Köbbing

Declaration of Authorship

Ich erkläre hiermit, dass ich die vorliegende Arbeit selbstständig verfasst und keine anderen als die angegebenen Quellen und Hilfsmittel benutzt habe. Alle wörtlich oder sinngemäß aus anderen Werken übernommenen Aussagen sind als solche gekennzeichnet. Außerdem erkläre ich, dass ich die Satzung der Universität Ulm zur Sicherung guter wissenschaftlicher Praxis in der gültigen Fassung beachtet habe. Weiterhin versichere ich, dass die Arbeit weder vollständig noch in wesentlichen Teilen Gegenstand eines anderen Prüfungsverfahrens gewesen ist. Die eingereichten Exemplare stimmen miteinander überein.

I hereby declare that I have written this thesis independently and have not used any sources or means other than those indicated. All statements taken verbatim or in content from other works are marked as such. Furthermore, I declare that I have complied with the statutes of the University of Ulm for the adherence to good scientific practice in the currently valid version. Moreover, I assure that this thesis has neither completely nor in essential parts been the subject of another examination procedure. The submitted copies agree with each other.

Place, Date

Lukas Köbbing